Thèse n° 7962

Additive Manufacturing of $L1_2$ Precipitate Strengthened Nickel and Aluminum Alloys

Présentée le 8 juillet 2020

à la Faculté des sciences et techniques de l’ingénieur
Laboratoire des matériaux photoniques et caractérisation
Programme doctoral en science et génie des matériaux

pour l’obtention du grade de Docteur ès Sciences

par

Seth James GRIFFITHS

Acceptée sur proposition du jury

Dr Y. Leterrier, président du jury
Prof. P. Hoffmann, Dr C. Leinenbach, directeurs de thèse
Prof. D. Dunand, rapporteur
Dr E. Jägle, rapporteur
Prof. R. Logé, rapporteur

École
polytechnique
fédérale
de Lausanne

2020

Acknowledgements

The work contained in this thesis was completed during my time at Empa (Swiss Federal Laboratories for Materials Science and Technology), August 2016 to July 2020, in the group for Alloy Design for Advanced Processes in the Laboratory for Advanced Materials Processing (Abt. 204). Funding for this work was provided by the Additive Manufacturing and Metallic Microstructure (AM3) challenge of the Competence Center for Materials Science and Technology (CCMX). Parts of this research work were done in collaboration with Northwestern University, Braidy Industries (formerly NanoAl LLC), and the Laboratoire de métallurgie thermomécanique (LMTM) at EPFL.

I would like to extend my utmost gratitude to my supervisor at Empa, Christian Leinenbach, for giving me the opportunity to do my PhD studies at Empa. I greatly appreciate his invaluable guidance during my studies, and the many opportunities he has provided for professional development.

I would also like to extend my utmost appreciation to my EPFL advisor, Patrik Hoffmann, for his valued mentoring and constant nudge for me to dig deeper into the fundamentals.

My thesis contains a decent amount of electron microscopy and that would not have been possible without the help from Marta Rossell. I greatly appreciate all of the invaluable STEM/TEM assistance she has provided me over years.

I would like to thank Franz Stebler for all of his assistance with the Additive Manufacturing machine and the countless samples he machined for me.

A large part of this thesis was done in collaboration with Northwestern University and Braidy Industries (formerly NanoAl LLC). I would like to thank Prof. David Dunand of Northwestern University for providing his expertise on Al alloys. I would also like to thank Dr. Nhon Q. Vo and Joe Croteau at Braidy Industries for allowing me to work with their new alloy, for mechanical testing, and invaluable support over the years.

This thesis would not have been possible without the contribution of countless individuals that provided scientific guidance, material/equipment support, and mentoring over the past few years. I would like to say thanks to: Dr. Toni Ivas, Dr.

Xiaoshuang Li, Dr. Anthony De Luca, Dr. Kai Zweiacker, Viktor Lindström, Dr. Ariyan Arabi-Hashemi, Rafał Wróbel, Michael Stiefel, Dr. Rolf Erni, Dr. Quang Tri Le, Shreyas Joglekar, Joanna Pado, Dr. Oleksii Liashenko, and Marvin Schuster.

Lastly, I would like to thank my family and friends for all of the support they have given me over the past few years. I would especially like to thank my wife, Melissa, who has always been supportive of me during these stressful times.

Abstract

Metal Additive Manufacturing (AM) technologies have enabled the manufacturing of parts with complex geometries that were previously not feasible with conventional manufacturing. Unfortunately, many commercial engineering alloys (with the exception of alloys for welding) were designed with conventional manufacturing in mind and can behave poorly in the rapid solidification and thermal conditions that go along with AM. Research is needed to optimize the higher performance engineering alloys, such as precipitation hardened alloys, for AM. One important class of precipitates in both the nickel-base and aluminum-base superalloys is the intermetallic $L1_2$ –structured (Strukturbericht notation) intermetallics. Many scientific challenges must be overcome prior to widespread industrial usage of these alloys. AM of $L1_2$-strengthened Ni-base superalloys results in extensive micro-cracking and AM of $L1_2$-strengthened Al-base alloys has been successful but requires further research to understand the material behavior. This thesis focuses on overcoming the scientific challenges for the AM of $L1_2$-strengthened alloys.

A new Al-Mg-Zr alloy strengthened via $L1_2$-structured Al_3Zr precipitates, Addalloy®,was successfully fabricated for the first time with Laser-Powder Bed Fusion (L-PPF). The as-fabricated Al-Mg-Zr alloy displayed a unique bimodal grain structure: (i) the bottom of the melt pools consisted of fine equiaxed grains (~1 µm) and (ii) the top of the melt pool consisted of columnar grains (up to 40 µm long). The bimodal microstructure was attributed to the changing solidification conditions during the lifetime of the melt. A new microstructure modification strategy, laser rescanning, was shown to refine the microstructure. The grain refinement was attributed to the reduced melt pool depths of the additional scans, thus breaking up the previously solidified columnar grains. Scanning transmission electron microscopy (STEM) investigations of peak-aged (400˚C, 8 h) samples reveal both continuous (~2 nm in diameter) and discontinuous (~5 nm wide and hundreds of nanometers long) coherent, secondary $L1_2$-Al_3Zr precipitates. The Al-Mg-Zr in the peak aged (400˚C, 8 h) condition had a 385 MPa yield strength and a 19% elongation at fracture. The excellent combination of strength and ductility was attributed to the bimodal microstructure. For short-term elevated temperature yield tests, as-fabricated samples displayed higher yield strengths than peak-aged samples at temperatures above 150˚C (e.g., 87 vs 24 MPa at 260˚C). For longer term creep tests at 260 ˚C, both as-fabricated and peak-aged samples displayed near-identical creep behavior. The reduced elevated temperature performance of the peak aged samples was attributed to coarsening of grain-boundary precipitates during aging, decreasing their ability to inhibit grain-boundary sliding (GBS) of the fine equiaxed grains.

The micro-cracking of CM24LC, a Ni-base superalloy, was attributed to both solidification and liquation cracking. Based on experimental evidence, reduction in the solidification interval of CM247LC was investigated as a candidate for micro-crack mitigation and a new alloy was developed. As Hf is found to have a significant influence on the freezing range of the alloy, a new CM247LC without Hf was produced and tested. Samples fabricated with the Hf-free CM247LC, CM247LC NHf, in combination with optimized processing conditions exhibit a reduction in crack density of 98%.

Keywords

Additive Manufacturing, Laser-Powder Bed Fusion, Al-base superalloys, Ni-base superalloys, solidification

Résumé

Les technologies de fabrication additives (AM) pour métaux permet la création de pièces à géométrie complexe, non réalisables par les méthodes conventionnelles. Malheureusement, de nombreux alliages commerciaux ont été conçus pour les méthodes conventionnelles, et peuvent se comporter de manière inadéquate lors de la fabrication additive. L'optimisation des alliages à hautes performances, tels que les alliages durcis par précipitation, doit être étudié. Une classe importante de précipités dans les superalliages à base de nickel et d'aluminium est celle des intermétalliques à structure L12. De nombreux défis scientifiques doivent être surmonté avant que ces alliages ne puissent être utilisés à grande échelle dans l'industrie. Les superalliages de nickel renforcés en L12 sont sujet aux microfissures. La consolidation d'alliages d'aluminium renforcés en L12 est prometteuse mais nécessitent l'étude du comportement du matériau. Cette thèse se concentre sur les défis scientifiques liés à l'AM d'alliages renforcés en L12.

Un nouvel alliage Al-Mg-Zr renforcé par des précipités L12-Al3Zr, Addalloy®, a été fabriqué avec succès par fusion laser sur lit de poudre (L-PPF). L'alliage, après impression, présente une structure granulaire bimodale unique : (i) le fond des bassins de fu-sion est constitué de grains équiaxes de taille réduite (~1 µm) et (ii) la partie supé-rieur des bassins de fusion est constitué de grains colonnaires (jusqu'à 40 µm de long). La microstructure bimodale a été attribuée aux changement des conditions de solidifi-cation au cour de la fonte. Une nouvelle stratégie de balayage laser, le rescannage, a permis d'affiner la microstructure. La réduction des grains a été attribué à la création de bassins de fusion moins profond, lors des balayages successifs, ce qui a permis de briser les grains colonnaires antérieurement solidifiés. La caractérisation d'échantillons traité thermiquement (400°C, 8 h) révèle des précipités L12-Al3Zr secondaires cohérents, à la fois continus (⌀~2 nm) et discontinus (~5 nm de large, >100 nm de long). Après ce traitement thermique, l'alliage Al-Mg-Zr présente une limite d'élasticité de 385 MPa et un allongement à la rupture de 19 %. L'excellente combinaison de résistance et de ducti-lité a été attribuée à la microstructure bimodale. Lors d'essais de limite d'élasticité à température élevée, les échantillons directement après impressions présentaient des limites d'élasticité plus élevées que les échantillons recuits, (par exemple, 87 contre 24 MPa à 260°C). Les tests de fluage à long terme, d'échantillons après fabrication ou re-cuit, présentent des comportements presque identiques. La performance réduite des échantillons recuit a été attribuée à la croissance des précipités sur les joints de grains, diminuant leur capacité à inhiber le glissement des joints de grains (GBS) dans les ré-gions équiaxes.

La microfissuration du superalliage de Nickel CM247LC, a été attribuée mécanismes de fissuration durant solidification et liquéfaction . Après la réalisation de tests ini-tiaux, la réduction de l'intervalle de solidification du CM247LC semble être la clé pour at-ténuer la formation de microfissures, et un nouvel alliage a été développé. L'hafnium ayant une forte influence sur l'intervalle de solidification de l'alliage, un nouvelle alliage CM247LC sans Hf a été produit et testé. Les échantillons fabriqués avec l'alliage expéri-mental, CM247LC NHf, en combinaison avec des conditions de traitement optimisées, montrent une réduction des fissures de 98%.

Mots-clés

Fabrication additive, Fusion laser sur lit de poudre, Superalliage d'aluminium, Superalliage de nickel, Solidification

Contents

Acknowledgements i

Abstract iii

Keywords iv

Résumé v

Mots-clés vi

List of Figures xi

List of Tables xxvi

Chapter 1 Introduction 27

Chapter 2 State of the Art 31

- 2.1 Laser Powder Bed Fusion (L-PBF) 31
- 2.2 Laser Melting/Welding Primer 32
- 2.3 Solidification Primer 35
- 2.4 Nickel-Base Superalloy Metallurgy Primer 42
- 2.5 Aluminum-Base Superalloy Metallurgy Primer 47
- 2.6 Elevated Temperature Mechanical Behavior Primer 48
- 2.7 PBF of Aluminum-Base Superalloys 50
- 2.8 PBF of Nickel-base Superalloys 52
- 2.9 Aim of the Thesis 55

Chapter 3 Materials and Methods 57

- 3.1 Aluminum-based Superalloy 57
- 3.1.1 Materials 57
- 3.1.2 Additive Manufacturing 57
- 3.1.3 Microstructure Characterization 59

3.1.4 Thermodynamic Simulations 60
3.1.5 Room Temperature Mechanical Properties 60
3.1.6 Elevated Temperature Mechanical Properties 60
3.2 Nickel-base Superalloys 61
3.2.1 Materials 61
3.2.2 Additive Manufacturing 62
3.2.3 Microstructure and Defect Characterization 63
3.2.4 Thermodynamic Calculations 64
3.2.5 Differential Scanning Calorimetry 64
3.2.6 X-Ray Diffraction 64
3.2.7 Crack Density Analysis 64
3.2.8 Liquation Cracking Experiments 65
3.2.9 Mechanical Properties 65
Chapter 4 Metallurgy of L-PBF Fabricated Addalloy 69
4.1 Powder Microstructure 69
4.2 As-fabricated Microstructure 70
4.3 Microstructure Formation 76
4.4 Microstructure Modification via Laser Rescanning 82
4.4.1 Motivation 82
4.4.2 Experimental Details 83
4.4.3 Microstructure 84
4.4.4 Mechanisms 87
4.5 Conclusions 93
Chapter 5 Metallurgy of Heat Treated Addalloy 95
5.1 Peak-Age Determination 95
5.2 Ex-Situ Microstructure Characterization 96
5.3 In-Situ STEM Experiments 101
5.3.1 Experimental Details 101
5.3.2 In-Situ STEM Results 102
5.4 Microstructural Evolution 105

5.5 Conclusions 107

Chapter 6 Addalloy Mechanical Properties 109

6.1 Room Temperature Mechanical Properties 109

6.2 Elevated Temperature Mechanical Properties 111

6.2.1 Elevated Temperature Yield Strength 111

6.2.2 Creep Testing 113

6.2.3 Microstructure of Crept samples 115

6.3 Discussion 120

6.3.1 Room Temperature Mechanical Properties 120

6.3.2 Elevated Temperature Mechanical Properties 123

6.4 Conclusions 126

Chapter 7 Metallurgy of L-PBF Fabricated CM247LC 127

7.1 Powder Microstructure 127

7.2 As-fabricated Microstructure 127

7.3 Microcracking in the as-fabricated samples 133

7.4 Chess Scanning Strategy 135

7.5 Microstructure and potential micro-crack formation mechanisms in CM247LC 137

7.6 Conclusions 138

Chapter 8 CM247LC Alloy Modification 139

8.1 Micro-Crack Mitigation – Alloy Design 139

8.2 Processing of CM247LC NHf and comparison with CM247LC 142

8.2.1 Powder Microstructure 142

8.2.2 As-Fabricated Microstructure 143

8.2.3 Defects 146

8.2.4 Thermal Analysis 148

8.2.5 Micro-crack Comparison with CM247LC 148

8.3 Discussion 151

8.3.1 Reduction of Micro-cracking in CM247LC NHf 151

8.3.2 Factors Influencing Melt Pool Width 153

8.3.3 Influence of Other Processing Conditions 158
8.4 Conclusions 162
Chapter 9 Metallurgy of heat treated CM247LC and CM247LC NHf 164
9.1 Peak Age Determination 164
9.2 Microstructure and defects of heat treated CM247LC and CM247LC NHf 167
9.3 Discussion 170
9.4 Conclusions 173
Chapter 10 Conclusions and Future Outlook 174
10.1 Conclusions 174
10.2 Future Outlook 175
Appendix A– Supplementary Data 178
References 190
Curriculum Vitae 200

List of Figures

Figure 2.1: Schematic of the L-PBF process. Image from [12] 32

Figure 2.2: Normalized power vs normalized traverse rate diagram. Tp=1 and Tp=2 signify the borders for melting and vaporization, respectively, and their definition can be found in [17]. Plot taken from [17]. 34

Figure 2.3: Two hypothetical binary phase diagrams highlighting the two possible elemental partition conditions (a) $k < 1$, solute enrichment of the liquid and (b) $k > 1$, solute enrichment of the solid. Figure based off of [24]. 37

Figure 2.4: (a) solute redistribution in the case of no solid diffusion, but complete mixing in the liquid. This is often termed Schiel solidification. (b) no diffusion in the solid, and limited liquid diffusion. 38

Figure 2.5: Constitutional undercooling diagram showing the influence of high and low thermal gradients. 41

Figure 2.6: G/R diagram showing the solidification mode as a function of thermal gradient and solidification front velocity. Also, a BSE image of a weld on CM247LC showing what different growth modes look like.41

Figure 2.7: Variation of the solidification front velocity (R) and the thermal gradient G in a moving laser beam generated melt. 42

Figure 2.8: Images of the microstructure of a CM247LC directionally solidified turbine blade. The images were taken from the root of the turbine blade. (a) Optical image of the microstructure. The blueish tint cross in the middle of the image is a dendrite and the orange tint areas are interdendritic. Carbides and γ/γ' eutectic (left over from casting) are visible. (b) BSE image showing the γ' precipitates (highlighted by a black arrow) 43

Figure 2.9: Plot of shear stress as a function precipitate radius. Dashed lines represent precipitate bowing and solid lines represent cutting. The high volume fraction of strengthening phase in the superalloys increases the strength from A to B. Ordering can further improve the strength. 44

Figure 2.10: A idealized creep curve. Region I is primary creep, Region II is secondary or steady state creep, and Region III is tertiary creep. 49

Figure 3.1: Parameter survey of the Al-2.90Mg-2.10Zr (wt. %, Batch 3) on the SismaMySint 100. Laser power was fixed at 175W (7.35x10^6 W/cm^2) and the layer thickness was fixed at 30 µm. Each data point is an average of three measurements. 59

Figure 3.2: Parameter survey of the CM247LC on the SismaMySint 100. Laser power was fixed at 175W (7.35x10^6 W/cm^2) and the layer thickness was fixed at 30 µm. Each point is an average of 3 measurements. 63

Figure 3.3: Temperature and pressure cycle of the HIP treatment. 67

Figure 4.1: BSE images of the cross-sectioned Al-3.66Mg-1.57Zr (wt.%, batch 5) powder. (a) Overview of the spherical powder (b) higher magnification image showing powder particles both with and without bright precipitates. (c) A single powder particle with minimal bright precipitates, assumed to be Al_3Zr. White arrow points to region rich in Zr and poor in Mg. (d) A powder particle with numerous bright precipitates (black arrow points to one such precipitate) assumed to be Al_3Zr. 70

Figure 4.2: Optical micrograph of an as-fabricated sample (Al-2.90Mg-2.10Zr, wt. %, Batch 3). 71

Figure 4.3: (a,b) BSE images of the single-scanned sample showing a duplex grain microstructure consisting of regions with columnar grains and equiaxed micron-size grains (most containing one primary Al_3Zr precipitate). (Al-3.60Mg-1.18Zr, wt. %, Batch 2). Figure from [90] 71

Figure 4.4: (a) EBSD Image Quality (IQ) map of asingle-scanned specimen showing the columnar and equi-axed grain regions. A melt pool boundary is shown by a black line. (b) EBSD pole figure from the fine grain region marked b in the IQ map. (c) EBSD pole figure from the coarse grain region marked c in the IQ map. (Al-3.60Mg-1.18Zr, wt. %, Batch 2). Figure from [90]....................72

Figure 4.5: (a) Low magnification ADF STEM image of a precipitate-rich region showing cuboidal, submicron $L1_2$-Al_3Zr precipitates and micron-sized α-Al grains. (b) Low Magnification ADF STEM image of the precipitate-free coarse grain region showing larger α-Al grains and oxide particles/pores (white arrow) (Al-3.60Mg-1.18Zr, wt.%, Batch 2)72

Figure 4.6: STEM HAADF and corresponding STEM-EDX elmental maps of a L12 precipitate in the fine grain region of an as-fabricated Al-3.60Mg-1.18Zr (wt.%, Batch 1) sample. Figure from [67] 73

Figure 4.7: Coarse-grain region of an as-fabricated sample (Al-3.60Mg-1.18Zr, wt.%, Batch 1) imaged via STEM (ADF- image and elemental EDX maps using Si-K, Zr-K, Al-K, Mg-K, Fe-K and O-K lines) showing three types of precipitates : (i) Mg- and O-rich oxide particles, ~100 nm in diameter; (ii) Mg- and Si-rich particles, ~50 nm in diameter, (iii) Fe-rich particles, ~50 nm diameter, on the grain boundaries. One example for each type of precipitates is highlighted on the ADF-STEM image, with labels O, S and F, respectively. The black arrow points to a circular feature of enhanced contrast. 74

Figure 4.8: (a) High resolution ADF-STEM image, along the [001] zone axis, of the upper left corner of the precipitate in Figure 3 and corresponding FFT of the highlighted precipitate area (black-rimmed square). (b) High resolution ADF-STEM image of the lower left corner of the precipitate in Fig-ure 3 and corresponding FFT of the highlighted matrix area (white-rimmed square). (c) Selected area electron diffraction pattern along [001] taken from a separate precipitate showing the 100- and 010-type superlattice reflections of the L12 structure. (Al-3.60Mg-1.18Zr, wt.%, Batch 2). Figure from [90] 75

Figure 4.9: (a) ADF-STEM image of an $L1_2$ structured precipitate with a feather appearance from an as-fabricated Al-3.60Mg-1.18Zr sample (wt.%, Batch 2). (b) Higher resolution ADF-STEM image of a corner of the precipitate. (c) FFT of (b) showing the 100- and 010- type superlattice reflections of the $L1_2$ structure. 75

Figure 4.10: (a) Low magnification TEM image of the coarse grain region of an as-fabricated Al-3.60Mg-1.18Zr sample (wt.%, Batch 2). The white circle approximately corresponds to the region where the SAED pattern shown in (b) was acquired from. The black circle approximately corresponds to the region where the SAED pattern shown in (c) was acquired from. No superlattice reflections characteristic of $L1_2$ precipitates were present. 76

Figure 4.11: Equilibrium Al-rich Al-Zr binary phase diagram (adapted from Murray [23]) with metastable Al_3Zr (L12) solvus line (dotted). Figure from [92] 77

Figure 4.12: Scheil-Gulliver solidification curve (calculation performed with Thermocalc) for Al-3.66Mg-1.57Zr-0.2Si-0.1Fe (wt. %). 78

Figure 4.13: Plot of molar Gibbs free energy as a function of temperature (calculation performed with Thermocalc) for Al-3.66Mg-1.57Zr-0.2Si-0.1Fe (wt. %) 79

Figure 4.14: Schematic of melt pool and associated plot of solidification front velocity as a function of depth z in the melt pool. Solidification front velocity increases towards the surface of the melt pool, crossing a threshold of solute trapping preventing the precipitation of Al_3Zr precipitates. 80

Figure 4.15: Optical micrographs comparing the melt pools of (a) single-scan and (b) double-scan sample. The rescanning results in shallower melt pools. (Al-3.60Mg-1.18Zr wt.%, Batch 2) 85

Figure 4.16: Optical micrographs comparing the melt pools of (a) single-scan and (b) double-scan sample. Higher magnification images of the single-scan and double-scan are shown in (c) ad (d) respectively. The rescanning results in shallower melt pools and a smoother surface finish. (Al-2.90Mg-2.10Zr wt.%, Batch 3) 85

Figure 4.17: a.) EBSD grain maps of (a) single, (b) double, and (c) triple scans showing grain refinement with additional scans. White areas on the EBSD grain maps are regions filtered out; d) Distribution of area fractions vs. grain diameter, showing that rescanning reduces the fraction of large columnar grains and increases the fraction of fine, equiaxed grains. (Al-3.60Mg-1.18Zr wt.%, Batch 2) 86

Figure 4.18: EBSD grain maps comparing double-scans where the second scan is performed (a) parallel or (b) perpendicular to the first scan. White areas on the EBSD grain maps are regions of low confidence index (0.1) (c) Area fractions of each grain diameter showing that rescanning perpendicular to the first scan results in more grain refinement than rescanning in a parallel direction. (Al-3.60Mg-1.18Zr wt.%, Batch 2) 87

Figure 4.19: Schematic of melt pool depth differences between single- and double-scan cases. Reduced laser absorptivity on a consolidated surface and increased heat transfer result in a shallower melt pool during the rescan. Scan direction is perpendicular to image plane. The micrograph of a double-scanned single line shows the melt pool boundaries (arrows). 88

Figure 4.20; (a) Single laser line scan experiment with two different surface roughnesses. The left was sand blasted and the right was ground with 4000 grit SiC paper. The laser movement is clockwise. The melt pool size is overall small in the polished regions than in the rough regions, although some areas in the polished region have large melt sizes likely due to increased coupling by defects. (b) Cross section of line scan on smooth surface. 110 μm wide and 45 μm deep (c) Cross section of melt pool on rough surface. 260 μm side and 180 μm deep. 90

Figure 4.21: Single laser line experiments with two different surface roughnesses on a Al plate. The left was sand blasted and the right was ground with 4000 grit SiC paper. The melt pool appearance is consistent in the rough surface. 91

Figure 5.1: Hardness evolution upon isothermal aging at 400 °C of Al-3.60Mg-1.18Zr wt.% (black circles) and Al-3.66Mg-1.57Zr wt.% (blue diamonds). Each data point is the average of multiple samples fabricated with various laser energy densities. Error bars represent one standard deviation of ten measurements of each sample. Plot courtesy of J. Croteau. [67] 96

Figure 5.2: BSE images of a peak-aged (400°C / 8 h) sample (Al-3.60Mg-1.18Zr, wt.% Batch 1) showing a duplex grain microstructure consisting of regions with columnar grains and equiaxed micron-size grains (each containing one primary Al_3Zr precipitate). (b) higher magnification BSE image taken from the white box in (a). White arrows point to a few sub-micron grain boundary particles observed in the coarse grain region. 97

Figure 5.3: BSE image of an overaged (400°C / 144 h) sample (Al-3.60Mg-1.18Zr, wt.% Batch 1). Black arrows point to a few elongated bright particles that are assumed to be $D0_{23}$ structured Al_3Zr....97

Figure 5.4: EBSD grain maps of (a) the peak-aged (400°C / 8 h) sample and (b) the overaged (400°C / 144 h) sample. (Al-3.60Mg-1.18Zr, wt.% Batch 1) . Measurements courtesy of A. Hashemi....98

Figure 5.5: ADF-STEM overview images of the (a) fine grain region and (b) coarse grain region. Z1 points to a Zr rich grain boundary precipitate. Z2 points to the filamentary shape precipitates. 99

Figure 5.6: Coarse-grain region of a peak-aged sample (400˚C for 8 h, Batch 1) imaged via STEM (ADF- image and elemental EDX maps using Si-K, Zr-K, Al-K, Mg-K, Fe-K and O-K lines) showing three types of precipitates : (i) Al_3Zr precipitates consisting of larger, equiaxed precipitates (labelled Z1) and finer, elongated precipitates within grains (labelled Z2); (ii) Mg- and O-rich oxide particles located at grain boundaries; (iii) Fe-rich precipitates (F) located grain boundary. 99

Figure 5.7: (a) STEM ADF-image of a coarse-grain region of a peak-aged (400˚C / 8 h) sample (Al-3.60Mg-1.18Zr, wt.% Batch 1) showing: (i) nanometric equiaxed Al_3Zr precipitates formed via continuous precipitation (upper grain) and (ii) elongated, aligned Al_3Zr precipitates formed via discontinuous precipitation. An oxide particle (O) is present at the image center (b) High-resolution ADF-STEM image of equiaxed Al_3Zr nano-precipitates (2 nm in diameter, continuous precipitation) in the upper half of boxed region in (a). (d) High-resolution ADF-STEM image of the 5 nm-wide, highly-elongated Al_3Zr precipitates formed by discontinuous precipitation in the lower half of boxed region in (a). (c, e) FFT of images (b) and (d), respectively, show the 010-type superlattice reflection of the metastable $L1_2$ structure for Al_3Zr. 100

Figure 5.8: STEM ADF-image and elemental EDX maps of the region highlighted by the black box in Figure 4, showing elongated, discontinuous $L1_2$-Al_3Zr precipitates (labelled Z1) and one Mg- and O-rich oxide particle (O) at the interface between continuous and discontinuous precipitation (dashed line). Chemical analysis was performed using the Zr-K, Al-K, Mg-K, and O-K lines. 101

Figure 5.9: In-situ experiment of coarse-grain region of as-fabricated Al-3.60Mg-1.18Zr (wt.%), Batch 2. (a) ADF-STEM image of the region of interest prior to thermal exposure. Oxides are highlighted by black arrows. (b) ADF-STEM image after 420 s of exposure at 400°C showing Al_3Zr precipitates (white arrows) and nano-scale Al_3Zr precipitates within the grains, highlighted by the white box and enlarged in the inset. (c) ADF-STEM image after 1000 s of exposure at 400 °C. Coarsening of equiaxed $L1_2$-Al_3Zr precipitates at grain-boundary occurred (black arrow). An acicular precipitate expected to be $D0_{23}$-Al_3Zr is observed (white arrow). (d) ADF-STEM image after 30 s at 500ºC showing further growth of the acicular $D0_{23}$-Al_3Zr precipitate (white arrow) (e) Higher magnification ADF-STEM image and STEM EDX map of the region highlighted by the black box in (c). Two spherical Mg- and O-rich oxide particles are surrounded by much finer Al_3Zr nanoprecipitates (white arrow). Particles enriched with F and Mg are also observed, but of unknown origin. Chemical analysis was performed using the Zr-K, Al-K, Mg-K, F-K and O-K lines. 104

Figure 5.10: In-situ STEM heating experiment of a fine-grain region of as-fabricated Al-3.60Mg-1.18Zr (wt.%, Batch 2): (a) ADF-STEM image of the region of interest prior to thermal exposure (b) ADF-STEM image taken after a 64-min ramp to 350˚C . Horns have grown on the nanoprecipitate corners (white arrow) and grain-boundary movement has occurred (black arrow) (c) ADF-STEM image taken after a subsequent 48 min-exposure at 350˚C . Further growth of the horn features occurred. (d) ADF-STEM image taken after temperature was increased to 500˚C during a 28-min ramp. The horns previously observed at 350˚C disappeared at 450˚C, during the ramp to 500˚C. (e) High-resolution ADF-STEM image of a horn feature, from precipitate imaged in (c), showing epitaxial growth of a horn feature. (f) Diffraction pattern created by FFT of images (e) and (d), respectively) showing the 100- and 010-type superlattice reflections of the metastable $L1_2$ structure for Al_3Zr. 105

Figure 6.1: (a) Yield and ultimate tensile strength (UTS) strength (MPa) of as-fabricated and as-fabricated rescanned Al-3.60Mg-1.18Zr (wt. %, Batch 1) and Al-3.66Mg-1.57Zr (wt.%, Batch 2) samples. (b) Elongation at fracture. Each data point is the mean of two test samples. Error bars represent the standard error of the mean. 110

Figure 6.2: (a) Yield and Ultimate tensile (UTS) strength (MPa) of peak-aged Al-3.60Mg-1.18Zr (wt. %, Batch 1) and Al-3.66Mg-1.57Zr (wt.%, Batch 2) samples. (b). Elongation at fracture. Each data point is the mean of two test samples. Error bars represent the standard error of the mean 111

Figure 6.3: Temperature dependence of yield strength for the high-Zr alloy, Al-2.90Mg-2.10Zr (wt. %, Batch 3), in three conditions: as-fabricated, peak-aged (400ºC, 8 h), and over-aged (400ºC, 60 h). Tests were performed on single samples (transverse orientation), from the highest to the lowest temperature. 112

Figure 6.4: Temperature dependence of yield strength for the Sisma fabricated high-Zr alloy, Al-2.90Mg-2.10Zr (wt. %, Batch 3), in two conditions: as-fabricated, and peak-aged (400ºC, 7 h). Tests were performed to fracture on single samples (parallel orientation). Each point represents the mean. Error bars represent the standard error of the mean 113

Figure 6.5: Double logarithmic plot of secondary creep rate vs. stress for creep testing at 260˚C of high-Zr alloy, Al-2.90Mg-2.10Zr (wt.%, Batch 3) in three conditions: as-fabricated, under-aged (260˚C , 168 h), peak-aged (400˚C , 8 h); total creep time is given in parentheses. Data for the as-fabricated state, with a short total creep time of 8 h, were collected by increasing the stress every 30 min, so that steady-state strain rate may not have been achieved at the two lowest strain rates (which are marked with black circles) 114

Figure 6.6: Displacement vs. time plot for the as-fabricated sample (Al-2.90Mg-2.10Zr, wt. %, Batch 3) crept tested to fracture at 260 ˚C for 168 h. 114

Figure 6.7: a,b,c) SE SEM images of the fracture surface of the as-fabricated sample (Al-2.90Mg-2.10Zr, wt. %, Batch 3, vertical direction) crept at 260 ˚C for 8 h. a.) Overview of fracture face. b.) higher magnification image showing dimples indicative of ductile fracture via microvoid coalescence. c.) Higher magnification image showing a region with the appearance of intergranular fracture. d,e,f) SE SEM images of the fracture surface of the as-fabricated sample (Al-2.90Mg-2.10Zr, wt. %, Batch 3, vertical direction) crept at 260 ˚C for 168 h. d.) Overview of fracture face. e.) Higher magnification image showing dimples indicative of ductile fracture via microvoid coalescence f.) Higher magnification SE image showing dimples..116

Figure 6.8: a,b,c) SEM images of a cross-section of the as-fabricated sample (Al-2.90Mg-2.10Zr, wt. %, Batch 3, vertical direction) crept at 260 ˚C for 8 h. a.) SE image overview b.) BSE image showing the microstructure next to the fracture c.) Higher magnification BSE image of (b). d,e,f) SEM images of the cross section of the as-fabricated sample (Al-2.90Mg-2.10Zr, wt. %, Batch 3, vertical direction) crept at 260 ˚C for 168 h. d.) SE image overview. Black arrow highlights a large void. e.) BSE image showing the microstructure at the fracture f.) Higher magnification BSE image of (e). White arrows point to sub-micron grain boundary particles. 117

Figure 6.9: a,b) BSE images showing the microstructure in the threads of the as-fabricated sample (Al-2.90Mg-2.10Zr, wt. %, Batch 3, vertical direction) crept at 260 ˚C for 8 h. c,d) BSE images showing the microstructure in the threads of the as-fabricated sample (Al-2.90Mg-2.10Zr, wt. %, Batch 3, vertical direction) crept at 260 ˚C for 168 h. ... 118

Figure 6.10: a.) ADF-STEM image and elemental STEM-EDX maps of the coarse-grain region (transverse microstructure) of an as-fabricated sample (Al-2.90Mg-2.10Zr, wt. %, Batch 3, vertical direction) crept-tested to fracture at 260˚C for 8 h. b.) ADF-STEM image and elemental STEM-EDX maps of the coarse-grain region (transverse microstructure) of an as-fabricated sample (Al-2.90Mg-2.10Zr, wt. %, Batch 3, vertical direction) crept-tested to fracture at 260˚C for 168 h. The Fe-rich and Mg+Si-rich precipitates are significantly larger and fewer in the long-duration creep sample when compared to the short-duration creep sample. 119

Figure 6.11: a.) ADF-STEM image of the coarser-grain region (transverse microstructure) of an as-fabricated sample (Al-2.90Mg-2.10Zr, wt. %, Batch 3, vertical direction) crept-tested to fracture at 260 ˚C for 8 h. b.) ADF-STEM image of the coarse-grain region (transverse microstructure) of an as-fabricated sample (Al-2.90Mg-2.10Zr, wt. %, Batch 3, vertical direction) crept-tested to fracture at 260 ˚C for 168 h. Discontinuous Al_3Zr precipitation was observed in both samples (white arrows), but the 168 h crept sample had significantly more discontinuous Al_3Zr precipitation. 120

Figure 7.1: BSE images of the cross-sectioned CM247LC powder(a) low magnification BSE image (b) Higher magnification BSE image showing bright regions that are enriched in Hf, Ti, and Ta. A few are highlighted with a black arrow. 127

Figure 7.2: Microstructure of CM247LC samples in the as-fabricated condition, fabricated using Condition 1 (a,c,e), and Condition 2 (100 mm build plate) (b,d,f). a,b) Optical images, with highlighted melt pool boundaries (dashed black lines). c,d) Backscatter electron images showing the columnar grain structure. e,f) Higher magnification backscatter electron images showing a cellular substructure. 129

Figure 7.3: EBSD IPF maps of samples fabricated with Condition 1 (a) and Condition 2 (100 mm build plate) (b). The IPF color is shown for the Y direction which is parallel to the solidification direction. White lines: low angle boundaries > 2°; black lines: high angle boundaries > 10°. Map sizes are 250 x 300 μm with 100 nm step size. 130

Figure 7.4: STEM characterization of the as-fabricated microstructure (transverse section) of a CM247LC sample fabricated with Condition 2 (100 mm build plate) a) ADF-STEM image showing ~0.5-1 μm diameter cells, surrounded by grain boundary precipitates, assumed to be carbides (bright particles highlighted by white arrow). b) BF-STEM image showing a high dislocation density (area highlighted by black arrow) on the cell boundaries. c) STEM-EDX map of cell boundaries. Precipitates are enriched in Ti/Hf/Ta/W/C and are presumed to be carbides. The chemical analysis is performed using the Al-K, Ti-K, Cr-K, Hf-L, Ta-L, W-L, Co-K, Ni-K, Mo-K, Zr-K, and C-K lines. 131

Figure 7.5: a) A low magnification BF-TEM image of the as-fabricated CM247LC sample, presented in Figure 2 (Condition 2, 100 mm build plate). (b) Selected area diffraction pattern along a [001] zone axis, acquired from the circled area in a) showing the 100- and 110-type superlattice reflections of the L12 structure. 131

Figure 7.6: STEM analysis of the as-fabricated CM247LC microstructure of a transverse section of a Condition 2 fabricated sample. a) ADF-STEM image showing a grain boundary enriched with elevated levels of Hf (white box). b) STEM-EDX map of region highlighted by the white box in a). Chemical analysis performed with Al-K, Ti-K, Cr-K, Hf-L, Ta-L, W-L, Co-K, Ni-K, C-K lines.......132

Figure 7.7: SE image of top surface of as-fabricated CM247LC cube (Condition 1). Cracking (one crack highlighted by white arrow) is perpendicular to the direction of laser travel (is indicated by the red arrows). 133

Figure 7.8: Electron microscope images taken from CM247LC samples fabricated from a,b,c) Condition 1 and d,e,f) Condition 2. a,d) BSE Image of a parallel cross section. b, e) BSE image of perpendicular cross section. c, f) SE image showing the features (white arrows) on the crack surfaces.......134

Figure 7.9: a) Optical image showing a specific area of the as-built sample before the Gleeble test. b) Optical microscope images taken from same zone as (a) after the fast heating and cooling treatment in the Gleeble machine, c) higher magnification optical image shows a thin 1 μm wide film formed after Gleeble test. d) Higher magnification SE image of the observed film, and e) SEM-EDX line scan analysis of the region. All images are parallel to the build direction. Figure courtesy of H. Ghasemi.......135

Figure 7.10: (a) BSE image from CM247LC sample fabricated from Condition 1, except for chess scanning. (b) EBSD unique grain color map (700 nm step size map) 136

Figure 7.11: ADF-STEM image and corresponding STEM-EDX maps the as-fabricated microstructure (transverse section) of a CM247LC sample fabricated with Condition 1, except with a chess scanning strategy. Chemical analysis performed with Al-K, Ti-K, Cr-K, Hf-L, Ta-L, W-L, Co-K, Ni-K, C-K lines. Co, C, and Mo maps not shown.......136

Figure 7.12: SE images of micro-cracks in a CM247LC sample fabricated with Condition 1, except for chess scanning (a) BSE image of a micro-crack running along a grain boundary. (b) SE image showing features on the face of the crack.......136

Figure 8.1: Scheil-Gulliver solidification curves for CM247LC and CM247LC NHf.......142

Figure 8.2: BSE images of the cross-sectioned CM247LC NHf powder(a) low magnification BSE image (b) Higher magnification BSE image showing bright regions, that are greatly reduced in size from the CM247LC powder. A few are highlighted with a black arrow.......143

Figure 8.3: Microstructure of as-fabricated CM247LC NHf (Condition 2, 100 mm build plate). (a) Optical image of an etched sample. Melt pools are highlighted by a dashed line. b,c) BSE images showing the elongated grain and subcell microstructure. 144

Figure 8.4: Optical images of etched samples processed by Condition 2 (34.5 mm build plate): (a) CM247LC (b) CM247LC NHf. Dashed lines hightlight the melt pools 144

Figure 8.5: STEM characterization of the as-fabricated microstructure (transverse section) of a CM247LC NHf sample produced using Condition 2 (34.5 mm build plate). a) ADF-STEM image showing ~0.5-1 μm diameter cells surrounded by grain boundary precipitates, assumed to be carbides. Black arrows point to script like precipitates assumed to be carbides. b) BF-STEM image showing a high dislocation density throughout. c) STEM-EDX map of cell boundaries. The black region is a crack. Precipitates are enriched in Ti /Ta/W and are presumed to be carbides. The chemical analysis is performed with Al-K, Ti-K, Cr-K, Ta-L, W-L, Co-K, Ni-K, Mo-K, Zr-K, and C-K lines. 145

Figure 8.6: XRD patterns of as-fabricated CM247LC and CM247LC NHf. Samples were fabricated with Condition 2 (100 mm build plate) with build plate of 100 mm diameter. Small peaks around 35° and 40° may correspond to the carbides. A slight peak shift between the two samples is likely the result of lattice parameter changes caused by the elimination of Hf. 146

Figure 8.7: a) A low magnification BF-TEM image of the as-fabricated CM247LC NHf sample (Condition 2, 34.5 mm build plate). b) Selected area diffraction pattern along [001] taken from the circled region in a) showing the 100- and 110-type superlattice reflections of the L12 structure. 146

Figure 8.8: SE image of the top surface of a CM247LC NHf as-fabricated cube (Condition 1) (unidirectional scanned sample with no change in direction of layers). Cracking is transverse to direction of laser travel.147

Figure 8.9: Electron microscope images taken from CM247LC NHf samples fabricated with Condition 1 and 2. a) BSE Image of a parallel cross section (Condition 1). b) BSE image of perpendicular cross section (Condition 1) c) Higher magnification BSE image of a crack observed in a parallel cross section (Condition 2, 100 mm build plate) d) Higher magnification BSE image of a crack observed in the perpendicular cross section (Condition 2 2, 34 mm build plate) e) SE image showing the features on the crack faces (Condition 2, 34.5 mm build plate). 147

Figure 8.10: DSC thermograms on heating for both as-fabricated CM247LC and CM247LC NHf samples, built with Condition 2. $T_{\gamma`}$ is the γ`dissolution temperature, T_S is the solidus temperature, T_C is the carbide dissolution temperature, and T_L is the liquidus temperature.148

Figure 8.11: a) Optical image of CM247LC sample fabricated by Condition 1 b) Optical image from CM247LC NHf sample fabricated with Condition 1. c) Optical image of CM247LC fabricated by Condition 2. d) Optical image of the CM247LC NHf fabricated by Condition 2. 150

Figure 8.12: a) Mean micro-crack density. Error bars represent standard error of the mean. b,c) Crack length histogram of cracks observed in a parallel cross section of b) CM247LC and c) CM247LC NHf samples (Condition 1) 151

Figure 8.14: Processing conditions used overlayed on normalized processing parameter plot from [17] 154

Figure 8.13: (a) Optical image of an etched CM247LC Condition 2 fabricated sample (b) Optical image of an etched CM247LC Condition 2, with 60 second delay, fabricated sample. Dashed lines highlight the melt pools. 155

Figure 8.15: (a) Cross section of Condition (a) melt pool. (b) Cross section of Condition b melt pool. (c) Overlay of the two melt pool profiles. 157

Figure 8.16: Surface tension of selected γ′ prime forming Ni-base superalloys as a function of temperature. The surface tension of a high and low O content CMSX-4 is shown to highlight the influence of O. Values taken from [142]. 158

Figure 8.17: a) Optical image of CM247LC sample fabricated by Condition 1, but with chess scanning. b) Optical image from CM247LC NHf sample fabricated with Condition 1, except with chess scanning.160

Figure 8.18: Optical images of metallographic cross-sections of CM247LC (a) and CM247LC NHf (b) of two as-fabricated 45 degree cylinders (complete images are shown in Figure 0.14). 161

Figure 8.19: SE images showing the rough surface of the crack faces in as-fabricated (a) CM247LC and (b) CM247LC NHf. 161

Figure 8.20: Optical images of (a) CM247LC and (b) CM247LC NHf fabricated with Condition 2 parameters except with a 60 second time delay between layers 162

Figure 9.1: Plot showing the evolution of microhardness with aging time at a temperature of 850°C. Figure courtesy of S. Joglekar and J. Pado and A. De Luca. 165

Figure 9.2: Equivalent radius of γ`precipitates at various isothermal aging (850°C) times. All samples were solutionized (1260°C, 2 hr) prior to aging. Figure courtesy of S. Joglekar and J. Pado and A. De Luca. 166

Figure 9.3: BSE images of (a) CM247LC and (b) CM247LC NHf solutionized(1260°C, 2 hr) and aged (850 C 8hrs). 166

Figure 9.4: (a) Equivalent radius of γ`precipitates in CM247LC at various isothermal aging (850°C) times. A bi-modal distribution is observed until 4 hrs. Figure courtesy of S. Joglekar and J. Pado and A. De Luca. (b) BSE image of the bi-modal γ`precipitate distribution. The white arrow point to 120 nm radius precipitates and the black arrow points to 37 nm radius precipitates. 167

Figure 9.5: BSE images of HIPed mechanical test bars. Images approximately taken from the center of the 80 mm bar length. (a,b) CM247LC (c,d) CM247LC NHf. 168

Figure 9.6: BSE images of HIPed and solutionized witness bars. Images approximately taken from the center of the witness bar. (a,b,c) CM247LC (d,e,f) CM247LC NHf. Black arrows point to the γ` precipitates. 168

Figure 9.7: SE imags of macro-crack in the HIPed and solutionized CM247LC witness bar. (a) overivew image of numerous cracks (b) overiveiw image of one crack. (c,d) SE images of the crack face. 169

Figure 9.8: BSE images of HIPed, solutionized, and aged witness bars. Images approximately taken from the center of the witness bar. (a,b) CM247LC (c,d,e) CM247LC NHf. Black arrow point to the γ` precipitates. An adequete image for the γ` precipitates in the CM247LC was not obtained. 170

Figure 9.9: Equilibrium phase fraction of γ and γ′ phases as a function of temperature for CM247LC and CM247LC NHf. Calculations were performed with Thermocalc and the TCNI5 database 171

Figure 9.10: Optical image of etched CM247LC. The cross section is parallel to the casting direction. The blueish tints in the image are dendtrites and the orange tint areas are interdentridic. 173

Figure 10.1: Dimensions of the dogbone specimens. Specimens were 3 mm thick. 177

Figure 0.1: SEM-EDX data of Al-3.66Mg-1.57Zr (wt.%, batch 5) powder shown in Figure 4.1. 179

Figure 0.2: SEM-EDX data of white precipitates in the Al-3.66Mg-1.57Zr (wt.%, batch 5) powder shown in Figure 4.1. 180

Figure 0.3: SEM-EDX data taken from an as-fabricated Al-3.60Mg-1.18Zr (wt. %, Batch 2) alloy. 181

Figure 0.4: STEM-EDX data taken from an as-fabricated Al-3.60Mg-1.18Zr sample (wt.%, Batch 2). (a) ADF STEM image and STEM-EDX data from a region adjacent from a primary L12 structured Al3Zr precipitate. (b) ADF STEM image and STEM-EDX data from a grain from the coarse grain region. 182

Figure 0.5: ADF-STEM image and STEM-EDX data taken from a grain (same grain as shown by the white circle in Figure 4.10) in the coarse grain region of an as-fabricated Al-3.60Mg-1.18Zr sample (wt.%, Batch 2). 182

Figure 0.6: STEM HAADF image and STEM-EDX data from the coarse grain region of an as-fabricated Al-2.90Mg-2.10Zr (wt. %, Batch 3) sample. Area #1 and Area #2 are the areas that HR-STEM was performed in. 183

Figure 0.7: (left) STEM HAADF image of region of interest. Area #1 in Figure 0.6. (middle) HR-STEM image (right) FFT of HR-STEM image taken down the [112] zone axis. Note the absence of superlattice reflections indicative of the $L1_2$ phase. 183

Figure 0.8: (left) STEM HAADF image of region of interest. Area #2 in Figure 0.6. (middle) HR-STEM image (right) FFT of HR-STEM image taken down the [112] zone axis. Note the absence of superlattice reflections indicative of the $L1_2$ phase. 184

Figure 0.9: SEM-EDX of an as-fabricated (double scanned) Al-3.60Mg-1.18Zr (wt.%, Batch 2) alloy. 184

Figure 0.10: SEM-EDX data of a CM247LC powder particle. Bright areas are enriched in Hf, Ti, and Ta. 185

Figure 0.11: Optical images, with highlighted melt pools (dashed lines) on etched, as-fabricated CM247LC samples, produced using a) Machine 2 with a 100 mm diameter build plate b) Machine 2 with a 34.5 mm diameter build plate. No significant differences in melt pool dimensions were observed. 185

Figure 0.12: STEM-EDX line profile (averaged over the line width) quantification data taken from the region highlighted by the white box in Figure 2c. Chemical analysis performed with Al-K, Ti-K, Cr-K, Hf-L, Ta-L, W-L, Co-K, Ni-K, Zr-K, C-K lines.......186

Figure 0.13: a) ADF-STEM image of the boundary shown in Supplement Figure 7. The green box highlights the region used for the STEM-EDX line profile. b) STEM-EDX line profile (averaged over the width) of the boundary in a). Hf enrichment on the boundary approaches 20 wt.%. Chemical analysis performed with the Hf-L lines. 187

Figure 0.14: (a) Optical image of cross section of as-fabricated CM247LC cylinder. (b) Optical image of cross section of as-fabricated CM247LC NHf.......188

List of Tables

Table 3-1: Chemical compositions and sizes of the powder (except batch 3) used in this study. 57

Table 3-2: Chemical composition of the powders used in the study. Measured by ICP-OES and combustion. 62

Table 3-3: Processing parameters utilized for the fabrication of CM247LC samples. 62

Table 7-1: STEM-EDX semi-quantification values taken from the area highlighted by the white box in Figure 3(c), highlighting the segregation behaviors of the various elements in as-fabricated CM247LC. Effective partition coefficients k` (Cell / Boundary composition) are calculated. The chemical analysis is performed using the Al-K, Ti-K, Cr-K, Hf-L, Ta-L, W-L, Co-K, Ni-K, and Mo-K lines 132

Table 0-1: Values used in the normalized enthalpy calculations....178

Table 0-2: Nominal composition of CM247LC used in TCNI5 calculations178

Table 0-3: Thermophysical properties and laser parameters used for the normalized power and normalized interaction time calculation...189

Chapter 1 Introduction

Additive manufacturing (AM) refers to a group of manufacturing techniques that are used to produce near net shape monolithic parts in a layer-by-layer fashion. Aside from the benefit of less waste, AM enables the rapid manufacturing of complex part geometries with minimal custom tooling. AM may enable previously unobtainable designs and repairs that can significantly impact device efficiency and economics, which explains the recent intense focus from industry and academia. For metallic materials, AM typically refers to the following: (i) Laser Powder Bed Fusion (L-PBF), (ii) Electron Beam Powder bed fusion (E-PBF), or (iii) Direct Energy Deposition (DED). In the PBF techniques, a layer of metallic powder is consolidated with either a laser (L-PBF) or an electron source (E-PBF). In DED, a stream of powder, or wire, is deposited into the focal point of a laser. The process, whether PBF or DED, in a simplistic way, can be viewed as a fusion welding process; therefore, many of the disadvantages associated with the rapid melting and solidification of metal, such as high residual stresses, undesirable metastable phases, and cracking, apply to AM. This implies that only weldable alloys, such as Ti-6Al-4V, and 316 stainless steels are well suited for AM; however, the high geometric freedom AM offers in comparison to conventional manufacturing techniques [1] means there is a desire to process all alloys with AM, even those considered to have poor weldability, such as the precipitation-strengthened superalloys.

One subset of precipitation-strengthened alloys greatly desired for industrial AM use are those strengthened by intermetallic precipitates. One category of intermetallic with industrial significance is the $L1_2$ (Strukturbericht notation) structured intermetallics. The $L1_2$ structure can be viewed as an FCC structure where the face atoms are different than the corner atoms, resulting in a X_3Y composition. This intermetallic, in the form of Ni_3Al (gamma prime, γ`) is responsible for the high temperature creep strength of the nickel superalloys. $L1_2$ is also a critical strengthening phase in the latest generation of high strength aluminum superalloys, Scalmalloy® (Al-Mg-Sc-Zr-Mn) for instance, where it takes the form of $Al_3(Sc,Zr)$. The goal of the $L1_2$ phase in Al is similar to the goal for Ni superalloys, improve creep resistance at temperatures approaching the melting point. However, there are a few key differences, aside from being two separate alloy systems. The solubility of Sc in Al is quite low (0.01 at% at 400°C in the binary); therefore the phase fraction of precipitates is substantially lower than in the Ni superalloys. Another key difference is in the solidification behavior (inoculation occurs in the Al-base superalloys) of the two alloys during rapid solidification. Despite the differences, both alloys utilize $L1_2$ precipitate-strengthening, and are of immense value to industry for applications where elevated temperature ($T>0.5T_m$) performance is required.

Before either the Al-base or Ni-base superalloys are able to be successfully used in a production setting, numerous challenges have to be overcome. The first hurdle for the nickel-base superalloys is micro-cracking. Numerous studies on PBF of precipitation strengthened Ni-base superalloys have reported extensive micro-cracking in as-fabricated samples [2–9]. Numerous micro-crack mechanisms exist for Ni-base alloys [10], which makes identification and mitigation of micro-cracking challenging. Post-processing technologies exist that can repair micro-cracks, but additional post processing is undesirable from an economic standpoint. Ignoring the micro-cracking problem, there is little understanding on the microstructure characteristics of AM fabricated superalloys and how this will influence mechanical performance. Decades of academic and industrial research work on microstructure and mechanical properties exists for Ni-base superalloys; however, a majority of this research focuses on directionally solidified or single crystal superalloys and is not applicable to the microstructures formed during AM.

The Al-base superalloys are not prone to in-process cracking, for reasons that will be discussed later, but are a relative newcomer to the AM process. Extensive work has gone into Al-base superalloy development and characterization, but most of that work has focused on alloys produced via traditional casting [11]. Aside from the grain microstructural differences that exist between AM fabricated and cast alloys, the solubility of the primary strengthening element in solid solution can be an order of magnitude different. The rapid solidification (estimated to be $\sim 10^4 - 10^6$ °C/s) inherent to beam based AM results in supersaturation of the solute (Sc, Zr for instance) that enables higher phase fractions of the $L1_2$ strengthening phase to be achieved. The supersaturation in combination with the fine grain microstructure that results from AM makes for a material that will behave quite differently than its cast counterparts. Prior to this work, few Al-base superalloys, most notably Scamalloy®, were produced via AM, and no work on high temperature properties existed.

The aim of this work is to address the current challenges that exist for AM-fabrication of Al-base and Ni-base superalloys. The work will be split into two distinct sections, Al-base and Ni-base alloys, but the overall theme of microstructure formation during the AM process and how this influences material properties is the same.

A few publications were published/submitted in my time as a student and they are listed below with author contributions noted. This thesis was partly based off these publications and uses many of the figures and text from the publications. There are still numerous unpublished results that were included for the sake of further scientific discussion and understanding. Figures and experiments that are not the author`s own, but included for complete discussion, are clearly mentioned in the text. Text was not copied (except for experimental details) from publications were I was not the first author; In the case of the *Microstructure and mechanical properties of Al-Mg-Zr alloys processed by selective laser melting*, it was rewritten with my own analysis and words. Lastly, the last chapter, Chapter 9, is mostly based off the work of S. Joglekar and J. Pado, who were intern/masers students under the supervision of A. De Luca (primary) and S. Griffiths (secondary).

- S. Griffiths, M. Rossell, J. Croteau, N. Vo, D.C. Dunand, C. Leinenbach, Effect of laser rescanning on the grain microstructure of a selective laser melted Al-Mg-Zr alloy, Mater. Charact. 143 (2018) 34–42.
    - SG fabricated the samples, SG and MR fabricated STEM samples, SG and MR performed STEM, SG analyzed STEM results (with MR assistance), SG analyzed EBSD data, SG performed all optical and SEM characterization and analysis, SG wrote the manuscript (with assistance from all authors)
- J.R. Croteau, S. Griffiths, M.D. Rossell, C. Leinenbach, C. Kenel, V. Jansen, D.N. Seidman, D.C. Dunand, N.Q. Vo, Microstructure and mechanical properties of Al-Mg-Zr alloys processed by selective laser melting, Acta Mater. 153 (2018) 35–44.
    - SG fabricated the samples; SG and MR fabricated STEM samples; SG and MR operated the STEM; SG analyzed STEM results (with MR assistance); JC performed mechanical property tests; SG contributed to mechanical property analysis; SG wrote some sections.
- N. Kalentics, N. Sohrabi, H.G. Tabasi, S. Griffiths, J. Jhabvala, C. Leinenbach, A. Burn, R.E. Loge, Healing cracks in selective laser melting by 3D laser shock peening, Addit. Manuf. 30 (2019) 100881.
    - SG fabricated the samples for microstructure characterization; SG fabricated STEM samples; SG operated the STEM and analyzed the data; SG performed fractography of micro-cracks; SG performed thermodynamic analysis
- S. Griffiths, J. Croteau, M. Rossell, R. Erni, A. De Luca, N. Vo, D. Dunand, C. Leinenbach, Coarsening-and creep resistance of precipitation-strengthened Al–Mg–Zr alloys processed by selective laser melting, Acta Mater. 188 (2020) 192–202.

    - SG fabricated all samples; SG and MR fabricated STEM samlples; SG, MG, and RE operated the STEM, SG analyzed the STEM data (with MR assistance); JC performed mechanical property testing; SG, ADL, JR analyzed the mechanical property data; SG wrote the manuscript (with assistance from all authors)

- S. Griffiths, H.G. Tabasi, T. Ivas, X. Maeder, A. De Luca, K. Zweiacker, R. Wrobel, J. Jhabvala, R.E. Logé, and C. Leinenbach, Combining Alloy and Process Modification for Microcrack Mitigation in an Additively Manufactured Ni-base Superalloy, Addit. Manuf. In Review ADDMA_2019_2511R1.
    - SG fabricated the samples, SG fabricated STEM samples; SG operated the STEM and TEM and analyzed the data; SG performed all optical and SEM characterization and analysis; SG performed thermodynamic simulations (with assistance from TI); SG, TI, and CL designed the modified alloy; SG performed micro-crack density and fractography analysis; HGT performed Gleeble testing; ADL performed DSC testing; KZ performed XRD measurements, SG analyzed the data; SG wrote the manuscript (with assistance from all authors)

Chapter 2 State of the Art

The following chapter contains primers on the fundamental topics central to this thesis, and also a literature review on the L-PBF fabrication of Al-base and Ni-base superalloys.

2.1 Laser Powder Bed Fusion (L-PBF)

A schematic overview of the L-PBF process is shown in Figure 2.1. In a simplistic sense, the process begins with a 3-Dimensional (3D) Computer Aided Design (CAD) model that is sectioned into a series of 2-Dimensional (2D) drawings, or slices as they are commonly called. Each slice represents one layer (typically 30 µm thick) of the 3D part and will define what regions of the layer needs to be consolidated and how they are consolidated (the scanning strategy). Once the above slices are loaded into the machine computer, a layer (same depth of the slice) of metallic powder (10-45 µm in diameter) is spread onto the build substrate by a rubber coating blade. Next, the laser, commonly a 1070 nm CW fiber-laser, is turned on and the scan head (mirrors driven by galvo-motors) will move the laser spot on the path specified by the 2D drawing resulting in melting of the powder. Once a layer is melted, the building surface will drop by the defined layer thickness and a new layer of powder will be deposited. The next layer is melted and the process is continued until a 3D part is additively produced. While the process is simple from a mechanical standpoint, the metallurgy and laser-material interactions involved in the process are quite complex and will be briefly discussed in the following sections.

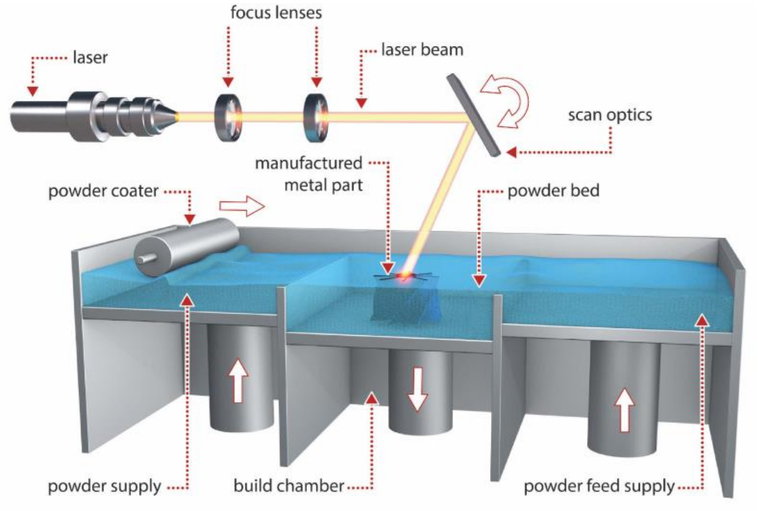

Figure 2.1: Schematic of the L-PBF process. Image from [12]

2.2 Laser Melting/Welding Primer

In L-PBF, the laser, in a simplistic view, provides heat for melting the powder. A majority of commercial L-PBF machines are equipped with a 1070 nm (near-infared radiation, ~1.2 eV) fiber laser operating in continuous wave mode with a Gaussian intensity distribution. When near-IR radiation illuminates a metal surface it excites only conduction band electrons (too low eV for bound electrons) in the top 10-100 nm of the metal surface [13,14]. The excess kinetic energy of the excited electrons results in particle collisions that lead to lattice vibrations (heating of the metal) [13]. This interaction, electron collisions, occurs in ~10^{-13} seconds [15]. Further heating of the material leads to melting, evaporation, and then plasma formation. It is important to note that metals in the solid state are highly reflective to IR radiation; polished Al and Ni have reflectivities to ~1064 nm radiation of 0.94 and 0.67, respectively [14]. Reflectivity decreases as temperature increases and further decreases once the material is molten (at Tm a liquid metal will have ~ 2x the absorptivity than the solid metal) [14], but reflectivity can still pose challenges for coupling the energy into the work piece. Surface modification (roughness, coatings, powder, etc) can lead to an increase in the absorption [13]. Metal vapor has minimal IR absorption due to lack of unbound electrons, and plasma can strongly absorb the IR laser radiation before it illuminates the metal [15]. Plasma formation can occur from ionization of the metal vapor or from ionization of the shielding gas. Plasma formation of a metal does not occur until high laser intensities (>10^8 W/cm^2 [16]) are applied, which are a few orders of magnitude above the laser intensities encountered in L-PBF (10^6 W/cm^2). Ionization energy of Ar shielding gas, the most common for L-PBF, is ~15 eV, and is high enough to suppress plasma formation [13]. For these reasons, plasma formation is generally not of great concern during L-PBF fabrication; however, plasma will still be present (thermionic emission from asperities leading to free electrons, leading to Inverse Bremstralhung absorption, leading to plasma formation). While metal vapor itself has minimal IR absorption, vaporization of metal will lead to metal particles in the atmosphere above the surface which can in turn lead to scattering of the incident laser light [15].

The laser-material interactions listed above, depending on intensity and interaction time, typically result in two distinct modes of melting/welding: (i) conduction mode and (ii) keyhole (a.k.a deep penetration) mode. Processing maps of laser intensity vs. interaction time have been generated to indicate what regime the process is in: heating, melting, or vaporization [13,14,17]. Laser intensity is given by equation 1,

$$I = \frac{q}{\pi r^2} \tag{1}$$

where q is the laser power, and r is the radius of the laser spot (the spot size is typically defined as the width, or diameter, where the intensity of the Gaussian beam falls to 1/e or 1/e^2 of maximum). These processing maps can provide information on the processing regime resulting from different laser parameter combinations; however, the laser power that reaches the material is often substantially less than the set laser power (due to scattering) and thermal diffusivity of the material will influence the interaction time required to go from one regime to the next. Therefore, it is useful to use dimensionless values when comparing parameter sets, especially when different machines or materials are used. The dimensionless power, q*, is given by equation 2,

$$q^* = \frac{Aq}{r_B \lambda (T_m - T_O)} \tag{2}$$

where A is the absorptivity, q is the laser power, r_B is the beam radius (1/e value), λ is the thermal conductivity, T_m is the melting point, and T_0 is the initial temperature [17]. The dimensionless interaction time, v*, is given by equation 3,

$$v^* = \frac{v r_B}{a} \tag{3}$$

where v is the laser velocity, and a is the thermal diffusivity [17]. A process diagram of the normalized parameters is shown in Figure 2.2.

Another dimensionless value that is useful for parameter comparisons is normalized enthalpy. In simplified terms, the normalized enthalpy is the heat input (absorbed) divided by (normalized by) the enthalpy required for melting a given material. Normalized enthalpy, first proposed by Hann et. al. [18] (the exact form given here is from Rubenchik et. al. [19]), is calculated with equation 4,

$$\frac{\Delta H}{h_s} = \frac{AP2^{3/4}}{\rho C T_m \sqrt{\pi D u a^3}} \tag{4}$$

where ΔH is the input enthalpy (absorbed), h_s is the enthalpy of the solid at the melting point, A is the absorptivity, ρ is the density, C is the specific heat at melting, T_m is the melting temperature, D is the thermal diffusivity, and a is the radius of the spot size.

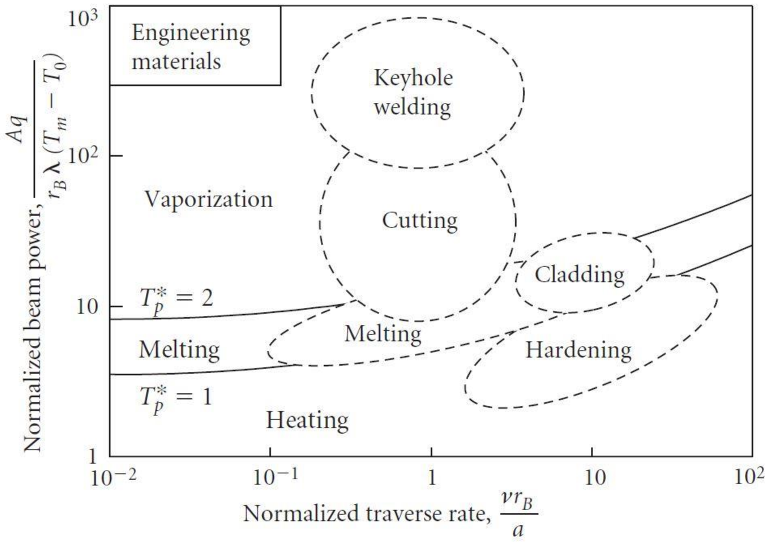

Figure 2.2: Normalized power vs normalized traverse rate diagram. Tp=1 and Tp=2 signify the borders for melting and vaporization, respectively, and their definition can be found in [17]. Plot taken from [17].

Keyhole mode melting typically occurs when 1070 nm laser radiation has a power intensity above ~10^6 W/cm^2. At this point, the metal is vaporized and a pressure stabilized "keyhole" is formed that acts as a blackbody that absorbs more of the laser radiation [15]. King et. al. [20] reported the threshold for keyhole formation in L-PBF to be at a normalized enthalpy of 30 ±4. In L-PBF, keyhole formation is seen as undesirable, due to void formation from keyhole collapse [21], thus the remainder of the discussion will focus on conduction mode melting.

In "conduction" mode melting, heat transfer in the melt occurs predominately via conduction and convection (primarily via surface tension driven flow). The dominate heat transfer mechanism will dictate the melt pool geometry and thus can influence the resulting solidification microstructure. There are three dimensionless numbers that are useful (others exist, but will not be discussed) when considering heat transfer in conduction mode melting: (i) the Prandtl number (P_r), (ii) the Peclet number (Pe), and the (iii) Marangoni number (Ma) [22,23]. The Prandtl number is the ratio of momentum diffusivity to thermal diffusivity and applies to a specific material. It is given by equation 5,

$$P_r = \frac{\mu/\rho}{k/C_p\rho} = \frac{C_p\mu}{k} \tag{5}$$

where Cp is the specific heat, k is the thermal conductivity, ρ is density, and μ is the dynamic viscosity of the fluid. The Prandtl number is ~0.02 for Al and ~0.1 for steel [13]. A lower Prandtl number suggests that thermal conductivity dominates and a more hemispherical melt pool shape will result, such as in aluminum. The Peclet number is useful when one wants to predict the melt pool geometry for a given material. The Peclet number is the ratio of heat transfer by convection over conduction and is mathematically given by equation 6

$$Pe = \frac{LV}{\alpha} \tag{6}$$

where L is the characteristic length (radius of melt pool or long axis of the melt pool depending on the condition), V is the characteristic velocity, and α is the thermal diffusivity. When the Peclet number is much greater than 1, heat transfer via convection dominates, and when it is much less than one, heat transfer via conduction dominates. The Marangoni number is a measure of the amount of surface tension driven flow in the system and is given by equation 7,

$$Ma = \frac{-\frac{\partial \gamma}{\partial T}(\Delta T)L}{\mu\alpha} \tag{7}$$

where $\frac{\partial \gamma}{\partial T}$ is the temperature dependence of the surface tension, ΔT is the temperature difference from the center to the edge of the melt pool, L is the radius of the melt pool surface, μ is the viscosity, and α is the thermal diffusivity [22]. As the Marangoni number is a measure of the amount of surface tension driven flow, it can be related to the characteristic velocity of equation 1. An increase in velocity due to increased Marangoni convection will result in a higher Peclet number per equation 1. The higher Peclet number implies that heat transfer via convection becomes more dominate, causing the melt pool to become wider and shallower [23].

2.3 Solidification Primer

The solidification microstructure of a laser weld/L-PBF melt track will directly influence the resulting mechanical properties of the part; therefore, it is important to understand the factors that influence the solidification microstructure. The solidification principles (mostly alloy, and not pure metal solidification) discussed below can be found in more detail in the following references, [24–26].

Figure 2.3 shows two hypothetical binary phase diagrams: (a) a binary phase diagram where the solute partitions to the liquid during solidification (higher solubility in the liquid phase) and (b) a binary phase diagram where the solute partitions to the solid during solidification (higher solubility in the solid phase). These two conditions can be quantified by the partition coefficient, k, given in equation 8,

$$k = \frac{C_S}{C_L} \qquad 8$$

where C_S is the concentration of solute in the solid phase, and C_L is the concentration of solute in the liquid phase for a given temperature. The partition coefficient is temperature dependent; however, the solidus and liquidus lines are typically approximated as linear and only a single partition coefficient is given. When k is greater than 1, the solute will partition to the solid during solidification, and when k is less than 1, the solute will partition to the liquid. During thermodynamic equilibrium solidification, a binary alloy of composition C_o will begin to solidify once the temperature decreases to the liquidus line (Figure 2.1). At this point, the initial solid will have a concentration of kC_o. As the temperature decreases, the solute concentration of the liquid and solid will follow the liquids and solidus lines respectively until the metal is completely solid with composition C_o at T_3. Equilibrium solidification assumes that there is complete diffusion in the solid and complete mixing in the liquid so that the composition of the liquid and solid is always uniform and equal to C_L and C_s, respectively. In a majority of processes involving solidification there is insufficient time for the solid composition to equilibrate via solid state-diffusion; therefore non-equilibrium solidification occurs. Equilibrium solidification occurs when the conditions of equation 9 (simplified solution of Ficks 2nd law), are met:

$$D_s t \gg l^2 \qquad 9$$

where D_s is the diffusion coefficient of solute in the solid, t is time, and l is length of solid phase. As diffusion in the solid is typically slow and time during welding or L-PBF is short, equilibrium is typically not reached and the solidification is non-equilibrium. Despite this, the equilibrium partition coefficients are a good indicator of micro-segregation behavior.

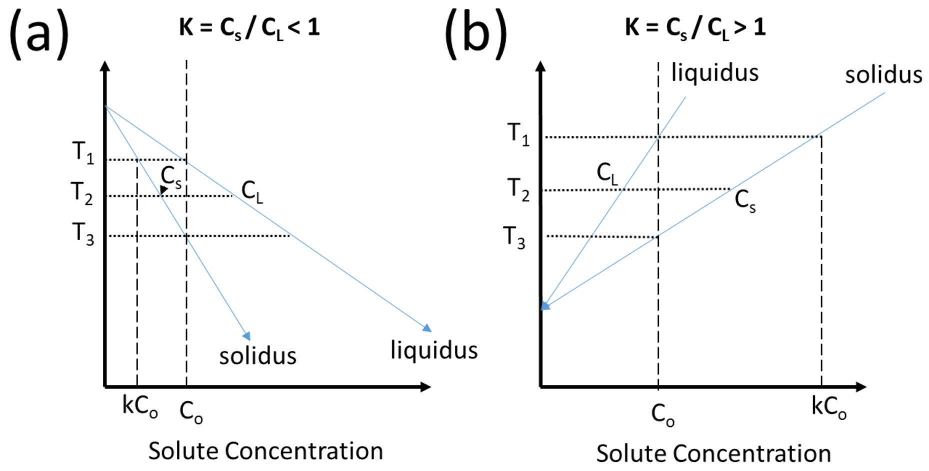

Figure 2.3: Two hypothetical binary phase diagrams highlighting the two possible elemental partition conditions (a) k < 1, solute enrichment of the liquid and (b) k > 1, solute enrichment of the solid. Figure based off of [24].

Aside from complete solute trapping, which will be discussed later, non-equilibrium solidification can be grouped into two different cases, although variations exist: (i) no solid diffusion, but complete liquid mixing and (ii) no solid diffusion, no liquid mixing, and limited liquid diffusion (Figure 2.4). In both cases, local equilibrium and a planar morphology at the interface is assumed. The following discussion will focus on a binary phase diagram where k < 1. In case (i), as shown in Figure 2.4a, the liquid composition will be uniform due to fluid convection (mixing) and/or diffusion in the liquid, and the solid will become increasingly solute enriched (no diffusion in the solid to allow the equilibrium concentration to be reached) as the solidification progresses. The resulting solidified metal will have low levels of solute in the core (first to solidify has a solute concentration of kC_o, per the phase diagram) and high levels of solute in the last regions to solidify. This model of non-equilibrium solidification is often called Scheil solidification. The solute concentrations of the solid and liquid are given by the following two equations (10 and 11),

$$C_S = kC_o(1 - f_s)^{k-1} \qquad 10$$

$$C_L = C_O \, {f_L}^{k-1} \qquad 11$$

where k is the equilibrium partition coefficient, C_o is the initial alloy composition, C_S is the solid concentration, C_L is the liquid concentration, f_S is the fraction of solid, and f_L is the fraction of liquid.

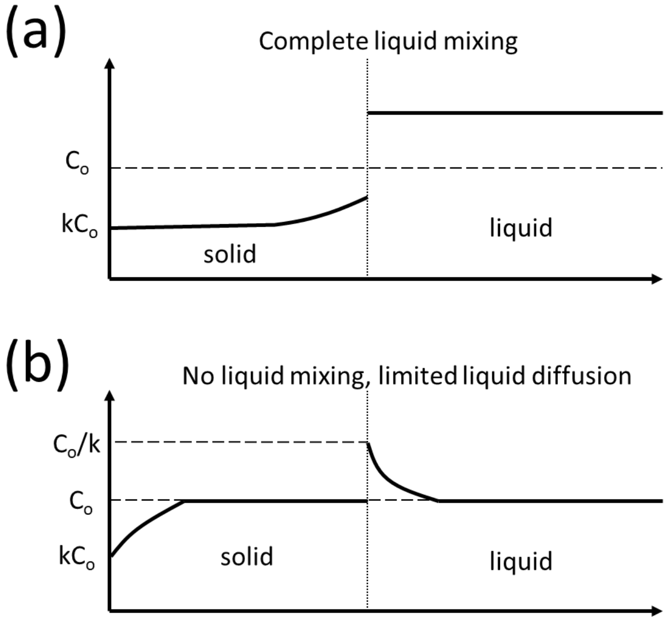

Figure 2.4: (a) solute redistribution in the case of no solid diffusion, but complete mixing in the liquid. This is often termed Schiel solidification. (b) no diffusion in the solid, and limited liquid diffusion.

In case (ii), as shown in Figure 2.4b, there is no liquid mixing and limited liquid diffusion; therefore, a solute-rich boundary layer will build up in front of the solid/liquid interface resulting in three different solute regimes: (i) initial transient (ii) steady state and (iii) final transient. At the initial stages of solidification, the solute concentration in the solid will be kC_o, just as in equilibrium solidification (local equilibrium maintained). As there is limited liquid diffusion, the concentration of solute in the boundary layer will rapidly increase, leading to a rapid increase in the concentration of solute in the solid (initial transient). A steady state is reached when the interface is at the solidus temperature of the overall alloy and the solute rich boundary layer has a concentration of C_o/k. When this occurs, the solid concentration will be the same as the overall concentration, C_o. At the last stages of solidification, there is minimal volume of liquid phase remaining and the concentration of solute in this layer exceeds C_o/k (final transient). It has been shown that the steady state interface layer width can be approximated by equation 12

$$\delta \approx \frac{D_L}{R} \qquad 12$$

where D_L is the diffusivity of the liquid and R is the solidification velocity [24].

Actual real-world solidification conditions in a weld/L-PBF melt track will likely be somewhere between the two idealized non-equilibrium solidification conditions listed above. Kou et al. [27] developed a mathematical model that predicted liquid velocities (due to surface tension gradients) of 3 m/s in laser welding of an Al 6063 alloy, suggesting that convection is significant in laser processing and cannot be neglected. However, surface tension driven convection is at a minimum near the solid/liquid interface [27] and it is likely that a solute-rich boundary layer exists. Despite the oversimplification of the Scheil solidification model, it can be readily calculated with commercial thermodynamic software and will be used in this thesis for solidification modeling.

Another case of non-equilibrium solidification occurs when there is complete solute trapping, in other words, no elemental partitioning (effective k = 1). Solute trapping is typically observed during rapid solidification processing, like welding or L-PBF, when solidification interface velocities, R, exceed 10 cm/s [25]. Solute trapping occurs when the solidification front velocity is greater than the interface diffusion rate of the solute, V_d, given by equation 13,

$$V_d = \frac{D_i}{\delta_i} \qquad 13$$

where D_i is the interface diffusion coefficient and δ_i is the interface length. Aziz et al developed a relationship for the solidification front velocity modified partition coefficient and it is shown in equation 14,

$$k_v = \frac{(k + P_i)}{1 + P_i} \qquad 14$$

$$P_i = \frac{R}{V_d} \qquad 15$$

where P_i is the interface Peclet number [28]. Both D_i and δ_i are challenging values to determine experimentally; howerver, Aziz et. al approximate $D_i \approx D_l \approx 10^{-5}\, cm/s$ [29] and DuPont suggests values of 0.5 to 5 nm for δ_i [30].

The discussion above focused on solute distribution during solidification but now microstructure formation during solidification will be discussed. Nucleation and growth of the solid phase can occur via homogeneous or heterogeneous nucleation. In homogeneous nucleation the solid phase directly nucleates from the liquid phase, but any new solid phase will come with a free energy increase from the new solid/liquid interface. The new free energy contribution to the solid can result in the solid phase having a higher free energy than the liquid, thus preventing further solidification. In order to overcome this barrier for homogenous nucleation, the liquid needs to be undercooled (undercooling need for metals is ~.2 Tm)[26]. Due to the significant energy barrier of homogenous nucleation, most solidification will occur via heterogeneous nucleation (nucleating off an existing surface). In laser welding/ L-PBF, there is always base metal present; therefore, epitaxial (same phase and crystal structure) growth of the solid phase occurs [31]. However, there are occasions where homogenous nucleation can still occur, and will be discussed in the next section.

The growth mode of the solid phase (solidification mode) in a metal alloy can be one of the following: (i)planar, (ii) cellular, (iii) columnar dendritic, or (iv) equiaxed dendritic [25]. The solidification mode that occurs is a function of the thermal gradient (G) and the solidification interface velocity (R) ratio, G/R. The cellular and columnar dendritic solidification modes are the result of a morphological instability in the planar solidification interface. A morphological instability, or protrusion, of the solidification interface can only occur when the protrusion is growing into a region where the liquid away from the interface is at a lower temperature than at the interface (inverse thermal gradient). If an instability grows into liquid that is at a higher temperature than the solid then its growth will slow and the interface will become planar again. In most situations (casting, welding) the solid will be at a lower temperature than the liquid; therefore, it is expected that only planar growth can occur, but this is not the case due to the solute boundary layer (for cases when k < 1). As previously discussed, the partitioning of solute into the liquid results in a solute-rich boundary layer. The solute-rich liquid immediately ahead of the solidification interface will have a lower liquidus temperature than the liquid t further away from the interface, which leads to a form of undercooling called constitutional undercooling (Figure 2.5). The solute boundary layer results in the liquid ahead of the interface actually being below the liquidus temperature (of the solute layer) allowing an instability to propagate. Low thermal gradients lead to larger degrees of undercooling and with sufficiently low thermal gradients equaixed dendrites can be formed in the melt ahead of the main solid/liquid interface. The solidification velocity will influence the extent of the solute-rich boundary layer, and hence the degree of undercooling and the solidification mode. The critical G/R ratio that needs to be exceeded for constitutional undercooling to occur is given by equation 16,

$$\frac{G}{R} \geq \frac{(T_L - T_S)}{D_L} \qquad 16$$

A qualitative G/R diagram showing the solidification mode as a function of G and R is shown in Figure 2.6. Control of G/R is essential for controlling the microstructure during solidification processing and process-microstructure maps have been produced for this purpose. For example, Gauman et al. [32] produced process-microstructure maps as a function of the laser power and scanning velocity in order to perform single crystal turbine blade repairs. While G/R determines the solidification mode, GxR, in other words, the cooling rate, determines the size of the solidification structure.

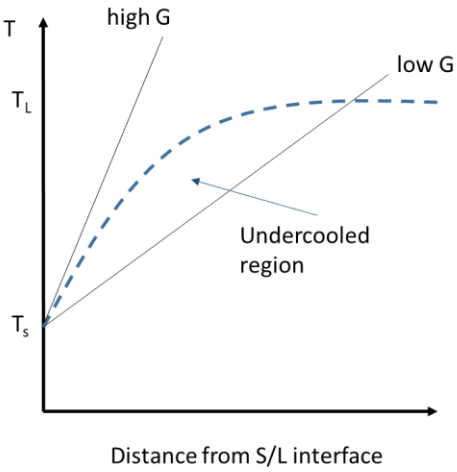

Figure 2.5: Constitutional undercooling diagram showing the influence of high and low thermal gradients.

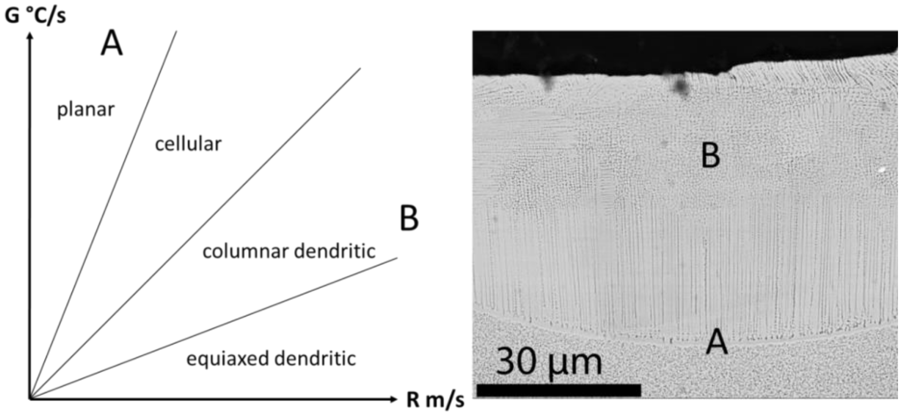

Figure 2.6: G/R diagram showing the solidification mode as a function of thermal gradient and solidification front velocity. Also, a BSE image of a weld on CM247LC showing what different growth modes look like.

All of the above solidification principles apply to welding/L-PBF, but in beam based processing the situation becomes more complicated since the G and R will vary throughout the melt pool [33]. Figure 2.7 shows how the G and R vary through the depth of the melt pool. At the bottom of the melt pool, the G is at its highest value and the R is at its lowest value. In a simple sense, G is at its highest at the bottom of the melt pool since the molten metal is in contact with the cold substrate. As the metal solidifies, the G will drop as the molten metal is now in contact with warmer solidified metal. The R is a function of the beam velocity, as shown in equation 17,

$$R = V\cos(\theta) \qquad 17$$

where V is the velocity of the beam [33]. At the bottom of the melt pool, the normal of the solid/liquid interface is perpendicular to the direction of beam travel; therefore, the R is 0. As the melt is solidifying, the normal to the solid/liquid interface becomes parallel to the beam direction and R will reach a maximum of the beam velocity. This variation of

G and R throughout a melt pool can be seen in the cross section of the laser weld in Figure 2.6. At the bottom of the melt pool, G is highest and R is lowest, therefore a planar front is stable (labelled A in Figure 2.6). Further up the melt pool, the G is lower and the R is higher, therefore; columnar dendritic growth is favored (labelled B in Figure 2.6).

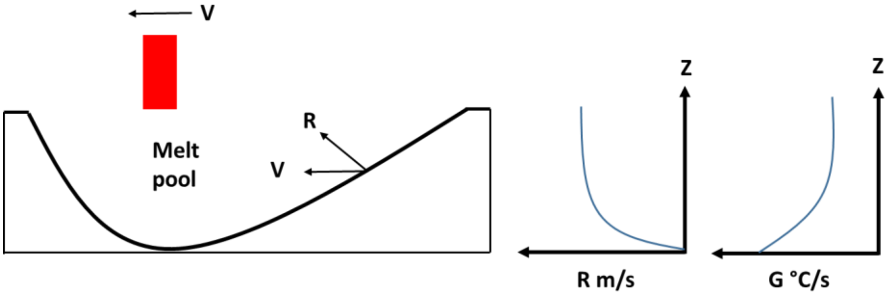

Figure 2.7: Variation of the solidification front velocity (R) and the thermal gradient G in a moving laser beam generated melt.

2.4 Nickel-Base Superalloy Metallurgy Primer

Nickel-based superalloys are used in applications where mechanical stability and corrosion resistance over extended periods at elevated temperatures is required, for example, turbine engines. Nickel is an ideal candidate for high temperature applications for a few reasons: (i) it has the Face Centered Cubic (FCC) structure, (ii) the FCC structure is stable until the melting point (no phase transformations), and (iii) there is a high solubility of several alloying elements in FCC nickel [34,35]. The advantage of FCC metals is that they have the lowest diffusivities out of the metals (Melting Point Diffusivities: ~10^{-13} – 10^{-12} m^2/s for FCC metals, ~10^{-12} – 10^{-11} m^2/s for BCC transition metals [36]) due to the close packed structure and exhibit good ductility with no brittle-to-ductile transition. Other elements, such as cobalt, are also used as a base material for high temperature applications, but nickel use is more widespread for economic reasons and higher elevated temperature performance (Co-base alloys do not have $L1_2$ strengthening) [34,35].

The nickel-base superalloys can be subdivided into two classes (i) solid-solution strengthened alloys, and (ii) precipitation strengthened alloys. Typical solid solution strengtheners in Ni-base superalloys are elements with sufficient atomic radius differences from Ni, such as W (13% larger), Mo (12% larger) and Ta (18 % larger), to provide sufficient lattice strain for strengthening. The precipitation-strengthened alloys mostly utilize $L1_2$-structured Ni_3Al precipitates (γ` phase) in high phase fractions (up to 70 volume %) for strengthening. A modern day precipitation-strengthened Ni-base superalloy, such as CM247LC, will have 12 elements (C, Cr, Co, W, Mo, Ta, Al, Ti, Hf, B, Zr, Ni) in total for an optimal combination of solid solution strengtheners, carbide/boride formers, and precipitate formers. Figure 2.8 shows the microstructure of a directionally cast CM247LC turbine blade.

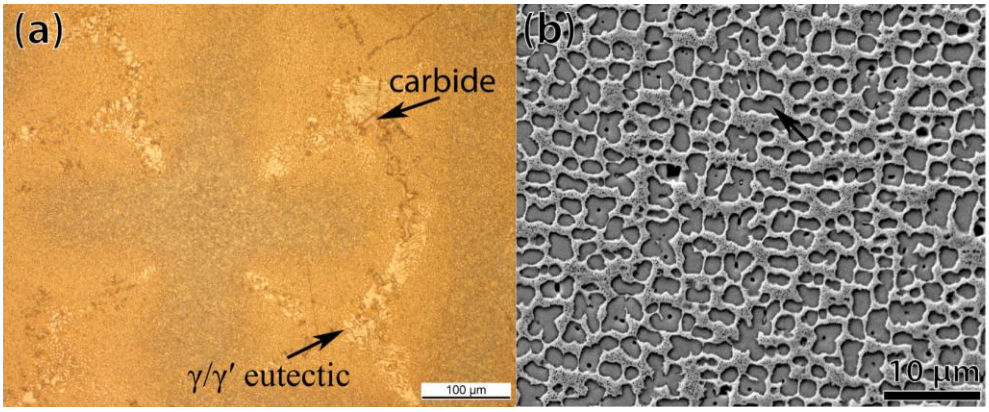

Figure 2.8: Images of the microstructure of a CM247LC directionally solidified turbine blade. The images were taken from the root of the turbine blade. (a) Optical image of the microstructure. The blueish tint cross in the middle of the image is a dendrite and the orange tint areas are interdendritic. Carbides and γ/γ′ eutectic (left over from casting) are visible. (b) BSE image showing the γ′ precipitates (highlighted by a black arrow)

Superalloys that are not destined to be cast as a single crystal require grain boundary strengthening via carbides and borides to prevent grain boundary sliding during creep [35]. The common carbide and borides phases observed are: MC, M_6C, $M_{23}C_6$, M_7C_3 and M_3B_2. The carbide formers (M) are typically Ta, Hf, Mo,Cr, and Ti. The MC carbides form from the liquid during solidification in the interdendritic regions but upon heat treatment transform to the $M_{23}C_6$ phase [35]. Zirconium is also added as a grain boundary element as it is thought to improve creep resistance but the reason why is still debated [35]. Hafnium is another grain boundary strengthening element that was originally added to increase the ductility of Ni-base alloys at elevated temperatures. It is hypothesized that the ductility increase is due to presence of eutectic γ/γ` at the grain boundaries, which Hf promotes [34]. Hf also modifies the morphology of the MC carbides that form during solidification, changing them from a script like to blocky morphology, which is more crack propagation resistant. One disadvantage associated with the grain boundary strengtheners is that they depress the solidus point of the alloy.

The γ` strengthened alloys, while containing the solid solution strengtheners and carbide formers listed above, utilize Al and Ti additions to form high fractions of γ’ phase. The γ’ precipitates are coherent with the matrix and have a cube-cube orientation relationship. The primary strengthening mechanism of the γ’ precipitates results from the effect of ordering on dislocation movement. Dislocations can overcome an obstacle, in this case the γ’, by either bowing around it (Orowon bowing) or shearing/cutting through it [37]. In traditional precipitate strengthening theory, for a fixed volume fraction of precipitate, dislocation cutting strength is proportional to $\boldsymbol{r^{1/2}}$ and dislocation bowing strength is proportional to 1/r. The mechanism that operates depends on the particle radius as shown in Figure 2.9 (bowing at large particle sizes due to the increase in particle-to-particle spacing). The advantage of an ordered phase, such as γ’, is that there is a free energy penalty associated with disrupting the chemical ordering of the lattice (Ni-Al bonds have the lowest free energy and the passage of a dislocation results in higher free energy Ni-Ni and Al-Al bonds). This energy penalty is referred to the Anti-phase Boundary (APB) energy and is similar to stacking fault energy [26]. If a dislocation is to shear/cut a γ′ precipitate then it will need to overcome the large opposing force created by the APB. The higher the APB energy associated with the precipitate, the more force that is required for a dislocation to shear the precipitate. In order for the precipitate to maintain ordering after shear/cutting, dislocations will travel as pairs, termed superdislocations, through the precipitate [35]. The first dislocation leads to the disruption of order (creation of the APB) and the second dislocation restores the order (elimination of the APB). These dislocations can further be sub-classified based on separation distances: (i) weakly-coupled dislocations (large spacing between the dislocations, one dislocation in a particle at a time, occurs for under-aged γ′) and (ii) strongly-coupled dislocations (small spacing between the dislocations and both dislocations can be in the particle at the same time, occurs for over-aged γ′) [35]. The shearing strength that results from the two potential dislocation spacings differs and there exists an optimal radius (between the two sizes) that gives the optimal cutting strength [35]. Optimal size of the γ’ precipitates will depend on the volume fraction of the phase but the optimal size in the high volume fraction alloys is often in the hundreds of nms in diameter [38]. The high shearing resistance of the γ’ phase means that deformation typically occurs via dislocation bowing in the matrix until sufficiently high stresses [39].

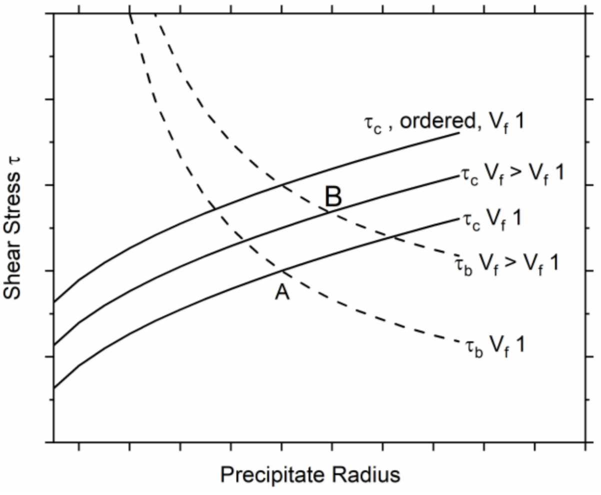

Figure 2.9: Plot of shear stress as a function precipitate radius. Dashed lines represent precipitate bowing and solid lines represent cutting. The high volume fraction of strengthening phase in the superalloys increases the strength from A to B. Ordering can further improve the strength.

Thermal stability (resistance to coarsening) of the γ' precipitates (or any precipitates) is critical for strength at high-temperature. The stability is dependent upon the precipitate size, concentration of solute (temperature dependent), diffusivity of solute in the matrix (temperature dependent), and of the interfacial energy [26]. When considering thermal stability, it is important to look at the thermodynamics and kinetics of precipitate coarsening. Particle coarsening behavior can be mathematically described for a binary system with the following relationships, equations 18 and 19):

$$\bar{r}^3 - r_o^3 = kt \qquad 18$$

$$k \propto D\gamma X_e \qquad 19$$

where $\bar{r}$ is the mean particle radius, r_o is the starting particle radius, t is the time, D is the diffusion coefficient, γ is the interface free energy, and X_e is the equilibrium solubility of the precipitate [26]. The free energy change of a precipitate will depend on if it is a coherent or incoherent precipitate. The change in free energy for a coherent precipitate is given by equation 20,

$$\Delta G\ (coherent) = 4\mu\delta^2 \cdot {}^4\!/_3\,\pi r^3 + 4\pi r^2 \cdot \gamma_{ch} \qquad 20$$

where μ is the shear modulus of the matrix, δ is the misfit between the lattice and precipitate, r is the precipitate radius and γ_{ch} is the interfacial energy resulting from chemical differences [26]. The free energy change associated with a non-coherent precipitate is given by equation 21,

$$\Delta G\ (non - coherent) = 4\pi r^2(\gamma_{ch} + \gamma_{st}) \qquad 21$$

where $\gamma_{st}$is the structural contribution to the total interface energy. Since the γ' is coherent with the matrix and with a minimal misfit, the interfacial energy is at a minimum (no structural interface energy, only chemical), leading to a decrease in coarsening rate over a non-coherent precipitate. The coherent precipitate will be more thermodynamically stable (lower Gibbs free energy) than the non-coherent precipitate, given that the precipitate size and lattice mismatch is small (past a certain size, non-coherent precipitates are more stable). Aside from having coherent precipitates, the Ni-base superalloys will rely on additions of slow diffusing elements (such as W) to lower the coarsening rate further.

The processing of Ni-base superalloys has evolved from wrought blades, to equiaxed castings, to directionally solidified (DS) castings, and currently to single crystal directionally solidified (SXDS) castings. The process evolution was driven by the need to improve the creep lives of the superalloys. The advent of DS castings resulted in a microstructure shift from equiaxed grains to columnar grains. The elimination of the transverse grain boundaries from the DS casting process resulted in an increase in creep life. In the 1980s, single crystal superalloy castings began to appear, offering the highest creep lives due to the complete removal of grain boundaries. This processing change also drove changes to the compositions of superalloys. With the removal of grain boundaries, carbides were longer needed to provide grain boundary strengthening [35]. Directional solidification of the Ni-based superalloys occurs as dendritic solidification with a [100] orientation parallel to solidification direction. The dendritic solidification can result in substantial microsegregation where the dendritic regions become rich in W, Re, and the interdendritic regions become rich in Ti and Ta. This segregation can lead to non-uniform γ' precipitation and eutectics that can lead to incipient melting [35].

As AM is often equated to welding, due to the similarities in solidification behavior, it is important to look at the weldability of the superalloys. The solid-solution strengthened superalloys, and a few precipitation strengthened superalloys, such as IN 718, are known to have good weldability; however, the superalloys that contain high amounts of Al and Ti, to produce the $L1_2$ $Ni_3(Al,Ti)$ precipitation, such as CM247LC, are considered less weldable and are subject to cracking [38]. Micro-cracking of welded precipitation strengthened Ni-base superalloys can be attributed to the following mechanisms:

1. Solidification Cracking: Solidification cracking occurs during the final stages of solidification when solute-rich liquid becomes trapped between two solid interfaces. Shrinkage strain resulting from the liquid to solid phase transformation in combination with thermal contraction strain result in the remaining liquid being pulled apart (liquid has negligible shear strength). [10]
2. Liquation Cracking: Liquation cracking occurs in the heat-affected zone (HAZ) of a melt track. Micro-segregation of elements during solidification of the metal, whether from casting or from a previous melt track, in the case of AM, results in grain boundaries and/or interdendritic areas having a depressed solidus point due to the changed chemical composition. When these boundaries are subjected to elevated temperatures in the HAZ they liquefy and become susceptible to tearing. Liquation can also be the result of molten metal wetting and penetrating grain boundaries of previously solidified material. [10]
3. Strain Age Cracking (SAC): When a superalloy is undergoing a solutionizing heat treatment it will pass through the aging temperature upon heating. Precipitation of the strengthening phase, typically γ'-Ni_3M, during the ramp will result in reduced ductility. If the residual stresses generated during pro-

cessing, or from the precipitation itself (lattice mismatch), are not able to relax before the material loses ductility (from precipitation), then cracking can occur. [24,38]

4. Ductility Dip Cracking (DDC): Nickel-base superalloys are subject to a reduction in ductility at a temperature between the solidus (T_s) and 0.5 T_s. If sufficient strain exists in the material while at this temperature range then the material will crack. One suggested mechanism for the loss of ductility is grain boundary shearing. [10]

2.5 Aluminum-Base Superalloy Metallurgy Primer

The goal of the $L1_2$ phase in Al-base superalloys is similar to the goal for Ni-base superalloys; provide strengthening at elevated temperatures. The fundamentals of $L1_2$ phase strengthening and thermal stability that were discussed in section 2.3 apply for the Al-base alloys as well. The thermodynamically stable $L1_2$ phase in aluminum alloys has the composition of Al_3M, where M can be Sc, Er, Tm, Yb, Lu, U, or Np [11]. Other elements such as Ti, Zr, and Hf can also form the $L1_2$ phase in aluminum alloys, but are thermodynamically metastable ($D0_{22}$ or $D0_{23}$ structures at equilibrium) [11]. Despite being thermodynamically metastable, Al_3(Ti, Zr, Hf) will precipitate as the $L1_2$ structure during aging and remain as the $L1_2$ structure even after hundreds of hours of exposure above 450°C [11]. A majority of research into the Al_3M precipitates has focused on Sc [11]; however, Al_3Zr precipitate forming alloys are garnering interest [40–44].

The Al-Sc and Al-Zr systems have a few key differences. The Al-Sc system has a eutectic transformation, while the Al-Zr system has a peritectic transformation. This can result in a difference in solidification behavior at the Al rich end of the phase diagram (depending on if the alloy is to the left or right of the peritectic/eutectic point); at 0.2 at.% of solute (Sc, Zr), Al_3Zr forms from the liquid and Al_3Sc forms from the solid. The segregation tendencies are also different between the two systems: $k = 2.5$ for Zr [45], and $k = 0.52$ for Sc [46] . Another key difference, especially for thermal stability, is the significantly lower diffusivity of Zr in Al. At 400°C the diffusivity of Sc and Zr in Al is 1.98×10^{-17} and 1.20×10^{-20} m^2s^{-1}, respectively [11]. The lattice parameter mismatch with the Al matrix is lower for Al_3Zr than for Al_3Sc, 0.75% and 1.32%, respectively [11]. The lower lattice parameter of Al_3Zr could lead to lower particle strengthening (less lattice strain), but will also lower the free energy of the precipitate per equation 20 and therefore lower the coarsening rate per equation 19. Lastly, Zr is less expensive than Sc. Aluminum alloys with less than ~0.7 wt.% Zr processed via conventional casting have been studied extensively [40–44]. Rapid solidification of binary Al-Zr alloys has been researched, which is more applicable to the L-PBF process, and has shown that cuboidal $L1_2$-structured Al_3Zr precipitates form from the liquid [47,48] and that the Zr solubility in solid solution can be increased [49].

One key difference that separates these alloys from the Ni-base superalloys is the volume fraction of $L1_2$ phase that is achievable. The solubility of Sc in Al is quite low (0.01 at% at 400°C in the binary); therefore the phase fraction of precipitates is substantially lower than in the Ni superalloys. Because of the lower volume fraction of $L1_2$ phase, dislocations can climb over the precipitates during creep as opposed to the Ni-alloys where the high volume fraction prevents this [11]. The high supersaturation of Zr achievable in the AM process, and thus the high volume fraction of nanoprecipitates, could however further improve the creep resistance of Sc-free Al-Zr based alloys, despite the low lattice mismatch.

Similar to the Ni-base superalloys, solid solution strengthening elements, commonly Mg, are added to improve strength [50].

2.6 Elevated Temperature Mechanical Behavior Primer

Mechanical behavior of metals at elevated temperatures differ from that at room temperature due to the addition of thermally activated processes. In general, as the temperature increases, the yield strength will decrease and the elongation at fracture will increase (The Ni-base superalloys are a notable exception). There are numerous mechanisms responsible for the loss in yield strength as temperature increases: (i) lower dislocation frictional stress, albeit small change for FCC [51], (ii) more slip systems become active (thermally activated slip), (iii) recovery of dislocation networks that cause strain hardening, and (iv) dislocation climb (equilibrium concentration of vacancies increases as the temperature increases and diffusion rate increases) [37]. Since diffusional processes are involved, time becomes a factor and a distinction has to be made between short duration and long duration mechanical property tests. A long duration mechanical property test at elevated temperature is often referred to as a creep test, where strain rates at given loads and temperatures are measured. Simple tensile yield tests at elevated temperature typically involve quickly heating the sample to the test temperature and pulling it to fracture at a fixed strain rate, just like a normal tensile test. [52] Creep behavior and mechanisms will now be briefly discussed.

When a tensile creep specimen is loaded (constant load or constant stress conditions) at a given temperature (typically starting at 0.3 to 0.5 T_m for metals [37]) the creep rate will with vary with time as shown in Figure 2.10. Upon initial loading of a creep specimen there will be an immediate strain that has both elastic and plastic contributions [53]. The initial loading is then followed by what is called primary creep (Region I in Figure 2.10). The strain rate rapidly increases during primary creep as thermally activated slip occurs. The strain rate begins to lower once dislocations interact and strain hardening occurs. As the test is done at elevated temperatures, recovery of the material (dislocation alignment and annihilation) is also occurring at the same time. When the rate of strain hardening and recovery are equal, the strain rate will level off and the creep is said to be in secondary creep or steady-state creep (Region II in Figure 2.10) [37]. Tertiary creep is characterized by a rapid increase in the strain rate that is the result of the formation of metallurgical instabilities (necking, micro-void formation, etc.) that result in fracture of the specimen. It is important to note the creep curve shown in Figure 2.10 is an idealized creep curve and many combinations of stress, temperature, and material will lead to curves that differ. For example, some materials will not show a well defined primary creep region [53], and constant stress creep testing will typically not show a tertiary region [37].

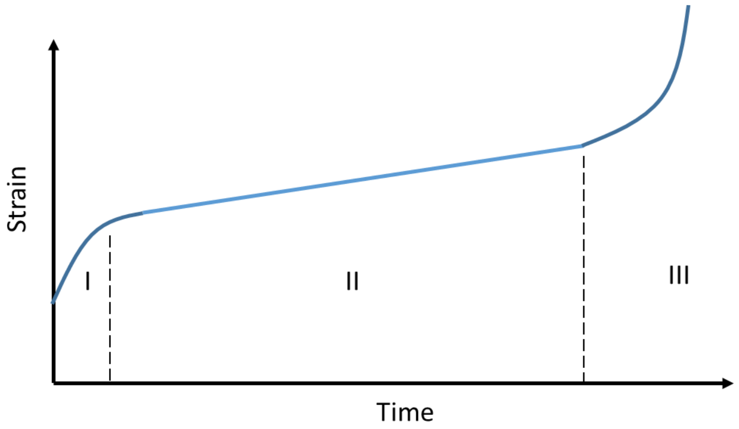

Figure 2.10: A idealized creep curve. Region I is primary creep, Region II is secondary or steady state creep, and Region III is tertiary creep.

The creep rate in the secondary creep regime, or steady-state creep rate, follows an Arrhenius-type equation, such as that in equation 22,

$$\dot{\varepsilon}_s = A\sigma^n e^{-Q/RT} \qquad 22$$

where A is a constant, σ is the stress, n is the stress exponent, Q is the activation energy for diffusion (lattice, solute, or grain boundary diffusion), R is the ideal gas constant, and T is the temperature. The values of n and Q can indicate the rate controlling creep mechanism [53]. The value of n is determined by calculating the slope of a fitted line through the data in a plot of the log of the strain rate vs the log of the stress. In a simple sense, underlying creep mechanisms can be split into the following: (i) diffusional creep, n = 1, (ii) grain boundary sliding, n = 2, and (iii) dislocation creep, n = 3-7 [53]. Values of n greater than 7 can be the result of the onset of tertiary creep or from precipitates. In the case of precipitates causing a large apparent n value, equation 22 is often modified to invoke a threshold stress so that the true value of n can be determined.

Diffusional creep can be divided into two main mechanisms, although other mechanisms do exist: (i) Nabarro-Herring creep and (ii) Coble creep [53]. In a simple sense, Nabarro-Herring creep refers to creep via lattice diffusion of vacancies and atoms and Coble creep refers to creep via grain boundary diffusion of vacancies and atoms. In general, diffusional mechanisms are dominant at low stress levels and at high temperatures. Coble creep is active at lower temperatures since the activation energy for grain boundary diffusion is lower than that of lattice diffusion. It is important to note that the grain size will have a profound impact on diffusional creep (also dislocation movement). As the grain size decreases in a polycrystalline metal, the number of short circuit diffusion paths greatly increase, vacancies sources increase, and the distance for Nabaro-Herring lattice diffusion decreases. For these reasons, a larger grain size and even a single crystal is most beneficial from a diffusional creep standpoint.

Dislocation creep can also be divided into two main mechanisms: (i) viscous dislocation glide, n =3, and (ii) dislocation climb, n=4-7. Dislocation creep is generally operable at high stress levels and lower temperatures. Despite being referred to as dislocation creep, both mechanisms are still diffusion controlled. Viscous dislocation glide is thought to be controlled by the diffusion of solute to a dislocation core (Cottrell atmospheres) [53]. Dislocation climb is controlled by the diffusion of vacancies in the lattice that are required for an edge dislocation to climb over an obstacle. It is important to highlight that at high enough stress levels dislocation glide can occur but unlike viscous dislocation glide, it is not a diffusion controlled process.

Lastly, creep deformation via grain boundary sliding (GBS), n=2, occurs when a applied stress causes two grains to slide past one another. Two forms of GBS can occur: (i) Rachinger sliding, and (ii) Lifshitz sliding [54]. Lifshitz sliding refers to the GBS that occurs due to the vacancy movement of Nabarro-Herring and Coble creep [54]. Rachinger sliding is GBS that is accommodated via dislocation movement.

2.7 PBF of Aluminum-Base Superalloys

Initially, most research on AM of aluminum alloys focused on the Al-Si system [55–59] due to the inherent weldability of this alloy family. Parts have been successfully produced by AM using this class of aluminum alloys; however, they suffer from relatively low strength and low ductility compared to the precipitation-strengthened 2000 (Al-Cu), 6000 (Al-Mg-Si), and 7000 (Al-Zn-Mg) series alloys. Unfortunately, the 2000, 6000, and

7000 series exhibit larger freezing ranges compared to the Al-Si alloys, which make them more prone to hot cracking. Hot cracking during AM of 7000 series alloys was successfully mitigated by modifying the alloy composition and the powder characteristics. Sistiaga et al. [60] fabricated dense, crack-free parts with L-PBF by using an 7075 Al powder blended with elemental Si powder (4 wt.%). The authors attributed the improvement to the lower viscosity of the molten alloy; however, adding large amounts of Si is detrimental for ductility. Martin et al. [61] added nanoscale hydrogen-stabilized Zr particles to the surface of 6061 and 7075 Al powders in order to preferentially nucleate equiaxed grains during solidification, due to the primary precipitation of Al_3Zr. Equiaxed grain microstructures, when compared to the typical columnar grain microstructures of AM aluminum parts, can better accommodate the strain induced by the AM process, thus resulting in crack-free parts.

Recent research on AM of aluminum alloys has focused on Sc- and/or Zr-modified Al-Mg based alloys [62–69]. This class of alloy benefits from solid-solution strengthening from Mg as well as precipitation strengthening from coherent $L1_2$ structured $Al_3(Sc,Zr)$ secondary nano-precipitates, formed on aging, that have a high dislocation cutting resistance and resist coarsening up to temperatures above 400˚C [11]. Primary $Al_3(Sc,Zr)$ precipitates formed on solidification also serve as grain-refiners which promote fine, equiaxed, Al matrix grains that increase alloy strength, and are thus also beneficial for hot-crack mitigation. Another benefit of AM processing is related to the extremely high cooling rates, which allow for increased solute solubility of Sc and Zr. Upon aging, this supersaturated solution induces the precipitation of higher volume fractions of the strengthening $L1_2$-$Al_3(Sc,Zr)$ secondary precipitates compared with that of conventional processing. Designing alloys optimized for fast cooling rates is thus the key to taking full advantages of AM processing. One such alloy is the Al-Mg-Sc-Zr alloy Scalmalloy® (Al-4.6Mg-0.49Mn-0.66Sc-0.42Zr (wt%)) which was shown to have good processability via L-PBF [68]. Spierings et al. [69] obtained dense (>99%), crack-free Scalmalloy® parts with yield strengths up to 300 MPa in the as-fabricated (L-PBF) condition, and in a separate study [70], reported a yield strength of 470 MPa for L-PBF processed Scalmalloy® in the aged condition (325˚C / 4 h). In a second example, Jia et al. [62] also developed an $Al_3(Sc,Zr)$-strengthened alloy, Al-4.52Mn-1.32Mg-0.79Sc-0.74Zr-0.05Si-0.07Fe (wt%), that takes advantage of the high cooling rates of L-PBF to allow for supersaturation of Mn. The use of Mn for solid solution strengthening, instead of Mg, would minimize the disadvantages associated with Mg such as: (i) Mg suffers from significant in-process (SLM) evaporation [67] and (ii.) precipitation of the β-phase(Mg_2Al_3) can lead to increased grain boundary corrosion susceptibility [71]. A bimodal microstructure of fine equiaxed grains and columnar grains was also observed, and yield strengths of ~440 MPa and ~560 MPa were reported for the as-fabricated and peak-aged condition (300˚C / 5 h), respectively.

Prior to more widespread industrial implementation of the aforementioned precipitation strengthened aluminum alloys for additive manufacturing, additional microstructure characterization and understanding of mechanical properties are required. Room temperature mechanical property testing has been investigated for SLM-fabricated aluminum alloys but high-temperature properties are few and even non-existent for the AM fabricated $Al_3(Sc,Zr)$ precipitate strengthened alloys. Significant amount of literature is available on the creep performance of conventionally-cast, $L1_2$-strengthened aluminum alloys [50,72–75]. The high supersaturation of Zr achievable in the AM process, and thus the high volume fraction of nanoprecipitates, could however further improve the creep resistance of Sc-free Al-Zr based alloys. Uzan et al. [76] reported on the creep properties of an L-PBF fabricated Al-10Si-Mg (wt.%) alloy tested in the 225-300˚C temperature range at stresses in the 117-147 MPa range. They described a dislocation creep mechanism and likened the creep resistance of the L-PBF fabricated alloy to that of particle reinforced aluminum composites.

2.8 PBF of Nickel-base Superalloys

Numerous studies focusing both on microstructure and defect formation have been published on the PBF of precipitation strengthened Ni-base superalloys [2–9]. Carter et al. [9] investigated the microstructure of L-PBF fabricated CM247LC and observed a columnar grain microstructure, with a <001> texture oriented parallel to the build direction, separated by regions of fine grains. The bimodal grain distribution was attributed to the scan strategy (chess strategy). They observed a majority of cracking in the highly misorientated fine-grain regions and attributed the cracking to DDC. Wang et al. [3] performed a detailed Transmission Electron Microscope (TEM) analysis on L-PBF fabricated CM247LC (as-fabricated condition) and observed columnar grains that were comprised of several 700 nm wide cells (low angle grain boundary). The cell boundaries had a high dislocation density and contained Hf/W/Ti/Ta-rich precipitates. A high density of 10 nm diameter γ`($Ni_3Al$) particles were observed within the cells and 50 nm diameter γ` was observed on the cell boundaries. It was hypothesized that the presence of Hf/W/Ti/Ta-rich precipitates and γ` led to dislocation accumulation at the cell boundaries. Divya et al. [4] also studied the microstructure and defect formation of L-PBF fabricated CM247LC. Electron Backscatter Diffraction (EBSD) analysis revealed several 500 nm diameter cells with small misorientations (less than 4°) making up a single grain.

Similar to Wang et al., Divya et al. observed 50 nm diameter carbides, 50 nm diameter γ`, and a high density of dislocations on the cell boundaries. Cracking was observed as well, however, they disputed the DDC mechanism, as the cracking was located mainly on cellular boundaries.

Cloots et al. [5] investigated the L-PBF of IN738LC and observed a similar columnar grain structure oriented along the build direction. Cracking was observed transverse to the laser scan direction, and SEM imaging inside of the cracks revealed a dendritic structure characteristic of solidification cracking. Atom Probe Tomography (APT) analysis of a grain boundary revealed high levels of Zr segregation, which is known to be a solidus depressant. Ramsperger et al. [7] studied the processing of E-PBF fabricated CMSX-4 and attributed its cracking to high internal stresses when part dimensions exceeded a certain value. The elevated processing temperatures associated with E-PBF also resulted in in-situ γ` precipitation. Chauvet et al. [6] performed an extensive study on cracking mechanisms affecting an unspecified Ni-Co-Cr-Mo-Al-Ti-B superalloy processed by E-PBF and concluded that a solidification cracking mechanism was at play based on the morphology observed on crack faces. Higher angle grain boundaries were found to be more susceptible to cracking than lower angle grain boundaries, and was attributed to the higher angle grain boundaries remaining wetted at lower temperatures (due to increased boundary energy) which in turn increases the solidification cracking susceptibility. APT studies revealed the presence of borides, which are known to depress the solidus temperature, on the grain boundaries.

A few different approaches to micro-crack mitigation in PBF fabricated Ni-base superalloys have been reported in literature, which can be categorized as the following: (i) alloy modification, (ii) process modification, and (iii) post-processing. Carter et al. [2] utilized X-ray Computerized Tomography (CT) scans, on a L-PBF fabricated CM247LC, to highlight the effectiveness of post-process Hot Isostatic Pressing (HIP) at healing internal micro-cracks. Surface cracks can not be healed with HIPing. Research into crack mitigation via process modification are mostly focused on the effects of pre-heating [7,77] and scan strategies [2]. Ramsperger et al. [7] reported crack-free CMSX-4 samples fabricated by E-PBF when using high fabrication temperatures (1040°C and above), which is possible in E-BPF due to the E-beam preheating. Hagedorn et al. [77] obtained L-PBF fabricated crack-free CM247LC by preheating the baseplate to 1200 °C. Carter et al. [2] investigated the influence of scan strategy on L-PBF fabricated CM247LC and found that a simple back and forth scan strategy resulted in a homogenous microstructure that was less susceptible to cracking. One novel approach to process modification is the 3D Laser Shock Peening (LSP) approach demonstrated by Kalentics et al. [78]. In this method, LSP was applied between layers during the L-PBF fabrication of CM247LC in order to impart a compressive residual stress, which induces crack healing through a reverse brazing mechanism. Crack mitigation through alloy modification has also been a successful technique. Harrison et al. [79] showed reduced cracking in an L-PBF fabricated Hastelloy X that was modified with increased solid-solution strengthening elements to improve the material strength. Engeli et al. [80] investigated the L-PBF processability of several batches of IN738LC and found that a Si content lower than 0.02 wt% was required to produce crack-free samples.

Each of the crack mitigation approaches listed above have advantages and disadvantages, and successful processing of precipitation strengthened Ni-base superalloys will require some combination of the different approaches. Post process HIPing is effective at micro-crack healing; however, it is an additional manufacturing step that will increase production time and cost. Sample preheating has proved to be a viable option for successfully PBF fabrication of the precipitation strengthened Ni-base superalloys; however, it remains only well suited for the E-PBF process since a majority of L-PBF machines do not have the ability to operate at such high temperatures. Alloy modification and/or control of impurity levels is another successful strategy but again, it does not always lead to crack-free parts. A better understanding of the underlying mechanisms is required in order to modify the process and alloys for successful production level AM of the precipitation strengthened Ni-base alloys.

In conventionally cast superalloys a solutionizing heat treatment and aging treatment are required to obtain the optimal size and volume fraction of γ'. Naturally, this is a next step for AM processed superalloys in order to obtain optimal γ' structures. Post process heat treatment has been investigated in numerous AM processed superalloys [4,81,82]. Divya *et al* [83] solutionized a SLM fabricated CM247LC sample at 1230˚C for two hours and observed limited recrystallization and a grain structure similar to that observed in the as processed condition. The γ' precipitates in recrystallized grains had a radius of ~100-250 nm and a similar size but more irregular morphology was observed within the unrecrystallized grains [83]. Carbides were located on the grain boundaries and were ~200-500 nm in diameter. Dislocation density at cell boundaries was also observed to decrease but this is to be expected in a solutionized sample [83]. Kunze et al. [81] HIPed (1180 °C 4 h), solutionized (1120 °C 2 h), and aged (850 °C 20 h) L-PBF fabricated IN738LC. No recrystallization or grain coarsening was observed. The HT samples had a duplex γ' precipitate size distribution of ~50 nm and ~500 nm in radius.

Kanagarajah et al.[82] solutionized (1160°C 4 h) and aged (850°C 16 h) L-PBF fabricated IN939. Recrystallization was observed in the heat treated samples. The γ' precipitate radius was ~30 nm.

Room and elevated temperature mechanical properties have been reported for IN939 [82] and IN738 [81]. Few studies with high γ` containing alloys, such as CM247LC, exist, likely due to the extensive micro-cracking observed in these alloys. Kanagarajah et al. [82] reported room temperature and 750°C yield strengths of ~1000 MPa (10-15 % elongation) and 800 MPa (~1% elongation), respectively, for L-PBF fabricated IN939 solutionized (1160°C 4 h) and aged (850°C 16 h). Rickenbacker et al. [84] performed room temperature and 850°C tensile testing on HIPed (conditions not reported), solutionized (1120 °C 2 h), and aged (850 °C 24 h) L-PBF fabricated IN738LC. The yield strength of HIPed, solutionized, and aged IN738 in the transverse direction (gauge section perpendicular to build direction) was reported as 933 ± 8 and 610 ± 1 MPa for the room temperature and 850°C condition, respectively. Samples parallel to build direction had slightly lower yield strengths of 786 ± 4 and 503 ± 1 MPa for the room temperature and 850°C condition, respectively. Elongation at fracture was lower in the transverse direction than in the parallel orientation (11.2 ± 1.9 % for parallel, and 8.4 ± 4.6 % for transverse at room temperature; 14.2 ± 3.9 % for parallel, and 8.0 ± 1.2 % for transverse at 850°C). Wang *et al.*[3] performed tensile testing on L-PBF fabricated CM247LC (tensile bars oriented parallel to the build direction) and observed a 792 MPa yield strength with a 6-8% elongation at fracture. Samples were not HIPed prior to testing.

Kunze et al. [81] performed creep tests at 850˚C of both SLM produced samples and traditionally cast samples and found the creep rupture strength to be lower for the SLM fabricated samples. This is not completely unexpected due to the known correlation between grain size and creep properties.

2.9 Aim of the Thesis

The above literature review of the L-PBF of Ni-base and Al-base $L1_2$-strengthened superalloys highlights a few gaps in knowledge and challenges that need to be addressed prior to more widespread use of these alloys. While some of the challenges differ between the two alloy systems, on a basic level, the overall challenge is to understand how the alloy and the process parameters influence the microstructure and therefore the mechanical properties. While decades of research exists for laser welding, and that research proves useful for understanding the fundamental processes, the AM process results in a part that is made of thousands of "welds" and introduces complexities not present in laser welding alone. The thesis will be split into two main portions, an Al-base superalloy portion, and a Ni-base superalloy portion. The specific research questions that are to be addressed by this work are highlighted below:

1) Al-Base Superalloys
    a) What is the processability of a new $L1_2$-strengthened Al-base superalloy called Addalloy® (Al-Mg-Zr alloy)?
    b) How does the unique bimodal microstructure of the L-PBF processed Al-Mg-Zr alloy, and other $L1_2$-strengthened Al-base superalloys, form?
    c) How can the process be modified to alter the microstructure?
    d) How does the Al-Mg-Zr alloy respond to heat treatment?
    e) What is the mechanical behavior of L-PBF fabricated Al-Mg-Zr alloys at both room and elevated temperature?
2) Ni-Base Superalloys
    a) What mechanisms are responsible for micro-cracking in L-PBF fabricated CM247LC?
    b) What changes to the composition of CM247LC can be made to make it less susceptible to micro-cracking?
    c) What process modifications will result in reduced micro-cracking?
    d) What is the microstructure and mechanical behavior of the modified CM247LC?

Chapter 3 Materials and Methods

3.1 Aluminum-based Superalloy

3.1.1 Materials

Addalloy®, an Al-Mg-Zr alloy developed by NanoAl LLC (Ashland, MA, USA) for additive manufacturing, was inert-gas atomized by Nanoval (Berlin, Germany) in three compositional variants (Table 3-1). The small batch sizes of the experimental Al-Mg-Zr alloy necessitated the use of numerous batches. Comparisons between results, such as mechanical property results, were only made between samples fabricated from identical batches. Silicon and iron are common impurities present in aluminum alloys and were present in all of the alloys.

Table 3-1: Chemical compositions and sizes of the powder (except batch 3) used in this study.

Batch #	Alloy Composition (wt. %, measured by ICP-OES)	Powder Size Range (μm)	Powder d_{50} (μm)
1	Al-3.60Mg-1.18Zr	10-45	13.7
2	Al-3.60Mg-1.18Zr	25-45	37
3	Al-2.90Mg-2.10Zr (as-fabricated)	10-45	24
4	Al-3.66Mg-1.57Zr	10-45	13.7
5	Al-3.66Mg-1.57Zr	25-45	37

3.1.2 Additive Manufacturing

A majority of samples were fabricated using a Concept Laser M2 (Concept Laser, Germany) L-PBF machine outfitted with a 200 W 1070 nm fiber-laser operating in continuous wave mode with a Gaussian intensity distribution and 90 μm spot size ($1/e^2$). Argon shielding gas kept oxygen content in the build chamber below 1% during processing. All batches were processed using a chess scanning strategy (5 x 5 mm islands) with full 200 W laser power (3.14×10^6 W/cm^2), 200 mm/s scanning speed, and a 135 μm hatch spacing. Scan lines were at a 45° orientation to the part edges. Batch 2 samples were fabricated with a 40 μm layer thickness (due to the larger powder size). All other batches were fabricated with a 30 μm layer thickness. Samples were fabricated on a 80 mm diameter Al base plate.

Samples for one set of elevated temperature yield tests were fabricated with a Sisma MySint 100 equipped with a 200 W 1070 nm fiber-laser operating in continuous wave mode with a Gaussian intensity distribution and a 55 μm spot size ($1/e^2$). The following processing parameters were used to fabricate the samples: 175 W (7.35×10^6 W/cm^2), 250 mm/s scanning speed, 30 μm layer thickness, a 100 μm hatch spacing, and a chess scanning strategy (4 x 4 mm islands). Samples were fabricated on a 100 mm diameter Al base-plate.

Optimal processing parameters were determined by using literature values for a similar alloy as a starting point [85] and then performing a targeted parameter survey on each commercial machine. A parameter survey consists of processing a series of samples, typically 1 x 1 x 1 cm (or 8 x 8 x 8 mm) cubes, with different processing parameters. Processing parameters are modified by one variable at a time, for example, fixing all parameters and processing each cube with a different scanning speed. Next, the relative density of sample is measured and the parameters that produced the highest density sample are then chosen as the optimal parameters. Figure 3.1 shows an example of a parameter survey performed with Al-2.90Mg-2.10Zr (wt. %, Batch 3) on the Sisma MySint 100. All processing variables are fixed (laser power, layer thickness, spot size, etc.) and the scanning speed was modified for two separate hatch distances. The relative density of the as-fabricated cubes was measured by the Archimedes method with pure ethanol as the liquid. A density of 2.7 g/cm^3 was chosen to represent a fully dense sample, although the true density of the Al-Mg-Zr will differ based on batch composition. A couple of the highest density samples were then mounted and metallurgically prepared so that the cross-section could be optically analyzed for density. The parameters that resulted in a sample with the least amount of visible lack of fusion voids and porosity were selected as the optimal parameters. In this specific case, the sample produced with 175 W, a 30 μm layer thickness, a 0.100 mm hatch spacing, and a 250 mm/s scanning speed had the least porosity despite having a slightly lower Archimedes density. Archimedes density measurements were observed to be prone to variability from unidentified causes.

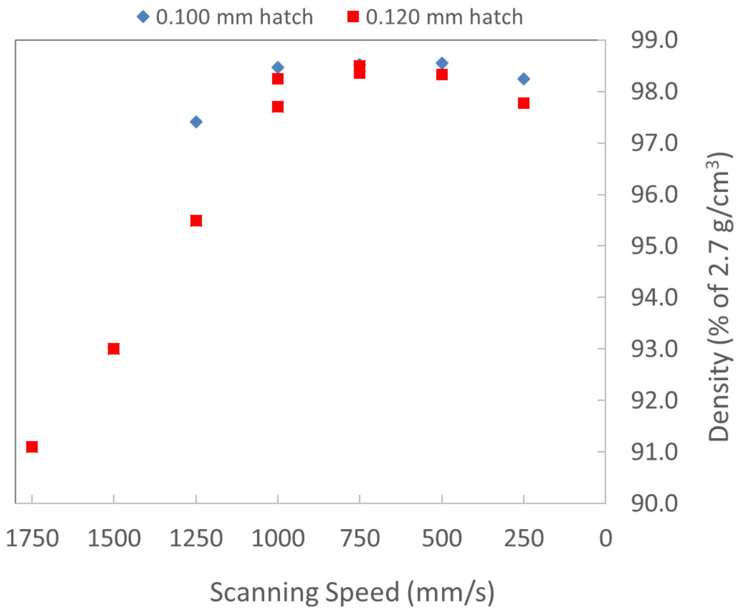

Figure 3.1: Parameter survey of the Al-2.90Mg-2.10Zr (wt. %, Batch 3) on the SismaMySint 100. Laser power was fixed at 175W (7.35x10^6 W/cm^2) and the layer thickness was fixed at 30 µm. Each data point is an average of three measurements.

3.1.3 Microstructure Characterization

Sample cubes were cold mounted in epoxy, ground, and polished with 1 µm monocrystalline diamond suspension. Final polish was done with 50 nm colloidal silica. Sections parallel to the build direction were characterized unless otherwise noted. Some samples for optical analysis were etched with Kellers Reagent (95 mL H_20, 2.5 mL NHO_3, 1.5 mL HCl, and 1.0 mL HF). Microstructure assessment was done with a FEI NanoSEM 230 in backscatter mode and a FEI Helios FIB in MD (Mirror detector, backscatter signal) mode. Energy Dispersive Spectroscopy (EDX) measurements was performed with the FEI NanoSEM 230 with an Oxford Instruments detector.

Lamellae for transmission electron microscopy (TEM) analysis were extracted from the fine grain region and coarse grain region of the samples with a FEI Helios NanoLab 600i focused ion beam (FIB). The lamellae were extracted such that the transverse structure was showing. Since Ga ions were utilized in the thinning of the lamellas, Ga was detected on the grain boundaries and edges of the precipitates. The electron diffraction data was obtained at 200 kV with a JEOL 2200FS microscope. Scanning transmission electron microscopy (STEM) was performed on a FEI Titan Themis microscope operated at 300 kV and equipped with a probe spherical aberration corrector and a SuperEDX system (ChemiSTEM technology) with four silicon drift detectors for energy-dispersive X-ray (EDX) spectroscopy. A convergence semi-angle of 25 mrad was used in combination with an annular dark field (ADF) detector with inner and outer collection semi-angles of 53 and 200 mrad, respectively.

Samples for Electron Backscatter Diffraction (EBSD) were either ion-milled (for the rescan study) or lightly etched (heat treated samples) prior to scanning. EBSD mapping of the samples was performed with a Tescan Lyria FIB with an EDAX EBSD detector. Scans were taken at 20kV with a 0.2 μm step size. The TSL OIM Analysis 7 software was used to generate EBSD grain orientation maps (unique colors for grains). Equivalent grain sizes were determined based on a circular approximation based on the area of the data points in the grain. ImageJ was used to threshold SEM images for particle size analysis.

3.1.4 Thermodynamic Simulations

Scheil-Gulliver (no diffusion in solid, complete mixing in the liquid) calculations were performed with the TCAL6 database in ThermoCalc. The Scheil-Gulliver calculations were performed with a composition of Al-3.66Mg-1.57Zr-0.2Si-0.1Fe (wt. %).

3.1.5 Room Temperature Mechanical Properties

Bar samples (10 mm wide, 40 mm long, 20 mm height, with build direction along the height axis) were fabricated from both the Al-3.60Mg-1.18Zr (wt. %, Batch 1) and Al-3.66Mg-1.57Zr (wt. %, Batch 4) powders on the Concept M2. Bar Samples were also fabricated with laser rescanning, resulting in a total of four bar samples: Batch 1, Batch 4, Batch 1 rescanned, and Batch 4 rescanned. Dog bone samples (gauge section 2.5 mm diameter and 8.0 mm long) were fabricated from the blocks so that some done bones were parallel to the build direction and others were traverse to the build direction. The dog bone specimens were tested to fracture on a mechanical test frame with a 0.5 mm/s strain rate.

Our project collaborator, NanoAl, performed the machining and testing of the specimens.

3.1.6 Elevated Temperature Mechanical Properties

Cylindrical samples (10 mm diameter, 34.5 mm height, with build direction along the long axis) and bar samples (10 mm wide, 75 mm long, 34.5 mm height, with build direction along the height axis) were fabricated from the high-Zr alloy (Batch 3) on the Concept M2 for elevated temperature tensile and creep testing. Cylindrical samples (10 mm diameter, 60 mm height, with build direction along the long axis) were fabricated from the high-Zr alloy (Batch 3) on the Sisma MySint 100 for elevated temperature tensile tests.

The bar samples fabricated on the Concept M2 were machined into dog-bone tensile samples (long axis of dog-bone transverse with the build direction) with threaded grips and a gauge section with 3 mm diameter and 12 mm length. These samples were tested either in their as-fabricated state or after a thermal treatment conducted in air. High-temperature tensile tests were conducted in air using a mechanical test frame operated at a fixed strain rate of 10^{-4} s^{-1}. Each sample was tested at multiple temperatures by deforming the sample just beyond its yield stress followed by unloading. The first such mechanical cycles was performed at 260°C, followed by five subsequent load-unload cycles performed at 205, 177, 150, 100 and 20°C, with a 30 min soaking time after the sample reached each temperature.

The cylindrical samples fabricated on the Sisma MySint 100 were machined into tensile specimens (long axis of specimen parallel with the build direction). High-temperature tensile tests (260, 205, and 177 °C) were conducted to fracture in air using a mechanical test frame operated at a fixed strain rate of 10^{-4} s^{-1}.

For the creep tests, the cylindrical and bar samples fabricated on the Concept M2 were machined into dog-bone tensile samples (with their long axis parallel to the build direction for the cylinders, and transverse for the bars) with threaded grips and a gauge section with 3 mm diameter and 12 mm length. Creep tests were conducted on the dog-bone specimens in air using tensile dead-loading, with the deformation of the sample measured by a digital displacement gauge in the cold part of the load train. After reaching thermal equilibrium, mass was added incrementally to the dead-load apparatus. Steady-state creep rate was taken as the linear region of the displacement curve. After a steady-state creep rate was reached, additional mass was added. Following this procedure, a full creep curve was generated in approximately one week. A variant of this test was performed in which mass was added at 30 min intervals until the first deformation was observed, at which time we reverted to prior method of observing steady-state creep, so that this test took approximately 8 h to generate a full curve.

Our project collaborator, NanoAl, performed the machining and testing of the specimens.

3.2 Nickel-base Superalloys

3.2.1 Materials

Unmodified CM247LC and a modified version of CM247LC, CM247LC NHf (Hf-free), were inert-gas atomized by Oerlikon Metco (Pfaeffikon, Switzerland). Chemical composition was measured by inductively coupled plasma optical emission spectrometry (ICP-OES) and combustion analysis (for carbon) and is listed in Table 3-2. Both batches of powder had a 15 – 45 µm size range and a D_{50} of approximately 32 µm.

Table 3-2: Chemical composition of the powders used in the study. Measured by ICP-OES and combustion.

wt. %	**Al**	**B**	**C**	**Co**	**Cr**	**Fe**	**Hf**	**Mo**	**Ni**	**Ta**	**Ti**	**W**	**Zr**
CM247LC	5.71	0.017	0.06	9.24	8.62	0.02	1.37	0.54	Bal	3.08	0.73	9.93	0.006
CM247LC NHf	5.56	0.01	0.07	9.14	8.36	0.07	0.005	0.53	Bal	3.18	0.63	9.48	0.018

3.2.2 Additive Manufacturing

Two distinct processing conditions were utilized for this study: Condition 1 and Condition 2. Condition 1 samples (10 x 10 x 10 mm cubes) were fabricated on a Concept M2 (Concept Laser, Germany) equipped with a 200 W 1070 nm fiber-laser operating in continuous wave mode with a Gaussian intensity distribution and a 90 µm spot size ($1/e^2$). The Concept M2 was modified by adding an aluminum support structure to hold an 80 mm diameter build plate instead of the standard 245 x 245 mm build plate. Condition 2 samples (8 x 8 x 8 mm cubes) were fabricated on a Sisma MySint 100 (Sisma S.p.A., Italy) equipped with a 200 W 1070 nm fiber-laser operating in continuous wave mode with a Gaussian intensity distribution and a 55 µm spot size ($1/e^2$). The Condition 1 samples were built on an 80 mm diameter stainless steel build plate and the Condition 2 samples were built on 100 mm and 34.5 mm diameter stainless steel build plates. All samples were processed with a bidirectional scan strategy (90 degree rotation between layers, except for two samples processed without layer rotation for surface analysis) with border contour. Melt tracks were at a 0° and 90° orientation to the part edges. Argon shielding gas (99.996 % Ar) was used in both machines (Condition 1 < 0.8 % O_2, Condition 2 < 0.5% O_2). The optimized parameter set, shown in Table 3-3, for each condition were identified via independent parameter surveys on each machine that focused on achieving the highest density (lowest porosity) parts. Thermo-physical property data (from [86,87]) used in the calculation of normalized enthalpy is given in Appendix Table 0-1.

Table 3-3: Processing parameters utilized for the fabrication of CM247LC samples.

Condition	Spot Size (µm, $1/e^2$)	Power (W)	Scan Speed (mm/s)	Hatch Spacing (mm)	Contour Spacing (mm)	Layer Thickness (µm)	Normalized Enthalpy
1	90	200	600	0.105	0.075	30	26.3
2	55	175	750	0.075	0.100	30	43.2

Optimal processing parameters were determined by performing a targeted parameter survey aimed at achieving the highest density (least porosity) on each commercial machine. The methodology of the parameter survey was similar to that done for the Aluminum alloys. Figure 3.2 shows an example of a parameter survey for CM247LC on the Sisma MySint100. All processing variables were fixed (laser power, layer thickness, spot size, etc.) and the scanning speed was modified for two separate hatch distances. The highest density cubes were sectioned for optical analysis. In this specific case, the sample produced with 175 W, a 30 µm layer thickness, a 0.075 mm hatch, and a 750 mm/s scanning speed had the least porosity.

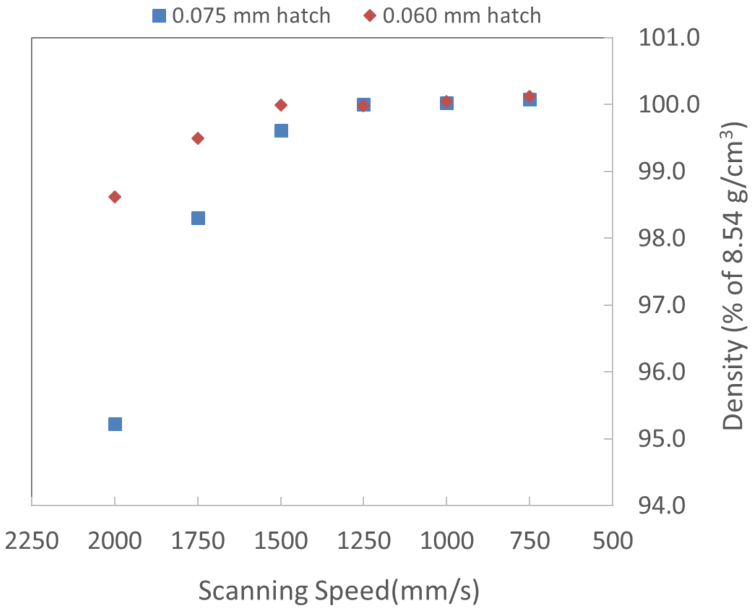

Figure 3.2: Parameter survey of the CM247LC on the SismaMySint 100. Laser power was fixed at 175W ($7.35x10^6$ W/cm^2) and the layer thickness was fixed at 30 µm. Each point is an average of 3 measurements.

3.2.3 Microstructure and Defect Characterization

Sample cubes for microstructure and defect characterization were sectioned in half (parallel to the build direction), cold-mounted in epoxy, ground, polished with monocrystalline diamond suspension and finally lapped with 50 nm colloidal silica. Some samples were etched with Glyceregia (15 ml HCl, 10 ml glycerol, 5 ml NHO_3) for melt pool and microstructure analysis. Scanning Electron Microscope (SEM) analysis was performed with a FEI NanoSEM 230 in secondary and backscatter electron imaging mode. Electron Backscatter Diffraction (EBSD) was performed on Tescan Lyra3 SEM equipped with a Symmetry camera from Oxford Instruments (UK) and operated at 20 kV with a 10 nA beam current.

Lamellae for scanning transmission electron microscopy (STEM) analysis were prepared from the aforementioned sample cubes (lamellae is perpendicular to build direction) using an FEI Helios NanoLab 600i focused ion beam (FIB). The selected area electron diffraction (SAED) data was obtained at 200 kV with a JEOL 2200FS microscope. A FEI Titan Themis microscope, equipped with a probe spherical aberration corrector and a SuperEDX system (ChemiSTEM technology) with four silicon drift detectors for energy-dispersive X-ray (EDX) spectroscopy, was used for STEM analysis. The microscope was operated at 300 kV with a beam convergence semi-angle of 25 mrad. The annular dark field (ADF) detector has a inner and outer collection semi-angles of 66 and 200 mrad, respectively. The Bright Field (BF) detector had a collection angle of 35 mrad. STEM-EDX spectrum images (with background correction) were pre-filtered (5 pixel average) for semi-quantification and displayed as wt. % and net intensity maps.

3.2.4 Thermodynamic Calculations

Scheil-Gulliver (no diffusion in solid, complete mixing in the liquid) and equilibrium solidification calculations were performed with the TCNI5 database in ThermoCalc. The Scheil-Gulliver calculations were performed with a nominal CM247LC composition that is listed in Appendix Table 0-2.

3.2.5 Differential Scanning Calorimetry

The phase transformation temperatures, in as-fabricated CM247LC and CM247LC NHf (Condition 2), were determined by differential scanning calorimetry (DSC) measurements, conducted using a NETZSCH DSC 404C Pegasus thermal analyzer. Samples of 22.2 mg were used for both alloys, with their surfaces ground down to P4000 to insure a better thermal conduction with the crucible. The experiments were carried out under argon atmosphere (99.9999% Argon) with a flow rate of 40 ml/min. The Al_2O_3 crucibles were heated at a rate of 10 K/min from room temperature to 1430°C, and cooled down at the same rates. Only the heating thermograms are considered in this study.

3.2.6 X-Ray Diffraction

X-Ray diffraction (XRD) θ to 2θ scans were performed on a Bruker Davinci D8 using Cu Kα radiation.

3.2.7 Crack Density Analysis

Three independent studies were conducted to compare the micro-crack density between CM247LC and CM247LC NHf samples. Samples fabricated for comparison between the two alloys were identical except for the alloy used i.e., same build plate size, same number and geometry of samples on the build plate, same parameters, etc. Crack density analyses were conducted on optical images captured with a Leica VZ700C microscope with automatic image stitching at 200x magnification. Approximately 100 images were stitched together to generate one uncompressed image of an entire cross section (parallel to the build direction). Each sample was ground, repolished, and imaged numerous times in order to improve statistics (Condition 1: 5 times, Condition 2: 5 times, Condition 2 repeat: 4 times). Optical image analysis for crack density comparisons was performed with ImageJ [88]. Uncompressed stitched images, merged together as one image, of the sample cross section were filtered with a 3 pixel median filter. Next, the images were manually thresholded to generate a binary image. The binary images of the cracks were analyzed with the Analyze Particle function in ImageJ. Particles under 20 pixels in size, touching edges, and with a circularity above 0.35 (ensuring pores were not counted) were ignored. Each crack was fitted as an ellipse. To differentiate cracks from horizontal lack of fusion defects, ellipses that were within ± 10 degrees of the horizontal axis (perpendicular to build direction) were ignored. Crack density for each sample is reported as an average of the numerous measurements taken per sample.

3.2.8 Liquation Cracking Experiments

The following experiments were performed by Hossein Ghasemi at EPFL on samples (Condition 2) fabricated by Seth Griffiths at EMPA. They are included as they are mentioned in discussion later on. In order to simulate cracking in the HAZ of the L-PBF samples (CM247LC and CM247LC NHf samples), Gleeble experiments were conducted using a Gleeble 3800 machine. Xu et al. have used this thermomechanical simulation technique to study the microstructure evolution in the HAZ of IN738LC samples produced by laser solid forming process [89]. In the Gleeble machine, the samples are heated by Joule effect, under vacuum, at a rate of 250 °C/s until 1250 °C, followed by water-quenching. The temperature is screened with thermocouples welded to the surface of the samples. Due to thermal expansion during the test in combination with the constraints of the grips, the samples were subjected to 5 MPa compressive stress.

3.2.9 Mechanical Properties

The isothermal aging experiments, hardness tests, and imaging of precipitate sizes were performed by Shreyas Joglekar and Joanna Pado during their internships/masters thesis work at Empa.

Isothermal aging experiments on CM247LC and CM247LC NHf were performed in air at 850°C on 5 x 5 x 5 mm cubes fabricated with processing Condition 2, followed by air cooling. The samples were solutionized at 1260°C for 2 hrs prior to the aging experiments. The sample cubes were mounted (parallel to build direction visible), ground, and polished (final step 50 nm colloidal silica). Microhardness measurements were performed with a Fischerscope HM2000 hardness tester with a standard Vickers diamond pyramid intender with a 136° face angle, an automated stage, and microscope. The Vickers microhardness was measured for all samples with a 1800 mN load for 60 seconds. Between 10 to 20 indentations were made per samples, typically in one line parallel to the build direction, with no variation of hardness with location of indent observed.

Average size distribution of the γ' precipitates after isothermal aging was determined via image analysis of BSE images of the aforementioned cross sections. Prior to analysis with the SEM (FEI NanoSEM 230), samples were vibro-polished with 50 nm colloidal silica and etched with V2A (200 ml H2O, 200 ml HCL 37%, 20 ml HNO3 65%) for 2 minutes at a temperature of 50 °C. Image analysis was performed with ImageJ [88]. BSE images were filtered with a FFT bandpass filter, and thresholded to highlight the γ' precipitates. Next, thresholding errors were corrected by a combination of filling holes inside of the precipitates and using a watershed tool to separate conjoined precipitates. The analysis particle feature was used to measure the equivalent γ' precipitate size (modeled as a circle).

Specimen blanks (21 x 21 x 81 mm blocks) were fabricated from CM247LC and CM247LC NHf with processing Condition 2 for future mechanical testing. Test blanks were sent to Deloro Htm GmbH (Biel, Switzerland) for HIPing at 1225°C and 1000 bar for 5 hours. The complete HIP cycle curve is shown in Figure 3.3. After HIPing, the specimen blanks (and witness coupons ~20 x 21 x 20 mm) were solutionized (1260°C 2 h) and aged (850°C 8 h).

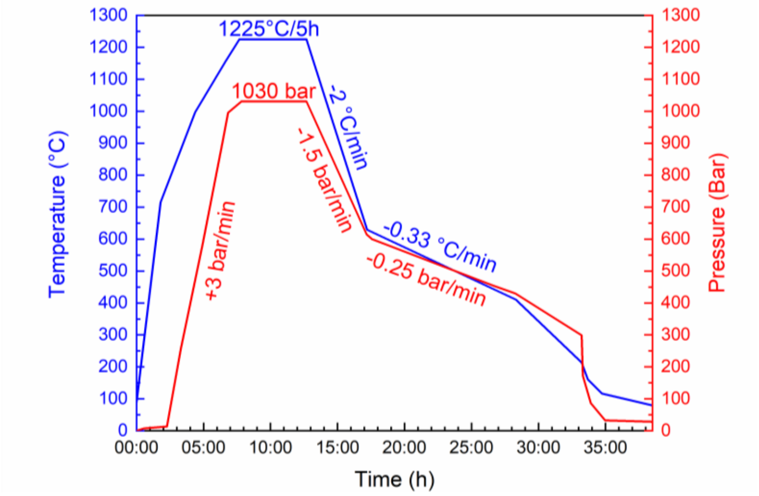

Figure 3.3: Temperature and pressure cycle of the HIP treatment.

Chapter 4 Metallurgy of L-PBF Fabricated Addalloy

4.1 Powder Microstructure

Figure 4.1 shows BSE images of cross-sectioned Al-3.66Mg-1.57Zr (wt.%, batch 5) powder. A majority of the powder is spherical and minimal amounts of defects (agglomeration, porosity, shells) were observed (Figure 4.1(a,b)). Closer examination of the cross sectioned powder revealed the presence of sub-micron bright white particles (an example is shown by the black arrow in Figure 4.1(d)). Some of the individual powders had a higher density of bright white particles than other individual powders (Figure 4.1(b)). No relation between individual powder size and presence/absence of bright white particles was observed. Higher magnification images of the individual powders are shown in Figure 4.1(c,d). White spherical regions (~1-2 μm diameter) of bright contrast were observed on many of the powder particles (an example is highlighted by the white arrow in Figure 4.1(c)). SEM-EDX analysis of the circular white regions revealed a Zr enrichment and Mg depletion in these regions (SEM-EDX data in Appendix A, Figure 0.1). SEM-EDX analysis of the bright white submicron particles revealed a significant Zr enrichment (SEM-EDX data in Appendix A, Figure 0.2).

The spherical regions enriched in Zr are the result of Zr partitioning ($k > 1$) to the solid (dendrite cores) during solidification. A similar behavior has been observed in as cast Al-Zr-Ti alloys [74]. In the binary Al-Mg system, Mg partitions ($k < 1$) to the liquid (interdendritic regions) resulting in a depletion of Mg, as observed, in the dendrites. The white particles highlighted in Figure 4.1(d) are assumed to be primary $L1_2$ Al_3Zr precipitates and their formation will be discussed in later sections.

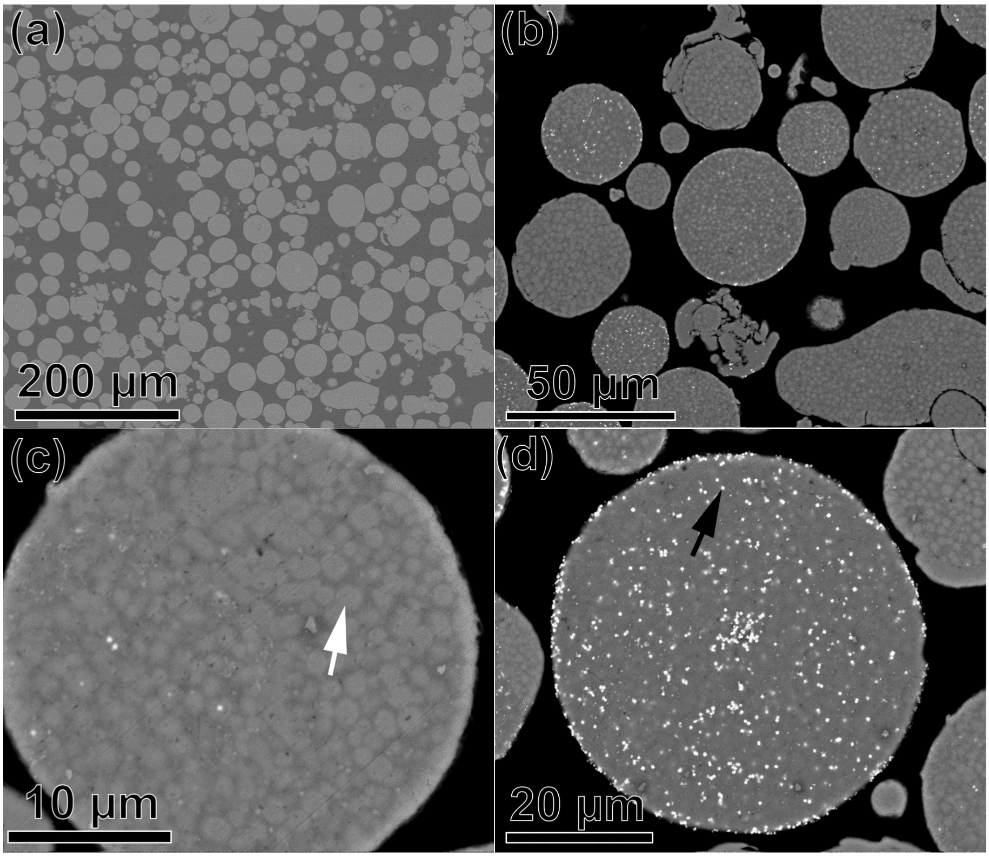

Figure 4.1: BSE images of the cross-sectioned Al-3.66Mg-1.57Zr (wt.%, batch 5) powder. (a) Overview of the spherical powder (b) higher magnification image showing powder particles both with and without bright precipitates. (c) A single powder particle with minimal bright precipitates, assumed to be Al_3Zr. White arrow points to region rich in Zr and poor in Mg. (d) A powder particle with numerous bright precipitates (black arrow points to one such precipitate) assumed to be Al_3Zr.

4.2 As-fabricated Microstructure

The density of as-fabricated samples exceeds 98% (as measured via the Archimedes method) and few defects (trapped oxides, voids) were observed on cross sections. An optical image of an etched as-fabricated Al-2.90Mg-2.10Zr (wt. %, Batch 3) sample is shown in Figure 4.2. The individual melt pools are easily visible due to the dark colored bands (one example highlighted by a white arrow) at the bottom of the melt pools. Higher magnification images of an as-fabricated Al-3.60Mg-1.18Zr (wt. %, Batch 2) sample is shown in Figure 4.3 and an EBSD Image Quality (IQ) map is shown in Figure 4.4. The duplex grain microstructure consists of fine-grain equiaxed regions (dark colored bands in the optical image), and coarse-grain columnar regions. Columnar grains (1-5 μm wide and up to 40 μm in length) are oriented in the build direction, which is expected from the directional solidification inherent to AM. However, these columnar grain region do not cross melt pools as observed in other alloys such as CM247LC [2]. Rather, fine grain regions are located at the bottom of the melt pools and consist of ~1.3 μm diameter equiaxed grains (number average). As shown in Figure 4.3, sub-micron cuboidal precipitates (100 - 400 nm in size, later shown to be primary Al_3Zr precipitates) are present in the fine-grain regions but not in the columnar regions. EBSD analysis showed that the fine-grain region is texture-less and the columnar grain region displays a slight (001) texture (Figure 4.4b,c). SEM-EDX measurements from an as-fabricated Al-3.60Mg-1.18Zr (wt. %, Batch 2) alloy gave the following composition: Al-3.09Mg-1.52Zr-0.16Si (wt. %) (See Appendix Figure 0.3). Similar fine- and columnar grain regions, with and without primary $Al_3(Zr,Sc)$ micron precipitates, have been observed by Spierings et al. [69] in an Al-Mg-Sc-Zr alloy (Scalmalloy®) processed by L-PBF.

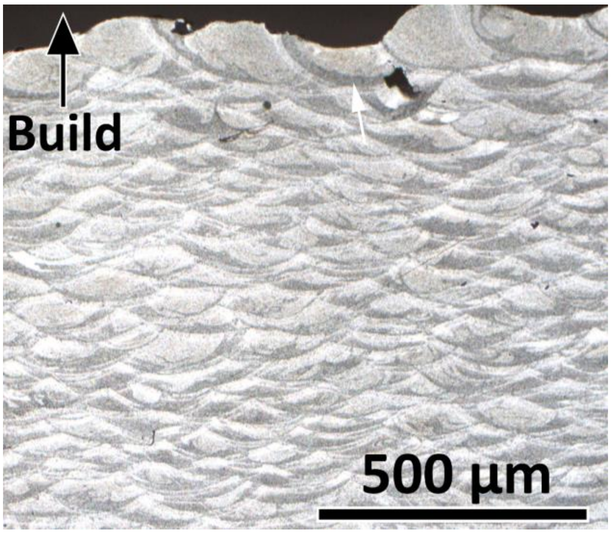

Figure 4.2: Optical micrograph of an as-fabricated sample (Al-2.90Mg-2.10Zr, wt. %, Batch 3).

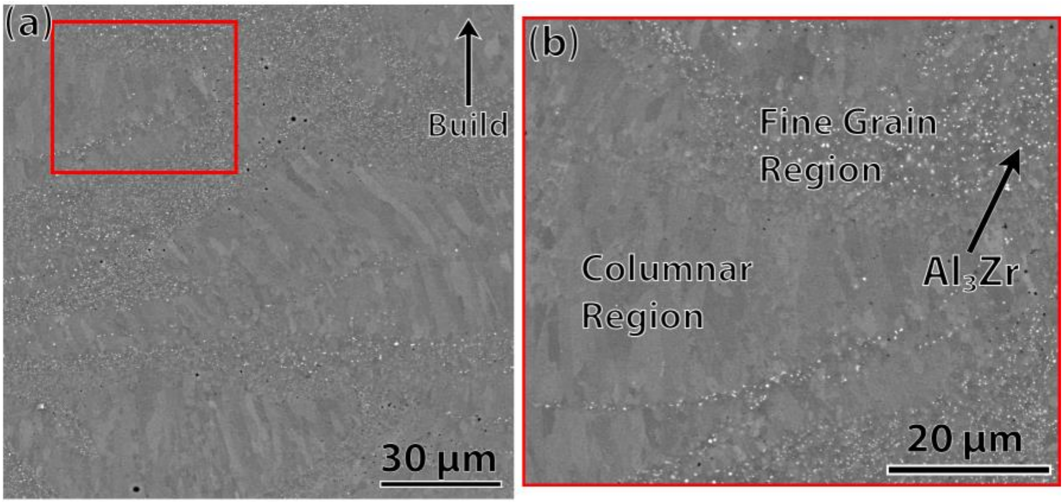

Figure 4.3: (a,b) BSE images of the single-scanned sample showing a duplex grain microstructure consisting of regions with columnar grains and equiaxed micron-size grains (most containing one primary Al_3Zr precipitate). (Al-3.60Mg-1.18Zr, wt. %, Batch 2). Figure from [90]

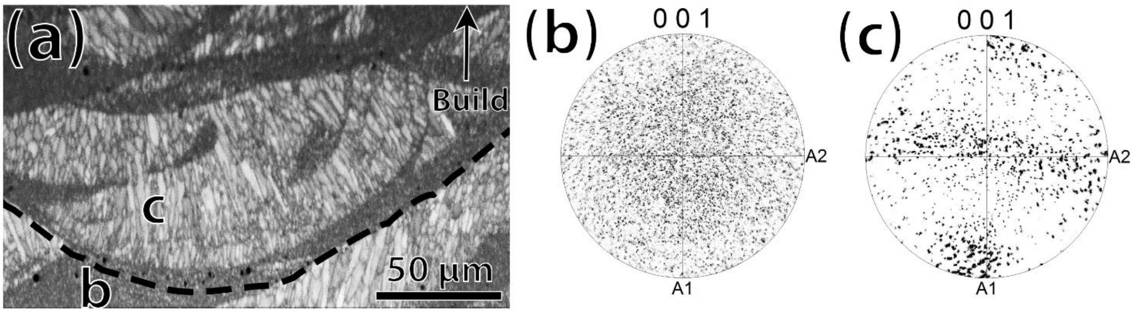

Figure 4.4: (a) EBSD Image Quality (IQ) map of asingle-scanned specimen showing the columnar and equiaxed grain regions. A melt pool boundary is shown by a black line. (b) EBSD pole figure from the fine grain region marked b in the IQ map. (c) EBSD pole figure from the coarse grain region marked c in the IQ map. (Al-3.60Mg-1.18Zr, wt. %, Batch 2). Figure from [90]

ADF-STEM overview images of the fine- and coarse-grain regions are shown in Figure 4.5. In the lamella from the fine-grain region, cuboidal precipitates are present both within the α-Al grains and at the grain boundaries. Cuboidal precipitates were not observed within the lamella from the coarse grain region. Black spherical (~100 nm diameter) precipitates (highlighted by a white arrow) are observed inside many of the grains of the coarse grain region (Figure 4.5(b)). There is a network of ~200 nm diameter regions with higher brightness (easier to discern in Figure 4.7, black arrow) similar to appearance to those observed in the powder.

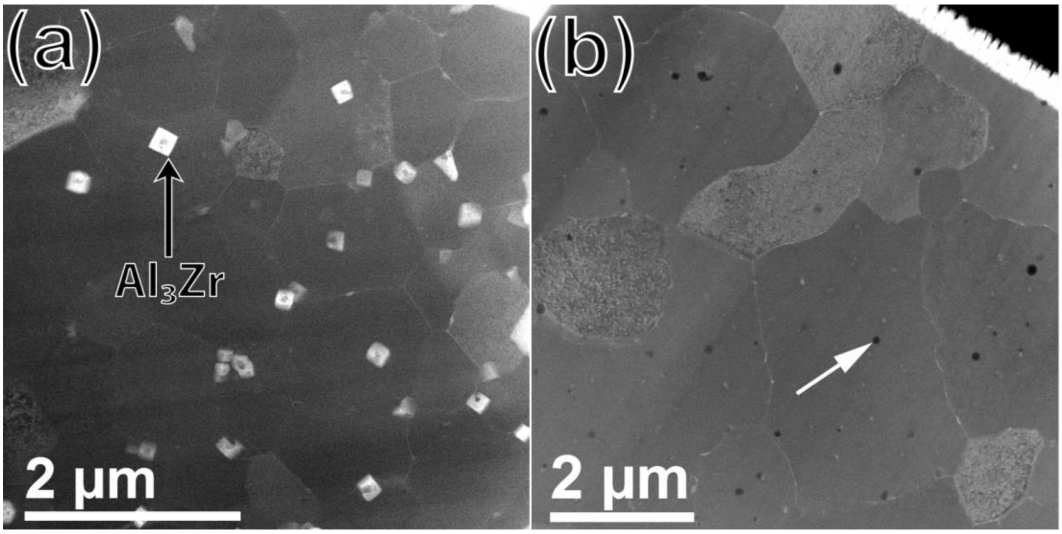

Figure 4.5: (a) Low magnification ADF STEM image of a precipitate-rich region showing cuboidal, submicron L1$_2$-Al$_3$Zr precipitates and micron-sized α-Al grains. (b) Low Magnification ADF STEM image of the precipitate-free coarse grain region showing larger α-Al grains and oxide particles/pores (white arrow) (Al-3.60Mg-1.18Zr, wt.%, Batch 2)

STEM-EDX chemical mapping taken in the fine grain region of an as-fabricated Al-3.60Mg-1.18Zr (wt.%, Batch 2) sample is shown in Figure 4.6. The cuboidal precipitates in the fine grain regions are enriched in Zr. The Zr-depleted region in the center of precipitate is believed to be due to porosity but the origin of the porosity is unknown. STEM-EDX chemical analysis adjacent to primary precipitates display slightly lower Zr content (0.95 to 1.19 wt.%) than in a grain from the coarse grain region (Appendix Figure 0.4) suggesting the grains in the fine grain region will have a depletion of Zr when compared to the coarse grain regions.

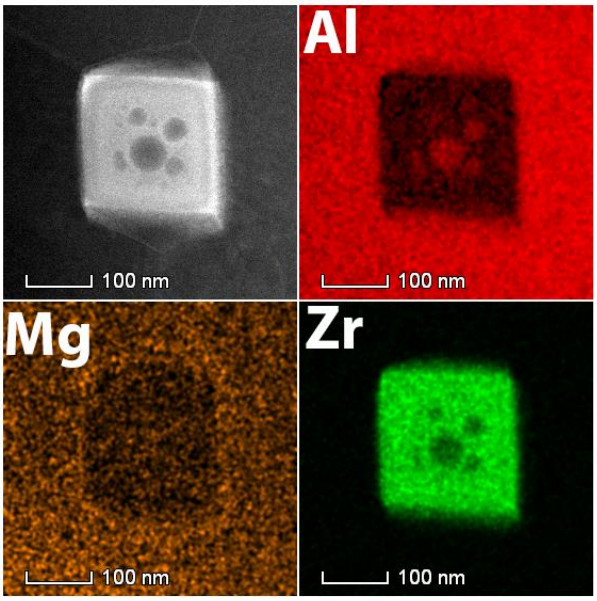

Figure 4.6: STEM HAADF and corresponding STEM-EDX elmental maps of a L12 precipitate in the fine grain region of an as-fabricated Al-3.60Mg-1.18Zr (wt.%, Batch 1) sample. Figure from [67]

Figure 4.7 shows an ADF-STEM image and a series of STEM EDX maps taken from a coarse-grain region of the Al-3.60Mg-1.18Zr (wt.%, Batch 1) as-fabricated sample. As expected, no primary Al_3Zr is present, and Zr is detected uniformly throughout the mapped region, indicative of Zr being in solid-solution. No chemical gradients were observed within the grains but bright circular regions ~200 nm diameter (black arrow) were observed in the ADF-STEM image as discussed prior. The chemical differences between the circular features may be too low to show a significant difference on EDX maps, but a higher contrast on the ADF-STEM image suggests the partitioning of heavier elements. Magnesium enrichment and Al depletion are observed at the grain boundaries, but there is no evidence of a continuous secondary phase (i.e., β-Al_2Mg). Three types of precipitates are visible: (i) Mg- and O-rich particles, ~100 nm in diameter, which are likely oxide inclusions originating from the powder surface and/or created during the printing process; (ii) Mg- and Si-rich precipitates, ~50 nm in diameter, which are located both within the grains and at grain boundaries; (iii) Fe-rich precipitates, ~50 nm diameter, predominately on the grain boundaries. It is important to note that many of the aforementioned particles that are within the grains are usually in-between the bright circular regions. The occurrence of Fe-rich and Si-rich precipitates will be discussed in the next section. The black spherical particles mentioned prior are often aforementioned oxide particles; however, some observed black spherical particles did not have oxide enrichment (not shown) and are likely the result of porosity.

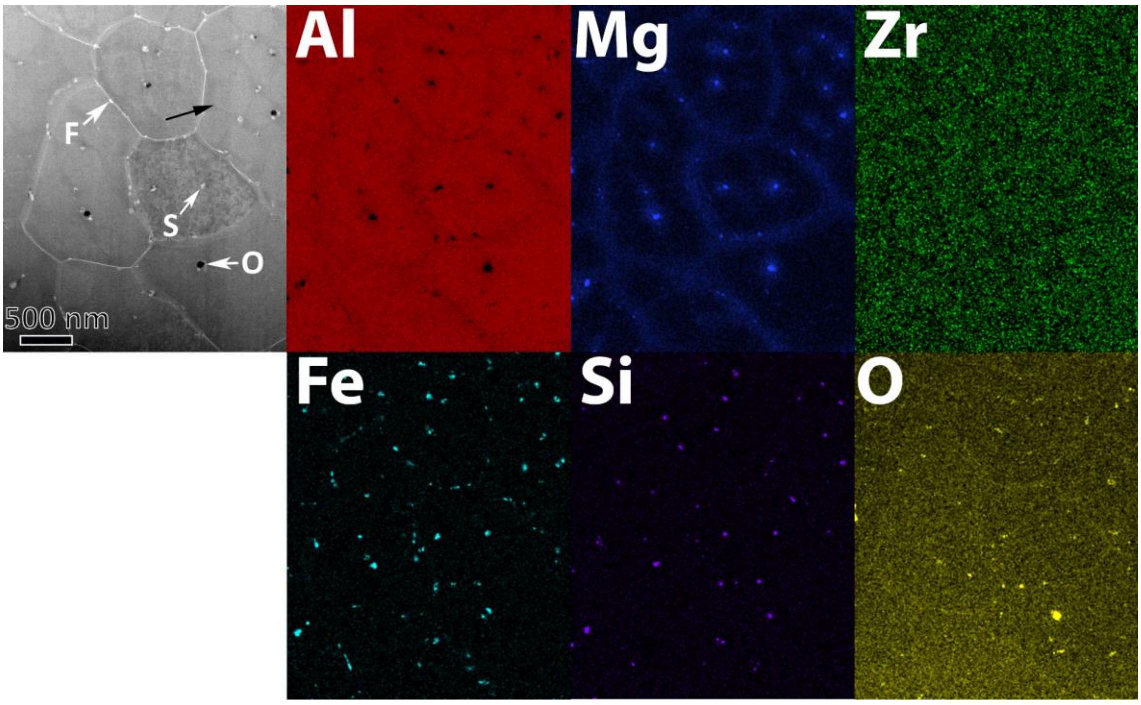

Figure 4.7: Coarse-grain region of an as-fabricated sample (Al-3.60Mg-1.18Zr, wt.%, Batch 1) imaged via STEM (ADF- image and elemental EDX maps using Si-K, Zr-K, Al-K, Mg-K, Fe-K and O-K lines) showing three types of precipitates : (i) Mg- and O-rich oxide particles, ~100 nm in diameter; (ii) Mg- and Si-rich particles, ~50 nm in diameter, (iii) Fe-rich particles, ~50 nm diameter, on the grain boundaries. One example for each type of precipitates is highlighted on the ADF-STEM image, with labels O, S and F, respectively. The black arrow points to a circular feature of enhanced contrast.

High resolution ADF-STEM images and selected area electron diffraction (SAED) patterns of the cuboidal precipitates of the fine-grain region are shown in Figure 4.8. The atomically resolved ADF-STEM images of the precipitate-matrix interface, recorded along the [001] zone axis, show the coherent nature of the precipitates with the matrix. Additionally, the Fast Fourier Transform (FFT) pattern, which for our purpose can be treated as a selected area diffraction pattern (SAD), obtained from the precipitate (Figure 4.8(a)) clearly evidences the presence of 100- and 010-type reflections which are not present in the FFT pattern of the aluminum matrix (Figure 4.8(b)). The reflections are characteristic superlattice reflections of the $L1_2$ phase, and are also visible in the selected area diffraction pattern obtained from a separate precipitate (Figure 4.8(c)). The lattice parameters (a = b = c for cubic) of the precipitate and matrix were measured from the high resolution ADF-STEM image shown in Figure 4.8(b) and are ~0.414 nm and ~0.410 nm for the precipitate and matrix, respectively. While a majority of the primary Al_3Zr precipitates were cuboidal, some precipitates with a feathery appearance were observed (Figure 4.9). A high resolution ADF-STEM image taken down the [001] zone axis of the precipitate in Figure 4.9(a) is shown in Figure 4.9(b). The FFT of Figure 4.9(b) clearly evidences the presence 100- and 010-type reflections which are characteristic of the $L1_2$ phase. Since the precipitates are identified as having the $L1_2$ structure and are enriched in Zr, it can be concluded that they are $L1_2$-structured Al_3Zr precipitates

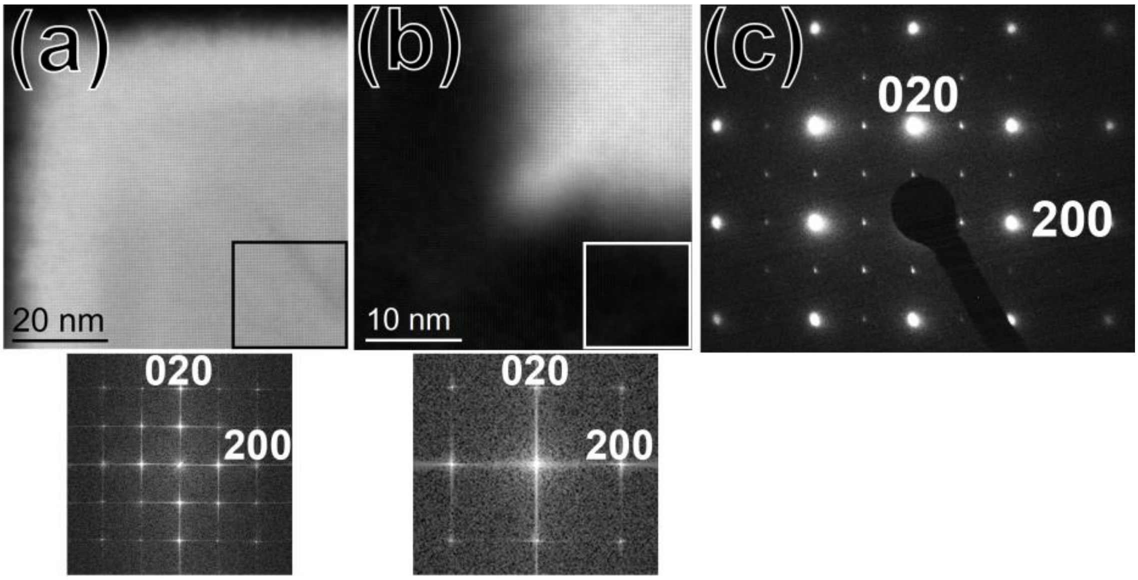

Figure 4.8: (a) High resolution ADF-STEM image, along the [001] zone axis, of the upper left corner of the precipitate in Figure 3 and corresponding FFT of the highlighted precipitate area (black-rimmed square). (b) High resolution ADF-STEM image of the lower left corner of the precipitate in Fig-ure 3 and corresponding FFT of the highlighted matrix area (white-rimmed square). (c) Selected area electron diffraction pattern along [001] taken from a separate precipitate showing the 100- and 010-type superlattice reflections of the L12 structure. (Al-3.60Mg-1.18Zr, wt.%, Batch 2). Figure from [90]

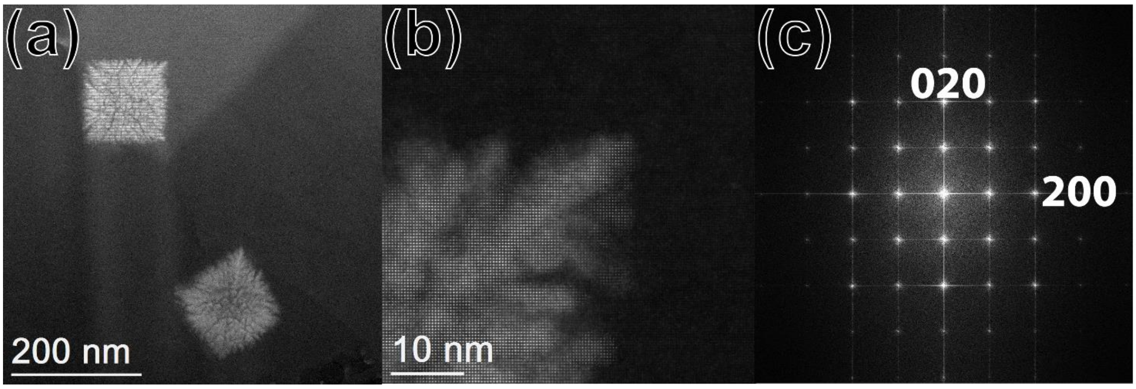

Figure 4.9: (a) ADF-STEM image of an $L1_2$ structured precipitate with a feather appearance from an as-fabricated Al-3.60Mg-1.18Zr sample (wt.%, Batch 2). (b) Higher resolution ADF-STEM image of a corner of the precipitate. (c) FFT of (b) showing the 100- and 010- type superlattice reflections of the $L1_2$ structure.

SAED patterns were acquired from individual grains in the coarse grain region of an as-fabricated Al-3.60Mg-1.18Zr sample (wt.%, Batch 2) to determine if nano-sized $L1_2$ precipitates were present (Figure 4.10). STEM-EDX data (Appendix A, Figure 0.5) indicated the presence of Zr, but superlattice reflections characteristic of the $L1_2$ phase were not observed in the SAED patterns (Figure 4.10) suggesting that the Zr is in solid solution. HR-STEM and STEM-EDX investigations were performed on a coarse grain region of an as-fabricated high Zr alloy, Al-2.90Mg-2.10Zr (wt. %, Batch 3), to determine if the Zr would also be in solid solution with higher Zr content. STEM-EDX data revealed the presence of Zr (Appendix A, Figure 0.6) but HR-STEM images and their corresponding FFTs (Appendix A, Figure 0.7, Figure 0.8) did not indicate the presence of the $L1_2$ phase, indicating that the Zr was in solid solution.

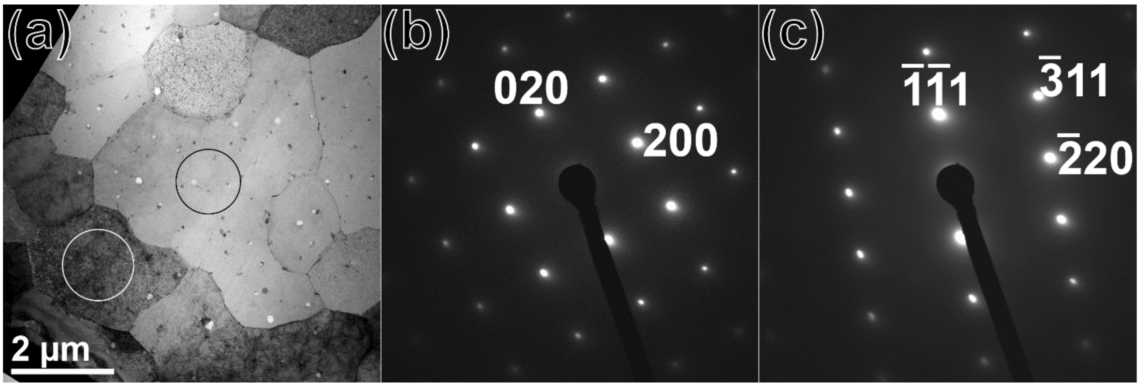

Figure 4.10: (a) Low magnification TEM image of the coarse grain region of an as-fabricated Al-3.60Mg-1.18Zr sample (wt.%, Batch 2). The white circle approximately corresponds to the region where the SAED pattern shown in (b) was acquired from. The black circle approximately corresponds to the region where the SAED pattern shown in (c) was acquired from. No superlattice reflections characteristic of $L1_2$ precipitates were present.

4.3 Microstructure Formation

In order to understand the microstructure formation in the as-fabricated Al-Mg-Zr alloys it is useful to first investigate the equilibrium Al-Zr binary system. The Al-rich end of the Al-Zr binary phase diagram (Figure 4.11) displays a peritectic reaction [91][11], meaning that the solute-rich phase, Al_3Zr, is the first to form (when the Zr content is above 0.01 wt.%) in the melt on cooling. The presence of Al_3Zr precipitates inside of and coherent with α-Al grains (in the fine grain region) provides evidence for this solidification path. Al_3Zr precipitates are known to serve as inoculants for the nucleation of fine, micron-size fcc-Al grains, as discussed by Knipling et al. [11]. Equilibrium partition coefficients give an indication of the microsegregation behavior of an alloy; for the elements that make up the Al-Mg-Zr alloys they are: Mg 0.51, Zr 2.5, Si 0.12, and Fe 0.02 [45]. The elements with a partition coefficient below 1, Mg, Si and Fe, will be rejected by the solid and segregate to the liquid phase (interdendritic regions). Elements with a partition coefficient greater than 1, Zr, will segregate to the solid phase (dendritic regions). The circular regions of higher brightness observed in Figure 4.7 (black arrow) may be the result of Zr partitioning to the solid (dendritic regions) during solidification. The partitioning of the Mg, Fe, and Si is clearly shown in Figure 4.7 by the Mg, Si, and Fe containing phases predominately being located on grain boundaries. As some impurities were observed within the grains but between the aforementioned circular features, it is assumed that these regions are interdendritic areas that do not correspond to a high angle grain boundary (a single grain can compose of many dendritic/indendritic boundaries).

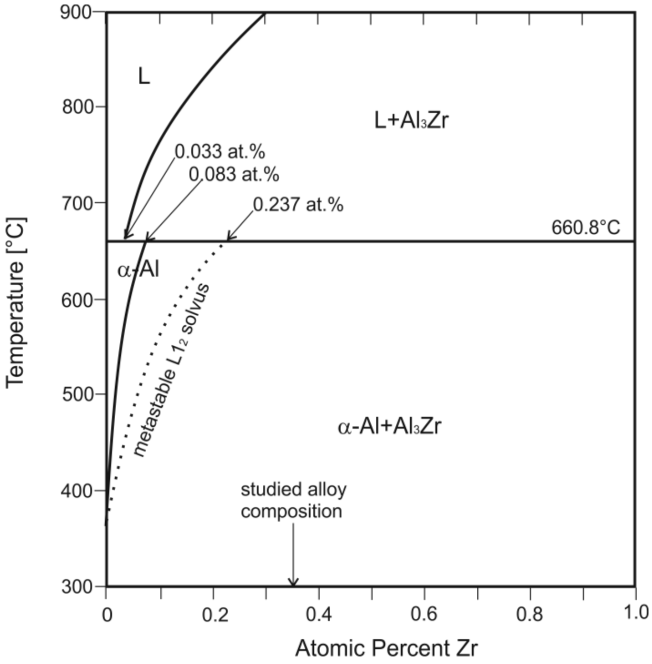

Figure 4.11: Equilibrium Al-rich Al-Zr binary phase diagram (adapted from Murray [23]) with metastable Al_3Zr (L12) solvus line (dotted). Figure from [92]

While a binary phase diagram is useful for roughly predicting solidification behavior, the studied alloy also contains Mg, Fe, and Si; therefore, it is beneficial to use thermodynamic simulations to further study the solidification behavior. A Scheil-Gulliver solidification calculation (equations 10 and 11) of the Al-3.66Mg-1.57Zr alloy (wt. %), including Fe (0.1 wt.%) and Si (0.2 wt. %) impurities, is shown in Figure 4.12. The Al_3Zr phase, albeit with the $D0_{23}$ structure, is the first solid phase to form from the liquid beginning at ~980°C. Next, at ~640°C, the α-Al phase forms. At ~580°C the first impurity phase forms, $Al_{13}Fe_4$ (not labeled). A second impurity phase, Mg_2Si, forms at ~570°C (not labelled). Lastly, the AlMg β-phase forms at ~450°C (not labeled). Crystallographic data was not obtained from the impurity phases observed in the L-PBF fabricated samples but literature on casting of Al alloys suggests that Fe precipitates as Fe-rich intermetallic phases and Si, in the presence of Mg, precipitates as the Mg_2Si phase [93].

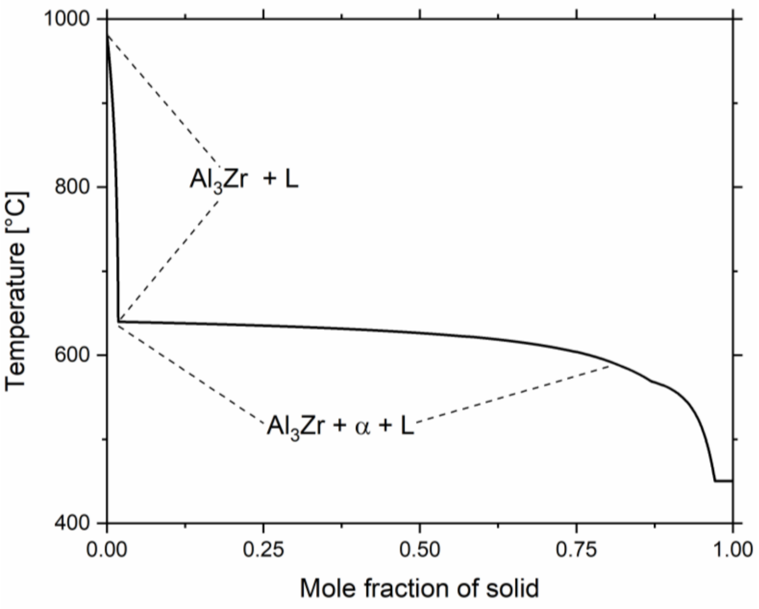

Figure 4.12: Scheil-Gulliver solidification curve (calculation performed with Thermocalc) for Al-3.66Mg-1.57Zr-0.2Si-0.1Fe (wt. %).

One key difference between the thermodynamic simulations and experimental observations is that the primary Al_3Zr precipitates in the as-fabricated alloys had a $L1_2$ and not a $D0_{23}$ structure. It is important to note that thermodynamic simulations present the thermodynamically stable phases, but real world solidification conditions, especially in the rapid solidification present in L-PBF, differ from thermodynamic equilibrium. A plot of the molar Gibbs free energy as a function of temperature for a Al-3.66Mg-1.57Zr-0.2Si-0.1Fe (wt. %) alloy is shown in Figure 4.13. The $L1_2$-structured Al_3Zr has a slightly higher molar Gibbs free energy than the $D0_{23}$-structured Al_3Zr; hence explaining why the $D0_{23}$-structured Al_3Zr is the equilibrium form of Al_3Zr. In order to answer why the metastable $L1_2$-structured Al_3Zr is the observed phase, it is important to look at factors influencing nucleation, specifically, interface energy. Interface energy can be calculated with thermodynamic software, ThermoCalc in this case, but it is important to note that it does not take structural contributions into account, which can be significant. At a temperature of 800°C, the interface energies of $L1_2$-structured Al_3Zr in a liquid matrix and $D0_{23}$ structured Al_3Zr in a liquid matrix are 0.12760 and 0.13243 J/m^2, respectively. Since the interface energy of the $L1_2$-structured Al_3Zr is lower, it may have a lower barrier to nucleation than the $D0_{23}$ structured Al_3Zr, thus potentially explaining why the primary Al_3Zr precipitates are $L1_2$-structured. The free energy barrier for nucleation can be calculated by equation 23

$$\Delta G^* = \frac{16\pi\sigma^3}{3\left(\frac{\Delta G}{V}\right)^2} \qquad 23$$

where σ is the interface energy, ΔG is the driving force for nucleation, and V is the molar volume [26]. Using driving forces calculated from ThermoCalc for the Liquid-Solid transitions ($L1_2$ Al_3Zr 2289 J/mol, $D0_{23}$ Al_3Zr 3544 J/mol) and a molar volume of 0.00001 m^3/mol) for Al_3Zr (nearly identical between $L1_2$ and $D0_{23}$ phases), free energy barriers to nucleation were calculated as $6.64\text{x}10^{-19}$ J for liquid → L12 phase and $3.10\text{x}10^{-19}$ J for liquid → $D0_{23}$ phase. While the calculation prior predicts a lower barrier to nucleation for the $D0_{23}$ phase than the $L1_2$ phase, our experimental observations prove the opposite; therefore, there must be a structural factor to the interface energy that favors the $L1_2$ phase. If one considers a solid state transformation, instead of the liquid one, the coherency of the $L1_2$ phase would provide the lower interface energy over the $D0_{23}$ phase. Previous work on rapid solidification of Al-Zr alloys confirms our observations that the metastable $L1_2$-structured Al_3Zr forms upon solidification and not the $D0_{23}$ phase [47,48,92]. Another deviation from the solidification behavior predicted by the thermodynamic simulations is the lack of primary Al_3Zr precipitation in the coarse grain regions of the melt pool. The reasons for this deviation from equilibrium relate to the dynamic solidification conditions in the melt pool.

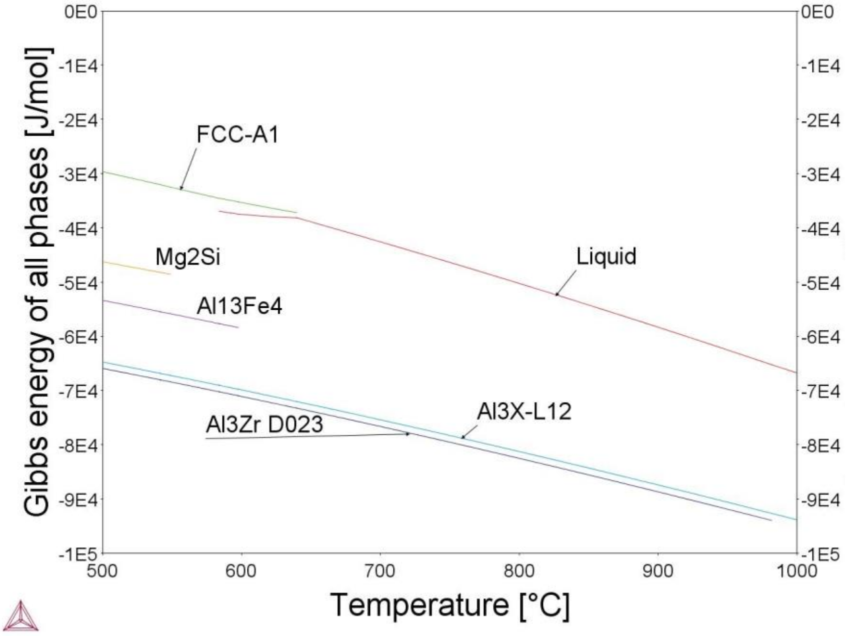

Figure 4.13: Plot of molar Gibbs free energy as a function of temperature (calculation performed with Thermocalc) for Al-3.66Mg-1.57Zr-0.2Si-0.1Fe (wt. %).

The duplex grain microstructure and inhomogeneous primary precipitate distribution can be explained by the change of the solidification front velocity at different regions of the melt pool and the order in which the phases form, as schematically shown in Figure 4.14. At the bottom of the melt pool, where the solidification velocities are the slowest, Al_3Zr is the first solid phase to form from the liquid, as per the Scheil-Gulliver calculations. The primary Al_3Zr precipitates then serve as inoculants for the nucleation of fine, micron-size fcc-Al grains, as discussed by Knipling *et al.* [11]. The absence of equiaxed grains toward the surface of the melt pool is consistent with the suppression of this inoculation effect due to an increase in the solidification front velocity. In laser-melting/welding, the solidification front velocity increases, approaching the beam scanning velocity, as the melt pool surface is approached [33], per equation 17. For example, pronounced microstructure changes over the depth of the melt pools (i.e., eutectic growth at the bottom and dendritic/cellular growth at the melt centerline) have been observed for a L-PBF processed Al-Ce eutectic alloy and were attributed to solidification front velocity increases [94]. In our alloy, it is expected that the solidification front velocity increased near the pool surface to the point that Zr was trapped in the solidifying fcc-Al grains, remaining in supersaturated solution. With no primary Al_3Zr present due to solute trapping, inoculation is inoperative close to the surface of the melt pool, consistent with the change to epitaxial columnar grain growth oriented parallel to the direction of the heat flow. However, the totality of the Zr is available for precipitation of nanosize Al_3Zr precipitates upon subsequent aging in the columnar grains, with the potential to make them stronger than the equiaxed grain where less Zr is present in solid solution.

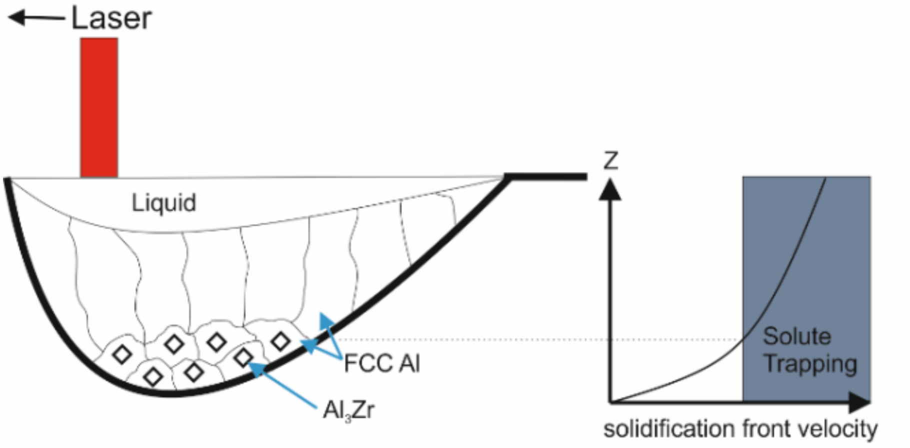

Figure 4.14: Schematic of melt pool and associated plot of solidification front velocity as a function of depth z in the melt pool. Solidification front velocity increases towards the surface of the melt pool, crossing a threshold of solute trapping preventing the precipitation of Al_3Zr precipitates.

SEM and STEM-EDX measurements taken in the columnar grain region of numerous melt pools showed an average Zr concentration of ~1.5 wt.%, which is much higher than the equilibrium maximum solid solubility of 0.28 wt% Zr for stable D0$_{23}$-Al$_3$Zr or even the 0.80 wt.% value for metastable L1$_2$-Al$_3$Zr in binary Al-Zr [11]. Since Zr is present in the columnar grain regions but primary Al$_3$Zr precipitates are not, this suggests that solidification velocities are high enough to suppress Al$_3$Zr formation. Solute trapping implies a partition coefficient of 1; however, the equilibrium partition coefficient of Zr in Al is 2.5. The velocity corrected partition coefficient can be calculated using equation 14. For a solidification front velocity of 200 mm/s (highest velocity that can be achieved), a D_i of 10^{-5} cm/s, and an interface length of 5 nm, the effective partition coefficient for Zr is 1.75. This calculation suggests that the velocity is high enough for reduced partitioning, but not complete solute trapping. It should be noted that exact values for D_i and δ_i are unknown and those used are rough approximations. Evidence for elemental Zr partitioning was observed in the form of the bright circular regions on the ADF-STEM image from the coarse grain region (Figure 4.7); however, no Zr chemical difference was observed on the STEM-EDX data, suggesting suppressed Zr partitioning. Knipling et al. [92] summarized the cooling rates required to suppress the formation of Al$_3$Zr and Al$_3$Ti in binary Al-Zr and Al-Ti alloys, respectively. According to their work, a cooling rate between 10^2 and 10^3 K s^{-1} is sufficient to prevent the formation of Al$_3$Zr. Hori et al. even reported that over 2 wt. % Zr can be kept in solid solution with a cooling rate of 10^5 °C/s [95]. These cooling rates can be easily achieved in the melt pools during L-PBF processing.

The prior model of microstructure formation ignores surface tension driven convection in the melt pools. Surface tension induced flow can have a significant influence on melt pool geometry [96]; although with a material with a low Prandtl number, ~0.02 for Al, the influence will be minimal. In our situation, the surface tension driven flow may result in the transport of primary Al$_3$Zr. Surface tension driven convection is difficult to measure experimentally, but Kou et al. [27] have developed a mathematical model that predicted liquid velocities of 3 m/s in laser welding of an Al 6063 alloy. While being a significant factor in melt pool dynamics, it is anticipated that the surface tension convection will have negligible influence on the overall mechanism proposed. The overall basis for the above microstructure mechanism is the formation of primary L1$_2$-structured Al$_3$Zr precipitates at the bottom of the melt pool that serve as inoculants for α-Al grains. Near the liquid-solid interface the liquid velocities are predicted to be significantly lower than the maximum of 3 m/s, 30 cm/s [27]. The lower fluid velocities at the bottom of the melt pool was experimentally observed in CO$_2$ laser melted NaNO$_3$ (NaNO$_3$

has similar surface tension driven flow as in welding Al alloys)[97]. Since the liquid velocity is minimal where the primary precipitation occurs, it will have a minimal influence on the primary precipitation, as is observed in the uniform distribution of the fine grain region in the top surface melt pools shown in Figure 4.2. If primary Al_3Zr precipitates were indeed transported by convection one would expect to see a less uniform band at the bottom of the melt.

Evidence of Mg loss in the as-fabricated Al3.60Mg-1.18Zr (wt. %, Batch 2) was observed, 3.60 wt.% Mg in the powder compared to 3.09 wt.% Mg in the as-fabricated sample. Some discrepancies may arise due to the different testing techniques used (ICP-OES, SEM-EDX), but due to the comparatively high vapor pressure of Mg, it is reasonable to assume there is Mg loss during processing. Indeed, Li et al. [63] have noticed a similar effect in a L-PBF fabricated Al-Mg-Sc-Zr alloy.

The above scenario for our Al-Zr-based alloy is similar to that proposed by Spierings *et al.* [66] for their Al-Sc-Zr-based alloy, who also identified primary $Al_3(Sc,Zr)$ precipitates as nucleant for their fine-grain Al regions deep in the melt pool, and the suppression of primary precipitation as the reason for the columnar grain regions near the melt pool surface. However, given that the Al-Sc and Al-Zr systems are eutectic and peritectic, respectively, the primary precipitation of mixed $Al_3(Sc,Zr)$ precipitates is more complex than in the present simpler Al-Zr peritectic system.

4.4 Microstructure Modification via Laser Rescanning

4.4.1 Motivation

The AM microstructure typically consists of columnar grains oriented in the build direction, but regions of equiaxed grains are also observed [98]. The grain and precipitate microstructure of any material depends on its thermo-mechanical history from solidification to heat treatment. In AM, this history is affected by numerous factors, e.g., the alloy composition, the specific AM process, and the scanning strategy. For example, studies have observed repeating patterns in the microstructure of an L-PBF fabricated CM247LC that was correlated to the scanning strategy implemented [2]. Ni-based superalloys fabricated with Electron beam melting (EBM) have precipitation in the as-fabricated condition [7] but superalloys fabricated with L-PBF have minimal to no precipitation in the as-fabricated state [83]. This difference in precipitation behavior can be attributed to the high preheat temperatures in the EBM process that leads to in-situ aging. The high number of variables present in the AM process means that there are numerous possibilities to control the microstructure.

It is well known that grain microstructure has a major influence on materials properties. For example, a fine grain structure is beneficial for tensile and fatigue strength, but not for creep resistance. A columnar grain microstructure is more beneficial for creep resistance. For any given application, the choice of grain microstructure (columnar, equiaxed, duplex, fine or coarse, etc) can be just as important as the choice of alloy and phases. Therefore, understanding grain microstructure formation and evolution during AM is of great importance. An AM part can, in a simplistic way, be viewed as a multi-pass weld; therefore it is important to relate microstructure to the solidification (thermal gradient, G and velocity, R) conditions. A study on EBM of IN718 found agreement between observed grain microstructure and that predicted by a solidification map [99]. It is known that one can change the microstructure by controlling the thermal gradients and velocities. It was shown in IN718 that changes in local grain crystallographic orientation (transitioning from columnar to equiaxed microstructure) can be controlled by the scanning strategy [100]. One downside to this modification strategy is that some scanning strategies can result in long process times and high residual stresses and part defects. Another grain microstructure modification strategy is to add grain inoculants to the L-PBF powders. Martin *et al.* [61] added nanoscale hydrogen-stabilized Zr particles to the surface of Al powders to preferentially nucleate equiaxed grains during solidification. The equiaxed grain microstructure can accommodate the strain induced by the AM process, thus resulting in crack-free parts. While the strategy was successful, it requires addition of nano-size particles to the Al powder which adds to the process complexity and cost. Therefore, it is desirable to develop more than one modification strategy to allow for grain microstructure tailoring, when altering the scan strategy or the powder production are not possible. Laser rescanning is a strategy where the solidified layer is scanned again by the laser prior to the deposition of the next powder layer, thus remelting the material. Kenel *et al.* [101] showed that laser rescanning can reduce the crack density for an oxide dispersion strengthened TiAl alloy. Yasa *et al*. [102] showed that laser rescanning of 316L stainless steel results in increased part density, better surface finish, and a finer grain microstructure. Little information exists on the potential benefit of laser rescanning on the grain microstructure of aluminum alloys, which is the focus of the following study.

4.4.2 Experimental Details

The ConceptLaser (Concept Laser, Germany) M2 machine was utilized for the laser rescanning study. Sample cubes (8 x 8 x 8 mm^3 and 10 x 10 x 10 mm^3) were fabricated with the full 200 W laser power, a 200 mm/s laser scanning speed, a 0.135 mm hatch distance, and a 40 μm powder layer. An island scanning strategy, as described by Carter *et al.* [2], was utilized for the study of number of rescans and a bi-directional scan strategy, also described by Carter *et al.*, was utilized to study the effect of rescan orientation. A change in scanning strategy (from chess to bi-directional) to study rescan orientation had to be made due to machine software constraints. The study on the number of rescans was conducted so that the rescan laser path followed the same path as the original melting path. Once the rescans were completed, the powder was distributed and the island scanning strategy resumed. All other machine parameters (laser power, hatch distance, layer thickness) were kept constant. In another condition, the laser rescan orientation was modified so that the rescan occurred at a 90° angle to the original melting scan. Single line scans (200 W, 200 mm/s) were also performed on an aluminum base plate with a 70 μm powder layer. The solidified melt trace was rescanned with the same parameters.

A small replication study (single and double scan) was performed with the Al-2.90Mg-2.10Zr (wt. %, Batch 3) powder. The ConceptLaser (Concept Laser, Germany) M2 machine was utilized with identical parameters as above (except for a 30 μm layer thickness) to fabricate sample cubes (10 x 10 x 10 mm^3).

4.4.3 Microstructure

Optical micrographs of double- and single-scan samples are shown in Figure 4.15 and Figure 4.16 . The melt pools exhibit a reduced depth with laser rescanning; using the line intercept method, the single- and double-scan samples show 10 and 14 pool boundaries over a 500 μm length, respectively (Figure 4.15). The double-scan samples have significantly lower surface roughness than the single-scan samples (Figure 4.16). Archimedes density of the samples did not increase with additional scans. EBSD grain maps showing the effect of repeated laser scans for each layer are shown in Figure 4.17(a,b,c). Area fractions of the equivalent grain sizes are shown in Figure 4.17(d), which indicates that additional laser scanning refines the grains: each rescan reduces the area fraction of the coarser, elongated grains and increases the area fraction of the finer, equiaxed grains. SEM-EDX measurements of the double scanned sample did not indicate further loss of Mg (See Appendix Figure 0.9).

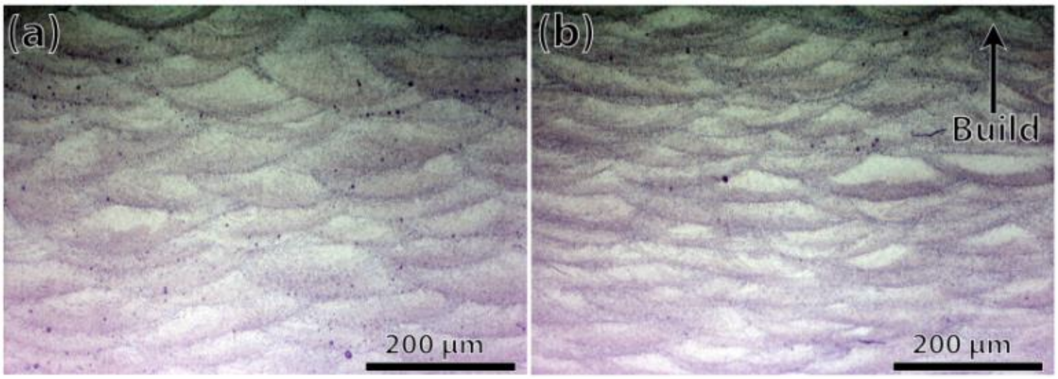

Figure 4.15: Optical micrographs comparing the melt pools of (a) single-scan and (b) double-scan sample. The rescanning results in shallower melt pools. (Al-3.60Mg-1.18Zr wt.%, Batch 2)

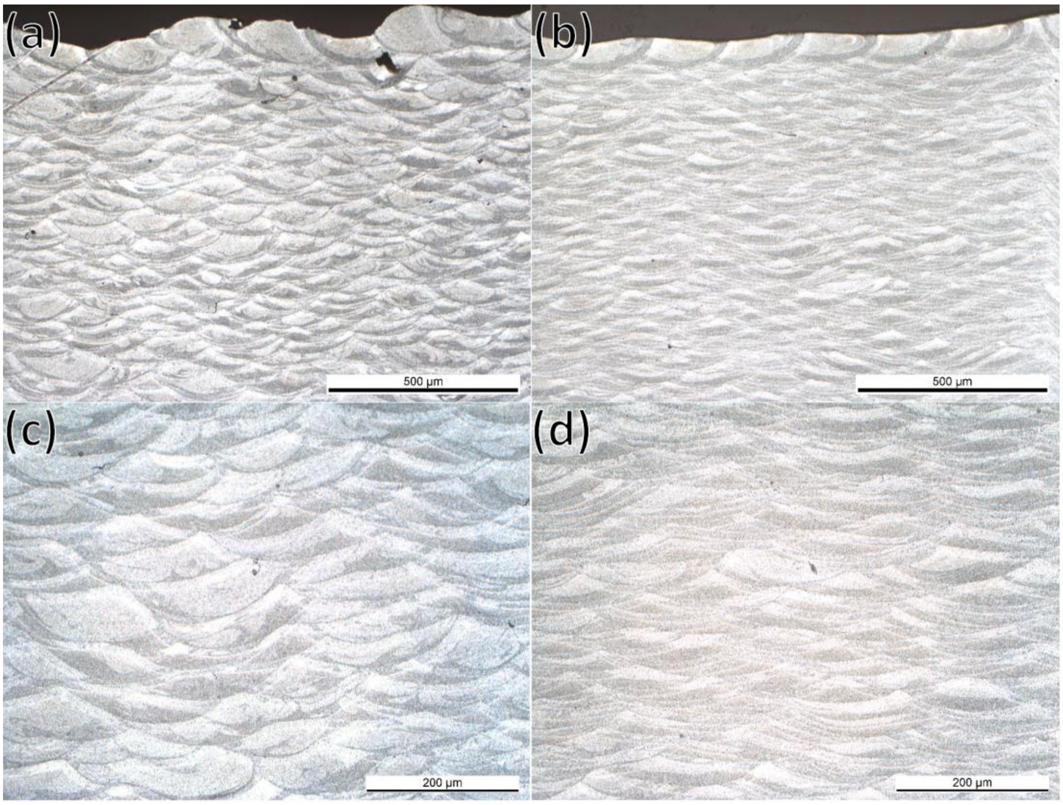

Figure 4.16: Optical micrographs comparing the melt pools of (a) single-scan and (b) double-scan sample. Higher magnification images of the single-scan and double-scan are shown in (c) ad (d) respectively. The rescanning results in shallower melt pools and a smoother surface finish. (Al-2.90Mg-2.10Zr wt.%, Batch 3)

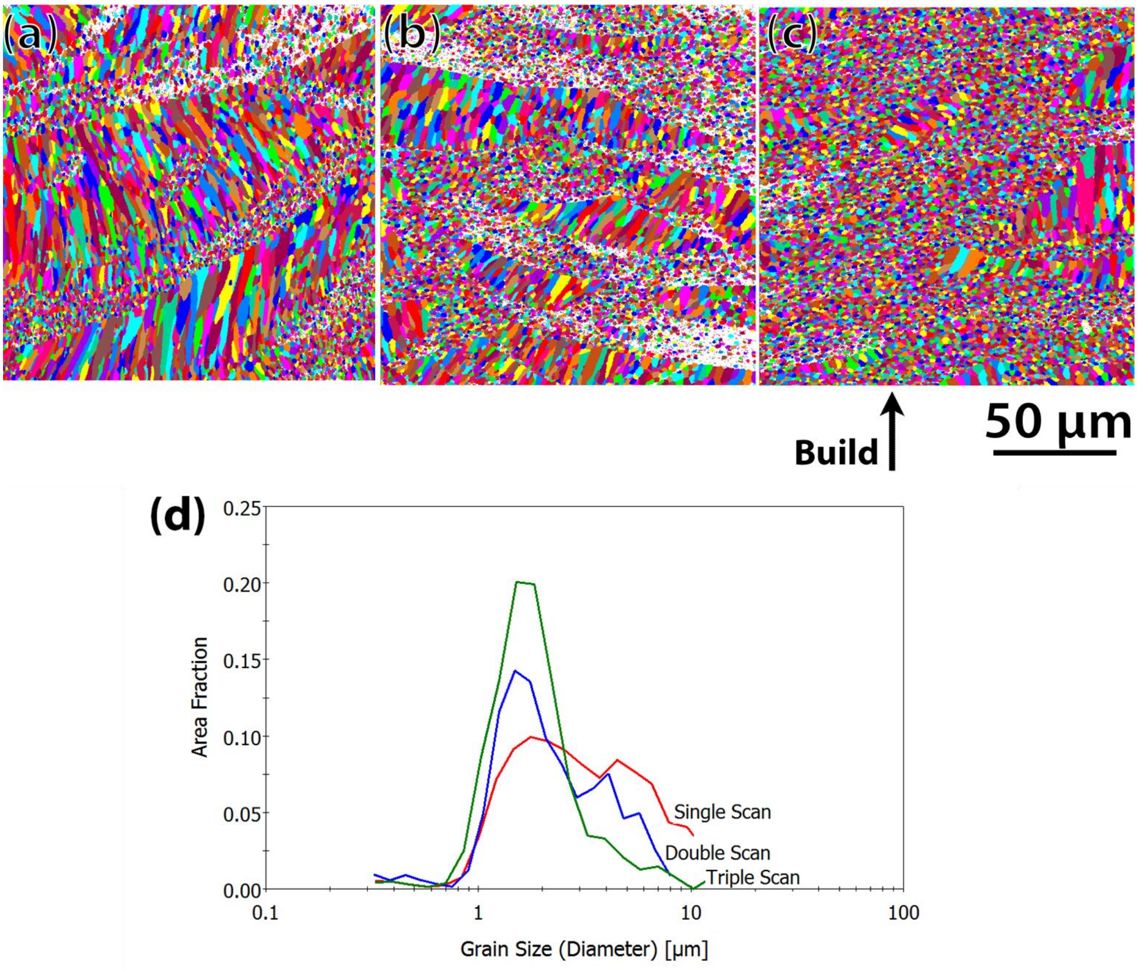

Figure 4.17: a.) EBSD grain maps of (a) single, (b) double, and (c) triple scans showing grain refinement with additional scans. White areas on the EBSD grain maps are regions filtered out; d) Distribution of area fractions vs. grain diameter, showing that rescanning reduces the fraction of large columnar grains and increases the fraction of fine, equiaxed grains. (Al-3.60Mg-1.18Zr wt.%, Batch 2)

The unidirectional scan with 90° rescan yielded an even more refined structure than the chess-board strategy with same trace rescan sample, as shown in Figure 4.18. However, a direct comparison between rescanning on the same laser trace and at 90° to the first laser trace for the chess-scanning strategy was not possible due to machine software limitations. The resulting crisscross of melt pools may serve to remelt the columnar grains more than rescanning on the same melt trace does. Further investigation into the impact of different re-scanning strategies is required.

This study only examined the effect of number of rescans and orientation, but further processing parameters can be changed during re-scanning. For example, the melt pool dimensions can be controlled by altering laser power and scan velocity of the rescans. It is also possible to modify the microstructure, e.g. by recrystallization or in-process aging, by adjusting the laser rescanning parameters so that the former melt pool remains in the solid state.

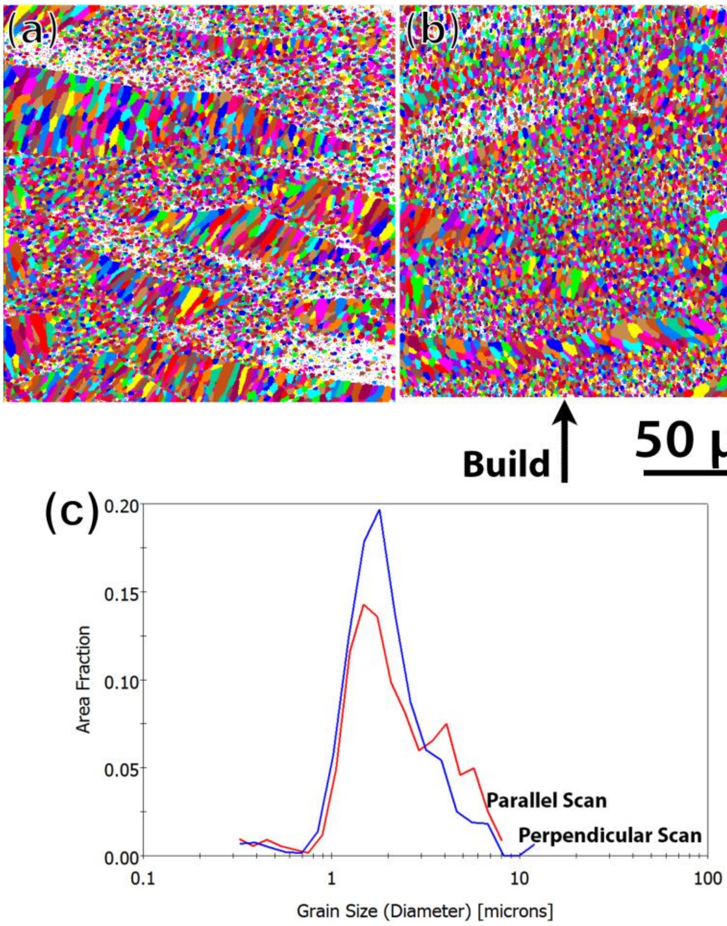

Figure 4.18: EBSD grain maps comparing double-scans where the second scan is performed (a) parallel or (b) perpendicular to the first scan. White areas on the EBSD grain maps are regions of low confidence index (0.1) (c) Area fractions of each grain diameter showing that rescanning perpendicular to the first scan results in more grain refinement than rescanning in a parallel direction. (Al-3.60Mg-1.18Zr wt.%, Batch 2)

4.4.4 Mechanisms

The shallower melt pools and subsequent grain refinement observed in double- and triple-scanned samples are likely due to the difference in laser-material interaction and heat transfer conditions. Figure 4.19 shows a schematic of the melt pool structures, with an image from a double-scanned single line track showing the melt pool depth difference (30 μm surface penetration from first scan with powder layer; approximately 5 μm penetration from second scan on bulk surface). Thus, the shallower melt pool for the second scan does not completely remelt the first melt pool but rather remelts preferentially the columnar grain structure near the top of the pool, while the equiaxed grains at the bottom of the first pool remain unmelted. It can be assumed that the solidification in the second shallower melt pools occurs in the same way as in the original melt pools, with the formation of equiaxed grains nucleated by primary Al_3Zr precipitates in the lower part of the pool and elongated, Al_3Zr-free grains near the top, when the high solidification front velocity inhibits the formation of the Al_3Zr inoculating particles. The new equiaxed grains form in place of the columnar grains created during the first scan. It is important to note that the melt pool of the first scan (melting the powder) must not be deep enough to completely remelt the previously solidified layer; otherwise the rescan-influenced microstructure will be destroyed upon melting of the subsequent powder layer.

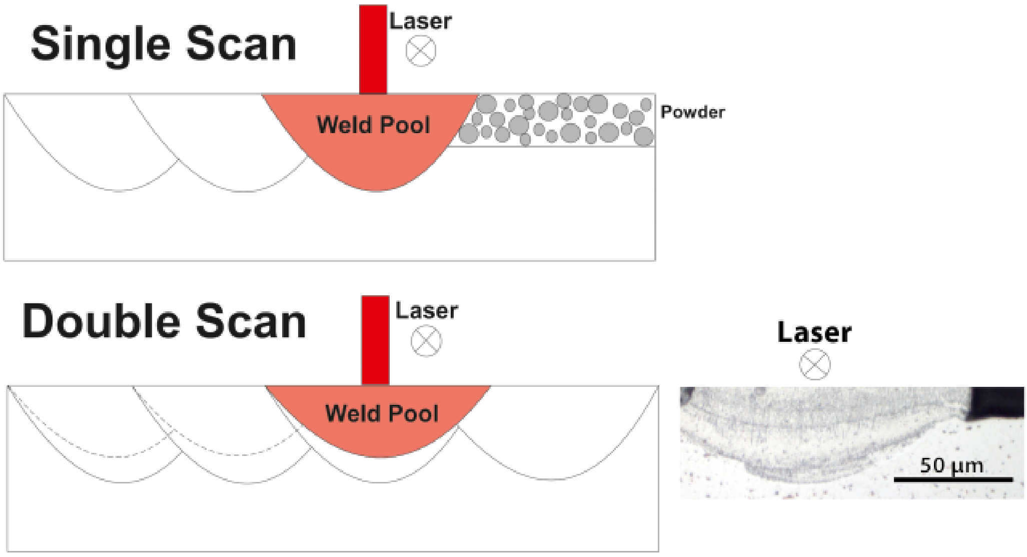

Figure 4.19: Schematic of melt pool depth differences between single- and double-scan cases. Reduced laser absorptivity on a consolidated surface and increased heat transfer result in a shallower melt pool during the rescan. Scan direction is perpendicular to image plane. The micrograph of a double-scanned single line shows the melt pool boundaries (arrows).

Many factors can contribute to the melt pool geometry differences between the single- and multi-scan conditions and a few are listed below:

1. Laser-Solid interaction
2. Laser-Liquid interaction
3. Wetting and spreadability of the molten metal
4. Thermal boundary conditions

Unfortunately, due to the complexity of the process and the physical phenomena at work, isolating one dominate mechanism will be difficult and out of scope of the current study. What follows is a discussion of how each factor could influence the observed effect.

An important contributing factor to a deeper melt pool on the first scan is related to laser-solid interaction. Surface roughness is known to have a major influence on laser absorptivity in metals [103–105]. Forsman et al. demonstrated that a sand blasted 6063 Al-alloy sheet had double the absorption (14% for as-received sheet) of low intensity (100 W/cm^2) 1064 nm radiation [106]. Tolochko *et al.* [107] reported that the 1.06 µm wavelength laser absorptivity of W and Pb powders is nearly twice that of the consolidated material, due to the scattering in the gaps between powder particles. It can be assumed that this is also the case for the present Al alloys. A reduction in the absorptivity from powder to consolidated material would result in reduced energy transfer during the second scan, and thus remelting of a shallower, narrower material volume. The influence of the surface roughness (a smoother surface has higher reflectivity) on the melt pool size and geometry for laser scanned Al-Mg-Zr alloy is qualitatively demonstrated in Figure 4.20. Even though the experiment was performed without powder on the sample surface, it is observed that for the same laser parameters a rough surface leads to the formation of a wider and deeper melt pool than a smooth surface. In this experiment a sample of Al-Mg-Zr alloy was ground down to a 4000 grit finish. Half of the sample was masked with copper tape and the sample was grit blasted with alumina. The masking was removed revealing a sample with half of the surface having a grit blasted surface and the other half having a much smoother finish. The same L-PBF machine, Concept Laser M2, and the same laser parameters described in the paper were utilized for this experiment. A contour scan in the form of a 5 x 5mm box was utilized for the test. The laser started in the lower left corner and moved in a clockwise direction. The melt pool in the rough region is fairly consistent in appearance but the melt pool in the polished region has an inconsistent appearance, with some regions appearing similar to that of the rough region but most regions having a narrower and darker appearance. It is clear from Figure 4.20(a) that the melt pool changes from the grit blasted area and the ground region. Cross sections were taken at the red lines and presented in Figure 4.20 (c) and (d). The melt pool in the grit blasted region measured 260 µm wide and 180µm deep. The melt pool in the ground region measured 110 µm wide and 45 µm deep. This provides proof for surface roughness induced melt pool depth and profile changes. The melt pools can be roughly classified as a high-energy absorption melt pool (rough surface) and a low-energy absorption melt pool (smooth surface).

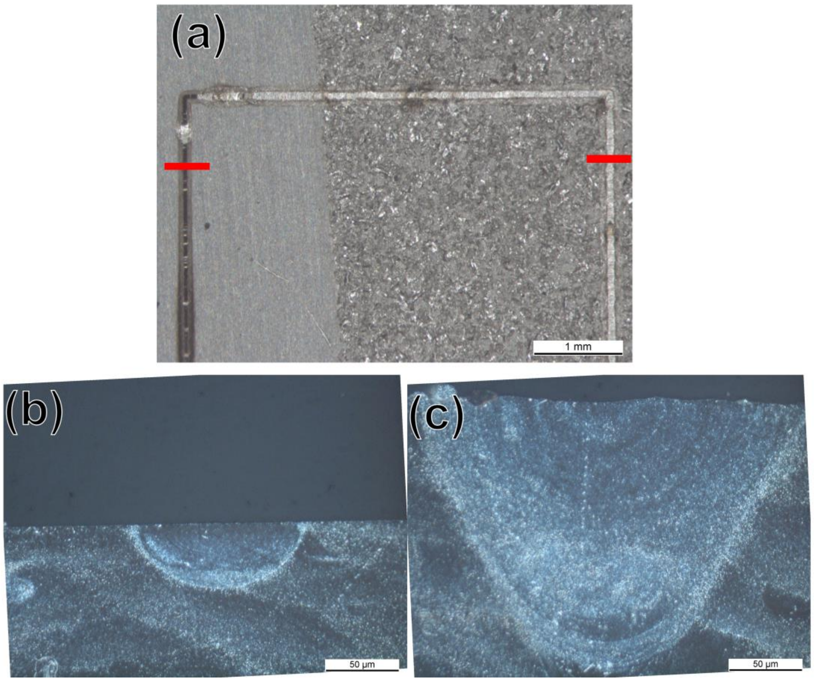

Figure 4.20; (a) Single laser line scan experiment with two different surface roughnesses. The left was sand blasted and the right was ground with 4000 grit SiC paper. The laser movement is clockwise. The melt pool size is overall small in the polished regions than in the rough regions, although some areas in the polished region have large melt sizes likely due to increased coupling by defects. (b) Cross section of line scan on smooth surface. 110 µm wide and 45 µm deep (c) Cross section of melt pool on rough surface. 260 µm side and 180 µm deep.

One potential issue with the above experiment is that the starting position of the laser is only on one type of surface. In order to isolate the influence of the laser starting position (smooth surface), a second experiment was performed (albeit on a pure Al plate) similar to the prior experiment but with two boxes, one completely in the rough surface, and one completely on the polished surface. Similar results were observed with this experiment as the prior experiment (weld pool width and appearance). Again the melt pool in the smooth region appears to switch between high and low energy absorption conditions but predominately remains in the low-energy absorption condition. This may be explained by locally increased laser absorption from porosity or surface contamination resulting in temporary periods of high-energy absorption condition. The intermittent increased laser absorption may also be due to defects (pores, particles, etc.) inside the material as well. This experiment demonstrates the substantial effect that surface roughness can have on melt pool size and shape. It is hypothesized that a similar effect is present when scanning on powder compared to solid material as discussed in prior.

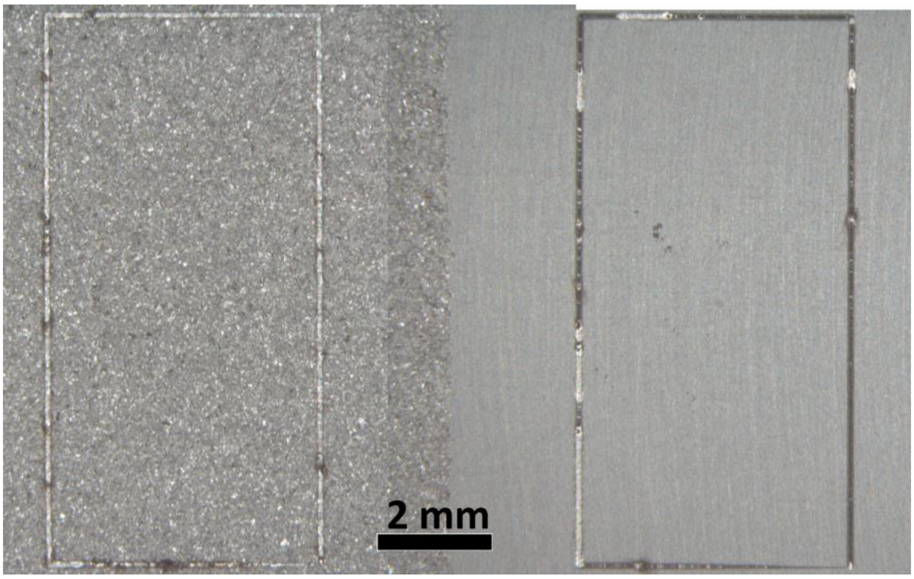

Figure 4.21: Single laser line experiments with two different surface roughnesses on a Al plate. The left was sand blasted and the right was ground with 4000 grit SiC paper. The melt pool appearance is consistent in the rough surface.

Several studies indicate that, during optimal laser-based processing, the beam mostly interacts with the liquid metal [105,108]. Forsman et. al. [106] also performed absorption experiments for high intensity (3000 W, unreported beam diameter) 1064 nm radiation and found that the surface roughness has minimum influence on the absorptivity. This is likely due to welding occurring in the keyhole mode where the absorption is mainly due to the formation of the keyhole. Even if this is true for the processing parameters used in the study, the laser will still interact with solid, and not liquid, when the laser is first turned on. As stated prior, a rough surface will result in higher laser absorption than a smooth surface. Since the dwell time from laser on to the scanning mirror movement is kept constant, the initial melt pool for a rough surface will be larger due to more laser absorption. A larger starting pool may result in the entire laser beam diameter hitting liquid, but if the melt pool fails to reach the size of the beam diameter by the time the laser moves, then the laser may be interacting with both solid and liquid, resulting in a smaller melt pool. The occasionally wider melt pools observed in the smooth surfaces of the above experiments may be due to locally increased absorption due to defects.

Laser-liquid interaction may also vary between the single-scan and rescan cases. Matthews *et al*. observed that the melt pool during powder based processing is very dynamic [109]. Kaplan *et al.* showed that the absorptivity of the molten weld pool can change based on the surface conditions of the melt [108]. A wavier surface was shown to improve the absorptivity for materials processed with a 1 μm wavelength laser radiation. It is conceivable that the highly dynamic melt pool observed in L-PBF can result in surface-induced absorptivity increases over a typical laser weld melt pool, as would be the case with the rescanning. However, experimental evidence does not exist to support or invalidate this hypothesis.

Once a liquid melt is formed, then liquid-solid interactions will also need to be considered, specifically, the wettability. The wetting behavior of a molten metal in L-PBF has been shown to be important for defect formation such as balling [110]. It is reasonable to assume that the wetting will also influence the melt pool dimensions. When considering the wetting of molten aluminum on solid aluminum, it is important to note that, even in low oxygen partial pressure environments, an oxide layer has been observed on molten aluminum in sessile drop experiments [111]. L-PBF processing in this study was done in argon shielding gas, but the oxygen content was measured at ~0.5 %. Even in this low oxygen environment, a native oxide layer will be present on the melted and solidified Al and potentially even as as shell surrounding the molten aluminum, thus one needs to consider a few combinations of Al/Al_2O_3 and their wettability. Bao et al. [111] studied the wettability of molten Al on solid Al_2O_3 in both vacuum and in an Ar atmosphere at different temperatures. At 1200°C, the apparent contact angle (time = 0) between the aluminum droplet and Al_2O_3 was 160° and 138° in Ar and vacuum, respectively. The higher contact angle in the argon atmosphere was attributed to the influence of the oxide shell. Raising the temperature by 200°C resulted in a 20 to 25° drop in contact angle. When time was taken into account at 1000°C in vacuum, the contact angle was initially ~140°C and after 400 minutes dropped to below 90°. The large drop with time was attributed to the removal of the oxide layer, suggesting the actual Al/ Al_2O_3 contact angle is near 90°. Wang et. al [112] also performed experiments of oxide-less molten aluminum on Al_2O_3 and reported a 90° contact angle at 700°C. It is clear that any real world scenario of L-PBF processing of aluminum alloys will involve the influence of oxidation and result in contact angles greater than that of the perfect wetting of Al on Al. As melt balling was not a significant problem during L-PBF processing of this alloy, it has to be assumed that there is partial wetting (contact angle below 90°) and that the oxide is not a significant issue.

The above argument on wetting assumed an ideal surface, which is absent in L-PBF processing. Rough surfaces lead to an increase in the contact angle for systems having ideal contact angles greater than 90° and lead to a decrease in the contact angle for systems having ideal contact angles less than 90° (Wenzel Model) [113]. If wetting does occur in the L-PBF of Al-Mg-Zr alloys, then the rough surface present in the scanning of a powder surface will result in greater penetration (due to increased wetting) than scanning on the smoother solidified surface.

It is known that the thermal conductivity of the base material in laser welding influences the depth of the melt pool [20]. For a L-PBF process when each layer is scanned only once, the laser radiation and resulting melt pool interact with a layer of powder. In the case of rescanning, the laser radiation and subsequent melt pool interacts with a powder layer (on at least one side of the pool) in the first scan, but upon remelting in the second scan, the pool is surrounded with dense material, which is changing the heat transfer conditions. Since powders are less heat-conducting than dense material, heat transfer from the melt pool into the powder direction may be reduced as compared to directions where solid material is in contact. With laser rescanning of the already consolidated part, heat can dissipate more uniformly in all directions. The reduced heat transfer of the powder-contacting melt could then lead to a more pronounced heat transfer to the dense alloy below and thus to a deeper melt pool. If this was a major mechanism, one would expect the melt pools of a single scanned sample to be highly asymmetric, but this is nearly impossible to tell due to the poor surface roughness of the top layer of a single scanned sample.

Assuming a laser interaction with the solid rather than the liquid (in the case of poor laser-material coupling), the further grain refinement resulting from the third laser pass may be explained by a further decrease in the energy input. It is has been shown by Yasa *et al.* [102] that laser rescanning results in a smoother surface finish. The improved surface finish after the second scan may decrease the surface roughness enough that the absorptivity further decreases. A further decrease would result in even shallower melt pools and a further replacement of the columnar grains with equiaxed grains *via* remelting and re-solidification. However, no noticeable difference of the melt pool size between the double- and triple-scanned samples was observed in metallographic cross sections. Additional heating from repeated laser scans can also influence the grain microstructure. A higher bulk temperature will result in lower cooling rates; as a result, the melt pool might have lower solidification velocities, leading to a later transition from fine- to coarse-grain solidification microstructure. It might also be expected that the additional thermal input caused by the rescanning results in some grain recrystallization; however, grains are likely to be pinned by the Al_3Zr and Fe-rich precipitates and the oxide particles.

4.5 Conclusions

- The new Al-Mg-Zr alloy was successfully fabricated via L-PBF with minimal defects and high density. The as-processed alloy (single scan) has a duplex grain microstructure consisting of regions of fine, equiaxed grains (~1.3 μm in diameter) at the bottom of the melt pools and regions of coarse, columnar grains (~40 μm long) at the top of the pool.

- Sub-micron (~100-400 nm diameter), cuboidal primary Al_3Zr precipitates act as nucleation sites for the equiaxed fcc-Al grains. No primary precipitates are visible in the columnar grain regions, consistent with the lack of nucleation: this is attributed to Zr solute trapping from increasing solidification front velocities as the melt pool surface is approached.
- Laser rescanning of the consolidated Al-Mg-Zr alloy results in grain refinement which is attributed to the formation of shallower melt pools upon rescanning due to reduction of laser energy transfer to the solid and modification in heat transfer in the solid. The shallower melt pool upon rescanning melts the columnar grain region at the top of the original melt pool but not the lower equiaxed region. The equiaxed grains from the original scan remain and the columnar region is replaced with new equiaxed grains (and some new columnar grains) from the new melt pool.

Chapter 5 Metallurgy of Heat Treated Addalloy

5.1 Peak-Age Determination

A conventional heat treatment schedule for a precipitation hardened alloy typically involves a solutionizing cycle followed by a rapid cooling, and then an aging cycle. Since the degree of strengthening provided by precipitates is dependent on their size and inter-particle spacing, it is desirable in the end condition to have a uniform size and dispersion of precipitates. Often times during fabrication, whether casting or welding, some of the solute will have already formed precipitates, making for a non-unifom size and distribution. A solutionizing heat treatment is done in order to bring as much of the solute element (the element responsible for the precipitation, Zr in this instance) into solid solution so that during aging the size and dispersion will be uniform. The unique solidification conditions present in the L-PBF fabricated Al-Mg-Zr alloys make a solutionizing heat treatment not desirable. As seen in the binary phase diagram in Figure 4.11, the maximum solid solubility of Zr in an α-Al matrix is 0.28 wt.% (0.083 at. %). There is ~2 wt. % Zr in solid solution of the L-PBF fabricated alloys due to an increase in solubility from the rapid solidification. If the L-PBF fabricated alloy was subjected to a solutionizing heat treatment (maximum solid solubility is at the solidus temperature), than a majority of the Zr that was present in solid solution would now be precipitated out as Al_3Zr in the size and crystal structure not conducive to maximum strengthening. For these reasons, the L-PBF Al-Mg-Zr alloys are subjected to only a direct aging heat treatment.

Peak-aged condition was determined by our project collaborator, NanoAl LLC., via Vickers hardness measurements of isothermally aged (400°C, 0.5 to 144 h) samples of L-PBF fabricated Al-3.60Mg-1.18Zr (wt.%, Batch 1) and Al-3.60Mg-1.57Zr (wt.%, Batch 4) alloys (Figure 5.1). The as-fabricated Al-3.60Mg-1.18Zr and Al-3.60Mg-1.57Zr alloys had an average microhardness of ~875 MPa and ~961 MPa, respectively. The higher microhardness of the higher Zr alloy can be attributed to the increased solid solution strengthening provided by the higher levels of Zr in solution. In-situ precipitation of nanoscale $L1_2$ Al_3Zr during processing could also explain the higher hardness values of the high Zr alloy, but no evidence of this has been observed in STEM analysis of as-fabricated samples. The first peak hardness is observed after two hours of aging and the second, higher peak is observed after ~8 hours of aging at 400°C. Potential mechanisms of the two peak aging curve will be discussed in a latter section.

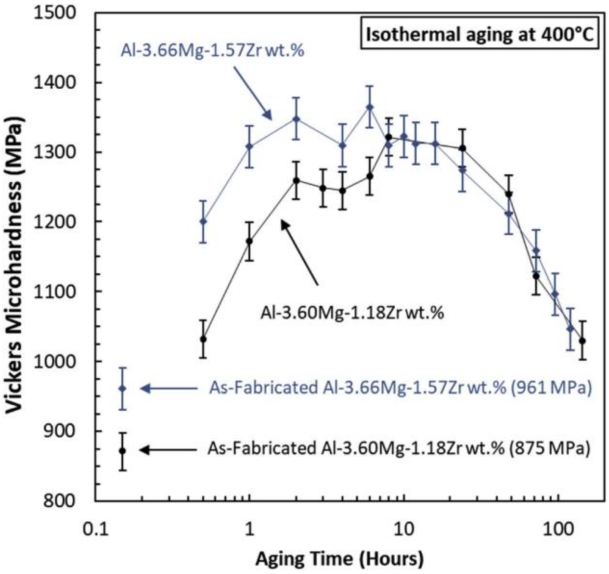

Figure 5.1: Hardness evolution upon isothermal aging at 400 °C of Al-3.60Mg-1.18Zr wt.% (black circles) and Al-3.66Mg-1.57Zr wt.% (blue diamonds). Each data point is the average of multiple samples fabricated with various laser energy densities. Error bars represent one standard deviation of ten measurements of each sample. Plot courtesy of J. Croteau. [67]

5.2 Ex-Situ Microstructure Characterization

A majority of the ex-situ microstructure characterization that follows will be focused on the microstructure of the peak-age (400°C, 8 h) condition. The overaged condition will be briefly discussed.

Figure 5.2 shows BSE images of the microstructure of a Al-3.60Mg-1.18Zr (wt. %, Batch 1) alloy after peak-aging (400°C, 8 h). The overall bimodal grain microstructure, fine grain regions with primary Al_3Zr precipitates, and coarse grain regions without primary precipitates, remains after peak aging. Higher magnification images (Figure 5.2) show the presence of sub-micron bright particles (later identified as Al_3Zr and Fe-rich intermetallics) on the grain boundaries in the coarse grain region (highlighted by white arrows in Figure 5.2). Figure 5.3 shows a BSE image of the microstructure of a Al-3.60Mg-1.18Zr (wt. %, Batch 1) alloy after overaging (400°C / 144 h). Many of the bright precipitates are acicular (highlighted by black arrows in Figure 5.3), which is indicative of the $D0_{23}$ structured Al_3Zr (equilibrium phase). The bimodal grain structure is less apparent but still exists.

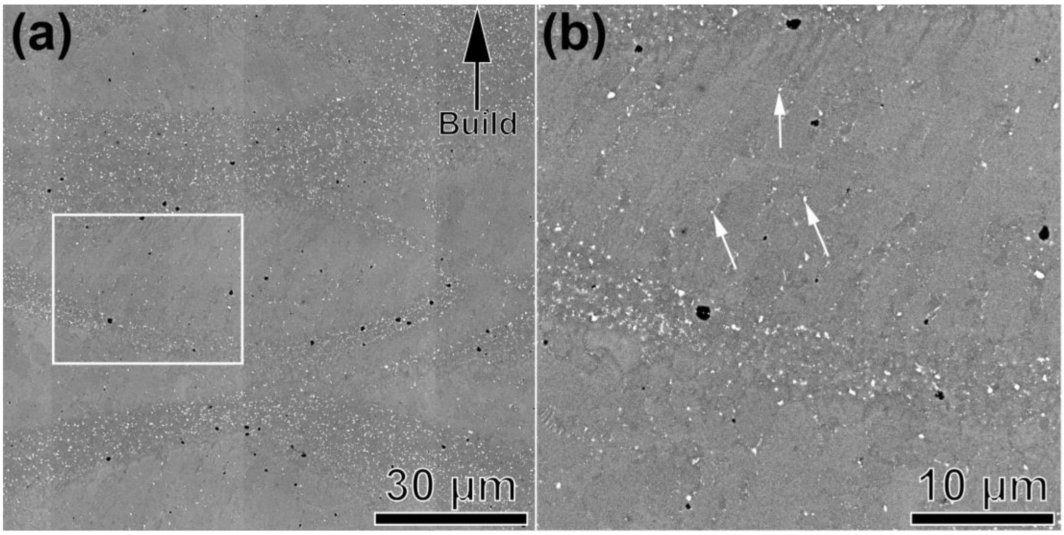

Figure 5.2: BSE images of a peak-aged (400°C / 8 h) sample (Al-3.60Mg-1.18Zr, wt.% Batch 1) showing a duplex grain microstructure consisting of regions with columnar grains and equiaxed micron-size grains (each containing one primary Al_3Zr precipitate). (b) higher magnification BSE image taken from the white box in (a). White arrows point to a few sub-micron grain boundary particles observed in the coarse grain region.

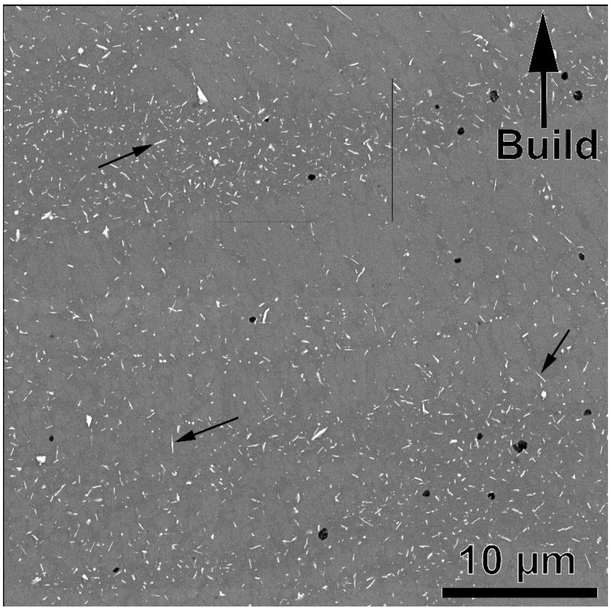

Figure 5.3: BSE image of an overaged (400°C / 144 h) sample (Al-3.60Mg-1.18Zr, wt.% Batch 1). Black arrows point to a few elongated bright particles that are assumed to be $D0_{23}$ structured Al_3Zr.

EBSD grain maps for the peak-aged (400°C / 8 h) and overaged (400°C / 144 h) samples (Al-3.60Mg-1.18Zr, wt.% Batch 1) are shown in Figure 5.4. The bimodal microstructure is apparent in both samples. The average grain size in the fine grain regions of the peak-aged and overaged conditions are 0.84 and 1.28 µm, respectively. For comparison, as-fabricated Al-3.60Mg-1.18Zr (wt.% Batch 1) samples had an average fine-grain region grain size of 0.77 µm. As mentioned in the prior chapter, as-fabricated Al-3.60Mg-1.18Zr (wt.% Batch 2) samples had a ~1.3 µm average grain size in the fine grain region.

It is not known if the observed difference between as-fabricated grain sizes is from sampling discrepancies or from layer thickness differences between the two batches. Regardless, minimal grain coarsening occurs in the L-PBF fabricated Al-Mg-Zr alloys. The reason for this will be discussed in a later section.

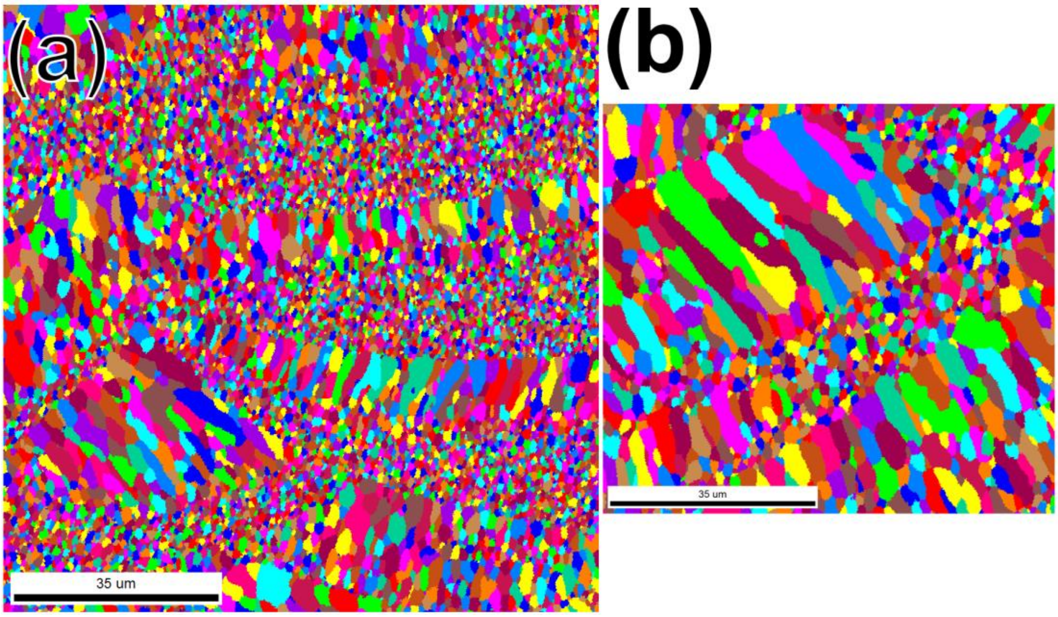

Figure 5.4: EBSD grain maps of (a) the peak-aged (400°C / 8 h) sample and (b) the overaged (400°C / 144 h) sample. (Al-3.60Mg-1.18Zr, wt.% Batch 1) . Measurements courtesy of A. Hashemi.

Figure 5.5 displays ADF-STEM images taken from both the fine and coarse grain regions of a peak-aged (400 °C for 8 h) Al-3.60Mg-1.18Zr (wt.% Batch 1) sample. The primary $L1_2$ Al_3Zr precipitates appear to be unchanged in the peak aged condition (the core shell appearance was observed in the as-fabricated state and is assumed occur during solidification). New precipitates, filamentary in shape, have appeared in the fine grain region (Z2 in Figure 5.5). These precipitates are also observed in the coarse grain region to a much greater degree (Z2 in Figure 5.5(b)). Figure 5.6 displays STEM-EDX maps taken from the coarse-grain region (grains appear sub-micron as the TEM lamellae was sampled perpendicular to the grains long dimension) of a sample aged at 400 °C for 8 h (second peak aging). Zr-rich precipitates are observed at the grain boundaries (larger, equiaxed in shape), expected to be primary $L1_2$-Al_3Zr formed during solidification. Finer $L1_2$-Al_3Zr nanoprecipitates within the grains, filamentary in shape, have also appeared due to aging. The same Mg- and O-rich equiaxed oxide particles formed during printing (~100 nm in diameter) are still present, and mostly at grain boundaries. Finally, the same Fe-rich particles are also observed, albeit at a lower number density and larger size when compared to as-fabricated state (Figure 5.6 shows a ~100 nm precipitate, twice the original size in Figure 4.7).

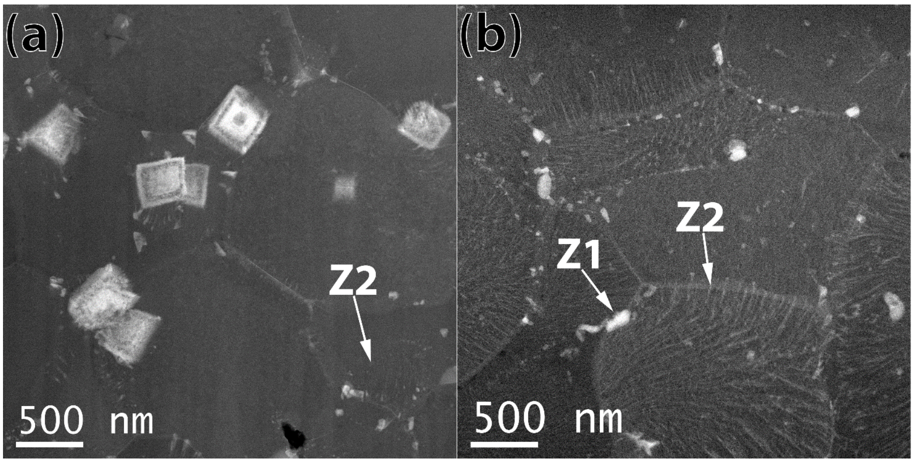

Figure 5.5: ADF-STEM overview images of the (a) fine grain region and (b) coarse grain region. Z1 points to a Zr rich grain boundary precipitate. Z2 points to the filamentary shape precipitates.

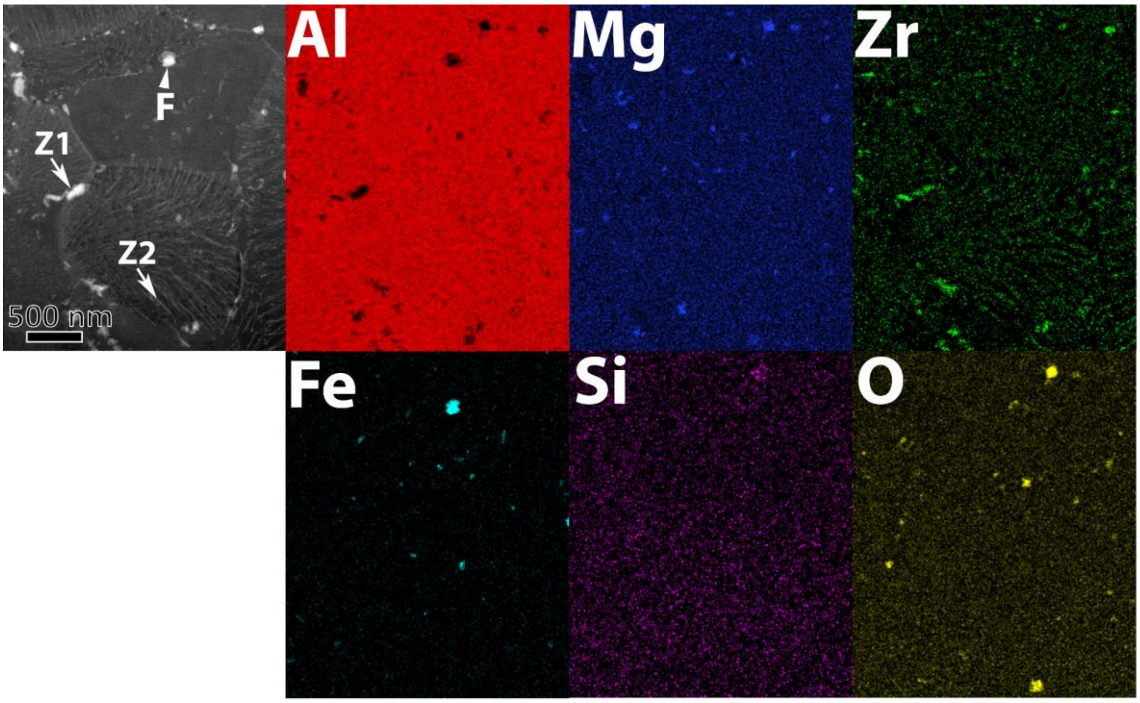

Figure 5.6: Coarse-grain region of a peak-aged sample (400°C for 8 h, Batch 1) imaged via STEM (ADF-image and elemental EDX maps using Si-K, Zr-K, Al-K, Mg-K, Fe-K and O-K lines) showing three types of precipitates : (i) Al_3Zr precipitates consisting of larger, equiaxed precipitates (labelled Z1) and finer, elongated precipitates within grains (labelled Z2); (ii) Mg- and O-rich oxide particles located at grain boundaries; (iii) Fe-rich precipitates (F) located grain boundary.

Closer examination of the peak-aged sample illustrates the two types of Zr-rich precipitates (spherical and acicular) within the grains (Figure 5.7(a)). Although both types of precipitation are observed in the fine-grain region as well, to a lesser extent, the following figures and discussion focus on the observations made in the coarse-grain region. High-resolution ADF-STEM of the upper half of the highlighted region of Figure 5.7(a) reveals spherical precipitates ~2 nm in diameter (Figure 5.7(b)). A (FFT) of Figure 5.7(b) reveals the 010-type superlattice reflections of the $L1_2$ structure (Figure 5.7(c)), consistent with metastable $L1_2$-Al_3Zr precipitates which forms upon aging of a super-saturated solid solution. A high-resolution ADF-STEM image of the bottom half of the highlighted region in Figure 5.7(a) shows the presence of narrow (~5 nm wide), highly elongated (hundreds of nm) filamentary precipitates (Figure 5.7(d)). An FFT of Figure 5.7(d) reveals again the 010-type superlattice reflections of the $L1_2$ structure (Figure 5.7(e)). STEM-EDX mapping of the boxed region in Figure 5.7(a), shown in Figure 5.8, indicates that these filamentary precipitates are enriched in Zr, indicating that they are also the $L1_2$-structured Al_3Zr phase.

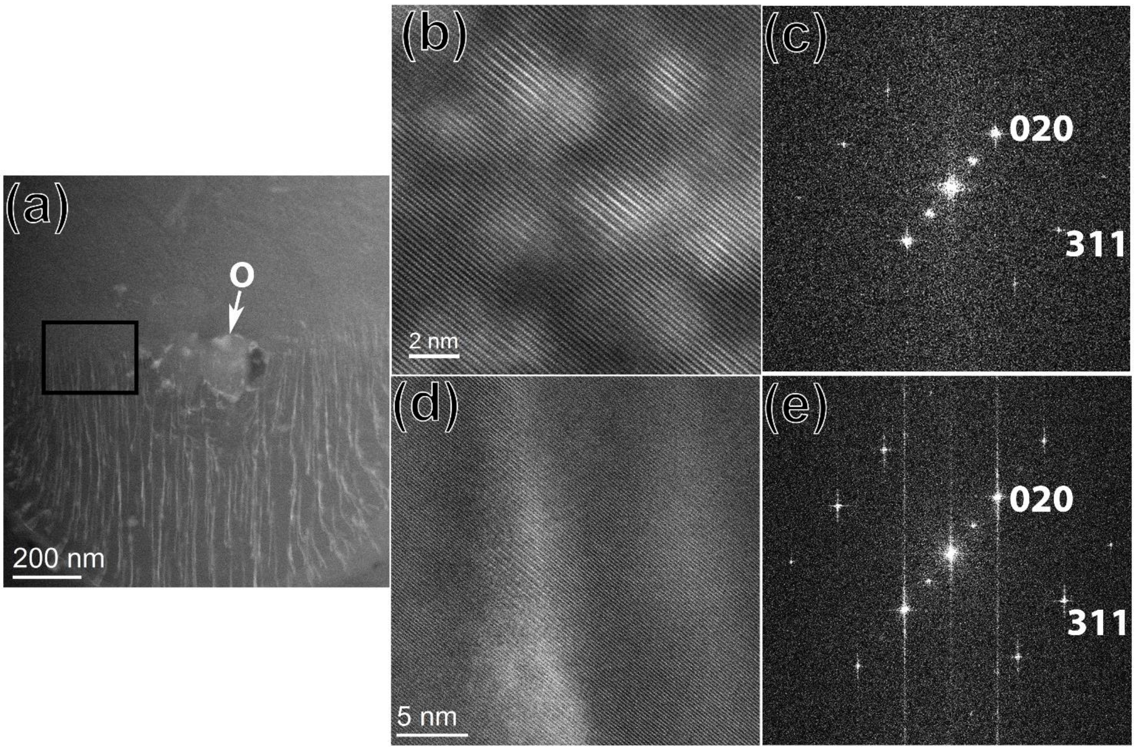

Figure 5.7: (a) STEM ADF-image of a coarse-grain region of a peak-aged (400˚C / 8 h) sample (Al-3.60Mg-1.18Zr, wt.% Batch 1) showing: (i) nanometric equiaxed Al_3Zr precipitates formed via continuous precipitation (upper grain) and (ii) elongated, aligned Al_3Zr precipitates formed via discontinuous precipitation. An oxide particle (O) is present at the image center (b) High-resolution ADF-STEM image of equiaxed Al_3Zr nano-precipitates (2 nm in diameter, continuous precipitation) in the upper half of boxed region in (a). (d) High-resolution ADF-STEM image of the 5 nm-wide, highly-elongated Al_3Zr precipitates formed by discontinuous precipitation in the lower half of boxed region in (a). (c, e) FFT of images (b) and (d), respectively, show the 010-type superlattice reflection of the metastable $L1_2$ structure for Al_3Zr.

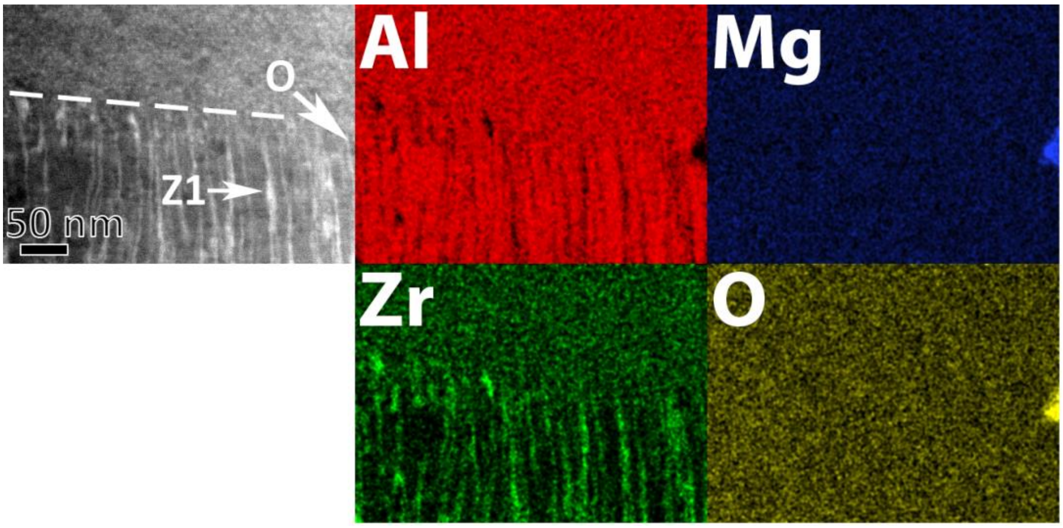

Figure 5.8: STEM ADF-image and elemental EDX maps of the region highlighted by the black box in Figure 4, showing elongated, discontinuous $L1_2$-Al_3Zr precipitates (labelled Z1) and one Mg- and O-rich oxide particle (O) at the interface between continuous and discontinuous precipitation (dashed line). Chemical analysis was performed using the Zr-K, Al-K, Mg-K, and O-K lines.

5.3 In-Situ STEM Experiments

5.3.1 Experimental Details

Two in-situ STEM aging experiments were carried out to investigate the evolution of primary and secondary precipitates during thermal exposure. The use of in-situ STEM experiments, as opposed to ex-situ, allows for the direct monitoring of individual features of interest. Kinetics (coarsening rates) will not be discussed as thin film effects, discussed later, of STEM/TEM samples make reaction kinetics incomparable to bulk.

Two *in situ* STEM thermal aging experiments were performed with a Protochips Fusion 500 heating stage on the same FEI Titan Themis microscope described in chapter 2. A first sample was extracted from the coarse-grain region of a sectioned Al-3.60Mg-1.18Zr (wt.%) cube (Batch 1) and a second sample was extracted from a fine-grain region of the same cube. Both extractions were done with an FEI Helios NanoLab 600i focused ion beam (FIB) so that the lamellae were perpendicular to the build direction. The *in situ* aging experiment of the coarse-grain sample began with a 160 s ramp from 20 to 400˚C. The sample was held for 480 s before it was quenched back to 20˚C. EDX mapping was conducted on regions of interest on the quenched sample. The sample was subsequently held at 400˚C for 600 s. Finally, the sample was heated to 500˚C and held at that temperature for 116 s until the diffusion of Pt from the protective layer of the lamella destroyed the sample. The fine-grain sample was exposed to a range of temperatures, from 150 to 350˚C (with 25˚C increments) over 64 min. Once the sample reached 350˚C, it was held there for 48 min to observe the precipitate growth. The sample was then heated from 350 to 600˚C (with 25˚C increments) over 40 min until its destruction at 600˚C.

5.3.2 In-Situ STEM Results

The first experiment was performed with a lamella taken from a coarse-grain region, with no primary Al_3Zr phase, in an as-fabricated Al-3.60Mg-1.18Zr (wt.%, Batch 2) sample. An ADF-STEM image of the lamella prior to thermal exposure is shown in Figure 5.9(a). Several spherical, Mg- and O-rich particles, ~100 nm in diameter and assumed to be oxides, are observed both on grain boundaries and within the grains (a few are identified by black arrows in Figure 5.9(a)). The sample was ramped from room temperature to 400˚C in 160 s and then held at this temperature for 480 s. An ADF-STEM image taken thereafter is shown in Figure 5.9(b). Numerous white precipitates, assumed to be $L1_2$-Al_3Zr, are observed to nucleate both on the grain boundaries (~100 nm diameter, highlighted by white arrows, nucleation began during the ramp at 360˚C) and within the grains (nanometer scale, observed starting at the end of the ramp to 400˚C). The $L1_2$-Al_3Zr nanoprecipitates within the grain are grouped in dendritic regions, as evidenced in the inset of Figure 5.9(b)), consistent with the peritectic solidification of dilute Al-Zr alloy causing Zr segregation in Zr-rich dendritic arms and Zr-poor interdendritic regions [92].

Figure 5.9(e) shows a STEM-EDX map taken after quenching the sample back to room temperature after 480 s at 400˚C. The ring-like features highlighted by the black arrows in Figure 5.9(a) are Mg- and O- rich oxides particles. Particles similar to the small dark precipitates highlighted in Figure 5.9(c) are enriched in Mg, F, and O. Although the source of the F is unknown, the particles are assumed to be oxides. The bright nanoparticles observed during the aging treatment are enriched in Zr. Crystallographic data was not obtained during this specific experiment, but given the crystallographic data obtained from the peak aged sample shown in Figure 5.7, they are assumed to be the metastable, $L1_2$-structured Al_3Zr.

Figure 5.9(c) presents a subsequent ADF-STEM image taken after an additional 600 s of exposure at 400˚C. Compared to Figure 5.9(b), there is a decrease in the number of grain-boundary Al_3Zr precipitates (in particular on the right grain boundary) which is associated with a growth of the Al_3Zr precipitate located in the lower right quadrant (black arrow). Also, a new acicular precipitate grew in the bottom left (white arrow), which may be the Al_3Zr with the stable $D0_{23}$ structure, identified based on its acicular geometry (but this was not confirmed via crystallographic analysis). Furthermore, an increase in the number of small (~10-20 nm in diameter) dark precipitates (highlighted by empty arrow) was observed. The increase in number of oxide particles during the experiment may be the result of the coarsening of existing oxide particles that make them more visible. Further aging at 500˚C was performed on the sample (Figure 5.9); only the disappearance of the intragranular Al_3Zr particles and growth of the acicular Al_3Zr precipitate were observed.

Figure 5.10 presents a second in-situ STEM experiment performed on a lamella taken from a fine-grained region of as-fabricated Al-3.60Mg-1.18Zr (wt.%, Batch 2). An ADF-STEM image of the room temperature condition is shown in Figure 5.10(a). Numerous primary $L1_2$-Al_3Zr precipitates are observed within the central grain. During the 64 min ramp to 350˚C, a grain boundary precipitate (unidentified) is observed to form at 200˚C and later disappears at 300˚C (not shown). Precipitate coarsening at the grain boundaries is assumed to occur faster due to short circuit diffusion on the boundaries. Figure 5.10(b) shows the ADF-STEM image taken after a 64 min ramp to 350˚C. Two horn-like features are observed growing from the corners of one of the Al_3Zr precipitates. The grain boundary also appears to shift from its initial position, before being pinned after the appearance of a dark particle (black arrow). The horn-like feature was observed to grow during the course of the 48 min of exposure at 350˚C (Figure 5.10(c)). A further movement of the grain boundary is observed to follow the horns. A high-resolution ADF-STEM image of the rightmost horn is shown in Figure 5.10(e). The horn is epitaxially grown from the Al_3Zr precipitate, with the corresponding FFT, shown in Figure 5.10(f), confirming the existence of 010- and 100- type superlattice reflections consistent with an $L1_2$ structure. The sample was subsequently heated to 500˚C, Figure 5.10(d). The horn-like features disappeared and the particle corners became rounded. Further heating to 600˚C induced additional coarsening (not shown).

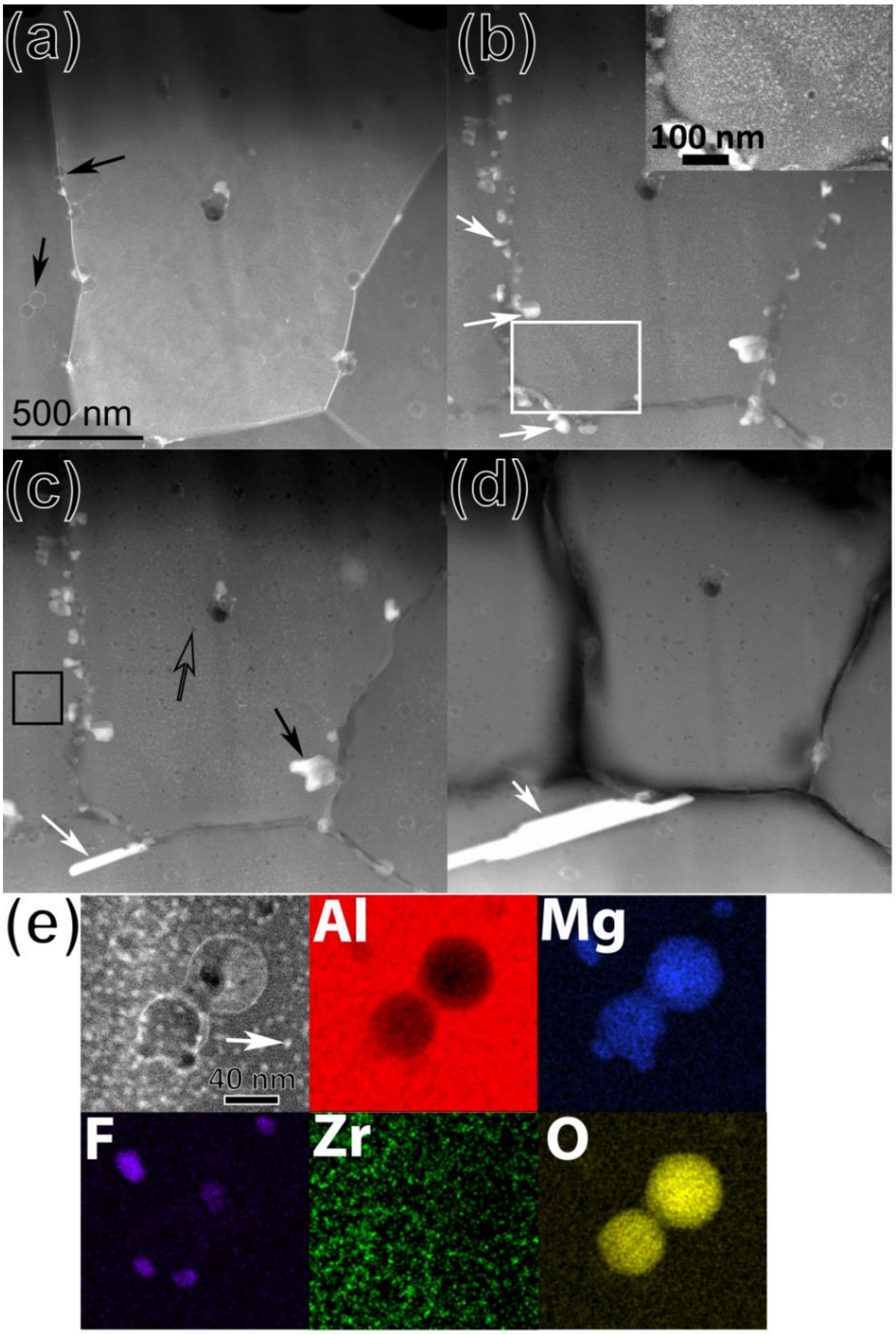

Figure 5.9: In-situ experiment of coarse-grain region of as-fabricated Al-3.60Mg-1.18Zr (wt.%), Batch 2. (a) ADF-STEM image of the region of interest prior to thermal exposure. Oxides are highlighted by black arrows. (b) ADF-STEM image after 420 s of exposure at 400°C showing Al$_3$Zr precipitates (white arrows) and nano-scale Al$_3$Zr precipitates within the grains, highlighted by the white box and enlarged in the inset. (c) ADF-STEM image after 1000 s of exposure at 400 °C. Coarsening of equiaxed L1$_2$-Al$_3$Zr precipitates at grain-boundary occurred (black arrow). An acicular precipitate expected to be D0$_{23}$-Al$_3$Zr is observed (white arrow). (d) ADF-STEM image after 30 s at 500ºC showing further growth of the acicular D0$_{23}$-Al$_3$Zr precipitate (white arrow) (e) Higher magnification ADF-STEM image and STEM EDX map of the region highlighted by the black box in (c). Two spherical Mg- and O-rich oxide particles are surrounded by much finer Al$_3$Zr nanoprecipitates (white arrow). Particles enriched with F and Mg are also observed, but of unknown origin. Chemical analysis was performed using the Zr-K, Al-K, Mg-K, F-K and O-K lines.

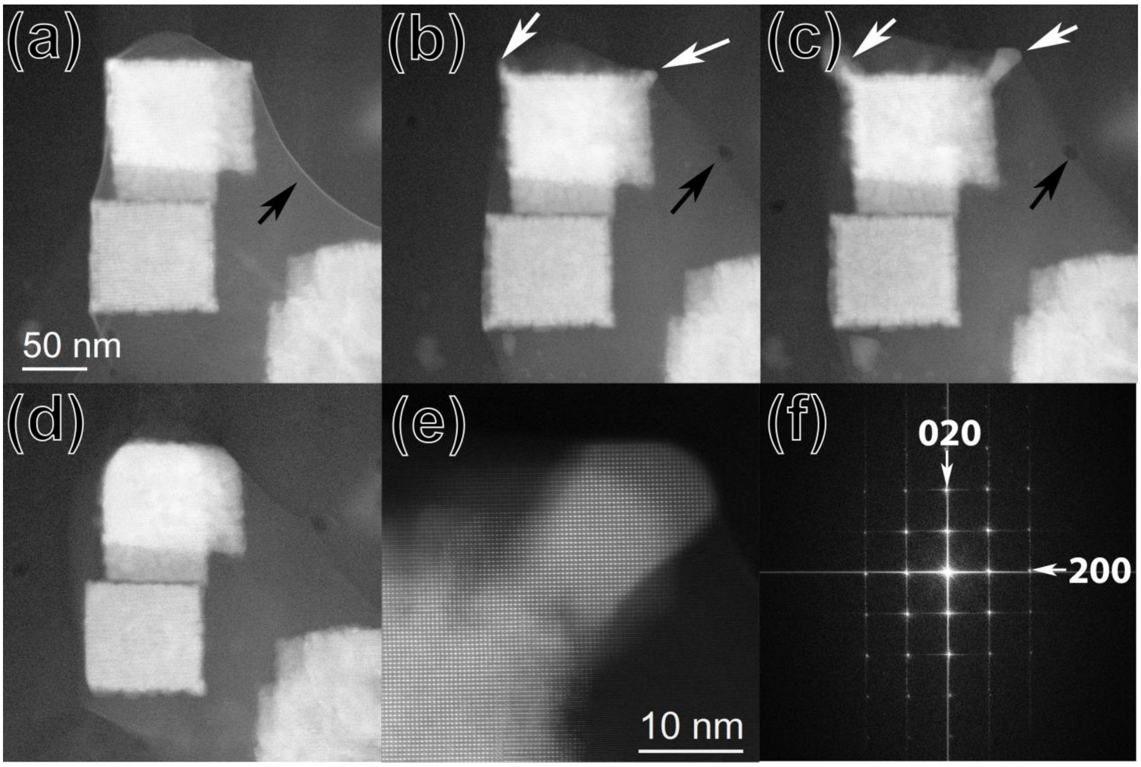

Figure 5.10: In-situ STEM heating experiment of a fine-grain region of as-fabricated Al-3.60Mg-1.18Zr (wt.%, Batch 2): (a) ADF-STEM image of the region of interest prior to thermal exposure (b) ADF-STEM image taken after a 64-min ramp to 350°C . Horns have grown on the nanoprecipitate corners (white arrow) and grain-boundary movement has occurred (black arrow) (c) ADF-STEM image taken after a subsequent 48 min-exposure at 350°C . Further growth of the horn features occurred. (d) ADF-STEM image taken after temperature was increased to 500°C during a 28-min ramp. The horns previously observed at 350°C disappeared at 450°C, during the ramp to 500°C. (e) High-resolution ADF-STEM image of a horn feature, from precipitate imaged in (c), showing epitaxial growth of a horn feature. (f) Diffraction pattern created by FFT of images (e) and (d), respectively) showing the 100- and 010-type superlattice reflections of the metastable $L1_2$ structure for Al_3Zr.

5.4 Microstructural Evolution

After peak aging, grain boundary Al_3Zr particles, fine Al_3Zr nanoprecipitates within the grains, and line-like Al_3Zr precipitates within the grains are observed (Figure 5.6). Mikhaylovskaya et al. [114] observed line-like Al_3Zr precipitates, similar to those in Figure 5.7, after annealing a cast Al-3Mg-0.25Zr (wt.%) alloy for 8 h at 360°C . Similar filamentary morphology has been observed in many other Al-Zr alloys and is commonly referred to as discontinuous precipitation [114–116]. Phases which are continuously precipitated within a supersaturated crystalline matrix tend to be uniformly distributed throughout the matrix, and typically have equiaxed, plate- or rod-like shapes showing crystallographic relationships with the matrix; the spherical, coherent Al_3Zr precipitates shown in the upper half of Figure 5.7(a) are a good example of such continuous precipitates. By contrast, discontinuous precipitation is a form of grain-boundary precipitation that results in colonies of thin lamellar or filamentary precipitates, extending from grain boundaries into the grains, often with a much higher aspect ratio than continuously precipitated rods or plates. Nes and Billdal studied Al_3Zr precipitation in Al-0.8Zr (wt.%) alloys and proposed that grain-boundary movement into a supersaturated matrix was responsible for the lamellar discontinuous precipitation [115]. In this mechanism, Al_3Zr precipitation initiates at the grain boundary. Since grain boundary diffusion is faster than bulk diffusion, Zr diffuses to the existing precipitates *via* the grain boundaries. As the precipitates grow, they drag the grain boundary into the supersaturated matrix resulting in lamellar growth and a bowed grain boundary. The driving force for this acicular growth results from surface energy minimization between the Al_3Zr precipitates, the supersaturated matrix, and the depleted matrix. The surface energy between the Al_3Zr and the supersaturated matrix is the highest, hence the system minimizes this surface.[115]

As seen in Figure 4.7, there are numerous precipitates other than Al_3Zr present in the as-fabricated condition. Mg- and O-rich particles are observed and are likely oxides from either the powder surface or in-process oxidation. Also, Mg- and Si-rich particles are located both within the grains and on grain boundaries. Finally, Fe-rich particles are dispersed along the grain boundaries. Silicon and iron are common impurities present in aluminum alloys: Fe has very low solubility in Al and thus precipitates as Fe-rich intermetallic phase, while Si has a higher solubility in Al, but, in the presence of Mg, it precipitates as the Mg_2Si phase [93]. While the aforementioned elements are impurities and their concentration is kept low, they still play a significant role in mechanical properties as they likely lead to grain boundary pinning. After thermal aging, it was observed that these impurity grain-boundary precipitates coarsen, which effectively reduce their ability to pin grain boundaries. The Fe-rich grain-boundary particles show a significant reduction in number density and increase in size in the peak-aged condition as compared to the as-fabricated condition.

Both grain-boundary Al_3Zr and continuous Al_3Zr precipitation, but not discontinuous Al_3Zr precipitation, were observed during the in-situ STEM experiment of the coarse grain region (Figure 5.9). The lack of discontinuous Al_3Zr precipitation observed in situ may be due to the limited number of grains examined during the experiment (not all grains have discontinuous precipitation). Also, the contribution of surface diffusion of the thin lamella sample may alter the precipitation behavior by increasing the kinetics of the continuous Al_3Zr precipitation. Furthermore, the finite volume associated with a thin lamella will result in less Zr being available for precipitation. Grain-boundary Al_3Zr precipitates were observed to coarsen during the 400˚C exposure and once a temperature of 500˚C was reached, only one Al_3Zr particle remained in view (Figure 5.9(d)). Grain-boundary particle coarsening during thermal exposure will reduce the boundary pinning which, as described later, will have implications on the mechanical properties. The oxide inclusions remained stable even at temperatures of 500˚C, which suggest they play a critical role at impeding grain growth during 400˚C aging [67].

Primary Al_3Zr precipitate stability and coarsening behavior was studied in the second in-situ STEM experiment (Figure 5.10). Horn-like features were observed growing from a primary Al_3Zr precipitate. Corner growth of precipitates has been observed for $L1_2$-Al_3Zr [117], and $L1_2$-Al_3Sc [118] growing from the liquid and $L1_2$-Ni_3Al [119] precipitates growing from solid solution within a Ni(Al) matrix. Preferential corner growth of cuboidal precipitates exists for Ni_3Al precipitates with positive misfits (larger lattice parameter for precipitate than matrix) in Ni-base superalloys [119]. In the case where there is a positive misfit, as is the case with Al_3Zr in an Al matrix, the compressive stresses on the precipitate are at a minimum in the <111> direction which therefore becomes the favorable growth direction [119]. The low strain also allows for a more favorable diffusion path resulting in further <111> growth [119]. Haugan et al. observed Al_3Zr precipitates with a dendritic appearance in an Al-1.4Zr (wt.%) alloy cooled at intermediate cooling rates (~200˚C/s). Precipitates with a dendritic appearance have also been observed in our alloy (shown in Figure 4.9). Hyde et al. observed the same behavior for Al_3Sc precipitates in a Al-0.7Sc (wt.%) alloy cooled at 1000˚C/s and attributed the corner growth due to the large constitutional undercooling gradients that are present at the cube corners compared to the cube faces. In the in-situ experiment shown in Figure 5.10, it is likely that the corner growth mechanism observed previously for Ni_3Al precipitates is active since the other mechanisms are operative during solidification rather than in the solid state. The horn-like features eventually disappeared at 450˚C and this may be due to dissolution into the matrix and/or re-precipitation to nearby coarsening precipitates. Interestingly, the grain boundary that was pinned earlier in the experiment (Figure 5.10 (b)) by the dark particle still remains pinned even at a temperature of 500˚C (Figure 5.10(c)). This is direct evidence for impurity particles effectively pinning grain boundaries during elevated temperature exposure.

5.5 Conclusions

The microstructural response to aging was investigated in Al-3.6Mg-1.18Zr (wt.%) processed by L-PBF. It was concluded that:

- The grain microstructure of the as-fabricated samples consists of fine-grained regions with sub-micron equiaxed grains, and coarse-grain regions of columnar grains 1 to 5 µm in width and up to 40 µm in length. Submicron precipitates - including Fe-rich particles, Mg_2Si particles, and Al_3Zr - are observed at the grain-boundaries of the alloys in the as-fabricated and peak-aged (400˚C, 8 h) conditions.

- Both continuous and discontinuous precipitation of coherent, secondary $L1_2$-Al_3Zr occurs during peak aging (400˚C, 8 h). The continuous precipitates are spheroidal (~2 nm in diameter) and the discontinuous precipitates are highly elongated (~5 nm wide and hundreds of nanometers in length).
- In-situ STEM experiments on a thin lamella from the coarse grain region (with no primary Al_3Zr particles) showed that aging for 480 s at 400˚C results in grain boundary Al_3Zr, 100 nm wide, and intragranular nanometer-sized spherical Al_3Zr located in Zr-rich dendritic arms. Aging for an additional 600 s at 400˚C resulted in a near disappearance of intragranular Al_3Zr, coarsening of Al_3Zr grain boundary precipitates, and the formation of an acicular Al_3Zr precipitate indicative of the equilibrium $D0_{23}$ structure. At 500˚C the only second phases remaining were an acicular precipitate believed to be of the $D0_{23}$ structure and oxides.
- Coarsening of the primary $L1_2$-structured Al_3Zr precipitates behaves similarly to positive misfit Ni_3Al in Ni base superalloys where growth occurs on the particle corners, resulting in horn-like features.

Chapter 6 Addalloy Mechanical Properties

6.1 Room Temperature Mechanical Properties

Yield and Ultimate tensile strengths of as-fabricated and as-fabricated rescanned Al-3.60Mg-1.18Zr (wt. %, Batch 1) and Al-3.66Mg-1.57Zr (wt.%, Batch 2) samples are shown in Figure 6.1a. The as-fabricated Al-3.60Mg-1.18Zr (wt. %, Batch 1) samples had transverse and parallel yield strengths of 220 and 221 MPa, respectively. The as-fabricated Al-3.66Mg-1.57Zr (wt.%, Batch 2) samples exhibited higher yield strengths of 290 and 282 MPa in the transverse and parallel orientation, respectively. Laser rescanning had minimal influence on the yield strengths for both alloys. The rescanned Al-3.60Mg-1.18Zr (wt. %, Batch 1) samples had transverse and parallel yield strengths of 229 and 227 MPa, respectively. The rescanned Al-3.66Mg-1.57Zr (wt.%, Batch 2) samples exhibited yield strengths of 284 and 288 MPa in the transverse and parallel orientation, respectively. Elongation at fracture for as-fabricated and rescanned Al-3.60Mg-1.18Zr (wt. %, Batch 1) and Al-3.66Mg-1.57Zr (wt.%, Batch 2) samples is shown in Figure 6.1b. Unlike the yield strengths, there is a slight anisotropy in elongation between the transverse and parallel testing orientations. The as-fabricated Al-3.60Mg-1.18Zr (wt. %, Batch 1) samples had transverse and parallel elongations of 29.1 and 25.6 %, respectively. The as-fabricated Al-3.66Mg-1.57Zr (wt.%, Batch 2) samples exhibited lower elongations of 25.2 and 24.0 % in the transverse and parallel orientation, respectively. Rescanning had negligible effect on the elongations for both alloys tested in the transverse orientation, but rescanned samples had the lowest ductility when tested in the parallel orientation: 19.3 % for Al-3.66Mg-1.57Zr (wt.%, Batch 2) samples and 22.0 % for Al-3.60Mg-1.18Zr (wt. %, Batch 1) samples.

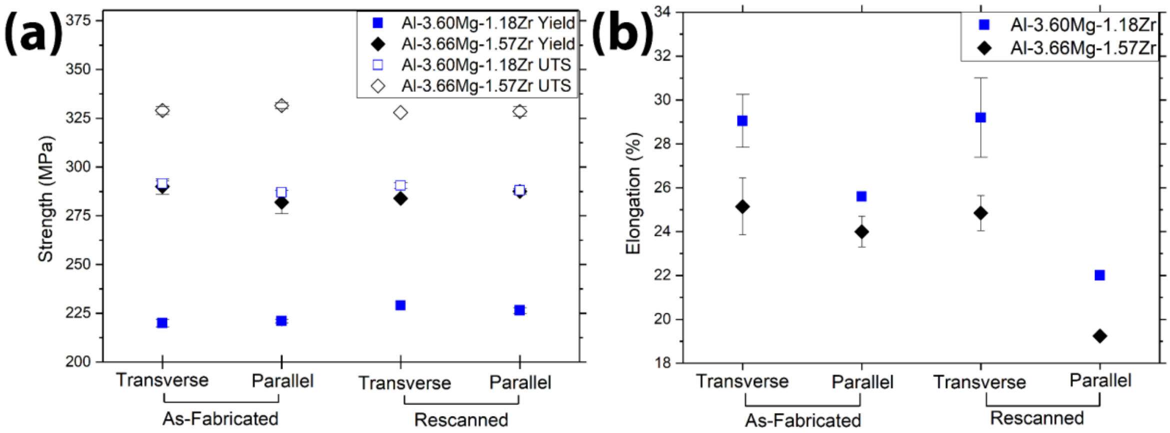

Figure 6.1: (a) Yield and ultimate tensile strength (UTS) strength (MPa) of as-fabricated and as-fabricated rescanned Al-3.60Mg-1.18Zr (wt. %, Batch 1) and Al-3.66Mg-1.57Zr (wt.%, Batch 2) samples. (b) Elongation at fracture. Each data point is the mean of two test samples. Error bars represent the standard error of the mean.

Yield and ultimate tensile strengths of peak aged (both 2 h and 8 h, 400°C) Al-3.60Mg-1.18Zr (wt. %, Batch 1) and (2 h, 400°C) Al-3.66Mg-1.57Zr (wt.%, Batch 2) samples are shown in Figure 6.2a. The peak aged Al-3.60Mg-1.18Zr (wt. %, Batch 1) had yield strengths ~125 MPa higher than in the as-fabricated condition and the peak aged Al-3.66Mg-1.57Zr (wt.%, Batch 2) samples had yield strengths ~60 Mpa higher than in the as-fabricated condition. There was minimal difference in yield strength between Al-3.60Mg-1.18Zr samples aged for 2 h (first peak) and 8 h (second peak): 349 and 351 MPa in the transverse orientation, respectively. The peak aged higher Zr content alloy, Al-3.66Mg-1.57Zr (wt.%, Batch 2), had higher yield strengths than the lower Zr alloy in the transverse orientation (359 MPa), but lower yield strength when tested in the parallel orientation (337 MPa). Overall, the difference between the orientations and alloys only represent a 22 MPa maximum spread. The elongation at fracture of the two alloys (Figure 6.2b) was reduced compared to the as-fabricated elongations at fracture. Again, there was a slight anisotropy present in the elongation values; the Al-3.66Mg-1.57Zr (wt.%, Batch 2) samples had transverse and parallel orientation elongations at fracture of 20 and 15.8%, respectively. This represents a ~5 % (25 to 20%) and a ~3 % (19 to 16 %) drop when compared to the as-fabricated Al-3.66Mg-1.57Zr (wt.%, Batch 2) samples tested in the transverse and parallel orientations, respectively.

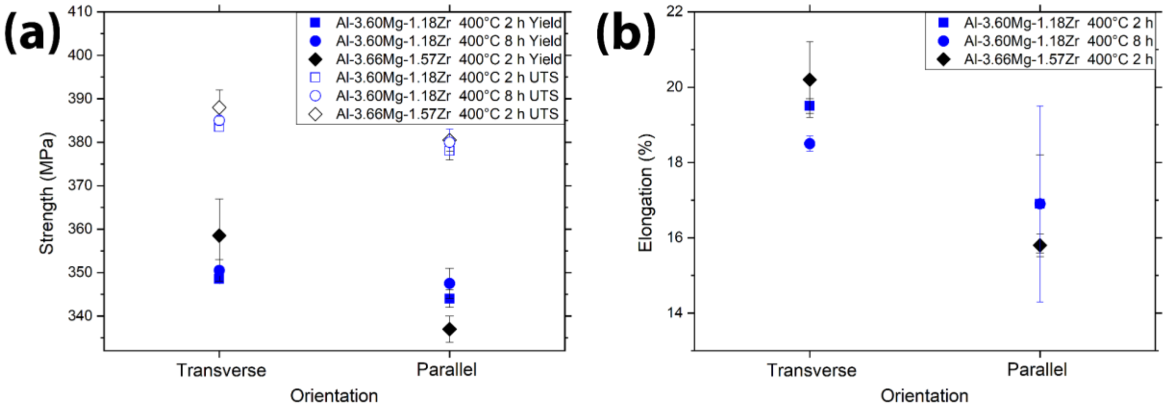

Figure 6.2: (a) Yield and Ultimate tensile (UTS) strength (MPa) of peak-aged Al-3.60Mg-1.18Zr (wt. %, Batch 1) and Al-3.66Mg-1.57Zr (wt.%, Batch 2) samples. (b). Elongation at fracture. Each data point is the mean of two test samples. Error bars represent the standard error of the mean.

6.2 Elevated Temperature Mechanical Properties

6.2.1 Elevated Temperature Yield Strength

The temperature-dependence of the yield strength is shown in Figure 6.3 for Al-2.90Mg-2.10Zr (wt.%, Batch 3), in the as-fabricated, peak-aged, and overaged states. Each data point represents one test. Tests were performed on single samples (transverse orientation), from the highest to the lowest temperature. The peak-aged samples (400°C / 8h) exhibit the highest room-temperature yield strength (330 MPa) but lower strengths as compared to the as-fabricated sample at temperatures at and above 150°C, dropping to 24 MPa at 260˚C. The alloy in the overaged state (aged at 400˚C for 60 h, corresponding to a 10% drop from peak-hardness [67]) shows a lower room-temperature strength (300 MPa) as compared to the peak-age state; this difference is maintained up to 150 ˚C (173 MPa), but disappears above that temperature. Interestingly, the as-fabricated samples, which have a lower room-temperature strength (295 MPa) than the aged samples, have far superior strength at elevated temperatures (87 MPa at 260˚C).

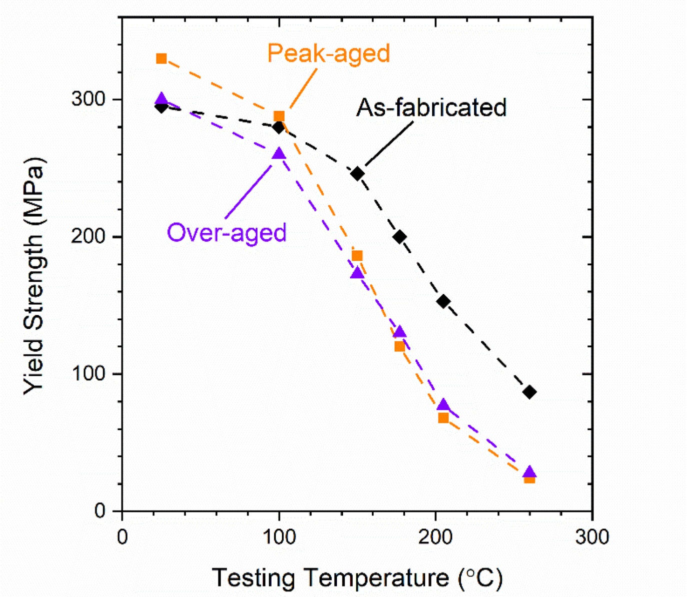

Figure 6.3: Temperature dependence of yield strength for the high-Zr alloy, Al-2.90Mg-2.10Zr (wt. %, Batch 3), in three conditions: as-fabricated, peak-aged (400ºC, 8 h), and over-aged (400ºC, 60 h). Tests were performed on single samples (transverse orientation), from the highest to the lowest temperature.

Additional full (pull to fracture) elevated temperature tensile tests on as-fabricated and peak-aged Al-2.90Mg-2.10Zr (wt.%, Batch 3) samples fabricated on the Sisma are shown in Figure 6.4. The trend of peak-aged samples having lower strength at elevated temperatures than as-fabricated samples is identical to that presented in Figure 6.3. Despite being fabricated with different parameters on different machines and having a different test methodology, the yield strengths nearly the same as the results presented in Figure 6.3.

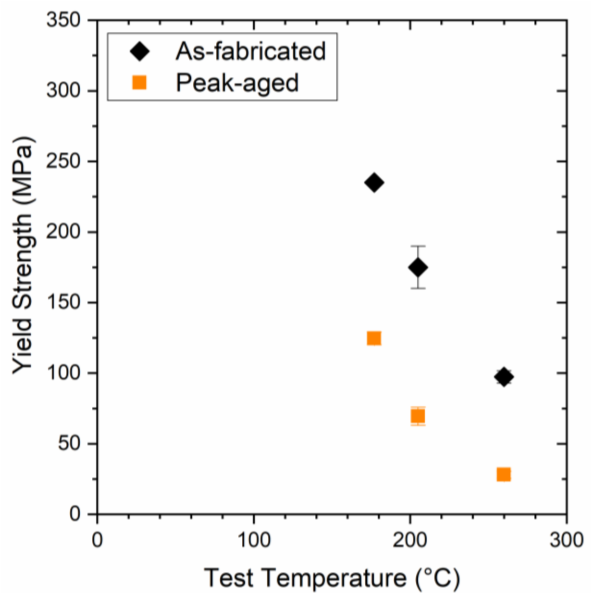

Figure 6.4: Temperature dependence of yield strength for the Sisma fabricated high-Zr alloy, Al-2.90Mg-2.10Zr (wt. %, Batch 3), in two conditions: as-fabricated, and peak-aged (400ºC, 7 h). Tests were performed to fracture on single samples (parallel orientation). Each point represents the mean. Error bars represent the standard error of the mean.

6.2.2 Creep Testing

Results of creep testing at 260°C (total creep duration t_c = 168 h and t_c = 8 h) of as-fabricated, peak-aged, and under-aged high Zr-alloy (Al-2.90Mg-2.10Zr, wt.%, Batch 3) samples are shown in Figure 6.5, in double-logarithmic plots of secondary strain rate vs. stress. A displacement vs. time plot for the as-fabricated sample crept for 168 h is shown in Figure 6.6 as an example. For the long duration creep tests (168 h), tensile loading started at ~5 MPa and was incrementally increased; no deformation was measured within the first 120 h, until a stress of 15 MPa was reached for the peak-aged condition. The short duration tests (8 h) were started with a ~25 MPa, load, which was incrementally increased every 30 min so that the full test was concluded within 8 h. In Figure 6.5, the 25 MPa point is not marked, since no strain was observed within the 30 min duration of this first step. For the two lowest stress/strain rate data points (as-fabricated, t_c = 8 h) plotted on Figure 6.5 - for 48 and 58 MPa - steady-state deformation may not have been achieved. The strain rates plotted in Figure 6.5 might thus be overestimated.

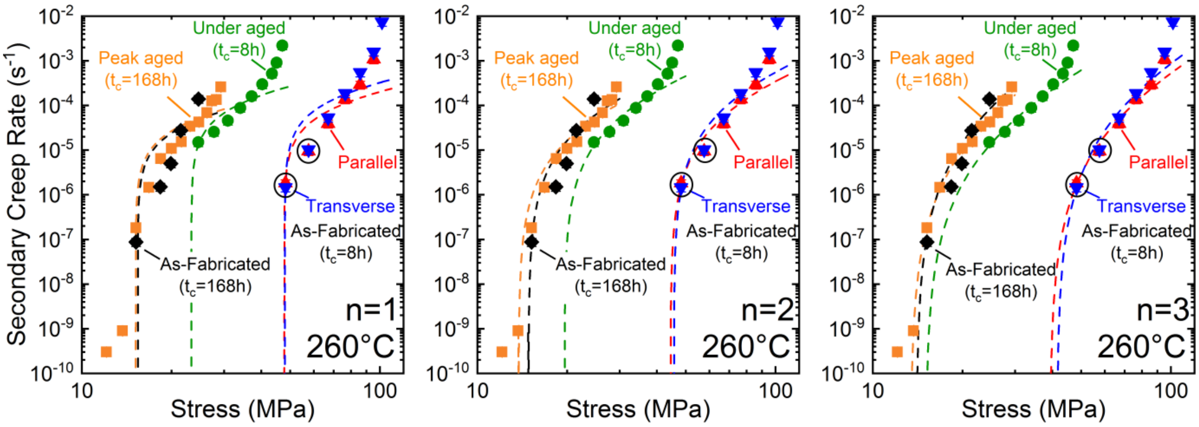

Figure 6.5: Double logarithmic plot of secondary creep rate vs. stress for creep testing at 260˚C of high-Zr alloy, Al-2.90Mg-2.10Zr (wt.%, Batch 3) in three conditions: as-fabricated, under-aged (260˚C , 168 h), peak-aged (400˚C , 8 h); total creep time is given in parentheses. Data for the as-fabricated state, with a short total creep time of 8 h, were collected by increasing the stress every 30 min, so that steady-state strain rate may not have been achieved at the two lowest strain rates (which are marked with black circles).

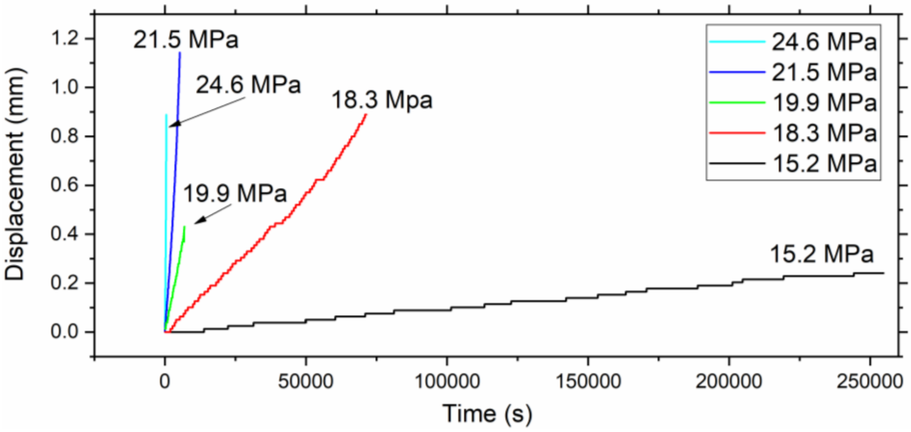

Figure 6.6: Displacement vs. time plot for the as-fabricated sample (Al-2.90Mg-2.10Zr, wt. %, Batch 3) crept tested to fracture at 260 ˚C for 168 h.

The very high stress sensitivity of strain rate in Figure 6.5 is indicative of a threshold stress, likely due to the presence of precipitates. In order to estimate the threshold stress, we used a modified version of the Mukherjee-Bird-Dorn power-law equation for the minimum strain rate ε̇:

$$\dot{\varepsilon} = A\left(\sigma - \sigma_{th}\right)^{n} \exp\left(\frac{-Q}{k_B T}\right) \qquad 23$$

where A is a constant, σ is the applied stress, σ_{th} is the threshold stress, n is the matrix stress exponent (n indicates the creep mechanism), Q is the matrix creep activation energy, k_B is the Boltzmann constant, and T is the absolute temperature. A best-fit procedure was employed to estimate the threshold stress, using stress exponents of $n = 1$ (diffusional creep), n = 2 (GBS) and $n = 3$ (viscous glide), which correspond to the rate-controlling mechanisms most likely for this alloy. It is apparent from Figure 6.5 that n = 2 and 3 both give satisfactory fit over many orders of magnitudes in strain rates.

The threshold stress for the peak-aged condition (aged 400˚C for 8 h) crept for a long duration (168 h) was determined to be 13.4 MPa from fitting the data with a stress exponent of n = 3, and 13.7 MPa for n = 2. The as-fabricated condition crept for a long duration (168 h) displayed a threshold stress of 14.0 MPa (n = 3) and 14.8 MPa (n = 2). The as-fabricated samples crept at high loads for short durations (8 h) displayed significantly higher threshold stresses, 39.3 and 41.5 MPa in the parallel and transverse direction, respectively (n = 3), and 44.4 and 45.6 MPa in the parallel and transverse direction, respectively (n = 2). Again, no significant difference exists in the creep resistance of samples loaded parallel or transverse to the build direction, consistent with isotropic mechanical properties. Finally, the under-aged sample (aged at 260 ˚C for 168 h), shows a low threshold stress of 15 MPa (n = 3) and 20 MPa (n = 2), however this test started with a stress of ~25 MPa with a steady-state strain rate already above 10^{-5} s^{-1}, so the accuracy of the threshold stress is lower than for the other tests.

6.2.3 Microstructure of Crept samples

Two as-fabricated samples, fractured after creep at 260˚C for 8 and 168 h respectively, were chosen for further microstructural investigation, as they represent two extreme states in the creep data.

Fractography, shown in Figure 6.7, of the fracture faces of both samples revealed the presence of dimple features indicative of micro-void coalescence during ductile fracture. In a minority of the fracture surface, regions of intergranular fracture were also observed. No significant differences were observed between the two fracture faces.

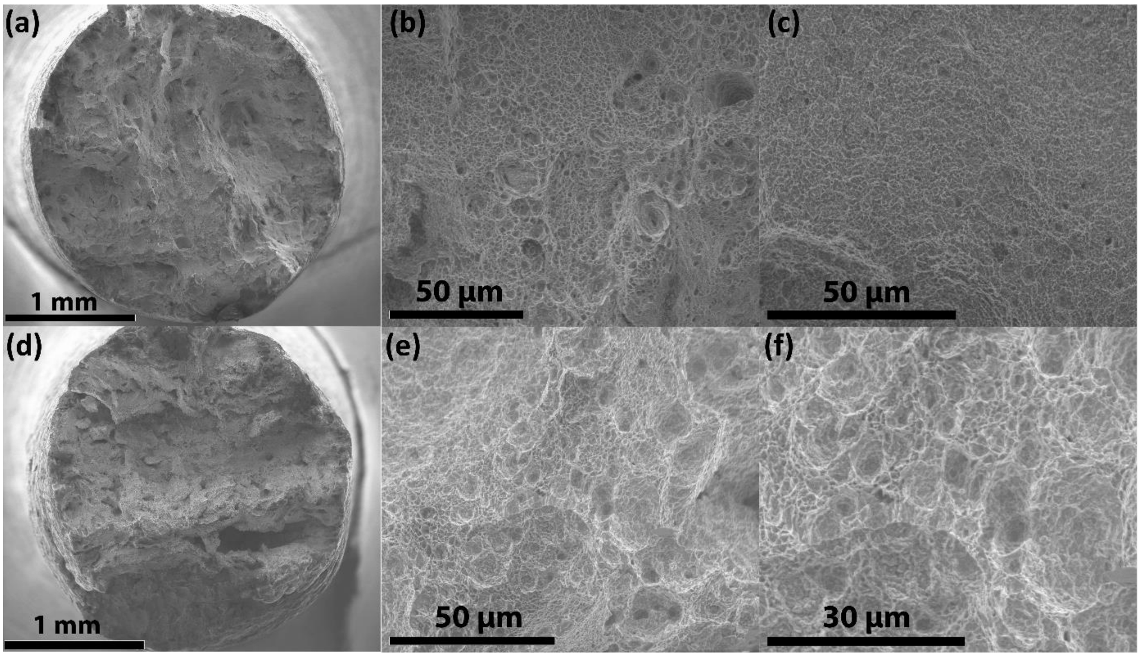

Figure 6.7: a,b,c) SE SEM images of the fracture surface of the as-fabricated sample (Al-2.90Mg-2.10Zr, wt. %, Batch 3, vertical direction) crept at 260 ˚C for 8 h. a.) Overview of fracture face. b.) higher magnification image showing dimples indicative of ductile fracture via microvoid coalescence. c.) Higher magnification image showing a region with the appearance of intergranular fracture. d,e,f) SE SEM images of the fracture surface of the as-fabricated sample (Al-2.90Mg-2.10Zr, wt. %, Batch 3, vertical direction) crept at 260 ˚C for 168 h. d.) Overview of fracture face. e.) Higher magnification image showing dimples indicative of ductile fracture via microvoid coalescence f.) Higher magnification SE image showing dimples.

Metallographic cross sections of the as-fabricated samples (Al-2.90Mg-2.10Zr, wt. %, Batch 3, vertical direction) crept at 260˚C for 8 and 168 h were prepared (approximately center of the cylinders) in order to investigate the microstructural response to creep. Figure 6.8 (a,b,c) shows SE and BSE images of the microstructure near the fracture face of the as-fabricated sample crept at 260 ˚C for 8 h. Figure 6.9 (a,b) shows BSE images of the microstructure in the threads of the as-fabricated sample crept at 260 ˚C for 8 h for a comparison to material that has not been strained. The fracture appears to be predominately confined to the fine grain regions. No significant differences were observed between the microstructure of the threads and the microstructure near the fracture face, except for an increase in voids in the gauge section that are likely the result of micro-void coalescence. No significant increase in grain size or grain elongation was observed, albeit the small grain size, low image contrast, and lack of EBSD data, does not exclude that there were grain size changes.

Figure 6.8 (d,e,f) shows SE and BSE images of the microstructure near the fracture face of the as-fabricated sample crept at 260 ˚C for 168 h. Figure 6.9 (c,d) shows BSE images of the microstructure in the threads of the as-fabricated sample crept at 260 ˚C for 168 h for a comparison to material that has not been strained. Similar to the 8 h crept sample, the fracture appears to be predominately confined to the fine grain regions. No significant differences were observed between the microstructure of the threads and the microstructure near the fracture face, except for an increase in voids in the gauge section that are likely the result of micro-void coalescence. Several large (hundreds of microns in size) voids were observed in the sample crept for 168 h. These large voids (highlighted by the black arrow in Figure 6.8(d)) are likely the result of micro-void coalescence. In general the voids are larger and more numerous than in the sample crept for 8 h. No significant increase in grain size or grain elongation was observed, albeit the small grain size, low image contrast, and lack of EBSD data, does not exclude that there were grain size changes. Numerous black sub-micron particles were observed in the sample crept at 168 h (Figure 6.8(f) white arrow). More detailed analysis of these particles are in the STEM analysis below.

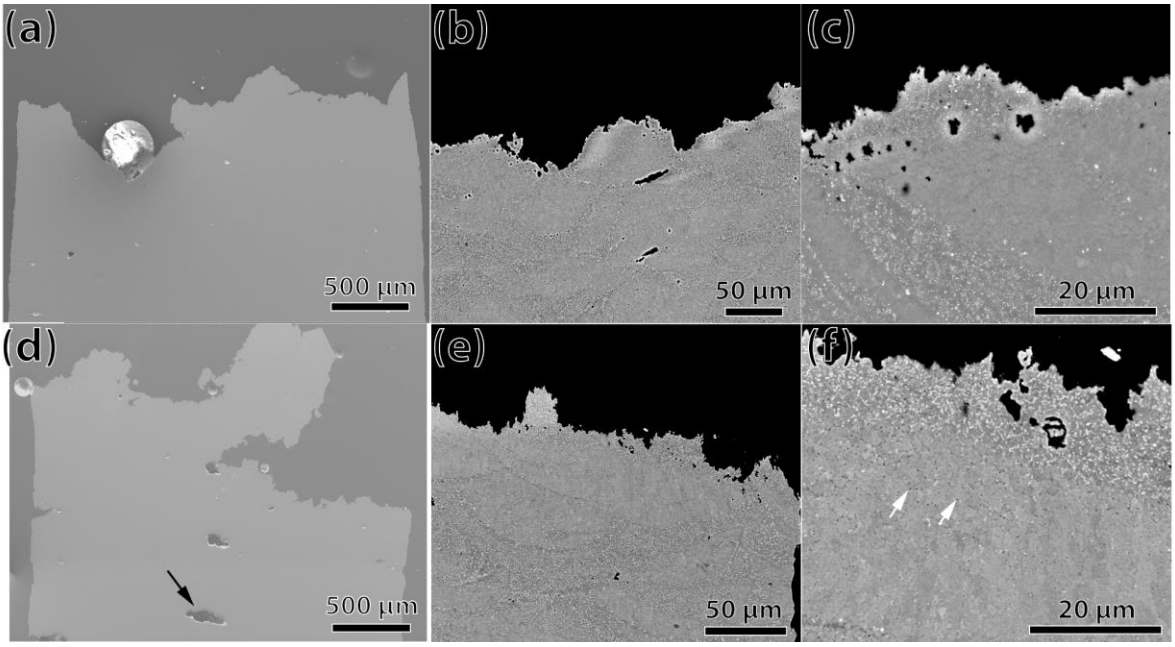

Figure 6.8: a,b,c) SEM images of a cross-section of the as-fabricated sample (Al-2.90Mg-2.10Zr, wt. %, Batch 3, vertical direction) crept at 260 ˚C for 8 h. a.) SE image overview b.) BSE image showing the microstructure next to the fracture c.) Higher magnification BSE image of (b). d,e,f) SEM images of the cross section of the as-fabricated sample (Al-2.90Mg-2.10Zr, wt. %, Batch 3, vertical direction) crept at 260 ˚C for 168 h. d.) SE image overview. Black arrow highlights a large void. e.) BSE image showing the microstructure at the fracture f.) Higher magnification BSE image of (e). White arrows point to sub-micron grain boundary particles.

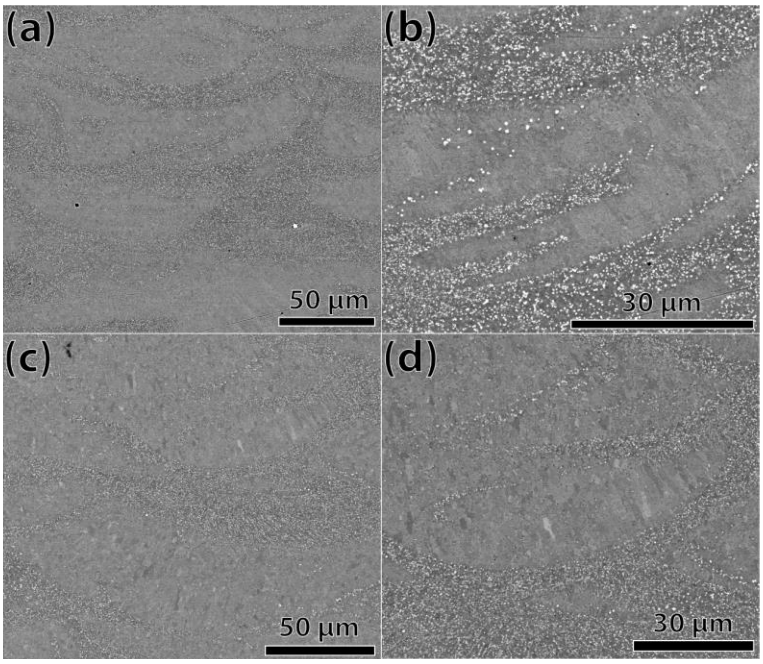

Figure 6.9: a,b) BSE images showing the microstructure in the threads of the as-fabricated sample (Al-2.90Mg-2.10Zr, wt. %, Batch 3, vertical direction) crept at 260 ˚C for 8 h. c,d) BSE images showing the microstructure in the threads of the as-fabricated sample (Al-2.90Mg-2.10Zr, wt. %, Batch 3, vertical direction) crept at 260 ˚C for 168 h.

Figure 6.10 displays ADF-STEM images and corresponding STEM-EDX maps from the coarse-grain regions of the fractured, as-fabricated samples crept for 8 h (Figure 10a) and 168 h (Figure 6.10b). The first specimen (as-fabricated and crept for 8 h) exhibits four types of precipitates: (i) Mg- and O-rich particles, ~50-100 nm in diameter, which are located both within the grains and at grain boundaries (ii) Mg- and Si-rich precipitates, ~50-100 nm in diameter, which are located both within the grains and at grain boundaries, (iii) Fe-rich precipitates, ~20-80 nm diameter, on the grain boundaries, (iv) discontinuous Al_3Zr precipitation (shown more clearly in Figure 6.11). The other specimen (as-fabricated and crept for 168 h) displays the same precipitates mentioned above, but with larger sizes and lower number density, except for the discontinuous Al_3Zr precipitates: the Mg- and O-rich particles are ~50-100 nm in diameter, the Mg- and Si-rich precipitates at grain boundaries are ~70-180 nm in diameter, and the grain-boundary Fe-rich precipitates are ~50-100 nm diameter.

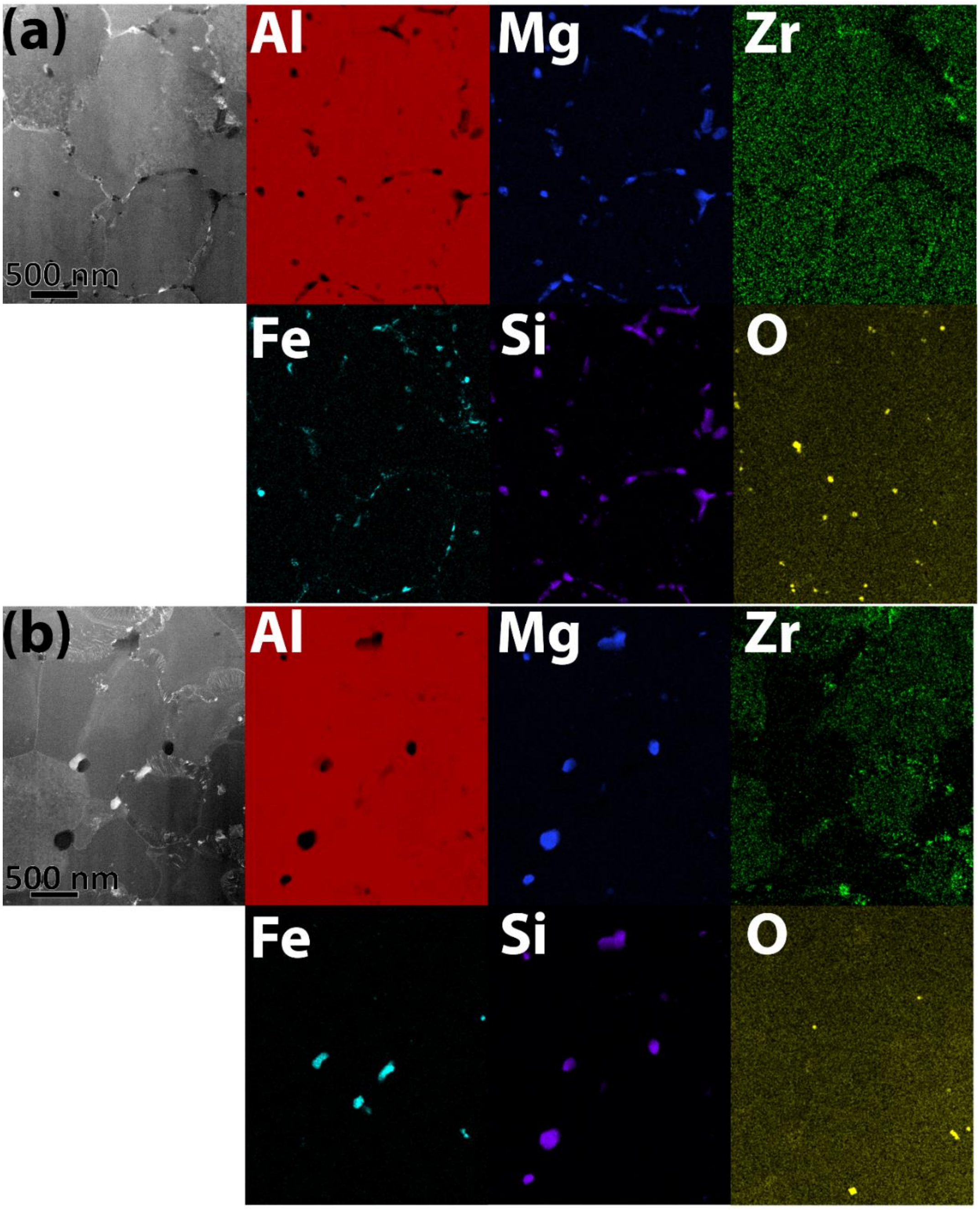

Figure 6.10: a.) ADF-STEM image and elemental STEM-EDX maps of the coarse-grain region (transverse microstructure) of an as-fabricated sample (Al-2.90Mg-2.10Zr, wt. %, Batch 3, vertical direction) crept-tested to fracture at 260˚C for 8 h. b.) ADF-STEM image and elemental STEM-EDX maps of the coarse-grain region (transverse microstructure) of an as-fabricated sample (Al-2.90Mg-2.10Zr, wt. %, Batch 3, vertical direction) crept-tested to fracture at 260˚C for 168 h. The Fe-rich and Mg+Si-rich precipitates are significantly larger and fewer in the long-duration creep sample when compared to the short-duration creep sample.

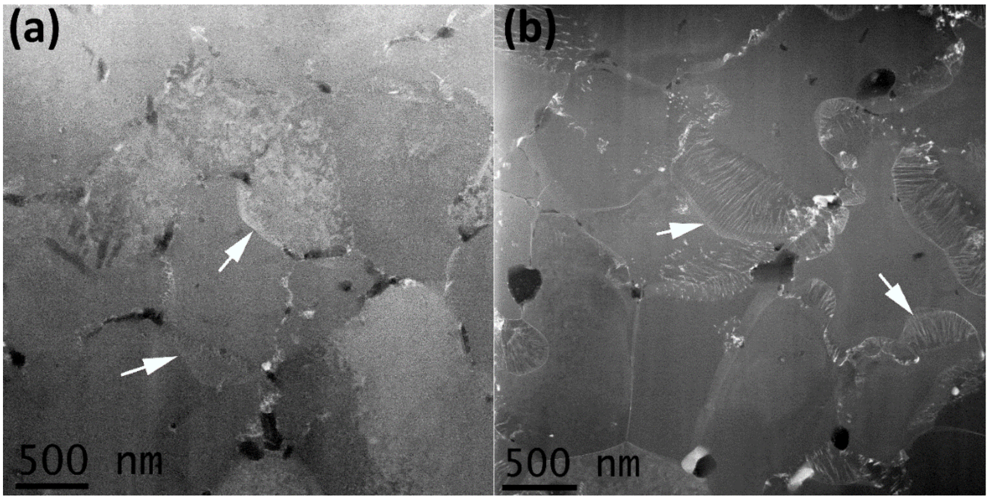

Figure 6.11: a.) ADF-STEM image of the coarser-grain region (transverse microstructure) of an as-fabricated sample (Al-2.90Mg-2.10Zr, wt. %, Batch 3, vertical direction) crept-tested to fracture at 260 ˚C for 8 h. b.) ADF-STEM image of the coarse-grain region (transverse microstructure) of an as-fabricated sample (Al-2.90Mg-2.10Zr, wt. %, Batch 3, vertical direction) crept-tested to fracture at 260 ˚C for 168 h. Discontinuous Al_3Zr precipitation was observed in both samples (white arrows), but the 168 h crept sample had significantly more discontinuous Al_3Zr precipitation.

6.3 Discussion

6.3.1 Room Temperature Mechanical Properties

Yield strengths of as-fabricated Al-3.60Mg-1.18Zr (wt. %, Batch 1) and Al-3.66Mg-1.57Zr (wt.%, Batch 2) samples do not significantly differ between testing orientations (Figure 6.1). The isotropic behavior is likely due to the bi-modal grain structure of the as-fabricated alloys. The as-fabricated yield strengths for the higher Zr alloy were ~ 60 – 70 MPa higher than that of the lower Zr alloy. One possible explanation for the higher yield strengths of the as-fabricated high-Zr alloy could be increased fraction of smaller equiaxed grains (strengthening via Hall-Petch) resulting from greater Al_3Zr inoculation. In aluminum casting it is known that increasing the concentration of grain refiners (Ti, B) will lead to a decrease in grain size due to inoculation [120]. Further detailed EBSD studies would be required to quantify the grain size of the between the two alloys to determine if there is a significant refining effect from the greater Zr content. Another possible explanation for the higher yield strength of the high-Zr alloy is increased solid solution strengthening of the Zr that is trapped in the coarse grain region. The Zr atomic radii is 74% larger than that of Al, meaning that lattice distortion and thus potency of solid solution strengthening would be significant.

Slight anisotropic behavior exists for the elongation at fracture for the as-fabricated Al-3.60Mg-1.18Zr (wt. %, Batch 1) samples but no significant anisotropic behavior exists for the as fabricated Al-3.66Mg-1.57Zr (wt.%, Batch 2) samples. One possible explanation for the reduced ductility of samples tested in the parallel orientation is lack of fusion defects that are generally orientated perpendicular to the building direction. Increased inclusion content is known to reduce ductility in metals [121]. Defects with the long axis perpendicular to the testing orientation will have an increased stress concentration factor that could lead to increased void formation during final stages of fracture.

In comparison to common AM-processable aluminum alloys, such as AlSi10Mg, the Al-Mg-Zr alloys display far greater ductility. Read et al. performed tensile tests on as-fabricated L-PBF AlSi10Mg samples and obtained yield strengths of ~250 MPa and elongations of ~1.5 % in the transverse orientation. The as-fabricated AlSi10Mg yield strength lies between the two Al-Mg-Zr alloys we tested (220 MPa for the Al-3.60Mg-1.18Zr (wt. %, Batch 1) samples, and 290 MPa for the Al-3.66Mg-1.57Zr (wt.%, Batch 2 samples), but the elongation to fracture is nearly 30 times lower than for the as-fabricated Al-Mg-Zr alloys.

The combination of high strength and high ductility of the as-fabricated Al-Mg-Zr alloys can be attributed to the bimodal microstructure. Bi-modal microstructures are known to display high strengths and high ductilities due to strain-gradient induced work hardening that delays the onset of necking [122]. Y. Zhao studied bimodal structured Cu alloys and found that both yield strength and ductility follow the rule-of -mixtures [123]. It is unknown if this is the case for the Al-Mg-Zr alloys, but this could help explain the observed variations in strength, as discussed later.

Yield strengths of as-fabricated rescanned Al-3.60Mg-1.18Zr (wt. %, Batch 1) and Al-3.66Mg-1.57Zr (wt.%, Batch 2) samples did not differ from that of the single scanned as-fabricated samples. In the transverse orientation, the elongation at fracture was identical to that of the single scanned samples, but in the parallel orientation there was a ~6 % drop in elongation. As discussed in Chapter 4.4, laser rescanning resulted in an increase in the fraction of smaller equiaxed grains. An increase in the fraction of smaller grains should result in an increase in yield strength per the Hall-Petch relationship. The increase in yield strength from grain boundary strengthening can be estimated with the Hall-Petch relationship [124] ,equation 24,

$$\Delta\sigma = kD^{-1/2} \tag{24}$$

where k is an experimental constant determined to be $0.17 \mathrm{MNm}^{-3/2}$ in a dilute Al-Mg-Li alloy [124], and where D is the grain size. The approximate average grain sizes for the single scanned and rescanned samples are 4 µm and 1.5 µm, respectively (based off of Figure 4.17). Per the Hall-Petch relationship given above, an average grain size of 4 µm and 1.5 µm would result in an 85 and 138 MPa increase in yield strength, respectively.

This suggests that, based purely off grain boundary strengthening, that rescanning would lead to a 50 MPa increase in yield strength. However, as this is not the case, there must be other mechanisms at play that negate the grain refinement. One possible explanation is that laser rescanning results in a loss of Mg, which provides solid solution strengthening. SEM-EDX measurements of the rescanned sample did not indicate Mg loss, but this measurement may not represent the bulk. Another possible mechanism is the reduction of Zr solid solution strengthening. The grain refinement of laser rescanning was attributed to precipitation of primary $L1_2$-structured Al_3Zr inoculants in the prior solidified columnar grain regions due to the reduced melt pool depth of the rescan. A higher fraction of $L1_2$-structured Al_3Zr inoculants would result in less Zr being available for supersaturation in the α-Al matrix.

Yield and ultimate tensile strengths of the 2 h and 8 h aged Al-3.60Mg-1.18Zr (wt. %, Batch 1) samples were nearly identical, despite the higher hardness of the 8 h sample (Figure 5.1). Elongations at fracture for samples tested in the parallel orientation were identical, but 8 h aged samples tested in the transverse orientation had a slightly lower elongation than the 2 h aged samples (~19 % to 18 %). Elongation at fracture was a few percent lower than the as-fabricated condition but this is expected. The peak aged Al-3.66Mg-1.57Zr (wt.%, Batch 2) sample had ~10 MPa higher yield strength than the lower Zr alloy in the transverse orientation but an ~10 MPa lower yield strength in the parallel orientation. A 10 MPa difference is minimal and less than some of the variation observed in the testing.

The peak aged higher Zr alloy was expected to have a higher strength than the peak aged low-Zr alloy; however, this was not the case; the two alloys had nearly identical peak aged yield strengths. A higher concentration of Zr would increase the volume fraction of strengthening phase (Al_3Zr nano-precipitates) thus improving the yield strength (assuming identical precipitate size). Identical yield strengths potentially suggest that the amount of Zr in solid solution available for precipitation is similar between the two alloys despite the different concentrations. However, the highest Zr content alloy studied, Al-2.90Mg-2.10Zr (wt. %, Batch 3), had complete Zr supersatruation in the matrix of the coarse grain region, hence, it is expected that the Al-3.66Mg-1.57Zr (wt.%, Batch 2) sample would indeed have greater Zr in solid solution which would result in a higher volume fraction of precipitate. As alluded to when discussing the property differences in the as-fabricated samples, there are three primary strengthening mechanisms operative in these alloys: (i) grain size strengthening (Hall-Petch), (ii.) solid solution strengthening, and (iii) precipitation strengthening. Quantifying the contribution to the overall strength of each of these mechanisms is challenging. In the as-fabricated condition, the Al-3.66Mg-1.57Zr (wt.%, Batch 2) samples had higher yield strength than the Al-3.60Mg-1.18Zr (wt. %, Batch 1) samples. As hypothesized earlier, the increase in strength could be from either grain refinement (more Al_3Zr inoculants), solid solution strengthening (more Zr in the coarse grain regions), or both. In the peak aged condition, the strengths were identical, suggesting that the contribution of precipitate strengthening to the overall strength is less in the higher Zr alloy. As the amount of Zr in solid solution is higher for the higher Zr alloys, then the fraction of supersaturated coarse grains must be reduced in the higher Zr alloy for the yield strength to be the same after aging. Further EBSD analysis comparing grain structure of the different alloys would be required to validate this hypothesis.

6.3.2 Elevated Temperature Mechanical Properties

The trend in room-temperature yield strengths (Figure 6.3) for the highest-Zr alloy (Al-2.90Mg-2.10Zr, wt. %, Batch 3) is expected for a precipitation strengthened alloy: aged, precipitated samples show higher yield strengths than the as-fabricated samples without precipitates. At test temperatures of 177°C and above, the yield strengths of the aged, and overaged samples fall below that of the as-fabricated samples, dropping by a factor of three at 260°C. The elevated temperature behavior is not as expected from an alloy that is precipitation-strengthened by thermally-stable ordered intermetallic phases with a uniform microstructure, as described below.

When considering this material's elevated temperature mechanical behavior it is important to recall that the bimodal grain microstructure consists of fine-grained regions with sub-micron equiaxed grains, and coarse-grain regions of columnar grains 1 to 5 μm in width and up to 40 μm in length. Despite the columnar grains being referred to as the coarse-grain region, the microstructure is still fine-grained compared to a conventionally-cast alloy. An equiaxed grain size of 770±340 nm for a peak aged sample (8 h at 400°C) and an equiaxed grain size of 1280±660 nm for an overaged sample (144 h at 400°C) were observed [67]. While grain coarsening occurs at elevated temperatures to some extent, the very modest growth suggests that grain boundary precipitates, such as Fe-rich intermetallics, Mg_2Si particles, grain-boundary Al_3Zr and especially Mg-rich oxides (as they do not change even at elevated temperatures as described above), are effective at impeding coarsening and maintaining the fine-grain size. Elevated temperature deformation of fine-grain aluminum alloys is often controlled by grain boundary sliding (GBS). Li et al. performed tensile tests between 450 and 570°C on an Al-5038 alloy (Al-4.5Mg-0.18Fe-0.6Mn-0.1-Si-0.12Cr-0.02Ti wt.%) with a 20 μm grain size and found that the material had superplastic behavior, which was attributed to GBS, controlled by intergranular dislocation climb, and conventional dislocation creep [125]. While the temperature range tested by these authors is much higher than in the present study, the grain size in our material is ~20 times smaller (corresponding to ~8,000 x decrease in grain volume). Small grain sizes are well known to reduce the temperature required for superplastic behavior [126]. The high-temperature deformation in alloys with our observed grain sizes can likely be attributed to GBS, however, the grain boundary precipitates responsible for maintaining the fine grain size during elevated temperature will also serve to impede grain boundary sliding. The lower yield strength of the thermally treated samples over the as processed state is potentially due to the coarsening of grain boundary strengthening phases such as Fe-rich intermetallics and Mg_2Si particles. Tang et al. [127] tested the high-temperature properties of an ultrafine-grained Al-5083 alloy and an ultrafine-grained Al-5083 that had SiC reinforcement and found the reinforced alloy had superior high-temperature strength. They attributed this difference to the presence of grain-boundary SiC particles that inhibited GBS [127]. A similar situation may be at play in our alloy but, instead of SiC on the grain boundaries, a combination of Fe-rich intermetallic, Mg_2Si particles, and grain boundary Al_3Zr inhibits GBS. While these grain boundary particles will occur in both the aged and as-fabricated alloy, the coarsening during thermal treatment, as shown in Figure 5.6, will reduce their effectiveness, explaining the greater yield strengths of the as-fabricated alloy.

The fine grain size will also have an influence on the creep performance. The fine grain size of the tested alloy may mean that grain boundary diffusion is dominant; hence a stress exponent of 1-2 could be active. Sklenicka et al. [128] performed creep tests at 200˚C on an ultrafine-grained (0.55 μm) Al-0.2Sc (wt.%) alloy produced by equal channel angular processing and in a second study [129] attributed this behavior to superplastic flow via GBS, which is generally associated with a stress exponent of $n = 2$. Marquis et al. [50] performed creep testing at 300˚C of an Al-2Mg-0.2Sc wt.% alloy, which is also solid-solution- and $L1_2$-precipitation strengthened, and attributed the creep behavior to viscous dislocation glide creep with a stress exponent of $n = 3$. As can be seen in Figure 6.5, using n values of 1 leads to a poor fit, while $n = 2$ or 3 more accurately fit the experimental data for the tested samples. A better fit is achieved with $n = 3$, suggesting that dislocation glide is the limiting creep mechanism; however, GBS may still contribute to the overall strain as Rachinger GBS (grain boundary sliding without grain shape change that is accommodated by intragranular dislocation movement in adjacent grains) was found to have a stress exponent of 3, as this form of GBS is dislocation controlled [54]. The presence of the grain boundary precipitates likely inhibits GBS to some extent, forcing GBS to make up a smaller portion of the total creep strain, but the potential contribution from dislocation and Rachinger GBS was not calculated.

STEM analysis of the microstructure of the as-fabricated samples crept for 8 h and crept at 168 h revealed the presence of discontinuous precipitation (Figure 6.11). Since discontinuous precipitates were not present in the as-fabricated samples, the precipitation may occur during the creep test. The diffusivity of Zr in Al at the temperature of the creep test, 260˚C , is six orders of magnitude lower than the diffusivity at peak aging temperature, 400 ˚C (1.4×10^{-25} vs. 1.6×10^{-19} m^2s^{-1}) suggesting that minimal to no Al_3Zr precipitation would usually be expected during 8 h at 260˚C; however, most theories describing the growth kinetics of discontinuous precipitation consider grain-boundary diffusion and not bulk diffusion [130]. Since grain boundary diffusion is several orders of magnitude faster than bulk diffusion [131], it is plausible that discontinuous precipitation can occur at 260˚C. It is also important to note that discontinuous precipitation reactions can be enhanced by the presence of strain [130], which is present in a creep test. Microstructural changes during creep testing of the as-fabricated samples suggest that the fitted stress exponent of 3 may not be representative of the actual creep limiting mechanisms.

Both as-fabricated and peak-aged alloys exhibit similar creep properties at 260˚C for the long duration test. The similarity of the creep behavior between the as fabricated and peak aged conditions for the long duration test may be due to aging that occurred in the as-fabricated sample during the 120 h of high-temperature exposure, before measurable deformation was achieved at 15 MPa. The short duration creep tests (8 h) show substantially improved creep behavior for the as-fabricated samples with a threshold stress that is triple that measured in the long-duration creep test (41 vs. 13 MPa). A possible explanation for this behavior is grain-boundary particle coarsening occurring during the long duration creep test as clearly observed in Figure 6.10. Coarsening would result in less effective grain-boundary pinning, thus lowering threshold stresses for deformation. The annealed samples have reduced creep performance compared to the as-fabricated sample during the short duration creep test, which may also be explained by grain-boundary particle coarsening that occurs during the under-aging treatment. Again, isolating the exact creep limiting mechanisms is difficult due to the many microstructural changes occurring during creep testing.

6.4 Conclusions

The room temperature and elevated temperature mechanical properties were investigated in Al-Mg-Zr alloys (Al-3.6Mg-1.2Zr, Al-3.60Mg-1.57Zr, Al-2.9Mg-2.1Zr, wt.%) processed by L-PBF. It was concluded that:

- As-fabricated Al-Mg-Zr alloys display yield strengths of 225-280 MPa and elongations at fracture of 20-30%. The high Zr alloy, Al-3.60Mg-1.57Zr, displayed higher as-fabricated strengths (280 MPa) than the low Zr alloy, Al-3.6Mg-1.2Zr, (225 MPa). This may be attributed to higher levels of Zr in solid solution providing more solid solution strengthening.
- The peak-aged Al-Mg-Zr alloys display both high strength, ~350 Mpa yield strength, and high ductility, ~18 % elongation at fracture. Starting alloy composition had minimal impact on peak-aged strengths. The combination of high strength and high ductility was attributed to the bimodal microstructure.
- Laser rescanning did not result in a change in the as-fabricated mechanical properties despite a measurable reduction in average grain size. It is hypothesized that the increase in grain-boundary strengthening from laser rescanning was offset by loss of solid-solution strengthening elements, Mg (evaporation losses) and Zr (less grains having Zr solid solution strengthening due to increased primary Al_3Zr precipitation).
- The as-fabricated alloys display higher yield strengths than the peak-aged alloys at temperatures of 150˚C and above. At 260˚C, the as-fabricated and the peak-aged alloys (400˚C, 8 h) show widely different yield strengths of 87 and 24 MPa, respectively. This strength reduction in the aged condition is attributed to the coarsening of grain-boundary precipitates during aging, which leads to less inhibition of grain-boundary sliding.
- Creep data at 260 ºC can be well fitted with a stress exponents n=2 or 3 (indicative of GBS or dislocation motion) and a threshold stress (from precipitation strengthening).
- During long-duration (168 h) creep tests, both as-fabricated and peak-aged samples display nearly-identical creep behavior, with the same threshold stress of ~14 MPa. The similarity in creep properties is explained by the in-situ aging that occurs for the as-fabricated sample during the creep test at 260 ºC.
- For short-duration (8 h) creep tests, as-fabricated samples show a much higher threshold stress than samples previously aged at 260 ˚C for 168 h (~40 vs. ~14 MPa). This is again consistent with different exposure times at 260 ˚C (8 vs. 176 h), during which grain-boundary particles are coarsening.

Chapter 7 Metallurgy of L-PBF Fabricated CM247LC

7.1 Powder Microstructure

Figure 7.1 shows BSE images of cross-sectioned CM247LC powder. A majority of the powder is spherical but defects (agglomeration, porosity, shells, non-spherical particles) were observed. Closer examination of the cross sectioned powder revealed the presence of sub-micron bright white particles (an example is shown by the black arrow in Figure 7.1(b)). SEM EDX analysis of the bright white particles in the powder revealed that they are enriched in Hf, Ti, and Ta (Appendix A Figure 0.10).

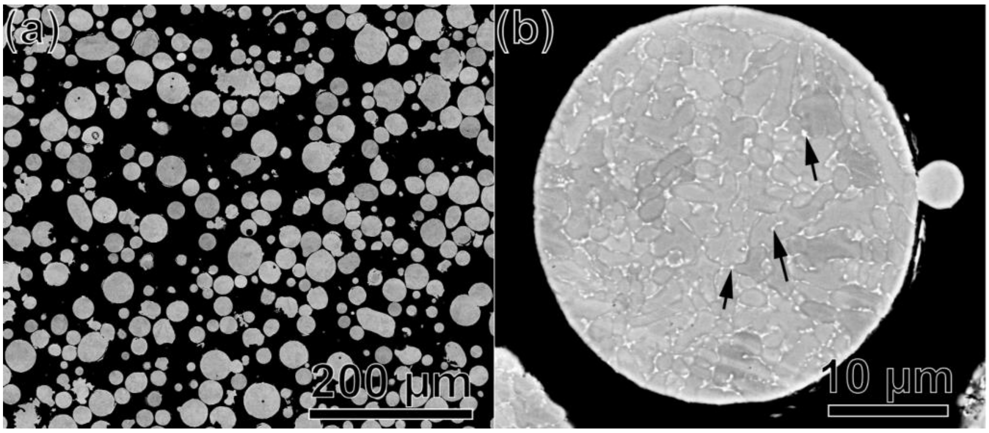

Figure 7.1: BSE images of the cross-sectioned CM247LC powder(a) low magnification BSE image (b) Higher magnification BSE image showing bright regions that are enriched in Hf, Ti, and Ta. A few are highlighted with a black arrow.

7.2 As-fabricated Microstructure

The Condition 1 and 2 as-fabricated microstructures of the CM24LC alloy is displayed in Figure 7.2. The melt pools are highlighted by dashed lines in Figure 7.2 (a) and (b). The melt pools dimensions are ~175 µm wide and ~105 µm deep for samples produced using Condition 1 (Figure 7.2(a)), and ~180 µm wide and ~55 µm deep for samples produced using Condition 2 (Figure 7.2(b)). No significant differences were observed between the melt pool dimensions of the samples fabricated on the 100 mm diameter and the 34.5 mm build plate of Condition 2 (Appendix A Figure 0.11). Regardless of the processing condition, in the as-fabricated condition, the samples are characterized by a grain microstructure predominately composed of columnar grains ranging from a few microns to ~50 µm in width, oriented parallel to the build direction (Figure 7.2(c) and (d)). Columnar grain regions are composed of ~1 µm wide substructures, later identified as cells (Figure 7.2(e) and (f)). EBSD Inverse Pole Figures (IPF) maps of Condition 1 and Condition 2 as-fabricated samples are shown in Figure 7.3. The EBSD IPF maps show elongated grains parallel to the build direction, as observed in the BSE images. The grains have a (100) fiber texture in the build direction. The high angle grain boundaries (HAGB, > 10°) represent 56 % and 36% of the total grain boundaries in Condition 1 and Condition 2 samples, respectively. The grain size (HAGB) in Condition 1 samples is ~ 30 - 50 µm wide and hundreds of µms in length, and the grain size (HAGB) in Condition 2 samples is ~40 – 80 µm wide and hundreds of µms in length. The Condition 2 sample shows more distinct sub-grain structures marked by low angle boundaries cells inside the larger grains.

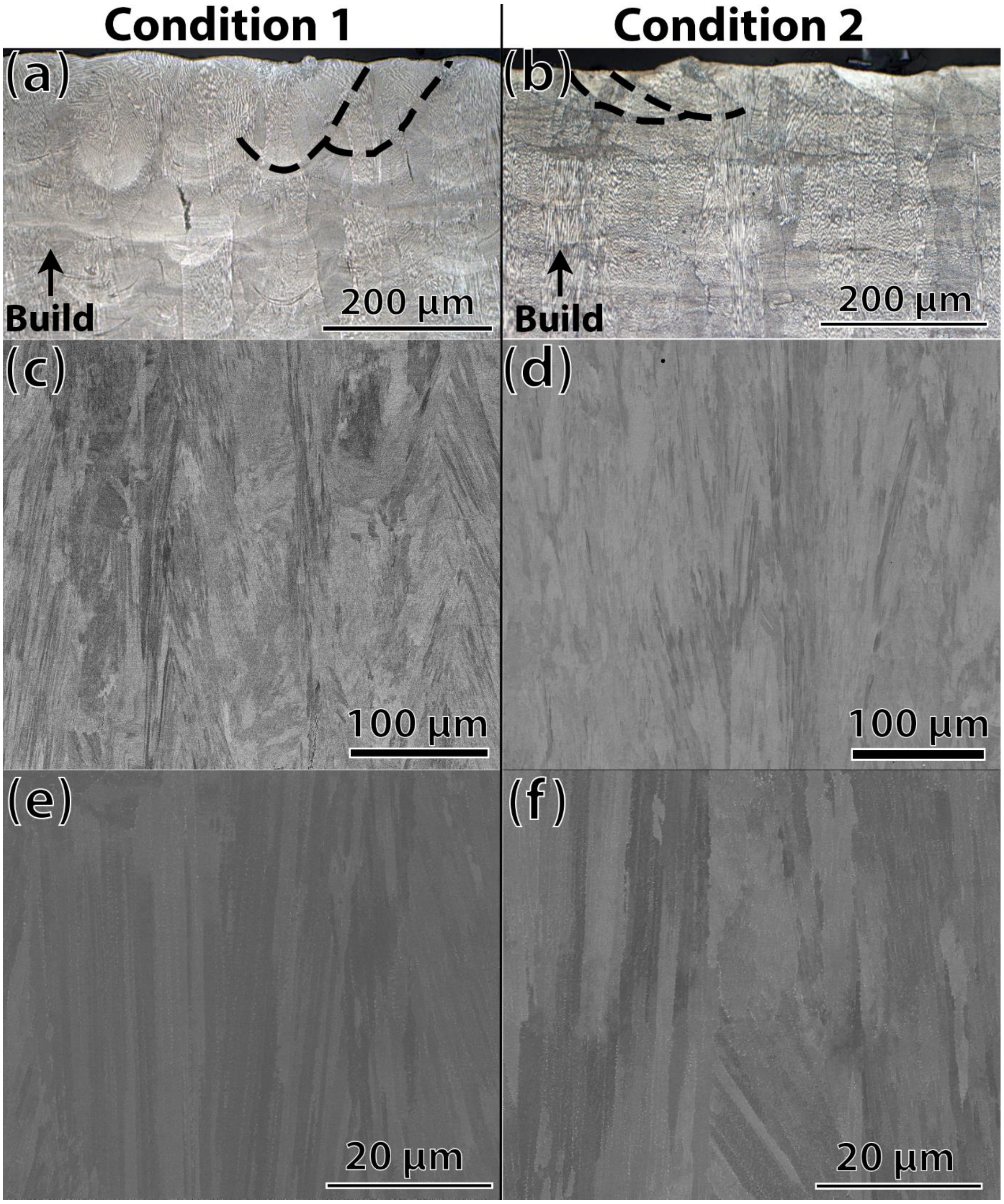
Condition 1
Condition 2
(a)
(b)
Build
Build
200 µm
200 µm
(c)
(d)
100 µm
100 µm
(e)
(f)
20 µm
20 µm

Figure 7.2: Microstructure of CM247LC samples in the as-fabricated condition, fabricated using Condition 1 (a,c,e), and Condition 2 (100 mm build plate) (b,d,f). a,b) Optical images, with highlighted melt pool boundaries (dashed black lines). c,d) Backscatter electron images showing the columnar grain structure. e,f) Higher magnification backscatter electron images showing a cellular substructure.

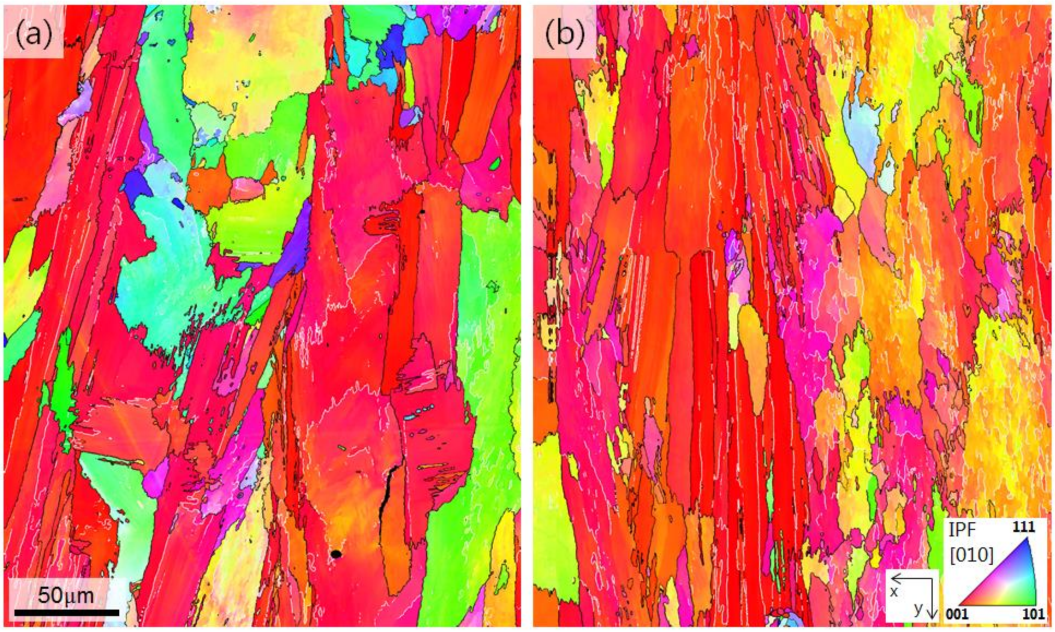

Figure 7.3: EBSD IPF maps of samples fabricated with Condition 1 (a) and Condition 2 (100 mm build plate) (b). The IPF color is shown for the Y direction which is parallel to the solidification direction. White lines: low angle boundaries > 2°; black lines: high angle boundaries > 10°. Map sizes are 250 x 300 µm with 100 nm step size.

STEM was used to investigate the presence of secondary phases and characterize the solute distribution. Figure 7.4 shows (a) a ADF-STEM and (b) a BF-STEM image, as well as (c) a series of STEM-EDX maps of the as-fabricated condition (transverse microstructure showing). The cell structure ranges from ~500 nm to ~1 µm in diameter (Figure 7.4(a)). A high dislocation density is observed on the cell boundaries (Figure 7.4(b)). Precipitates ~55 nm in diameter and rich in Ti/Hf/Ta/W/C are located on the cell boundaries and are presumed to be carbides (Figure 7.4(c)). A X-Ray diffraction (XRD) pattern of an as-fabricated Condition 2 sample (presented in the next chapter, Figure 8.6) did not reveal the presence of superlattice peaks of the γ` phase; however, a selected area electron diffraction (SAD) pattern (Figure 7.5) did reveal 100- and 110-type superlattice reflections of the $L1_2$ (γ`) structure. TEM dark-field imaging and HR-STEM imaging were attempted in order to image the γ` precipitates, but the precipitates could not be imaged, likely due to the small size. Significant micro-segregation was observed; Hf, Al, and Ti partitioning to the cell boundaries and W, Co, and Ni partitioning to the cell cores (Figure 7.4(c)). STEM-EDX semi-quantification values (line profiles are shown in Appendix A Figure 0.12) and the calculated effective partition coefficients are presented in Table 7-1. Levels of Hf enrichment varied considerably between grain boundaries, being estimated at 4 wt.% Hf in Figure 7.4(c), while 20 wt.% Hf was measured on another boundary (Figure 7.6, line profiles are shown in Appendix Figure 0.13). Zirconium K lines were observed in the EDX spectra but no partitioning of the Zr was observed. Similar segregation behavior in samples fabricated with the same parameters as Conditions 1 except with a chess scanning strategy is shown in the next section.

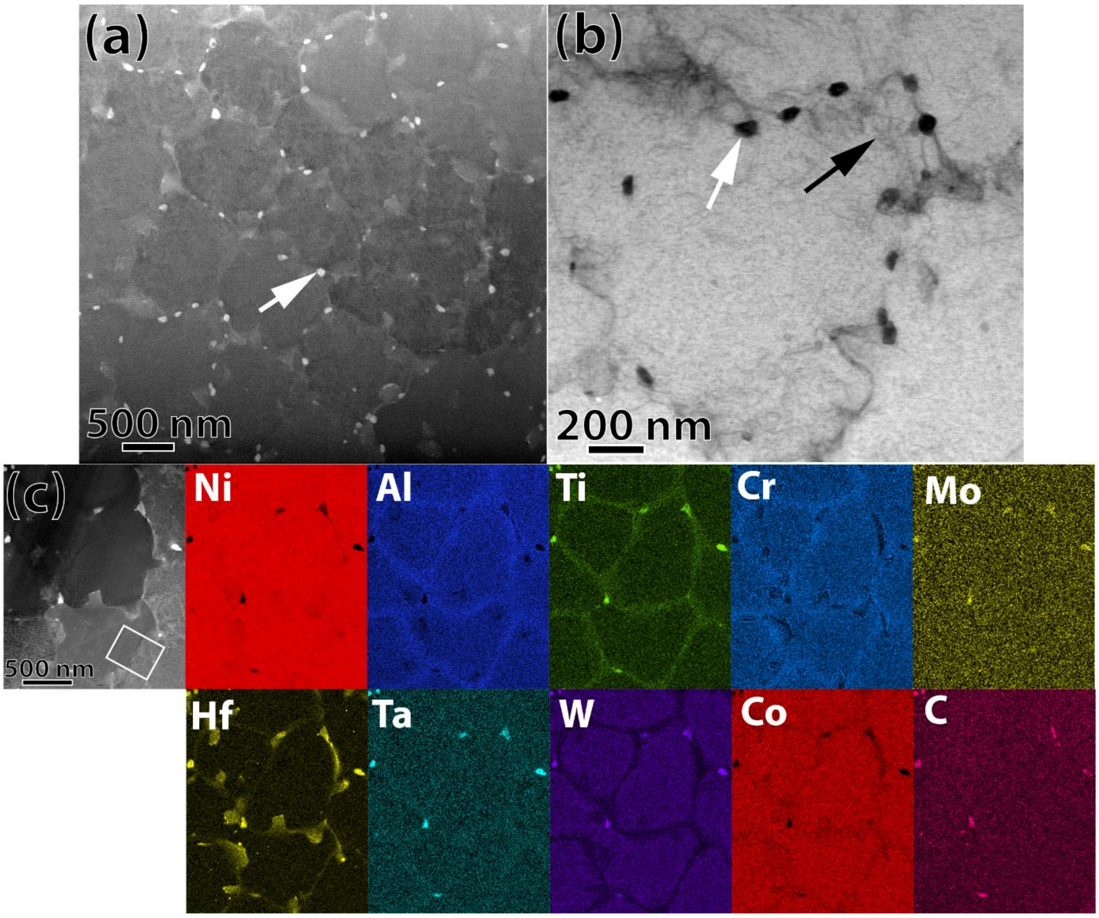

Figure 7.4: STEM characterization of the as-fabricated microstructure (transverse section) of a CM247LC sample fabricated with Condition 2 (100 mm build plate) a) ADF-STEM image showing ~0.5-1 μm diameter cells, surrounded by grain boundary precipitates, assumed to be carbides (bright particles highlighted by white arrow). b) BF-STEM image showing a high dislocation density (area highlighted by black arrow) on the cell boundaries. c) STEM-EDX map of cell boundaries. Precipitates are enriched in Ti/Hf/Ta/W/C and are presumed to be carbides. The chemical analysis is performed using the Al-K, Ti-K, Cr-K, Hf-L, Ta-L, W-L, Co-K, Ni-K, Mo-K, Zr-K, and C-K lines.

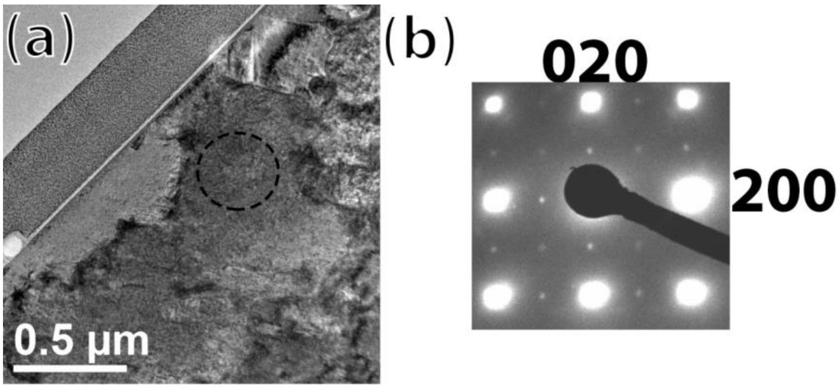

Figure 7.5: a) A low magnification BF-TEM image of the as-fabricated CM247LC sample, presented in Figure 2 (Condition 2, 100 mm build plate). (b) Selected area diffraction pattern along a [001] zone axis, acquired from the circled area in a) showing the 100- and 110-type superlattice reflections of the L12 structure.

Table 7-1: STEM-EDX semi-quantification values taken from the area highlighted by the white box in Figure 3(c), highlighting the segregation behaviors of the various elements in as-fabricated CM247LC. Effective partition coefficients k` (Cell / Boundary composition) are calculated. The chemical analysis is performed using the Al-K, Ti-K, Cr-K, Hf-L, Ta-L, W-L, Co-K, Ni-K, and Mo-K lines

	Al	**Co**	**Cr**	**Hf**	**Mo**	**Ni**	**Ta**	**Ti**	**W**
Cell wt. %	4.7	9.3	7.5	2.3	1.9	60	4.5	1.0	8.5
Boundary wt. %	4.1	8.6	8.1	4.1	1.9	59	5.5	1.5	6.5
k`	0.87	1.1	0.93	0.56	1.0	1.0	0.81	0.73	1.3

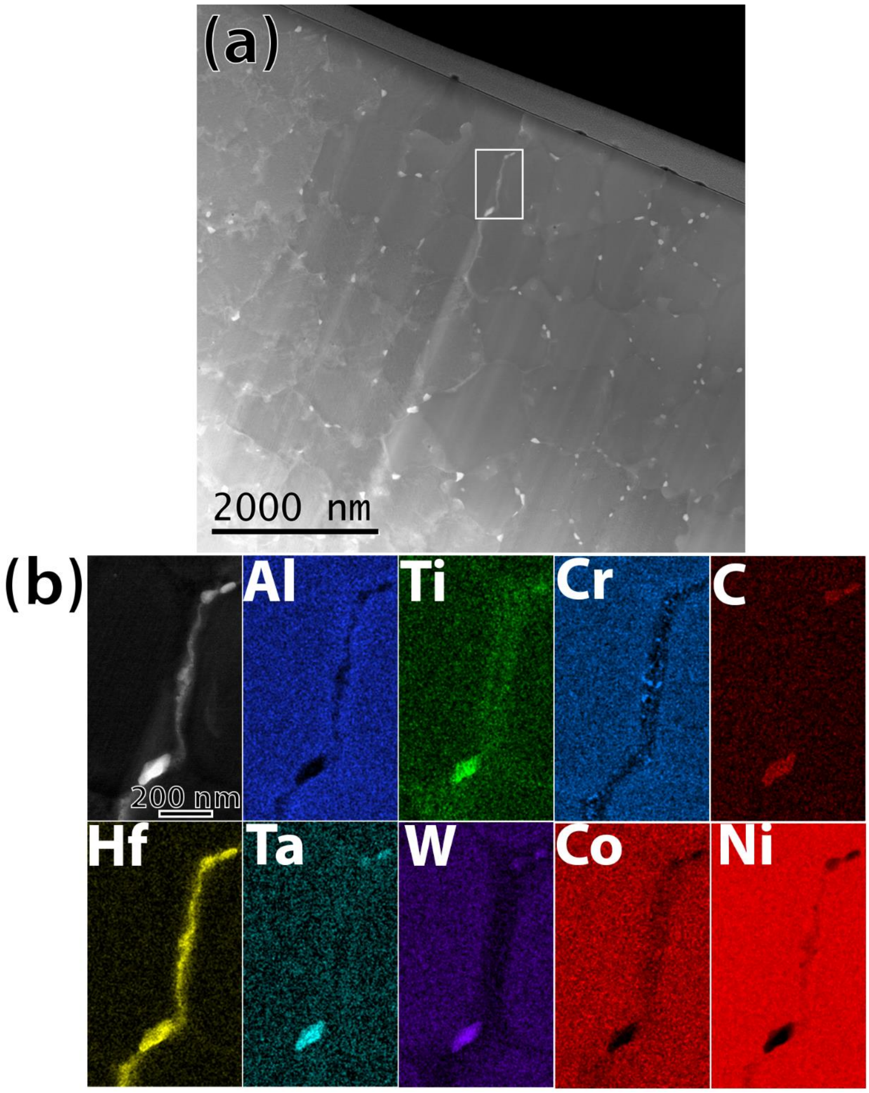

Figure 7.6: STEM analysis of the as-fabricated CM247LC microstructure of a transverse section of a Condition 2 fabricated sample. a) ADF-STEM image showing a grain boundary enriched with elevated levels of Hf (white box). b) STEM-EDX map of region highlighted by the white box in a). Chemical analysis performed with Al-K, Ti-K, Cr-K, Hf-L, Ta-L, W-L, Co-K, Ni-K, C-K lines.

7.3 Microcracking in the as-fabricated samples

The density of both Condition 1 and Condition 2 samples was measured at >99.9% with the Archimedes method and using a nominal density of CM247LC of 8.54 g/cm^3; however, the presence of defects such as micro-cracks, pores, and lack of fusion suggest that the density is slightly lower. The top surface of an as-fabricated (Condition 1) bidirectional scanned sample (no rotation between layers) is shown in Figure 7.7. Micro-cracks ~200 to 300 µm in length are oriented perpendicular to the beam travel. Similar observations were also made on the samples with bidirectional scanning and a 90° rotation between the layers (not shown). Micro-crack density was fairly uniform throughout the cross-section of Condition 1 samples, but Condition 2 samples did have a higher occurrence of micro-cracking ~300 µm from the side edge (visible in optical images presented in the next chapter).

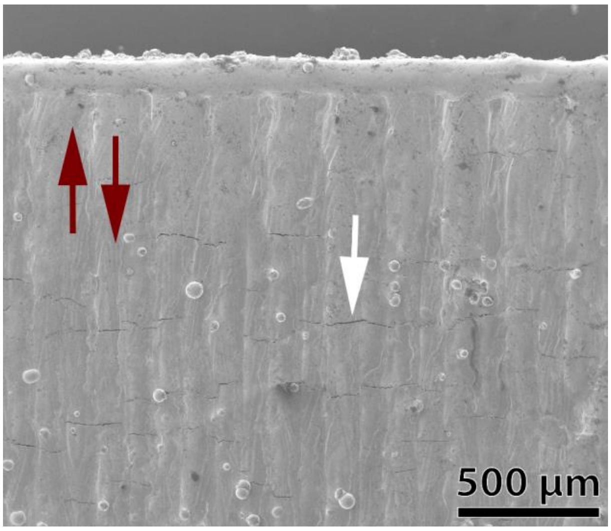

Figure 7.7: SE image of top surface of as-fabricated CM247LC cube (Condition 1). Cracking (one crack highlighted by white arrow) is perpendicular to the direction of laser travel (is indicated by the red arrows).

Figure 7.8(a,b,d,e) presents BSE images of parallel and perpendicular cross sections of CM247LC samples (Condition 1 and 2 samples). In the BSE image of a parallel cross section, micro-cracks ~100 µm in length are oriented parallel to the build direction (Figure 7.8(a)). In the images of the perpendicular cross sections, micro-cracks are observed oriented both parallel and perpendicular to the image frame (Figure 7.8(b)), which represent the X and Y scanning directions. Higher magnification imaging of a crack, both in parallel and perpendicular cross sections, reveals that cracking occurs on cell/grain boundaries, Figure 7.8(d) and (e). SE images of a representative micro-cracks observed in samples fabricated from both conditions are shown in Figure 7.8(c) and 5(f). The crack surfaces have a rough appearance indicative of fracture in the liquid phase [132]. Micro-crack location and morphology did not appreciably change between the two machines, only the crack density is higher in samples produced using Condition 1. Similar crack appearance in samples fabricated with the sample parameters as Conditions 1 except with a chess scanning strategy have been observed and will be discussed in the next section.

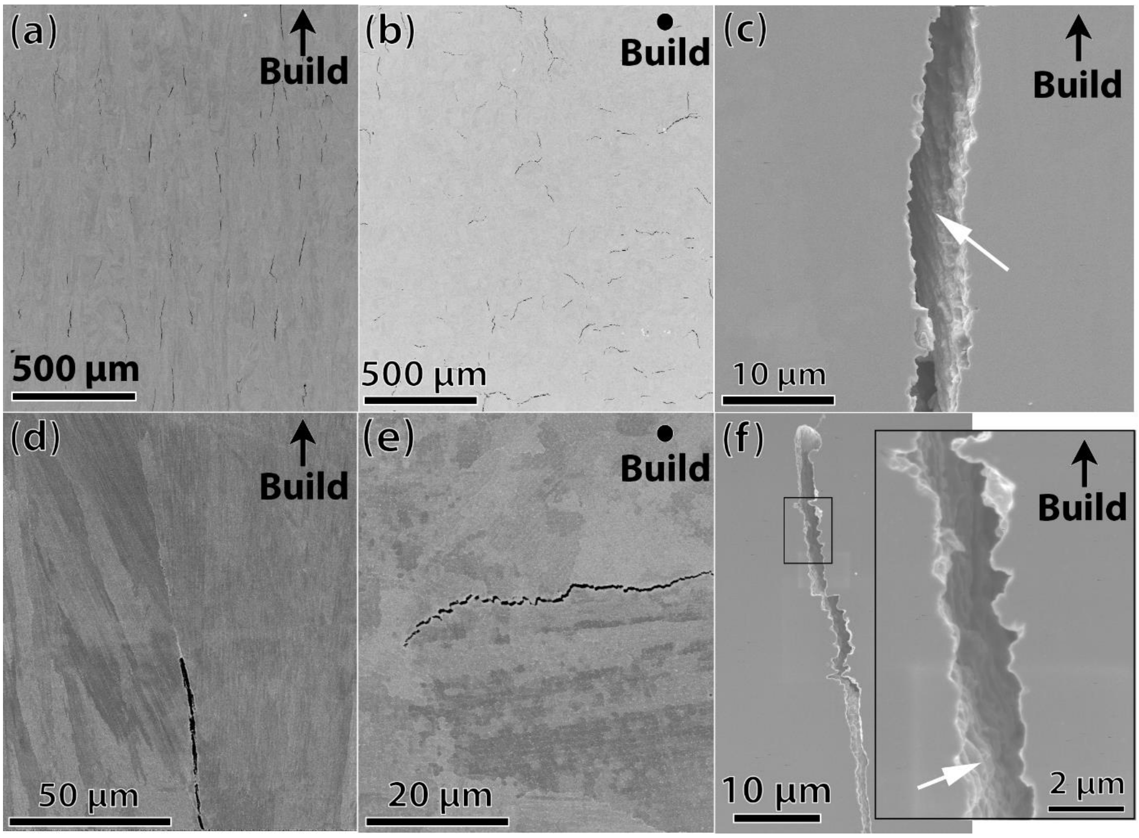

Figure 7.8: Electron microscope images taken from CM247LC samples fabricated from a,b,c) Condition 1 and d,e,f) Condition 2. a,d) BSE Image of a parallel cross section. b, e) BSE image of perpendicular cross section. c, f) SE image showing the features (white arrows) on the crack surfaces.

Gleeble tests (performed by H. Ghasemi at EPFL) have been conducted to further investigate the cracking mechanisms that may occur in the Heat Affected Zone (HAZ) during processing. The as-fabricated (Condition 2) CM247LC samples were heated up to 1250 °C at a rate of 250 °C/s and then water-quenched. Figure 7.9 indicates a specific part of the as-fabricated CM247LC sample that was chosen for investigation, prior to the experiment. The same zone has been imaged again after the experiment. A zone with the appearance of a grain boundary remelting and solidification after the fast heating/cooling was observed (Figure 7.9 (b-c)). SEM-EDX analysis indicates significant Hf enrichment on the remelted and re-solidified grain boundary after the Gleeble experiment (Figure 7.9 d and e).

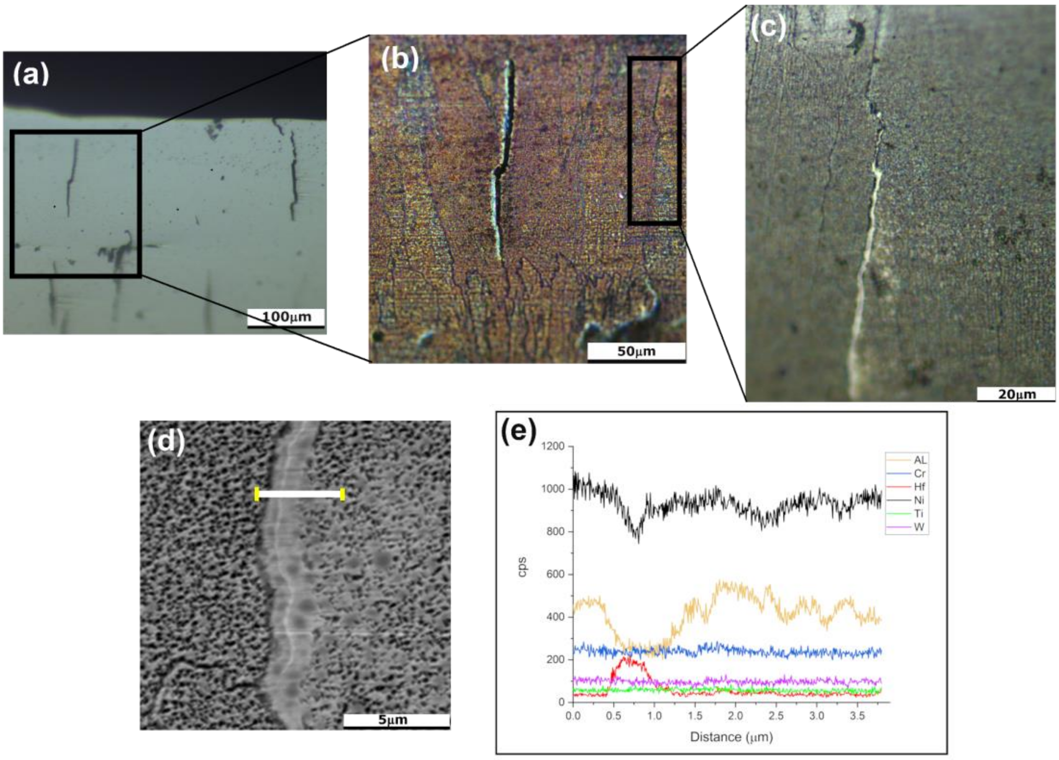

Figure 7.9: a) Optical image showing a specific area of the as-built sample before the Gleeble test. b) Optical microscope images taken from same zone as (a) after the fast heating and cooling treatment in the Gleeble machine, c) higher magnification optical image shows a thin 1 µm wide film formed after Gleeble test. d) Higher magnification SE image of the observed film, and e) SEM-EDX line scan analysis of the region. All images are parallel to the build direction. Figure courtesy of H. Ghasemi.

7.4 Chess Scanning Strategy

For the most part, the microstructure and defects of the CM247LC sample fabricated by chess scanning is similar to that of the bi-directional scanning. Figure 7.10 shows a BSE image of the microstructure and a EBSD unique grain color map. The grain microstructure is composed of columnar grains, elongated in the build direction, ~20-50 µm in width and ~100 µm long. There is also clusters of smaller equiaxed grains, that were not observed in the bi-direction scan. The columnar grains appear to have a cellular (~0.5 to 1 um) sub-structure elongated in the build direction (Figure 7.10(a)). An ADF-STEM image and corresponding STEM-EDX maps are shown in Figure 7.11. Precipitates ~70 nm in diameter and rich in Ti/Hf/Ta/W/C are located on the cell boundaries and are presumed to be carbides (Figure 7.11). Significant micro-segregation was observed; Hf, Al, and Ti partitioning to the cell boundaries and W, Co, and Ni partitioning to the cell cores. Micro-cracking was observed uniformly on the cross-section (shown in Chapter 8). Figure 7.12 shows a micro-crack and the crack face of another micro-crack. Similar to the bi-directionally scanned samples, the micro-cracks have a rough appearance.

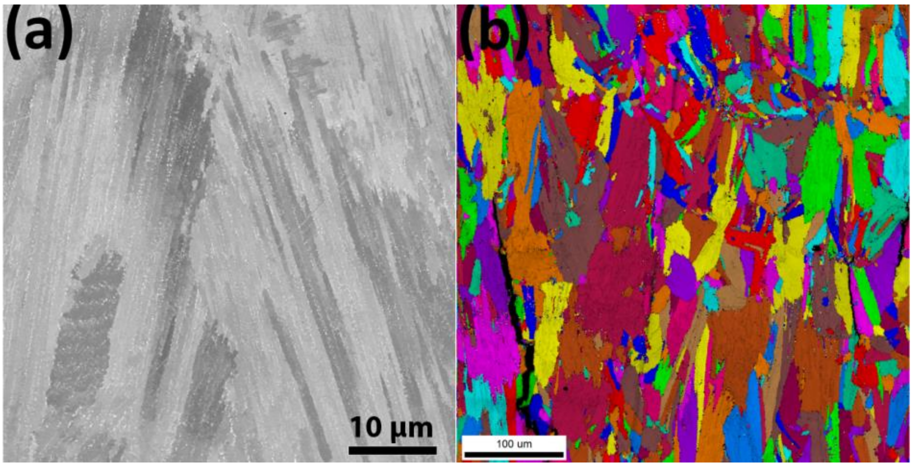

Figure 7.10: (a) BSE image from CM247LC sample fabricated from Condition 1, except for chess scanning. (b) EBSD unique grain color map (700 nm step size map) .

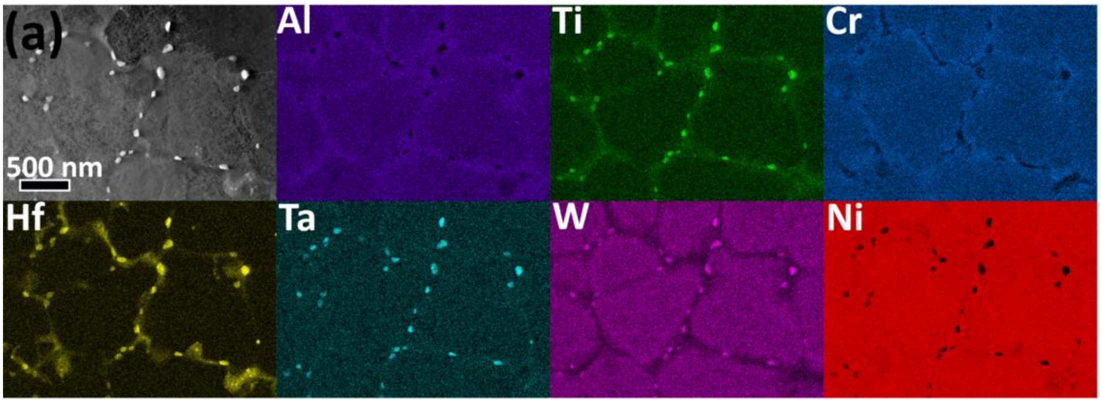

Figure 7.11: ADF-STEM image and corresponding STEM-EDX maps the as-fabricated microstructure (transverse section) of a CM247LC sample fabricated with Condition 1, except with a chess scanning strategy. Chemical analysis performed with Al-K, Ti-K, Cr-K, Hf-L, Ta-L, W-L, Co-K, Ni-K, C-K lines. Co, C, and Mo maps not shown.

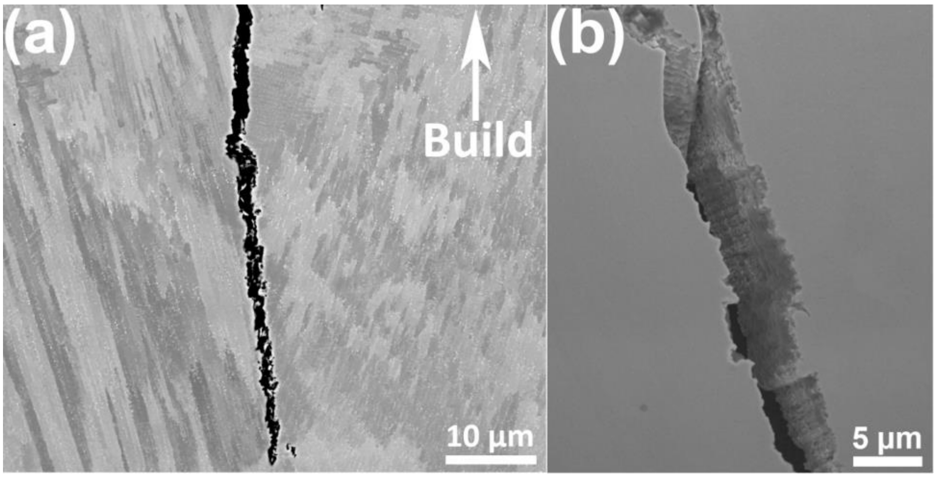

Figure 7.12: SE images of micro-cracks in a CM247LC sample fabricated with Condition 1, except for chess scanning (a) BSE image of a micro-crack running along a grain boundary. (b) SE image showing features on the face of the crack.

7.5 Microstructure and potential micro-crack formation mechanisms in CM247LC

The processing parameters utilized for Condition 1 and Condition 2 led to different melt pool profiles and incidence of HAGBs. While the melt pool profiles differ, the general microstructure, fine columnar grains composed of cells oriented predominately in the build direction, is similar between the two conditions. The influence of the processing parameters on the microstructure and crack density will be discussed in Chapter 8.

The observed grain microstructure, fine columnar grains with a (100) fiber texture oriented parallel to the build direction, is similar to that observed in L-PBF fabricated CM247LC studies by Wang et al. [3] and Divya et al. [4]. The observed grains were composed of ~1 µm cells with dislocations and carbides located on the boundaries, also similar to the aforementioned studies. Unlike the studies of Wang et al. and Divya et al., we were not able to directly observe the γ` phase. The appearance of superlattice reflections, characteristic of γ` precipitates, in the SAD patterns prove that it is present in the as-fabricated samples used in this study, but likely at nm to sub-nm sizes. The chemical micro-segregation observed is similar to that observed in the other CM247LC L-PBF studies. The effective partition coefficients (Table 7-1) of the various elements is comparable, except for Cr, to those observed in cast Ni/base superalloys, suggesting that the segregation tendencies do not significantly differ between L-PBF fabricated and conventionally cast alloys [39,133]. However, unlike the controlled solidification (controlled thermal gradients and interface velocities) typically encountered in superalloy casting, the L-PBF solidification conditions will vary substantially, leading to differences in micro-segregation within a single melt pool. This variation was shown by the observation of boundaries with 4 wt.% Hf enrichment and another boundary with up to 20 wt.% Hf enrichment. It should also be noted that the STEM-EDX measurements of the micro-segregation are ex-situ and actual levels of micro-segregation during solidification may be higher. Adjacent passes of the laser and additional building layers will result in a HAZ. The high temperatures in the HAZ in combination with the abundant short-circuit diffusion paths, may result in a partial homogenization. Therefore, actual levels of micro-segregation during solidification are likely different than that observed. The remelted Hf-enriched grain boundaries observed after the Gleeble experiment is indicative of liquation cracking. During the L-PBF process, in the HAZ of the samples, cracks form due to the presence of a liquid film and the presence of tensile residual stresses that pulls the liquid films apart. Unlike in liquation cracking, the remelted grain boundaries in the Gleeble experiment remained closed. This can be attributed to the fact that the sample was under a 5 MPa compressive stress due to thermal expansion, hence, the remelted grain boundaries were kept closed, which prevents their cracking.

Analysis of the micro-crack fracture faces (Figure 7.8(c,f)) revealed a dendritic-like morphology indicative of fracture occurring in the liquid phase. In welding literature, micro-cracks with this appearance are attributed to solidification cracking [132]. While the crack faces analyzed all had morphology indicative of solidification cracking, the Gleeble test results show that a liquation cracking mechanism can be active during the L-PBF process. Susceptibility to liquation cracking is not surprising given the significant segregation observed. While most liquation and solidification cracks observed in welding literature will run parallel to the welding direction [134], a majority of the micro-cracks observed in this study are perpendicular to the direction of beam travel. Transverse solidification cracking has been reported in laser welding literature for welding of Ni-base superalloys [135] and Al alloys [136]. Park et al. utilized finite element modeling to show that, for high ratios of scan velocity over laser power, stresses parallel to the beam travel are highest, thus resulting in transverse cracking. Hu et al. [136] investigated transverse cracking in laser welded Al-alloys and found that the more elongated the thermal gradient was in the direction of beam travel (result of higher beam velocities) the higher the longitudinal stresses were and thus the greater transverse cracking.

7.6 Conclusions

- As-fabricated CM247LC samples have a columnar grain microstructure that is oriented parallel to the build direction. The columnar grain are composed of cells approximately 1 μm in diameter. The cell boundaries contain precipitates (~ 55 μm in diameter) that are assumed to be carbides. The cell boundaries also have an increased dislocation density.
- Micro-cracking in CM247LC was attributed to both solidification and liquation cracking. The dendritic appearance of the micro-crack surfaces is indicative of fracture in the liquid phase and thus can be identified as solidification cracking. The Gleeble experiments showed that a liquation cracking mechanism is active in the HAZ.

Chapter 8 CM247LC Alloy Modification

8.1 Micro-Crack Mitigation – Alloy Design

Since the probable micro-cracking mechanisms at play have been identified as a combination of both solidification and liquation cracking, it is important to look at the factors that influence these mechanisms of cracking. Solidification and liquation cracking are influenced by a complex interplay of both process and material related variables. Some of the major variables, but not all, that influence solidification cracking are listed below.

1. **Solidification Interval**: A large solidification range results in a large mushy zone (liquid-solid mixture). As solidification cracking occurs in the mushy zone, a larger solidification range will result in a larger region of susceptibility. [24]
2. **Amount of terminal liquid**: Peak crack susceptibility typically occurs with moderate levels of solute content. High values of solute can lead to large volumes of remaining liquid that can back fill any cracks that develop. With minimal to no solute, a grain boundary liquid film will not form and cracking will not occur. [24]
3. **Stress State**: Cracking cannot occur without a tensile stress. Both solidification shrinkage and thermal residual expansion/contraction provide the stress that can lead to fracture. The level of restraint on the solidifying material will influence the stress levels and therefore the cracking susceptibility. [132]
4. **Melt pool geometry/profile**: Teardrop shaped welds, welds with large depth to width ratios, and welds with concave profiles are all more susceptible to solidification cracking. [132]
5. **Surface tension of the terminal liquid**: The condition where a continuous liquid film is on a grain boundary is the most susceptible condition. If the liquid does not wet the grain boundaries, then bridging of grains occurs and cracking can be prevented. [24]
6. **Grain Boundary Orientation**: Grain boundaries can be classified as attractive or repulsive based on the misorientation angle between them. If the grain

boundary misorientation exceeds a certain threshold, it becomes a repulsive boundary thus lowering the solidification temperature further. [137]

7. **Grain Morphology:** An equiaxed grain microstructure can more easily accommo-date strains than a columnar grain microstructure and will be less susceptible to solidification cracking. [61]

Stress state, melt pool geometry/profile, grain boundary misorientation, and grain morphology are all variables that are significantly influenced by the processing parameters. Some of the crack mitigation strategies based on addressing the aforementioned variables are discussed in the introduction. Many of these strategies are undesirable due to added processing steps and/or costly process modification that is not attainable in most commercial L-PBF machines. Process parameter optimization can lead to significant improvements (shown later) but the fact remains that L-PBF is a high energy density process. The high energy density typically results in high thermal gradients, and rapid heating and cooling, that in turn lead to columnar microstructures, and residual stresses that cannot be easily relaxed during the process. In order to broaden the processing window, the material specific variables need to be addressed as well. Variables such as solidification interval, amount of terminal liquid, and liquid surface tension are primarily determined by the material itself. The second part of this work will thus focus on the influence of the solidification interval.

Intentionally reducing the solidification interval of an alloy implies modification of the alloy composition; typically, this is done via reducing the content of elements that preferentially segregate to the liquid ($k < 1$). Ni-base superalloys are complex alloys that contain several elements, for example, CM247LC has 13 main elements (Table 3-2), and the presence of many of those elements result in an increase in solidification interval. Typical culprits for solidification cracking in nickel-base superalloy welds are elevated levels of minor alloying elements such as P, S, B, C, and Zr [10]. While P and S are deleterious to mechanical properties and are kept to low levels, B and Zr serve as grain boundary strengtheners and are known to improve creep properties [138]. Ti is another element that can increase the susceptibility to solidification cracking; however, Ti is intentionally added for (i) raising the γ` solvus temperature, (ii) increasing the anti-phase boundary energy for γ`, and (iii) increasing the lattice parameter of γ` [138]. It is clear that intentionally reducing the alloy solidification interval via alloy modification will result in alteration of mechanical properties; however, this consequence of alloy modification is not in the scope of the current study.

The STEM-EDX maps in Figure 7.4 reveal an enrichment of Al, Ti, C, Ta, and Hf on the cell boundaries. No Zr or B rich films were observed on the grain boundaries. Other STEM-EDX maps (not shown) have revealed minor Zr enrichment in carbides and Zr is known to exist in MC type carbides [38]. Out of the aforementioned elements, Hf has the lowest observed partition coefficient from the STEM-EDX data, k`= 0.56, and exists as continuous films on the cell boundaries. In the literature, Hf was originally added to Ni-base superalloys to improve ductility [138]. Hf also serves as an S scavenger and improves hot corrosion resistance. Hf additions are said to improve mechanical properties by promoting (i) eutectic γ/γ`at the grain boundaries and (ii) blocky MC carbide morphology instead of a script-like morphology at the grain boundaries [138]. Superalloys with elevated levels of Hf (~2.0 wt. %) generally display better castability (resistance to hot tearing) than alloys without Hf, despite Hf free alloys having a smaller solidification range [139,140]. This can attributed to the presence of Hf increasing the volume fraction of eutectic γ/γ` and, eutectic melt, that results in improved back-feeding during the casting process [139,140]. As the solidification rates in L-PBF are much higher than in traditional superalloy casting, it is feasible that the volume fraction of the eutectic melt is reduced, as evidenced by the lack of observed γ/γ` eutectic. Since Hf is a very potent melting point depressant it a prime target element for studies on the influence of solidification range on the micro-cracking tendencies of L-PBF fabricated CM247LC.

The influence Hf has on the solidification behavior of CM247LC has been investigated via thermodynamic simulations. Figure 8.1 shows the results of a Scheil-Gulliver solidification calculation for a standard CM247LC composition and a Hf-free version of CM247LC. The liquidus and solidus temperatures, calculated by the Scheil-Gulliver solidification calculation of nominal CM247LC, are 1383°C and 858°C respectively, resulting in a 525°C solidification interval. The liquidus and solidus temperatures, calculated by the Scheil-Gulliver solidification calculation, of the Hf-free CM247LC are 1394°C and 1241°C respectively, resulting in a 153 °C solidification interval. The results show that removal of Hf will significantly reduce the solidification interval of CM247LC. While Scheil-Gulliver solidification calculations are often used to simulate solidification behavior for AM processed superalloys [6,8], the approximation does not take into account solute build up at the solidification interface and may overstate actual micro-segregation [24]. Equilibrium solidification calculations (not shown) of CM247LC gives liquidus and solidus temperatures of 1383°C and 1249°C respectively, resulting in a 134°C solidification interval. The same calculation performed with a Hf-Free version of CM247LC gives liquidus and solidus temperatures of 1394°C and 1340°C respectively, resulting in a 54°C solidification interval. The Scheil-Gulliver model and equilibrium solidification represent the two extremes of solidification, with the actual solidus temperatures somewhere between those predicted by the two models. Regardless of the solidification mode, it is clear that Hf has a significant influence on the predicted solidification interval of the alloy. The next sections will focus on the results of experiments with a Hf free version of CM247LC, herein named CM247LC NHf.

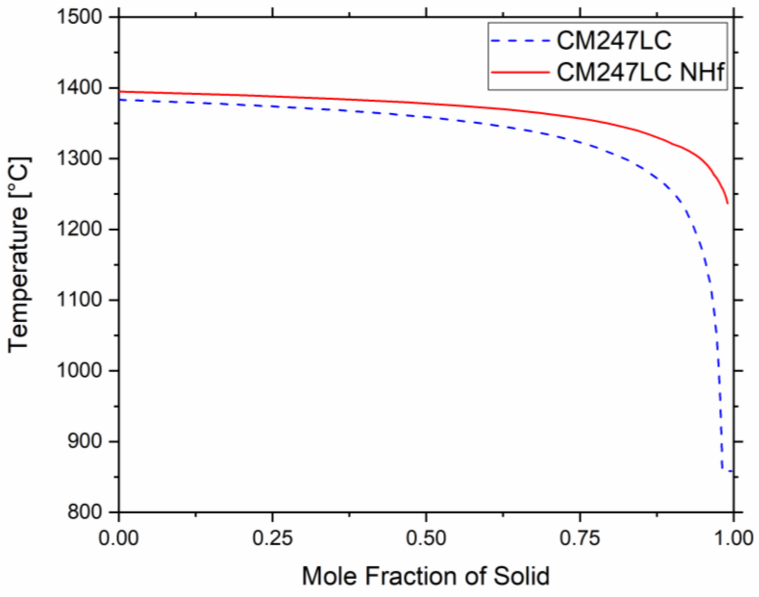

Figure 8.1: Scheil-Gulliver solidification curves for CM247LC and CM247LC NHf.

8.2 Processing of CM247LC NHf and comparison with CM247LC

8.2.1 Powder Microstructure

Figure 8.2 shows BSE images of cross-sectioned CM247LC NHf powder. A majority of the powder is spherical but defects (agglomeration, porosity, and non-spherical particles) were observed. Closer examination of the cross sectioned powder revealed the presence of sub-micron bright white particles (an example is shown by the black arrow in Figure 8.2(b)). Chemical analysis of the bright white particles in the powder was not conducted, but it is assumed they are similar to those of the CM247LC powder and enriched in Ti, and Ta. The smaller size of these bright particles and lower contrast is likely from the lack of Hf (Hf has a significantly higher electron scattering cross section than Ni). Compared to the CM247LC powder, the CM247LC NHf powder has a rougher surface finish.

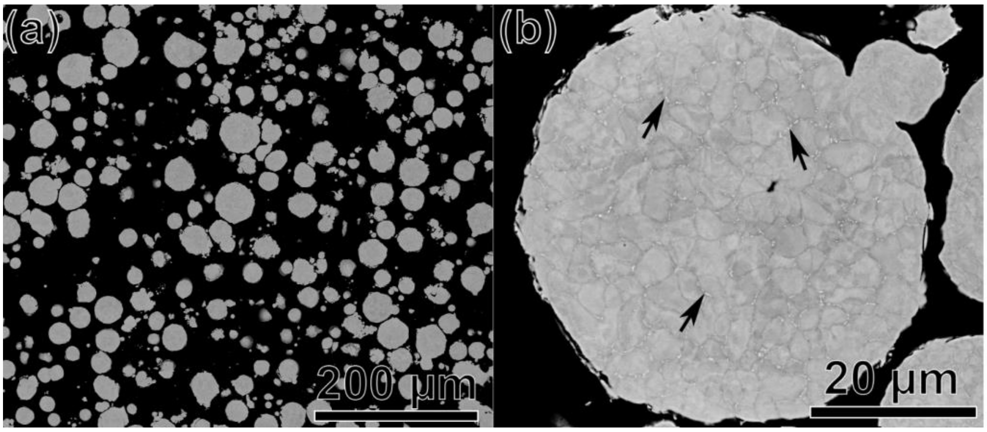

Figure 8.2: BSE images of the cross-sectioned CM247LC NHf powder(a) low magnification BSE image (b) Higher magnification BSE image showing bright regions, that are greatly reduced in size from the CM247LC powder. A few are highlighted with a black arrow.

8.2.2 As-Fabricated Microstructure

Figure 8.3(a,b,c) shows the microstructure of the as-fabricated condition of Condition 2 produced samples. The melt pools, highlighted by dashed lines in Figure 8.3(a), are approximately 200 µm wide and 60 µm in depth, which correspond to an aspect ratio comparable to the CM247LC alloy processed on the same machine. Figure 8.4 shows a side to side comparison of the two alloys melt pools. Similar to the standard CM247LC samples, the as-fabricated condition of CM247LC NHf display a grain microstructure predominately composed of fine columnar grains oriented parallel to the build direction (Figure 8.3(b)). Columnar grain regions are composed of ∼1 µm wide substructures, later identified as cells (Figure 8.3(c)).

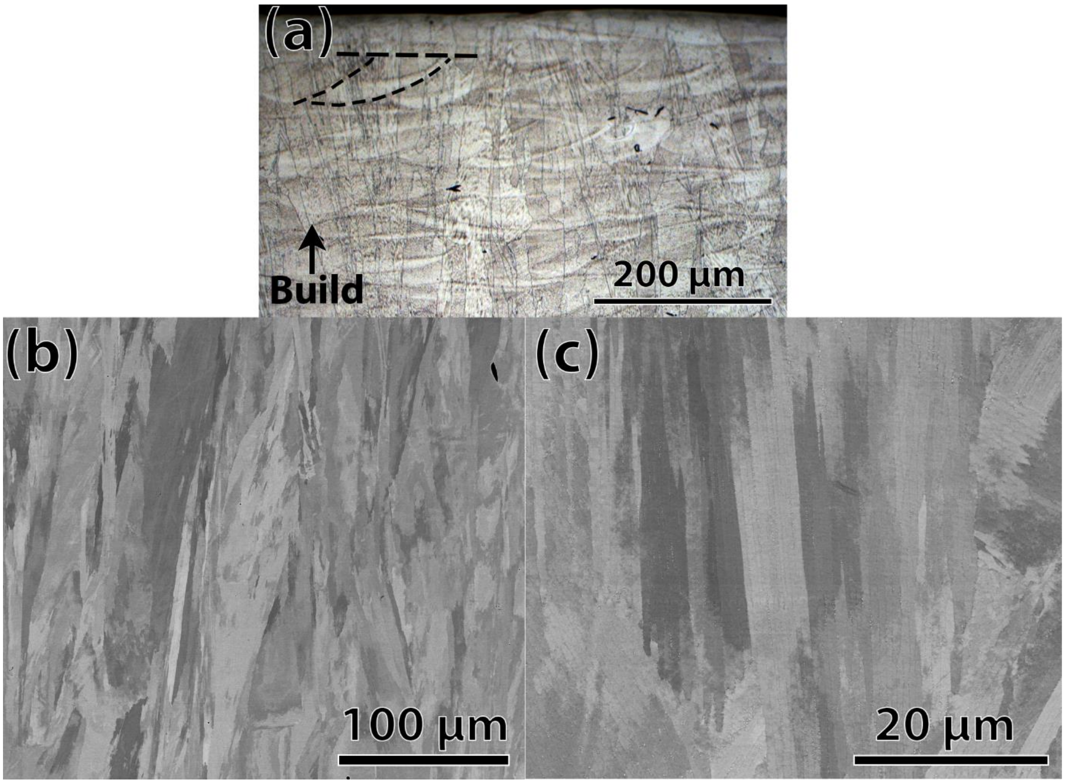

Figure 8.3: Microstructure of as-fabricated CM247LC NHf (Condition 2, 100 mm build plate). (a) Optical image of an etched sample. Melt pools are highlighted by a dashed line. b,c) BSE images showing the elongated grain and subcell microstructure.

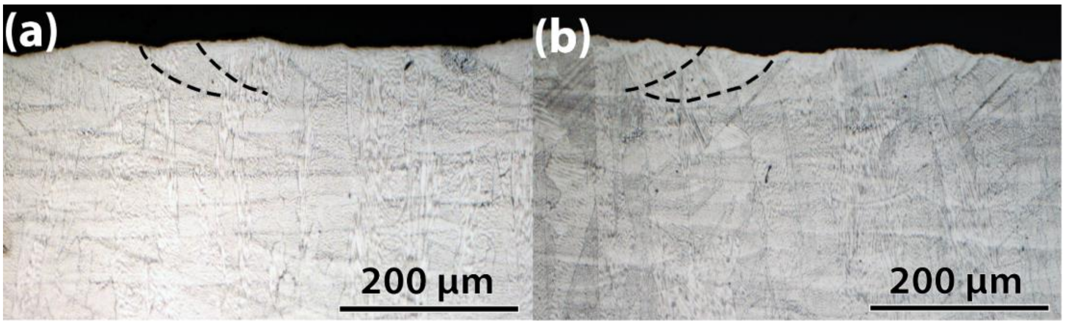

Figure 8.4: Optical images of etched samples processed by Condition 2 (34.5 mm build plate): (a) CM247LC (b) CM247LC NHf. Dashed lines hightlight the melt pools

Figure 8.5 shows an (a) ADF-STEM image, a (b) BF-STEM image, and a series of (c) STEM-EDX maps taken from a Condition 2 produced sample in the as-fabricated condition (perpendicular microstructure showing). The STEM lamella was extracted at the tip of a microcrack and the crack can be clearly seen in Figure 8.5(c). Like for the CM247LC alloy, the cell structure ranges from ~0.5 to ~1 µm in diameter (Figure 8.5(a)). A high dislocation density is observed throughout the sample (Figure 8.5(b)). Precipitates ~60 nm in diameter, rich in Ti /Ta/W/C, and located on the cell boundaries (Figure 8.5(c)) are presumed to be carbides. Elongated script-like carbides were observed on some boundaries (Figure 8.5(a) black arrows). Similarly to the CM247LC samples, X-Ray diffraction (XRD) patterns of a sample produced with Condition 2 (Figure 8.6) did not reveal the presence of superlattice peaks of the γ` phase; however, a SAD pattern (Figure 8.7) did reveal 100- and 110-type superlattice reflections of the $L1_2$ (γ`) structure. Similar to the original CM247LC samples, HR-STEM imaging were attempted in order to image the γ` precipitates, but the precipitates could not be imaged, likely due to the small size. Significant micro-segregation was observed; Cr, Ta, Al, and Ti partitioning to the cell boundaries and W, Co, and Ni partitioning to the cell cores (Figure 8.5(c)). Zirconium K lines were observed in the STEM-EDX spectra but no partitioning was observed.

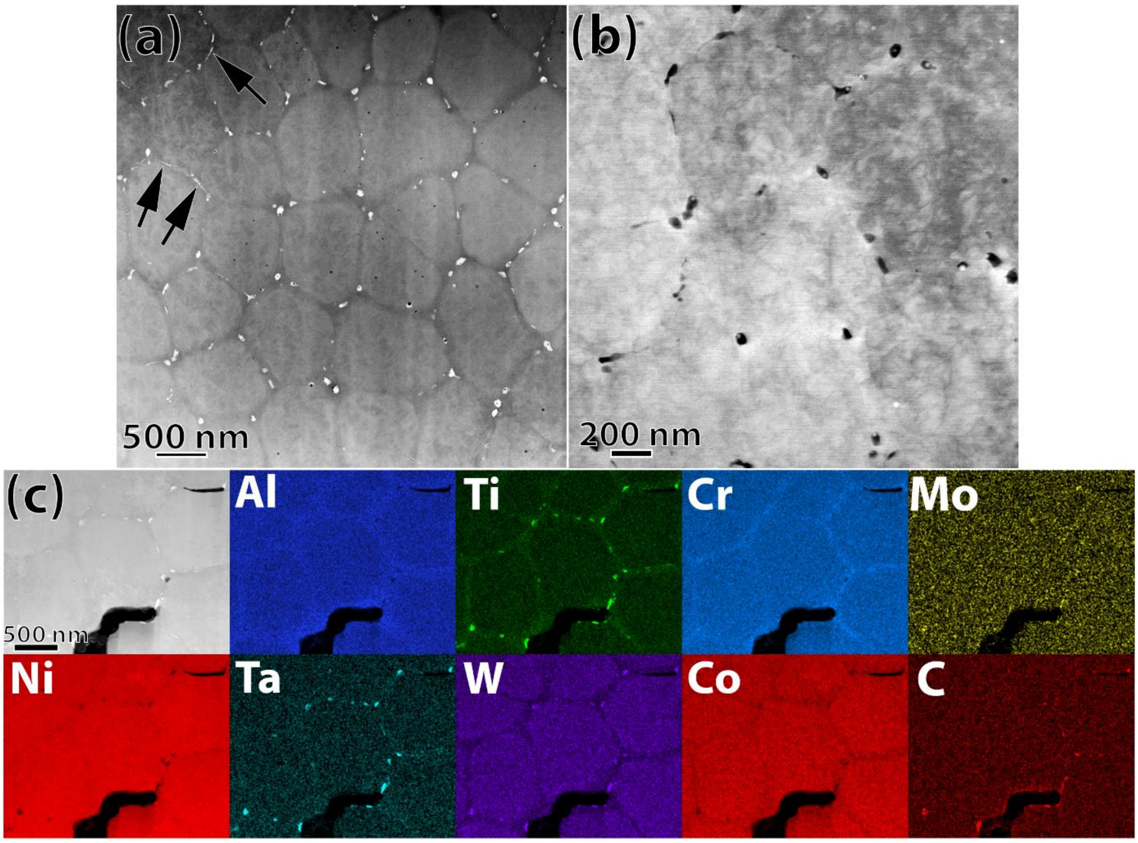

Figure 8.5: STEM characterization of the as-fabricated microstructure (transverse section) of a CM247LC NHf sample produced using Condition 2 (34.5 mm build plate). a) ADF-STEM image showing ~0.5-1 µm diameter cells surrounded by grain boundary precipitates, assumed to be carbides. Black arrows point to script like precipitates assumed to be carbides. b) BF-STEM image showing a high dislocation density throughout. c) STEM-EDX map of cell boundaries. The black region is a crack. Precipitates are enriched in Ti /Ta/W and are presumed to be carbides. The chemical analysis is performed with Al-K, Ti-K, Cr-K, Ta-L, W-L, Co-K, Ni-K, Mo-K, Zr-K, and C-K lines.

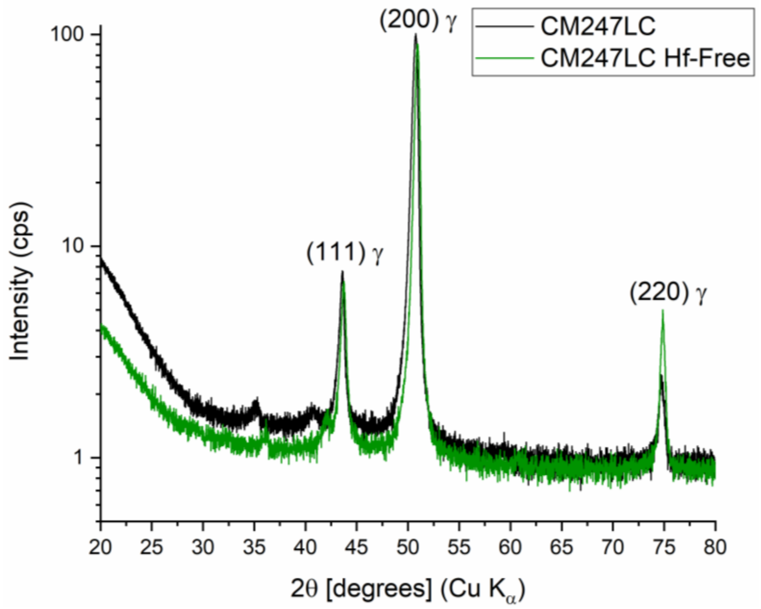

Figure 8.6: XRD patterns of as-fabricated CM247LC and CM247LC NHf. Samples were fabricated with Condition 2 (100 mm build plate) with build plate of 100 mm diameter. Small peaks around 35° and 40° may correspond to the carbides. A slight peak shift between the two samples is likely the result of lattice parameter changes caused by the elimination of Hf.

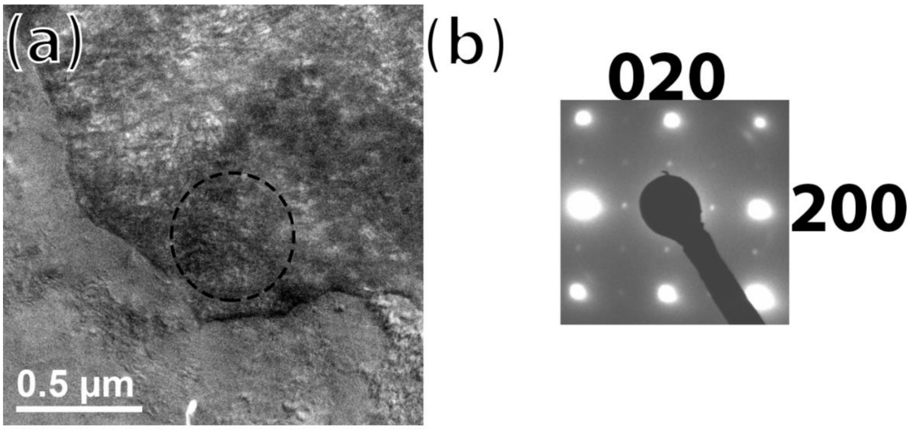

Figure 8.7: a) A low magnification BF-TEM image of the as-fabricated CM247LC NHf sample (Condition 2, 34.5 mm build plate). b) Selected area diffraction pattern along [001] taken from the circled region in a) showing the 100- and 110-type superlattice reflections of the L12 structure.

8.2.3 Defects

Micro-cracking was also observed in the CM247LC NHf samples and had similar behavior (perpendicular to beam travel direction) and similar appearance (dendritic appearance on the fracture faces) to the standard alloy described earlier (Figure 8.8 and Figure 8.9). The micro-crack density was significantly reduced. This point will be further developed in the next section.

Cracking behavior in the as-fabricated CM247LC NHf samples has also been studied using the same Gleeble test setup described prior. Analysis was performed to cover the full cross section and no new cracks or areas indicative of grain boundary melting were observed after the Gleeble experiment (not shown).

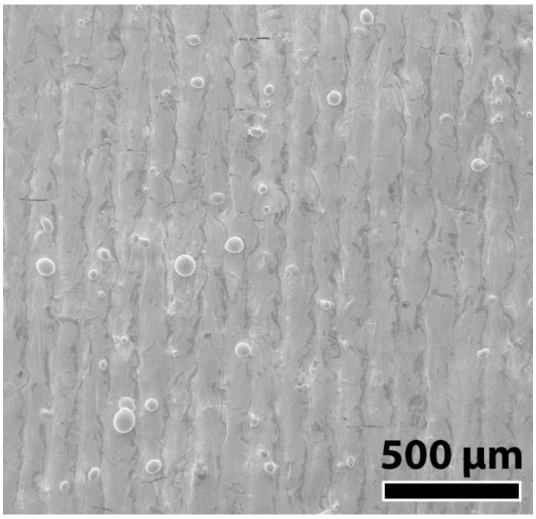

Figure 8.8: SE image of the top surface of a CM247LC NHf as-fabricated cube (Condition 1) (unidirectional scanned sample with no change in direction of layers). Cracking is transverse to direction of laser travel.

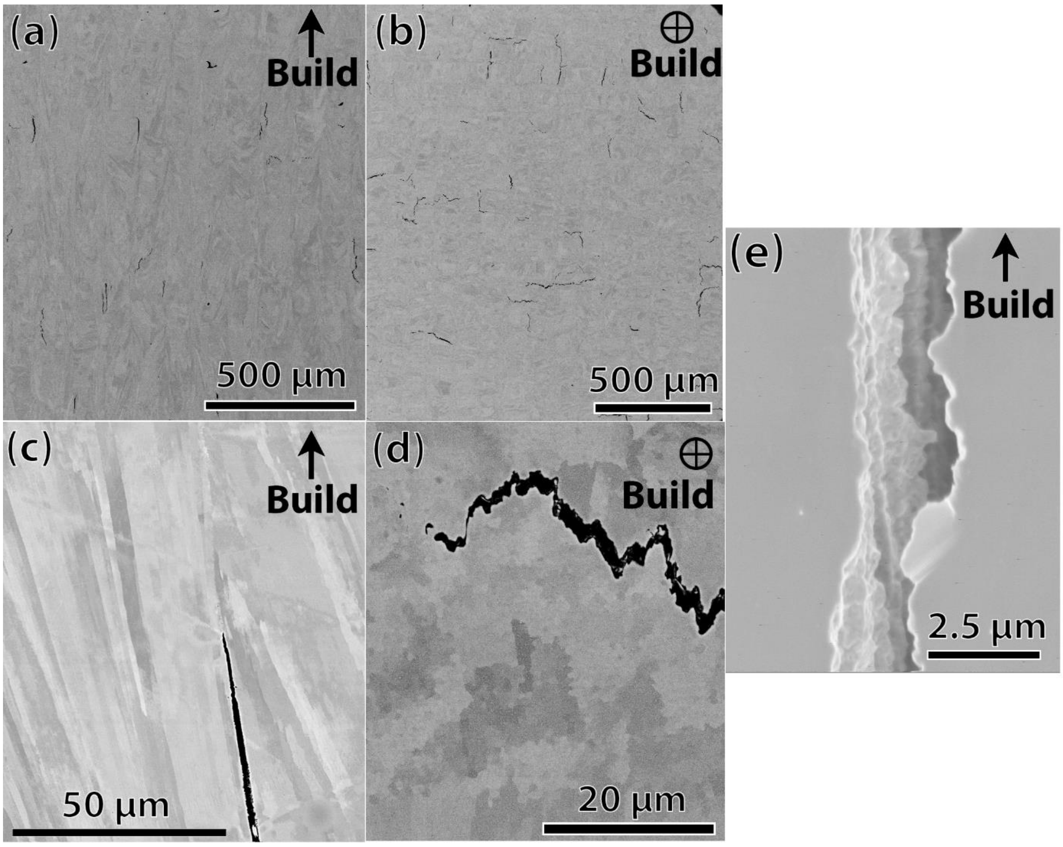

Figure 8.9: Electron microscope images taken from CM247LC NHf samples fabricated with Condition 1 and 2. a) BSE Image of a parallel cross section (Condition 1). b) BSE image of perpendicular cross section (Condition 1) c) Higher magnification BSE image of a crack observed in a parallel cross section (Condition 2, 100 mm build plate) d) Higher magnification BSE image of a crack observed in the perpendicular cross section (Condition 2 2, 34 mm build plate) e) SE image showing the features on the crack faces (Condition 2, 34.5 mm build plate).

8.2.4 Thermal Analysis

DSC measurements were performed on as-fabricated CM247LC NHf and CM247LC Condition 2 samples (Figure 8.10). Each thermogram is characterized by an exothermic reaction $T_{\gamma'}$, corresponding to the γ' dissolution, and two endothermic reactions which mark the carbide dissolution (T_C) and γ matrix melting (in the T_S-T_L range). The melting event is not sharply defined, more so in the CM247LC alloy. This phenomenon can be correlated to the dendritic segregation, which leads to incipient melting. For the CM247LC NHf alloy, the liquidus endset point is measured at 1392 °C and the solidus point is estimated at 1341 °C. The CM247LC sample had a liquidus point of 1384 °C and a solidus of 1282 °C. The γ' solvus temperature of the CM247LC NHf sample was lowered compared to the CM247LC sample, 1226 °C and 1255 °C respectively, which could correlate with a lower equilibrium γ' phase fraction. The CM247LC NHf carbide dissolution temperature increased compared to the CM247LC samples, 1368 °C and 1341°C respectively. The solidification range measured by DSC may understate the solidification interval as the Gleeble experiment on CM247LC performed at 1250 °C showed the presence of grain boundary melting. However, the experimental conditions for the DSC setup may not be optimal for getting a signal from minor grain boundary melting.

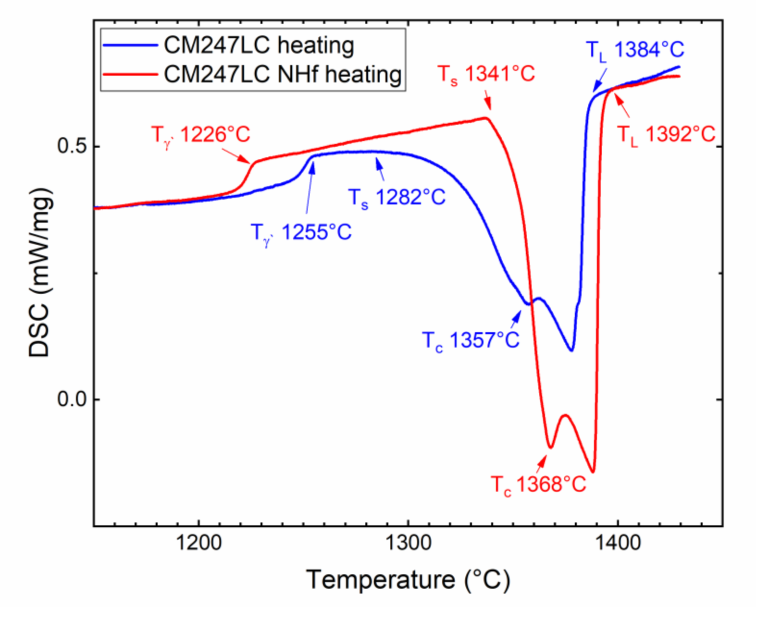

Figure 8.10: DSC thermograms on heating for both as-fabricated CM247LC and CM247LC NHf samples, built with Condition 2. $T_{\gamma`}$ is the γ`dissolution temperature, T_S is the solidus temperature, T_C is the carbide dissolution temperature, and T_L is the liquidus temperature.

8.2.5 Micro-crack Comparison with CM247LC

Optical images of parallel cross sections, showing representative micro-crack density, of as-fabricated CM247LC and CM247LC NHf produced with both Condition 1 and Condition 2 are shown in Figure 8.11. Results of the micro-crack density analysis are shown in Figure 8.12(a). Since micro-cracking was observed to be oriented at 0 and 90° to the image frame of the perpendicular cross section (Figure 7.8), the crack analysis of the parallel cross sections inherently exclude some cracks; however, the values are meant for comparison and the change in scanning direction after each layer ensures some homogeneity. The CM247LC, and CM247LC NHf samples fabricated with Condition 1 had mean crack densities of 1.27 mm/mm^2 and 0.81 mm/mm^2, respectively. The CM247LC, and CM247LC NHf samples fabricated with Condition 2 had mean crack densities of 0.12 and 0.03 mm/mm^2, respectively. A repeat experiment, to ensure validity of results, with Condition 2 parameters resulted in micro-crack densities of 0.14 and 0.02 mm/mm^2 for the CM247LC and CM247LC NHf, respectively. A Welch's unequal variances t-test was performed for each study to determine if the mean crack density between the CM247LC and CM247LC NHf were statistically different. The calculated *p* values, shown in Figure 8.12 (a), are all below 0.05, which is generally regarded as the threshold where one can say the difference in the means are statistically significant. The crack densities on the samples fabricated with Condition 1 were sufficiently high for crack length analysis. Histograms of the individual crack lengths from Condition 1 samples are shown in Figure 8.12(b) and (c). The mean crack length for both the CM247LC and CM247LC NHf samples is ~ 80 μm.

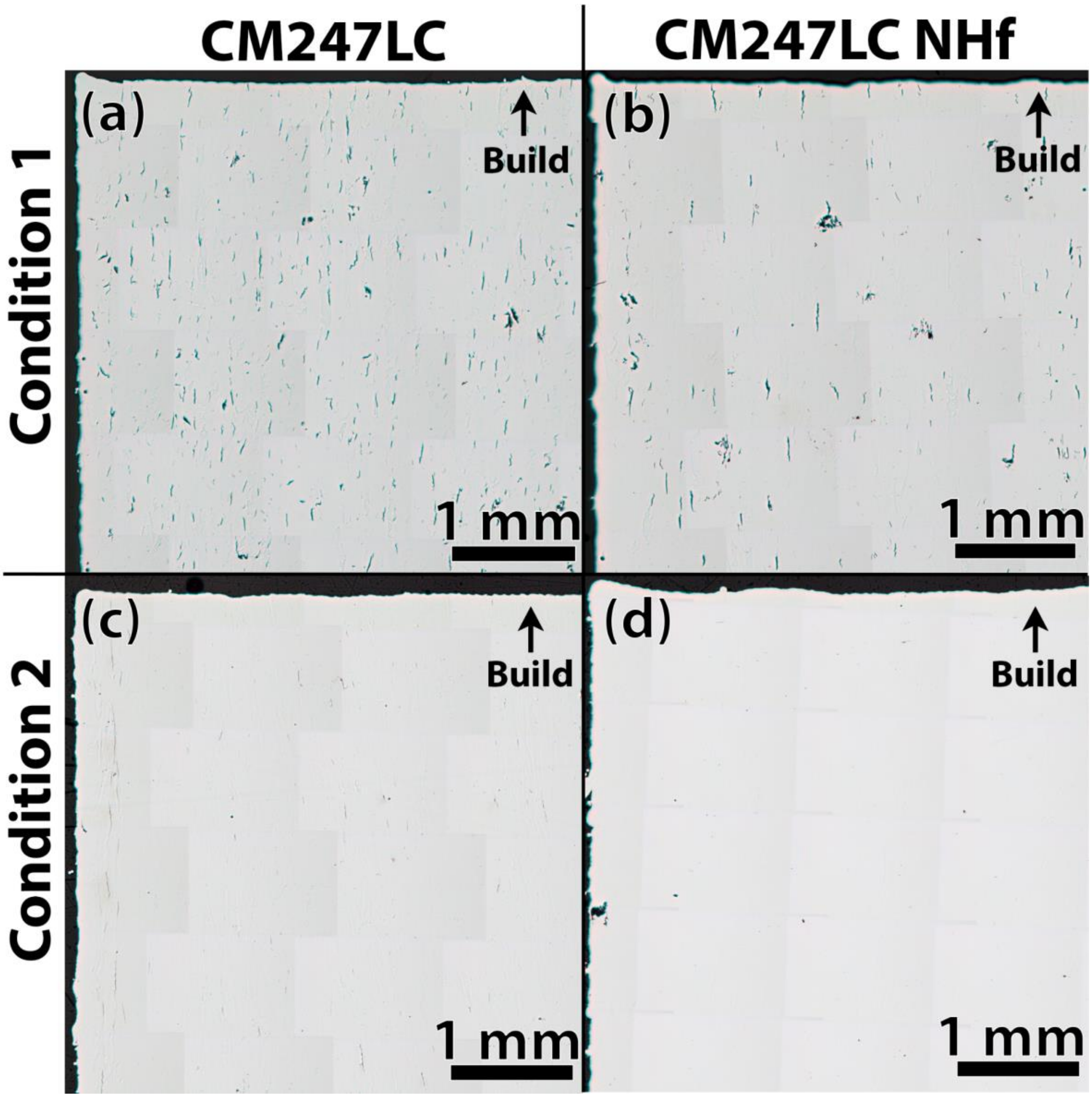
CM247LC
CM247LC NHf
Condition 1
Condition 2
(a)
(b)
(c)
(d)
Build
1 mm

Figure 8.11: a) Optical image of CM247LC sample fabricated by Condition 1 b) Optical image from CM247LC NHf sample fabricated with Condition 1. c) Optical image of CM247LC fabricated by Condition 2. d) Optical image of the CM247LC NHf fabricated by Condition 2.

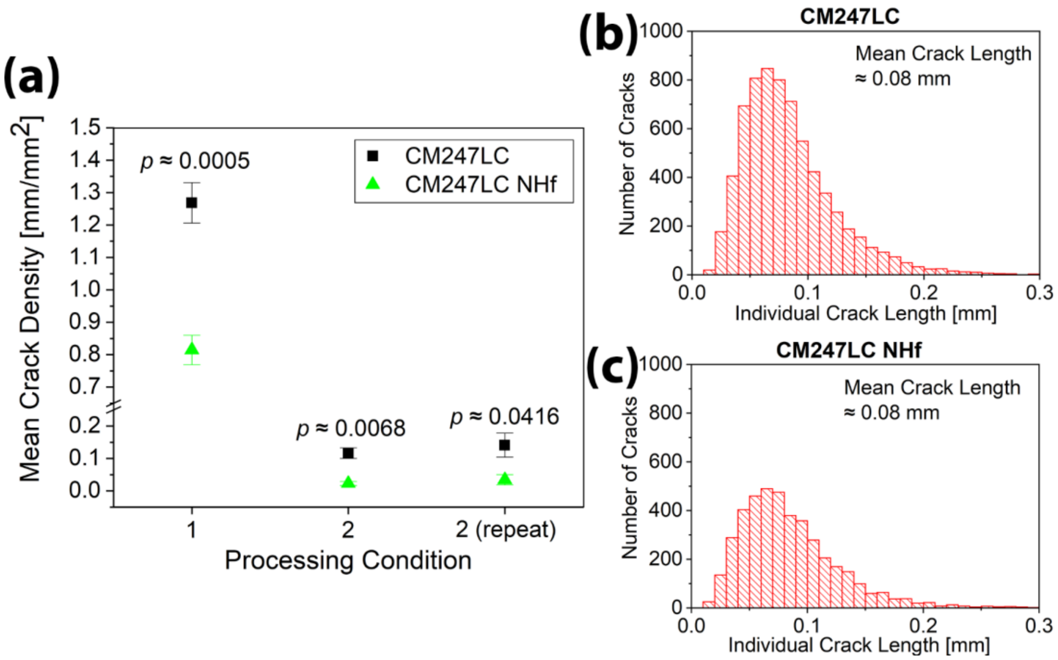

Figure 8.12: a) Mean micro-crack density. Error bars represent standard error of the mean. b,c) Crack length histogram of cracks observed in a parallel cross section of b) CM247LC and c) CM247LC NHf samples (Condition 1).

8.3 Discussion

8.3.1 Reduction of Micro-cracking in CM247LC NHf

The presented research highlights the importance of both alloy chemistry and processing conditions on micro-crack reduction of L-PBF fabricated γ` hardening Ni-base superalloys.

Samples fabricated with CM247LC NHf, when compared to the CM247LC samples, had a 36% and 75% reduction in crack density when fabricated using Condition 1 and Condition 2, respectively. The micro-cracks in the CM247LC NHf have a similar appearance to the micro-cracks in the CM247LC samples suggesting that solidification cracking is present in the modified alloy as well. Micro-crack length also did not change appreciably between the two alloys. Despite the reduction in the freezing range by removal of Hf, the alloy still has other alloying elements (Ti, Ta, Al, etc.) that partition to the liquid and increase the solidification range. The alloy CMSX-4, which is a derivative of CM247LC for single crystal use, does not contain Hf and is still susceptible to solidification cracking [6]. The Hf-free CM247LC alloy used in this study does have significantly higher levels of Zr (180 ppm compared to 60 ppm in the CM247LC alloy) which is known to contribute to hot cracking in these alloys. Reduction in the levels of B and Zr may reduce crack density further, but again may alter the creep performance of the alloy. The Gleeble test results show that the liquation cracking susceptibility of CM247LC NHf is lower than the

CM247LC. The CM247LC NHf still likely suffers from liquation cracking, but the increased solidus temperature of the boundaries means that less of the HAZ will be affected. The presented results are thus a strong evidence that modification of an alloy chemistry can reduce micro-cracking but, in the case of CM247LC; alone cannot eliminate the cracking. Process optimization will be required in addition to alloy modification to achieve the lowest possible micro-crack densities.

The micro-crack density of samples fabricated with Condition 1 were nearly an order of magnitude higher than samples produced with Condition 2. Micro-cracks were uniformly distributed throughout the cross sections of the Condition 1 sample, but Condition 2 samples did have a higher incidence of micro-cracking near the edges. The contour offset for Condition 2 was 25 µm larger than the hatch distance, and this may have resulted (for unknown reasons) in increased micro-cracking. Another potential explanation for the increased edge micro-cracking, is the existence of high tensile residual stresses at the part edges. It has been shown that tensile residual stresses are present in the top 1 mm of L-PBF fabricated CM247LC samples [78], and this may result in opening of cracks more on the edge than the bulk. The two most significant observed differences between Condition 1 and Condition 2 are in the melt pool profiles and fraction of HAGBs. While the melt pool widths were similar between the two conditions, Condition 1 melt pools were a factor of two deeper. Condition 1 samples also had a higher fraction of HAGBs compared to the Condition 2 samples. Both melt pool profile and grain boundary misorientation were discussed in section 4 as being factors that influence solidification cracking susceptibility. A narrow and deep melt pool is known to have a higher susceptibility to solidification cracking due to the increased level of restraint that is placed on the final solidification [132]. The melt pool dimensions will also influence the solidification conditions and the direction of columnar grain growth. As the melt pool aspect ratio increases (increasing depth), the misorientation between grains on opposite sides of the melt pool increases, thus leading to an increased amount of solidification cracking [134]. Other variables, such as the stress state, will be different between the two processing conditions, and will influence the solidification susceptibility; however, this was not characterized and the contribution to the overall susceptibility cannot be determined.

As previously mentioned, removal of any element will have implications for the alloy`s mechanical behavior and thus will need to be evaluated. Aside from the micro-crack reduction, three differences were observed when comparing the as-fabricated CM247LC and CM247LC NHf: (i) the CM247LC NHf sample had some script-like carbides on the cell boundaries, (ii) the γ` solvus temperature for the CM247LC NHf was reduced by 29 °C, and (iii) a decrease in lattice parameter of the CM247LC NHf sample due to the absence of Hf. Mechanical property tests will be conducted for both alloys in a future study to understand what changes the elimination of Hf causes in CM247LC.

8.3.2 Factors Influencing Melt Pool Width

Considering the spot size of Condition 2, 55 μm, the melt pool width, 180 μm, appears to be abnormally wide for a conduction mode melt. The reason for this wide and shallow melt pool, in regards to spot size, is likely due to the heat transfer mechanism that is dominant for this material. Using values for liquid Ni-base superalloys at a temperature of 1580°C (CMSX4: $k=0.328\ WK^{-1}cm^{-1}$, $Cp = 0.70\ JK^{-1}g^{-1}$, IN738LC: $\mu = 7.4$ mPa s) [86] and equation 5 a Prandtl number of 0.18 was obtained. The higher the Prandtl number, the more convection based heat transfer there is [13]. For instance, the Prandtl number for aluminum is 0.02, which means conduction dominates the heat transfer and the melt pools of Al will be more hemispherical [22]. The Prandtl number for stainless steels is 0.16, meaning that a flatter melt pool will result. Convective flow in a laser melt pool is largerly the result of surface tension driven flow and the extent of this flow will influence the melt pool profile as well. Anderson et. al [141] also observed wide and shallow melt pools on electron beam and laser welded CMSX-4 and attributed this behavior to the surface tension driven fluid flow from the center of the weld to the edges.

Tracking down the laser parameters that are the most responsible for producing the differences between condition 1 and 2 is challenging due to the large numbers of variables present (laser scan velocity, laser power, spot size, environment, etc.). Simply increasing the laser scan velocity may lower the interaction time enough that the transition from conduction mode to keyhole (or transition mode) is avoided. Also, decreasing the spot size, while keeping laser power constant, will result in a higher laser intensity that will favor keyhole formation. The laser intensity ($1/e^2$ radius) of Condition 1 and Condition 2 is $3.14x10^6\ W/cm^2$, and $7.35x10^6\ W/cm^2$ respectively. Despite the higher laser intensity of Condition 2, the scan velocity was 150 mm/s higher, which may explain why the Condition 2 melt pools have more of a conduction mode appearance. Due to the multiple variables involved, it is useful to calculate normalized values. Normalized power and normalized interaction time were calculated with equations 2 and 3 and overlaid on a plot of normalized power vs. normalized interaction time (Figure 8.13). The thermophysical parameters used in the calculations are shown in Appendix A Table 0-3. It is clear from Figure 8.13 that Condition 2 is further in the vaporization regime than Condition 1; however, Condition 2 resulted in conduction mode melting while Condition 1 resulted in a keyhole mode. In addition, normalized enthalpy values were calculated. The normalized enthalpy of Condition 2 (43.15) is higher than Condition 1 (26.34), suggesting that Condition 2 would be more favorable to keyhole formation; however, the opposite behavior is observed. One hypothesis for this behavior is based on the influence of in-process preheating.

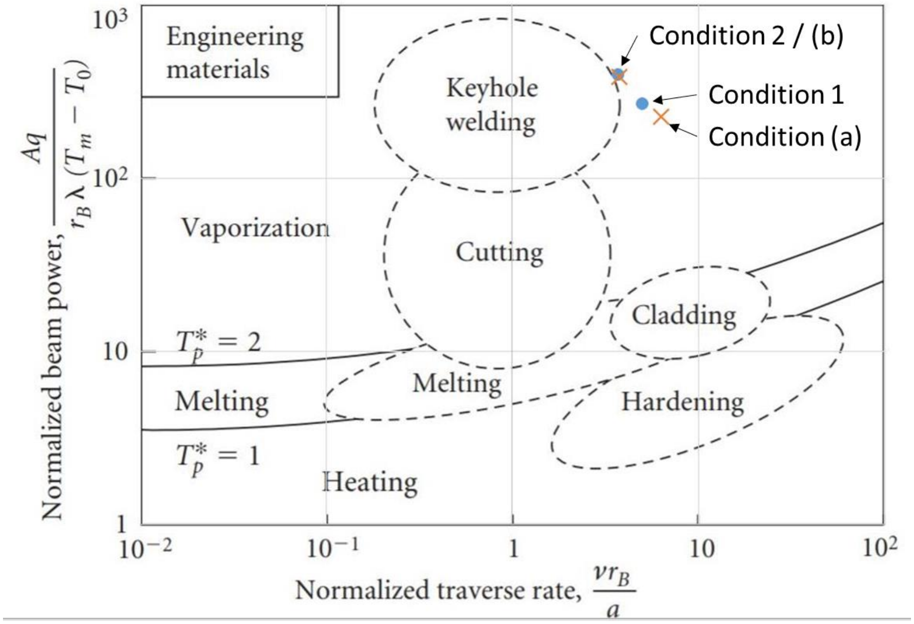

Figure 8.13: Processing conditions used overlayed on normalized processing parameter plot from [17]

There are several differences between the two commercial AM machines used in this study, such as, thermal mass, recoating time, sample size, and construction of machine modifications that would result in drastically different thermal conditions. The Condition 1 fabricated samples were fabricated on a machine with a much larger thermal mass (a larger amount of metallic parts are required to hold and move a 245 x 245 mm build plate) than the Condition 2 fabricated samples. The recoating time (time between laser scans) is generally longer for the Condition 1 samples than the Condition 2 samples, which would provide additional time for heat dissipation. The aluminum support structure used to hold the reduced build platform for the fabrication of Condition 1 samples would further dissipate heat. Lastly, the larger sample sizes of the Condition 1 fabricated samples would increase the thermal mass of the system. Also considering the higher normalized enthalpies of Condition 2, it can be assumed that the Condition 2 fabricated samples had a higher level of preheat than the Condition 1 fabricated samples.

A simple experiment highlighting the influence of preheat on melt pool geometry is shown in Figure 8.14. Figure 8.14 shows an optical image of an etched Condition 2 fabricated sample (Figure 8.14(a)) and an optical image of an etched Condition 2 fabricated sample with a 60 second cooling period added between each layer (Figure 8.14(b)). While no quantifiable data was gathered, it is a safe assumption that the 60 second time delay resulted in a lower baseline temperature, in other words, lower pre-heating, than the standard processing route. Interestingly, the "colder" sample showed extensive signs of keyhole formation (Figure 8.14). This behavior is somewhat counter-intuitive as a material with a higher starting temperature will require less absorbed enthalpy for vaporization (keyhole formation). One possible explanation for the keyhole formation in the "colder" sample is related to the thermal diffusivity. Aune et al. [86] reported thermal diffusivities in CMSX-4, a similar Ni-base superalloy, of ~0.025 cm^2/s and ~0.050 cm^2/s at ~300 K and at ~1500 K, respectively. A higher pre-heat in the standard process will result in a higher thermal diffusivity that may inhibit keyhole formation. Indeed, per the normalized enthalpy in equation 2 and using the extremes of thermal diffusivities listed above, the normalized enthalpy for the low diffusivity case (~0.025 cm^2/s) is 54.6 and for the high thermal diffusivity case (~0.050 cm^2/s) is 38.6. The higher normalized enthalpy of the "colder" condition may be sufficiently high enough that keyhole formation occurred. King et. al. [20] reported the threshold for keyhole formation to be at a normalized enthalpy of 30 ±4; however, it is plausible that the threshold for the conditions in this study is higher. It is important to note that once the threshold to keyhole mode melting is crossed the absorptivity and therefore the normalized enthalpy will greatly increase.

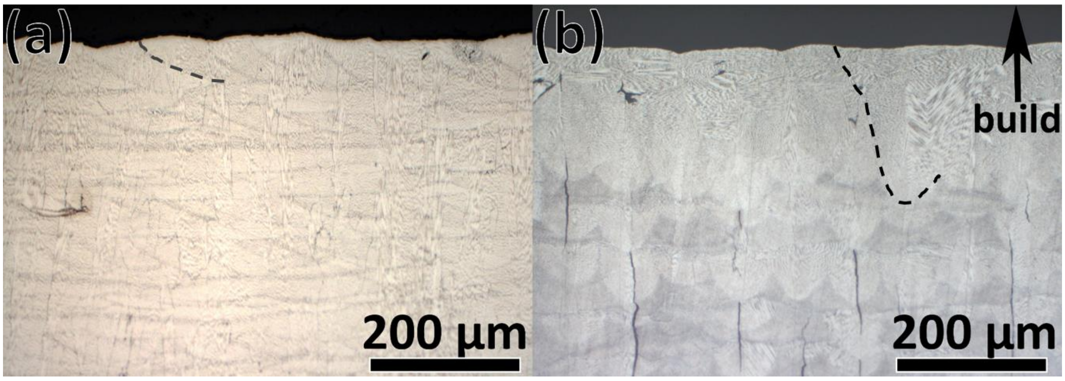

Figure 8.14: (a) Optical image of an etched CM247LC Condition 2 fabricated sample (b) Optical image of an etched CM247LC Condition 2, with 60 second delay, fabricated sample. Dashed lines highlight the melt pools.

It is hypothesized that the combination of the aforementioned factors led to a higher baseline temperature for the Condition 2 fabricated samples that resulted in a higher thermal diffusivity that favored lower crack density conduction mode melts. In addition, an increase in preheat would result in lower thermal residual stress, which may contribute to the lower micro-crack density of the Condition 2 fabricated samples.

A high pre-heat temperature may result in the modification of the convective heat transfer in the melt pool. Two dimensionless numbers which can describe melt pool profiles in laser welds are the Peclet and Marangoni numbers [22,23]. The viscosity of liquid

CM247LC decreases with an increase in temperature [86]. The higher baseline temperature of the Condition 2 fabricated samples may result in a melt with a lower viscosity that would increase the Marangoni number (assuming ΔT and α in the liquid is unchanged), per equation 7, and increase the Peclet number per equation 6. A higher Peclet number, due to the increased surface tension driven flow, indicates that convective heat transfer becomes more important, which would result in a wider melt pool. Since the major difference between the Condition 1 and Condition 2 melt pools is the melting mode (conduction vs. keyhole) and not simply a wider conduction mode melt, it is hypothesized that the differences in absorbed enthalpy and not the magnitude of convection are the primary responsible factors.

Another possible explanation for the observed melt pool profile differences between Condition 1 and 2 lies in the influence that the processing parameters have on the Marangoni convection in a conduction mode melt pool. For CM247LC and other Ni-base superalloys, the surface tension decreases with increasing temperature as shown in Figure 8.16. This means that the surface tension will be lowest in the center of the melt pool, where the temperature is the highest, and highest on the edges of the melt pool, where the temperature is the lowest. The surface tension gradient will then result in fluid flow from the center to the outside. One primary difference between the two processing conditions is the laser intensity. Condition 1 had an laser intensity of $3.14\text{x}10^6$ W/cm^2 and Condition 2 had a laser intensity a factor of two higher, $7.35\text{x}10^6$ W/cm^2 . An increase in laser intensity will result in a greater ΔT in the melt pool, which will in turn result in higher Marangoni flow per equation 7. An increase in velocity due to increased Marangoni convection will result in a higher Peclet number per equation 6. The higher Peclet number implies that heat transfer via convection becomes more dominate, causing the melt pool to become wider and shallower [23].

A model experiment was performed to investigate the influence of the spot size on the melt pool dimensions. In this experiment, two line scans were made on a sandblasted CM247LC (taken from root of a turbine blade) substrate with the following parameters: Condition a: 170 W, 750 mm/s, 90 µm spot (1/e^2, Concept) and Condition b (nearly identical to Condition 2): 170 W, 750 mm/s, 55 µm spot (1/e^2, Sisma). The process parameters were normalized using equations 2 and 3 from Chapter 2 and plotted on Figure 8.13. When all of the processing parameters, except for spot size, are held constant, Condition 2 (Condition (b)) is still further into the vaporization regime than Condition a, suggesting that the lower velocity of Condition 1 was not the primary reason why Condition 1 had a keyhole mode melt. Figure 8.15 shows BSE images of the cross section of Condition a and Condition b melt pools. The Condition a melt pool is ~140 µm wide and ~70 µm deep (Depth to width: 0.5), and the condition b melt pool is ~147 µm wide and ~110 µm deep (Depth to width: 0.75). The melt pools appear to follow what the normalized parameters suggest; Condition b is further in the vaporization regime and in result, it has a deeper melt pool than Condition a. It is interesting to note, that on a solid substrate, Condition 2 (Condition b) resulted in a keyhole model melt, as one would expect given the normalized power and normalized traverse speed, but during the L-PBF process it resulted in a wide conduction mode melt. This observation highlights the significant difference in melt pool behavior from laser welds to L-PBF.

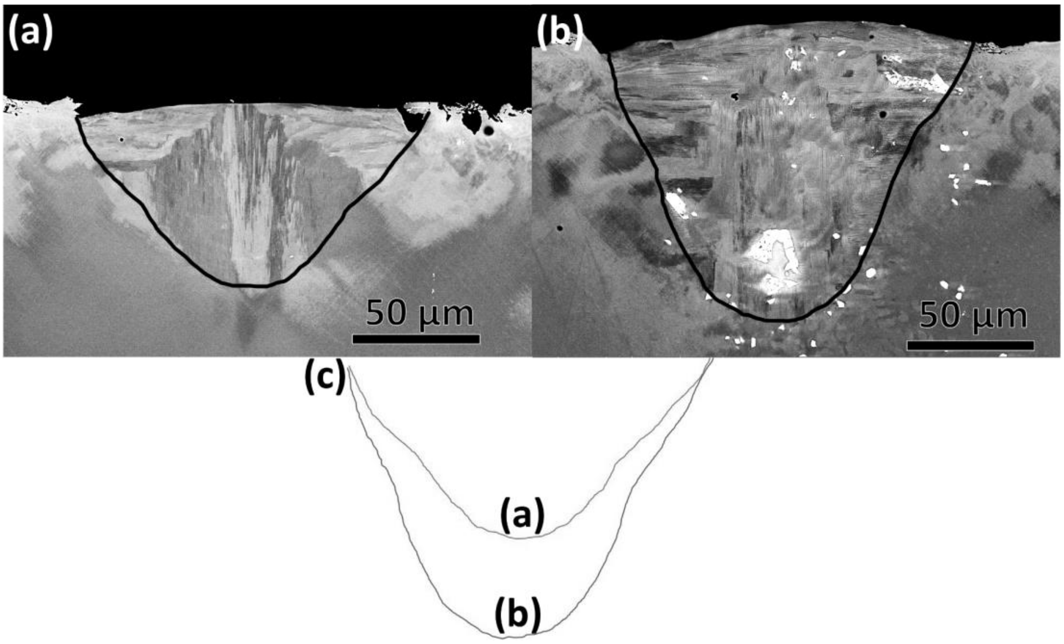

Figure 8.15: (a) Cross section of Condition (a) melt pool. (b) Cross section of Condition b melt pool. (c) Overlay of the two melt pool profiles.

Another difference between the two machines is the oxygen content (environment) while processing. It is impossible to determine the exact oxygen content where the laser-material interaction occurs, since the sensors for oxygen are not at that location. The oxygen sensors on commercial AM machines are typically located away from the processing zone. Furthermore, the oxygen sensors are mounted in different locations on each machine, making a comparison challenging. The influence oxygen has on surface tension for CMSX-4 is shown in Figure 8.16. An increase in O content reduced the surface tension and increases the gradient. Unlike the influence of S content on steel melt pool dynamics, oxygen does not reverse the slope of the surface tension gradient. While oxygen will still influence the surface tension driven flow, it is not expected to have a major impact on the melt profile.

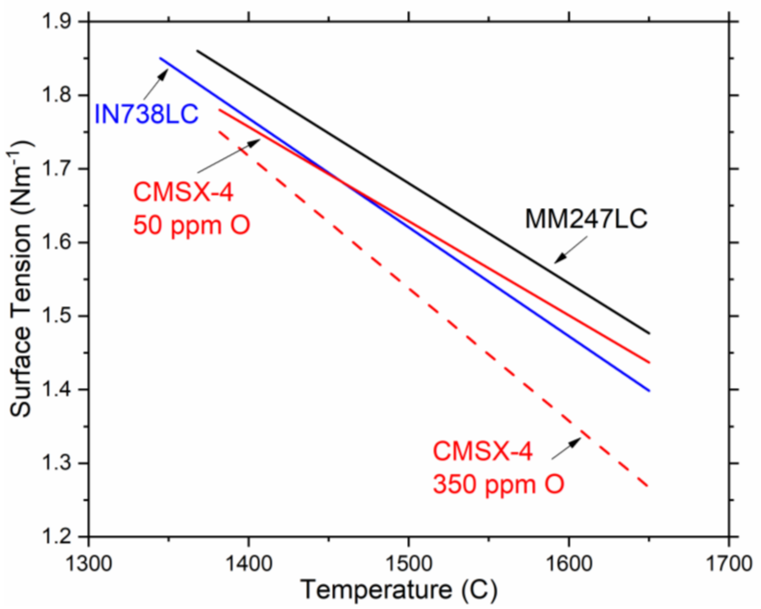

Figure 8.16: Surface tension of selected γ′ prime forming Ni-base superalloys as a function of temperature. The surface tension of a high and low O content CMSX-4 is shown to highlight the influence of O. Values taken from [142].

Lastly, another critical variable that can influence the melt pool profile is laser-vapor interaction. As previously mentioned in Chapter 2, the laser radiation that the material is exposed to can be substantially different than the laser radiation coming out of the lens. Plasma generated during the process can reduce the laser intensity, via Inverse Bremsstrahlung absorption, that reaches the substrate. Similarly, metallic vapor in the atmosphere will reduce the radiation reaching the substrate, due to scattering. It is known that Nd:YAG (1064 nm) welding results in nanometer sized particles in the welding plume and that these particles can result in scattering of the laser radiation [143]. The scattering can not only lead to a attenuation of the power, but also a broadening of the laser spot . One key difference between the Condition 1 and 2 is the laser beam intensity. The higher intensity of Condition 2 will lead to more metal vaporization, which in turn could lead to a higher density of metallic nanometer sized particles in the plume. The increase in scattering of the beam in Condition 2 could lead to an effective spot size that is much larger than the 55 μm manufacturer $1/e^2$ spot size. Measurement of particle density in the plume and modeling of the plume scattering would be required to prove/disprove this hypothesis.

8.3.3 Influence of Other Processing Conditions

Since most parts will not be cubes, and will likely have different thermal conditions than the previously presented cubes, it is useful to have a look at other geometries and other processing conditions (i.e. scan strategy). First, one of the more commonly used scanning strategy, chess scanning, will be investigated. Optical images of the CM247LC and CM247LC NHf samples fabricated with Condition 1 (chess scanned) are shown in Figure 8.17. Crack analysis was performed identical to that described in Chapter 3. The CM247LC and CM247LC NHf chess scanned samples had crack densities of 0.55 ± 0.03 and 0.54 ± 0.07 mm/mm^2, respectively (error represents the SE of the mean). No significant difference in micro-crack density was observed between the two alloys when fabricated with the chess scanning strategy. Compared to the bi-directional scanning strategy, the chess scanning had approximately half the micro-crack density. The only significant observed difference between samples fabricated by the chess and bi-directional scanning strategy was in the grain microstructure. The sample fabricated with the chess scan strategy sample did have a higher fraction of smaller equiaxed grains (qualitative observation from EBSD maps) compared to the bi-directional scanning strategy. This is expected due to the nature of the chess scanning strategy (scans never being directly in the same xy location) and similar observations of pockets of fine grains have been made on L-PBF fabricated CM247LC [9]. In general, finer more equiaxed grains are less prone to solidification cracking as discussed in Chapter 7. Also, crack propagation will be more stunted in a sample where the columnar grain microstructure is occasionally broken up like it is in the chess scanned samples. These two reasons may explain the lower micro-crack density of the chess scanned samples. Another possible explanation could be that the chess scanning strategy results in a lower residual stress than the bi-directional scanning strategy, but this was not investigated. Interestingly, Carter et al. [2] observed a higher incidence of microcracking in the chess scanning strategies than those with a bi-directional scanning strategy. While exact processing conditions used in their study is unknown, their opposite observation implies there is another variable more influential than scan strategy.

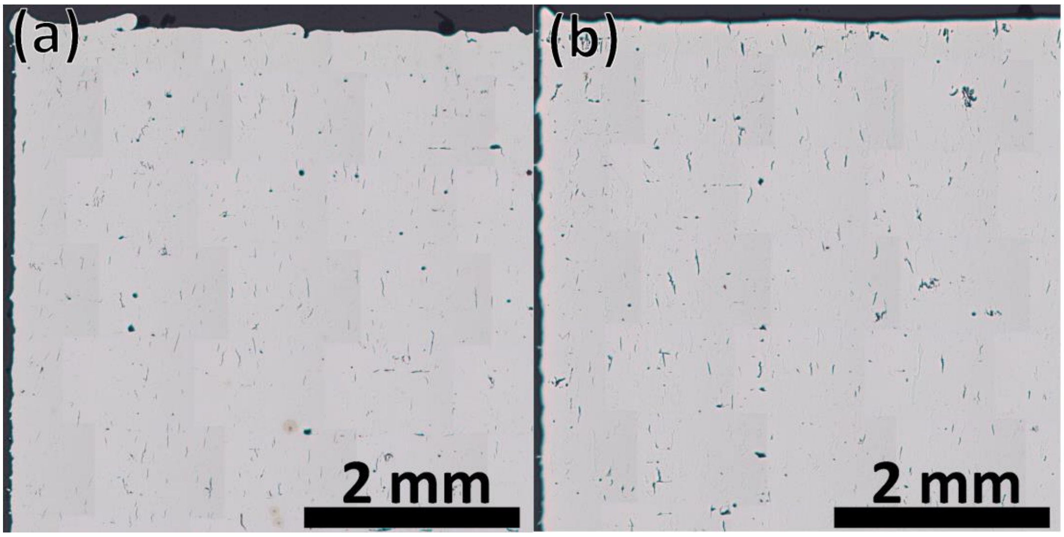

Figure 8.17: a) Optical image of CM247LC sample fabricated by Condition 1, but with chess scanning. b) Optical image from CM247LC NHf sample fabricated with Condition 1, except with chess scanning.

The investigation of a different sample geometry centered on an overhanging cylinder geometry that was presented in [8]. The geometry was selected in attempt to replicate the asymmetric cracking (less on the support side) that was observed. Figure 8.18 shows optical images of metallographic cross-sections of CM247LC (a) and CM247LC NHf (b) of two as-fabricated 45 degree cylinders (complete images are shown in Figure 0.14). Similar to the cubes, micro-cracking occurred parallel to the build dimension for both alloys. The micro-cracks had a similar appearance (Figure 8.19) to the micro-cracks observed in the cubes; therefore, it can be assumed that a similar mechanism is at play (solidification cracking). Crack density quantification was done using the same procedure as with the cubes, but only two slices per part were used. The CM247LC cylinder had a crack density of 0.40 ± 0.17 mm/mm^2 and the CM247LC NHf cylinder had a crack density of 0.31 ± .02 mm/mm^2 (± values represent SE of the mean). While the CM247LC NHf cylinder had a lower mean crack density, one of the slices of the CM247LC cylinders had a lower crack density. More slices would be needed to provide better statistics. Either way, the cylinders have ~3 times as many cracks as the cubes suggesting either the solidification conditions or the overall residual stress state is different between the two.

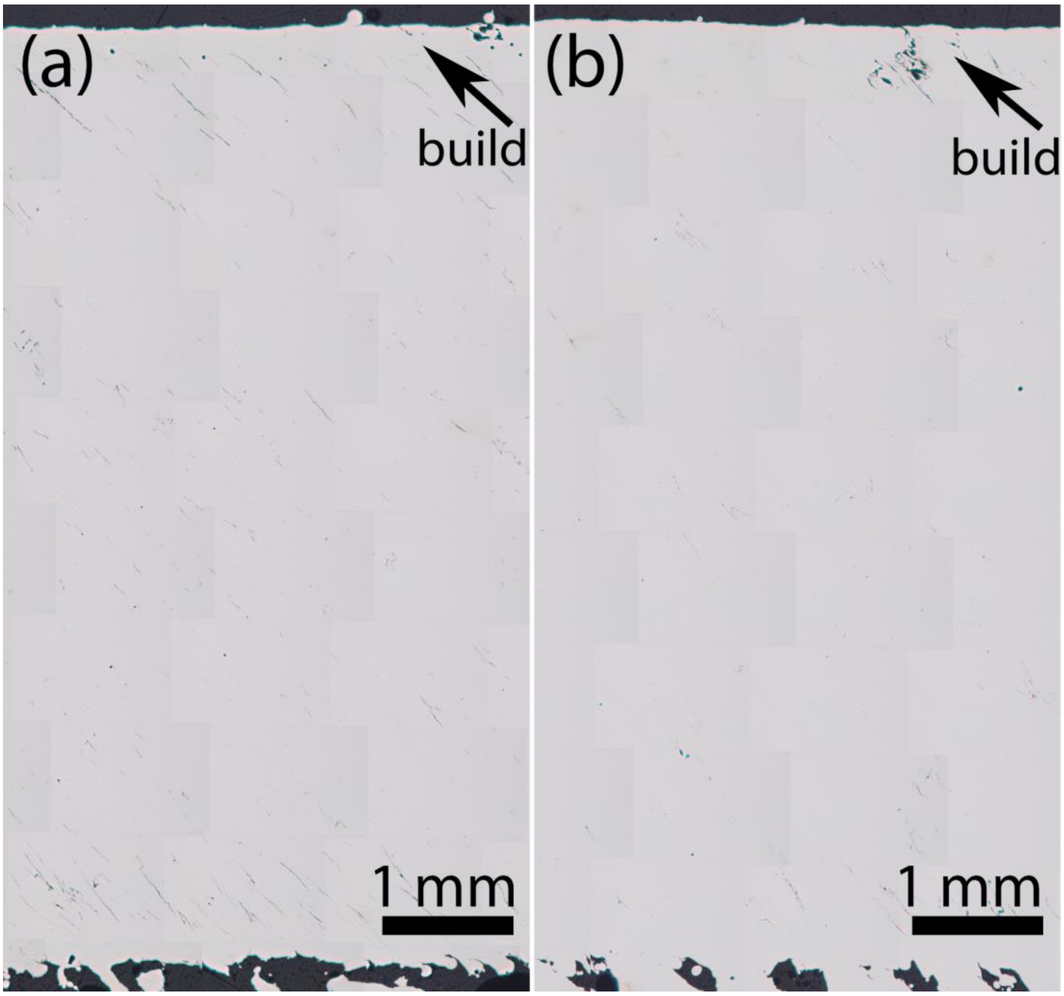

Figure 8.18: Optical images of metallographic cross-sections of CM247LC (a) and CM247LC NHf (b) of two as-fabricated 45 degree cylinders (complete images are shown in Figure 0.14).

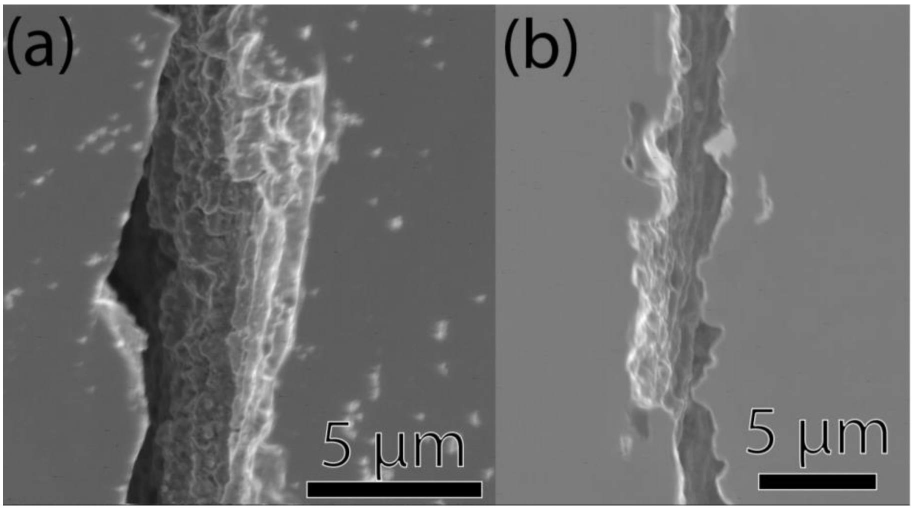

Figure 8.19: SE images showing the rough surface of the crack faces in as-fabricated (a) CM247LC and (b) CM247LC NHf.

Another interesting observation is made when a forced cool down period of 60 seconds between layers is implemented (the same experiment was discussed in the prior section), which can mimic a situation where the build plate is large and scanning time between layers is long. Figure 8.20 shows optical images of metallographic cross-sections of CM247LC (a) and CM247LC NHf (b) cubes processed with Condition 2 except for a 60 second time delay between each layer. Quantitative measurements were not made, but qualitatively, it is clear that the time delay resulted in significantly higher micro-cracking for both alloys and even resulted in edge porosity for the CM247LC NHf sample. One hypothesis for the increased micro-crack density is that keyhole mode melting occurred due to the cool down period, which was discussed in the prior section.

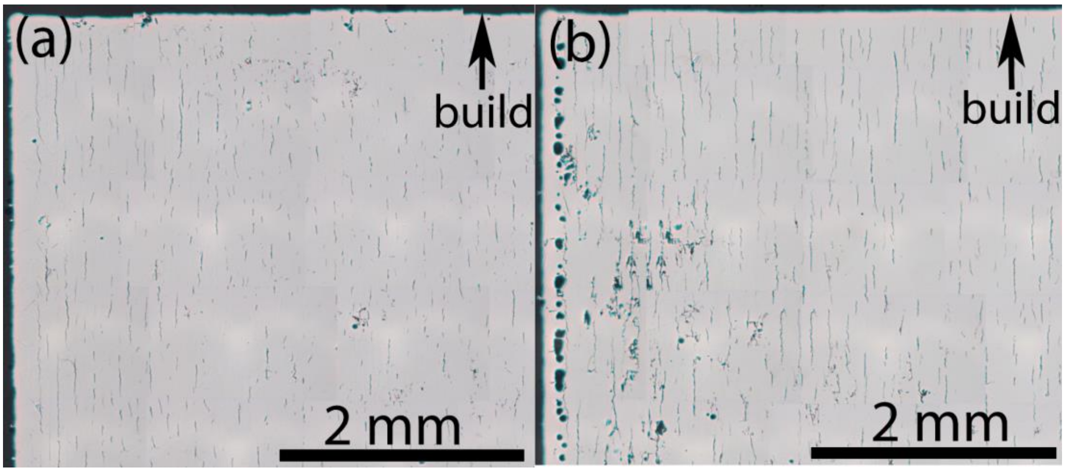

Figure 8.20: Optical images of (a) CM247LC and (b) CM247LC NHf fabricated with Condition 2 parameters except with a 60 second time delay between layers.

8.4 Conclusions

A reduction in micro-cracking was observed in the modified CM247LC, CM247LC NHf. The removal of Hf, a melting point depressant, reduces the solidification range of the alloy, and thus mitigates both solidification and liquation cracking of the heat-affected zone during fabrication. Additionally, the use of different machines, translated into differences in process parameters, was shown to be critical on mitigating the micro-cracking. Tight control on chemistry and processing is thus needed to produce defect-free parts. Particularly, the following conclusions were reached:

- Processing Condition 2 resulted in a lower micro-crack density compared to processing Condition 1. The melt pool profile of Condition 2 (shallow and wide) is far less susceptible to solidification cracking due to lower restraint and less HAGBs.

- It is hypothesized that the wider and shallower melt pools of Condition 2 are the result of in-process preheating that increased the thermal diffusivity of the sample enough that keyhole formation was avoided.
- A new Hf-Free version of CM247LC, CM247LC NHf, was developed to mitigate micro-cracking of CM247LC via solidification range reduction. Samples fabricated with CM247LC NHf had between 36% to 75% reduction in crack density, depending on the condition used, compared to the CM247LC alloy.

Chapter 9 Metallurgy of heat treated CM247LC and CM247LC NHf

9.1 Peak Age Determination

Unlike the Al-base superalloys, the Ni-base superalloys, such as CM247LC, have a high solid solubility for the γ'-formers; therefore, they are solutionized prior to aging. The solutionizing temperature for the Ni-base superalloys is generally limited at the upper end due to incipient melting concerns (1255°C to 1282°C solutionizing range for L-PBF fabricated CM247LC). The solutionizing temperature chosen for this study was 1260°C, which is the same for solutionizing of Directionally Solidified (DS) CM247LC [144]. The solutionizing window is much larger for CM247LC NHf (1226°C to 1341°C) due to the removal of Hf, but for comparison, it was solutionized at the same temperature. Aging for DS CM247LC is typically done at 870°C [38]; however, a temperature of 850°C was utilized for this study due to logistical reasons.

A plot of the microhardness of as-fabricated, solutionized (1260°C, 2 h), and solutionized and isothermally aged (850°C) CM247LC and CM247LC NHf processed with Condition 2 is shown in Figure 9.1. As-fabricated microhardness of CM247LC and CM247LC NHf was 4337±145 MPa and 4226±92 MPa respectively. After solutionizing, the microhardness of CM247LC and CM247LC NHf was 4534±92 MPa and 4575±65 MPa, respectively. Peak-age hardness for CM247LC was 5209±104 MPa after 8 hrs at 850°C. The CM247LC NHf appears to reach peak hardness (4999±115 MPa) after 2 hours at 850°C. At 8 hours at 850°C, the CM247LC NHf has a hardness of 4843±111 MPa. For both alloys, there is a slight plateau in the hardness values from 2 hours to ~100 hrs. After 100 hrs, the microhardness of both alloys decreases at a similar rate.

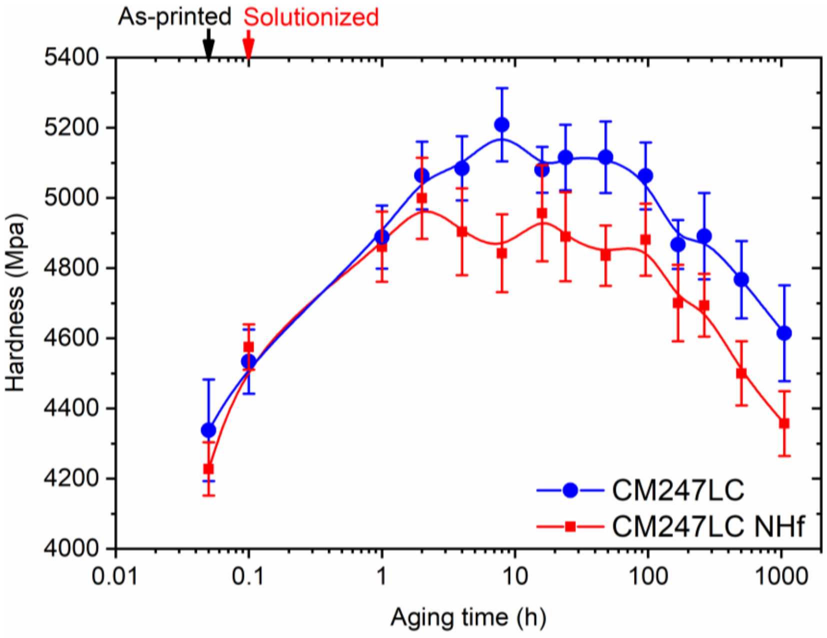

Figure 9.1: Plot showing the evolution of microhardness with aging time at a temperature of 850°C. Figure courtesy of S. Joglekar and J. Pado and A. De Luca.

Equivalent radius of the γ` precipitates in the isothermally aged samples is shown in Figure 9.2. After solutionizing, the CM247LC and CM247LC NHf have mean γ` precipitate radii of 120 and 70 nm, respectively. After aging at 850°C for 8 hours, the CM247LC and CM247LC NHf have equivalent radii of 55 and 34 nm, respectively. An inverse coarsening behavior (precipitates getting smaller) is observed until 8 hours and then the γ` precipitates coarsen after that. A bi-modal distribution of γ` precipitates was observed in the CM247LC samples during the initial hours of aging (at 1 hr, γ` precipitate mean radius of 120 and 37 nm.), but this was not observed in the CM247LC NHf samples (Figure 9.4). Given the smaller γ` precipitate size observed in the CM247LC NHf samples, the smaller size γ` precipitates may not have been resolvable.

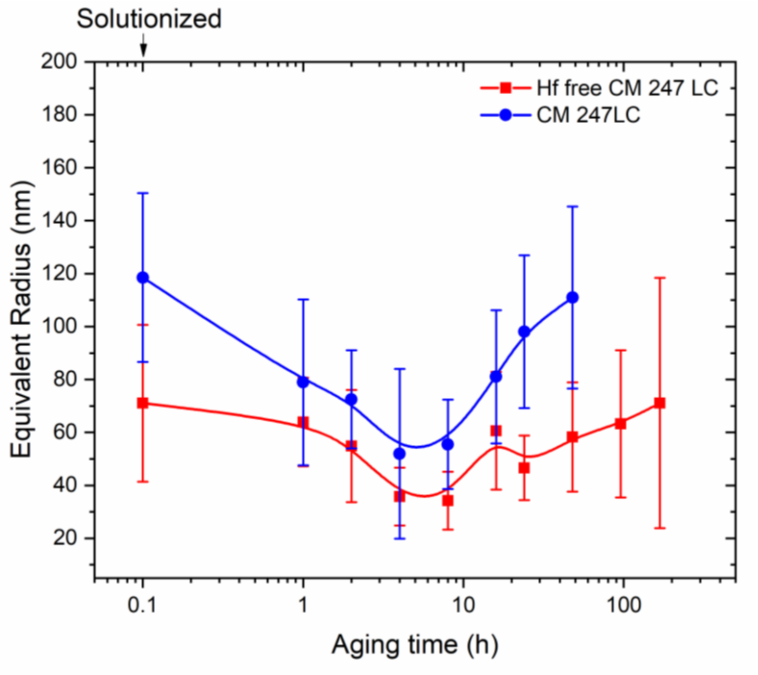

Figure 9.2: Equivalent radius of γ`precipitates at various isothermal aging (850°C) times. All samples were solutionized (1260°C, 2 hr) prior to aging. Figure courtesy of S. Joglekar and J. Pado and A. De Luca.

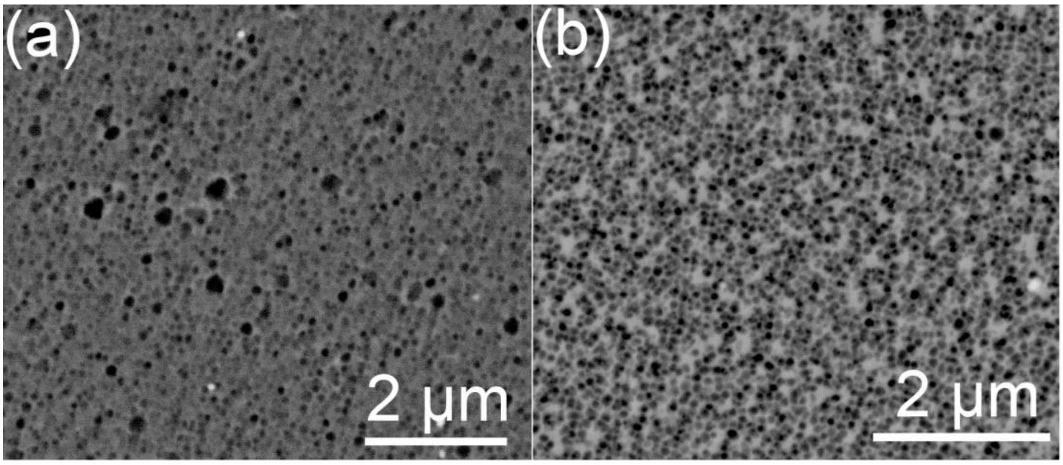

Figure 9.3: BSE images of (a) CM247LC and (b) CM247LC NHf solutionized(1260°C, 2 hr) and aged (850 C 8hrs).

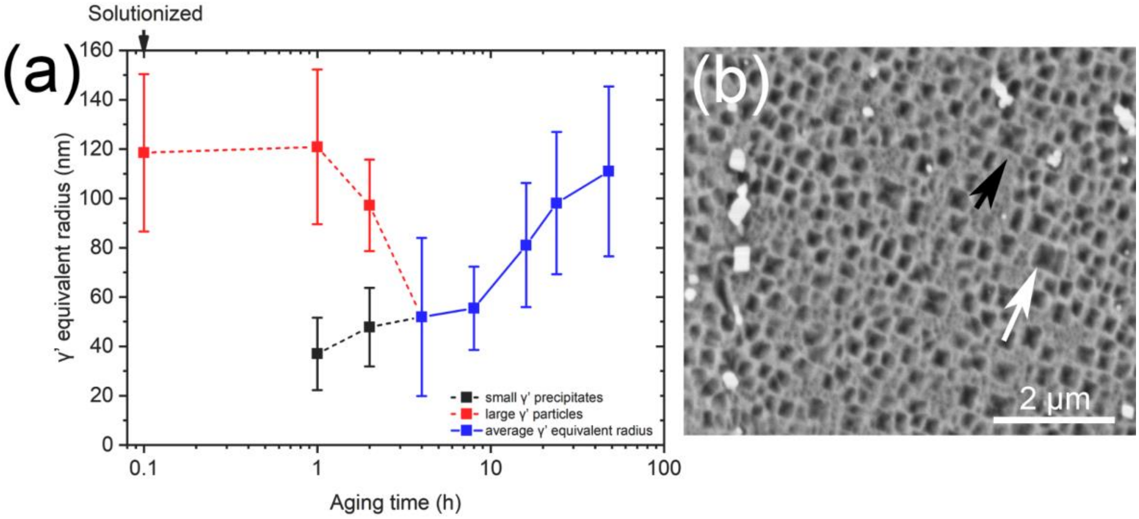

Figure 9.4: (a) Equivalent radius of γ`precipitates in CM247LC at various isothermal aging (850°C) times. A bi-modal distribution is observed until 4 hrs. Figure courtesy of S. Joglekar and J. Pado and A. De Luca. (b) BSE image of the bi-modal γ`precipitate distribution. The white arrow point to 120 nm radius precipitates and the black arrow points to 37 nm radius precipitates.

9.2 Microstructure and defects of heat treated CM247LC and CM247LC NHf

The microstructure of HIPed (1225°C, 5 h, 1000 bar) CM247LC and CM247LC NHf is shown in Figure 9.5. Minimal porosity and no micro-cracking was observed in the HIPed samples (not shown). No significant grain microstructure change was observed in the HIPed CM247LC samples, aside from carbide coarsening (~55 nm as-fabricated, ~100-800 nm HIPed). The grain microstructure of HIPed CM247LC NHf samples has recrystallized and numerous annealing twins are observed. Carbide coarsening was also observed in the HIPed CM247LC NHf samples (~60 nm as-fabricated, ~100-900 nm HIPed). Since the next stage in the thermal processing was solutionizing, γ` precipitates were not analyzed.

The microstructure of HIPed and solutionized (1260°C, 2 h) CM247LC and CM247LC NHf witness bars is shown in Figure 9.6. Recrystallization and grain growth has occurred for the HIPed and solutionized (1260°C, 2 h) CM247LC sample (Figure 9.6(a)). No significant difference in grain microstructure was observed for the HIPed and solutionized CM247LC NHf samples compared to the HIPed CM247LC NHf samples. Cuboidal γ` precipitates were observed in HIPed and solutionized CM247LC and CM247LC NHf samples. The γ` precipitates (in the center of the witness bar) were ~150-200 and~150-250 nm in radius for the CM247LC and CM247LC NHf samples, respectively. The carbide size (in the center) for the CM247LC and CM247LCNHF HIPed and solutionized samples is 0.44±1.50 and 0.35±0.4 µm, respectively. (feret size, measured by image analysis). The HIPed and solutionized CM247LC sample appears to have rougher grain boundaries than that of the CM247LC NHf samples, but this was not quantified.

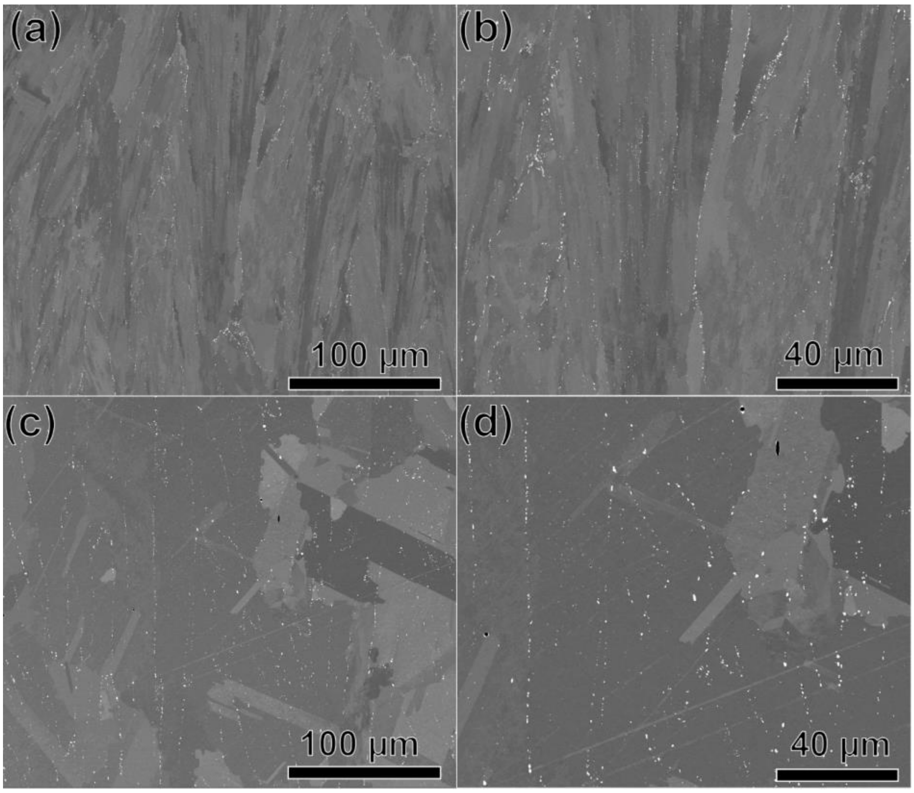
(a)
100 µm
(b)
40 µm
(c)
100 µm
(d)
40 µm

Figure 9.5: BSE images of HIPed mechanical test bars. Images approximately taken from the center of the 80 mm bar length. (a,b) CM247LC (c,d) CM247LC NHf.

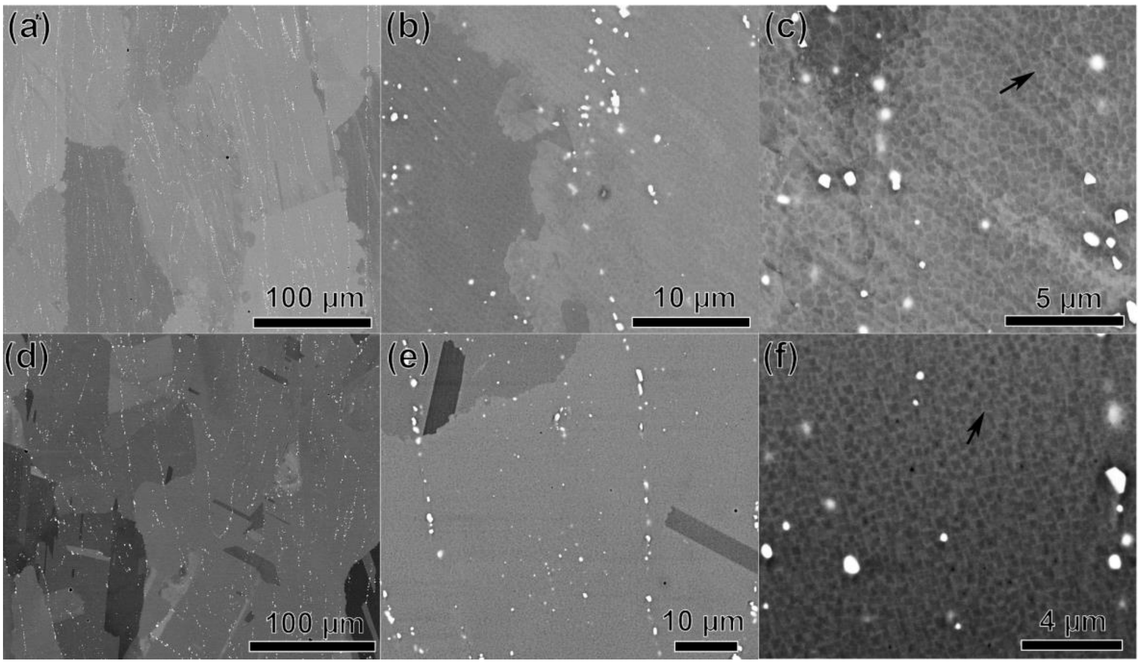
(a)
100 µm
(b)
10 µm
(c)
5 µm
(d)
100 µm
(e)
10 µm
(f)
4 µm

Figure 9.6: BSE images of HIPed and solutionized witness bars. Images approximately taken from the center of the witness bar. (a,b,c) CM247LC (d,e,f) CM247LC NHf. Black arrows point to the γ` precipitates.

Macro-cracks(cracks hundreds of µm to mm in length) were observed on the HIPed and solutionized (1260°C, 2 h) CM247LC witness bars (Figure 9.7), but not on the CM247LC NHf witness bars. The cracking appears to be randomly oriented and inter-granular (Figure 9.7(a)). The crack faces have a mostly smooth appearance (Figure 9.7(c,d)), with some small topography (small bumps) and bright particles observed (Figure 9.7(c,d)). A higher magnification image of Figure 9.7(c) is shown in Figure 9.7(e). Upon closer examination, there are line like features (black arrow) on the bump surfaces.

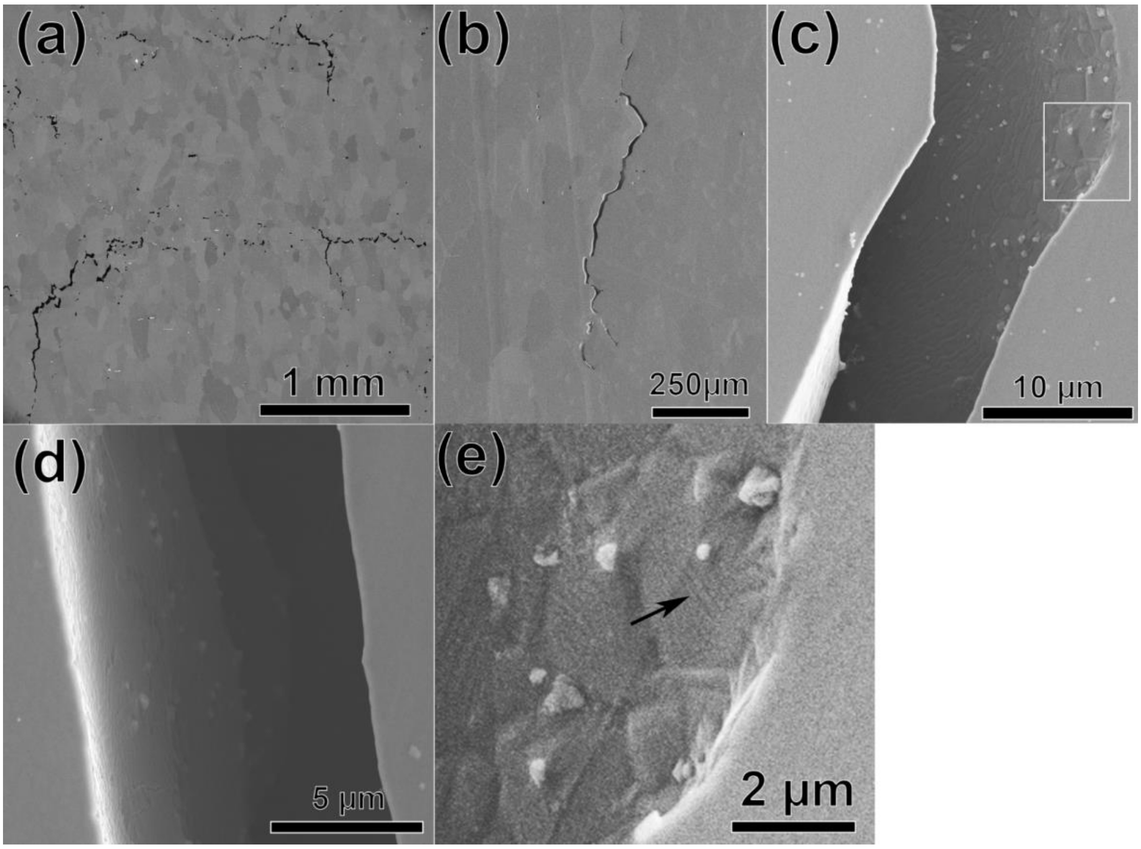

Figure 9.7: SE imags of macro-crack in the HIPed and solutionized CM247LC witness bar. (a) overivew image of numerous cracks (b) overiveiw image of one crack. (c,d) SE images of the crack face.

The microstructure of HIPed, solutionized (1260°C, 2 h), and aged (850°C, 8 h) CM247LC and CM247LC NHf witness bars is shown in Figure 9.8. No significant change in the grain microstructure occurred after aging. As expected, γ` precipitates were observed in HIPed, solutionized, and aged CM247LC NHf samples. The γ` precipitates of the CM247LC NHf samples were ~100 nm in radius, although without etching these measurements are prone to error. An adequate image for the γ` precipitates in the CM247LC was not obtained. The carbide size (in the center) for the CM247LC and CM247LC NHf HIPed and solutionized samples is 0.45±1.00 and 0.25±0.3 µm, respectively. (feret size, measured by image analysis). Just like in the HIPed and solutionized CM247LC sample, the HIPed, solutionized, and aged CM247LC sample appears to have rougher grain boundaries than that of the CM247LC NHf samples, but this was not quantified.

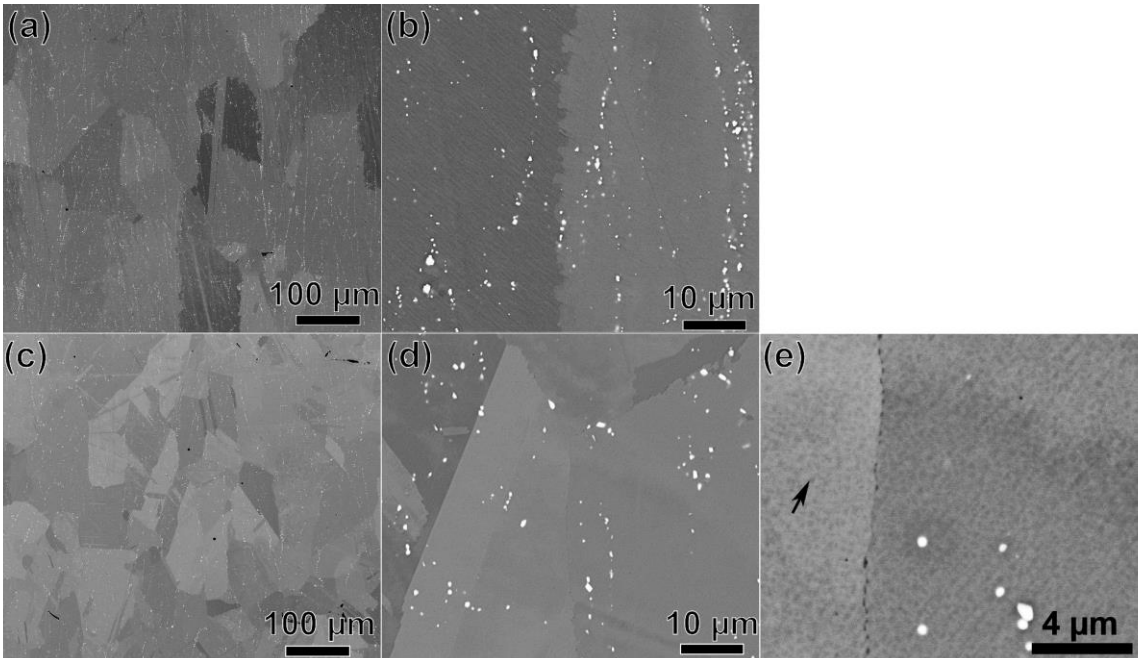

Figure 9.8: BSE images of HIPed, solutionized, and aged witness bars. Images approximately taken from the center of the witness bar. (a,b) CM247LC (c,d,e) CM247LC NHf. Black arrow point to the γ` precipitates. An adequete image for the γ` precipitates in the CM247LC was not obtained.

9.3 Discussion

Significant γ′ phase precipitation was observed in the as-solutionized condition, which is contrary to what is traditionally expected in solutionized alloys. The Ni-base superalloys are typically highly cooling rate sensitive from solutionizing and γ′ phase precipitation after solutionizing is not uncommon [145]. Air cooling (no convection) was utilized for all samples, but the cooling rate was not quantified. The peak-aged condition for the isothermally (850°C) aged CM247LC was obtained at 8 h and 2 h for CM247LC NHf; however, there is minimal hardness difference between 2 h and 8 h, hence 8 h was selected for both alloys as a comparison. Inverse coarsening behavior was observed in both alloys during the first few hours of aging. This behavior has been observed in other superalloys and is attributed to elastic stresses (caused by misfits between γ and γ′) resulting in larger precipitates growing smaller as small precipitates grow larger [146,147]. This effect will not be discussed further and the reader is directed to the references for a more thorough explanation. Most commercial γ′ strengthened superalloy aging treatments will be at a longer duration (20 h at 870°C for MAR-M-247, similar to CM247LC, [38]) than that observed for peak hardness. Other considerations such as optimal creep rupture strength, creep life, and fatigue life, are considered when designing heat treatments for commercial parts and these factors may necessitate coarser, over-aged, precipitates.

The smooth appearance of the crack faces, the intergranular nature and the discovery of the cracks after the solutionizing heat treatment strongly suggest strain age cracking is occurring in the CM247LC samples. Strain age cracking susceptibility is quite high for CM247LC due to the high fractions of γ′ precipitation [10]. The topography observed may be the result of γ′ precipitation and growth after fracture has occurred.

Two important observations from the heat treatment study is that the CM247LC NHf displays a lower hardness than the CM247LC and that the CM247LC NHf samples are not prone to cracking during heat treatment. Both of these observations can be explained by the influence of Hf on the γ′ phase. Despite being widely reported as a GB strengthening element, Hf does have solubility in the γ and γ′ phases. Figure 9.9 shows a plot of the equilibrium phase fraction of γ and γ′ phases as a function of temperature. At 850°C, the equilibrium phase fraction of γ′ is 66% and 61% for the CM247LC and CM247LC NHf respectively. The slightly lower fraction of γ′ explains why the peak hardness of the CM247LC NHf is lower. It also explains why the CM247LC NHf is less prone to strain age cracking.

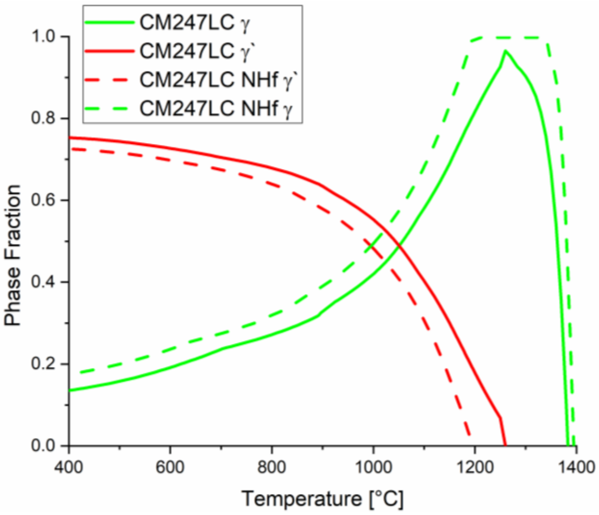

Figure 9.9: Equilibrium phase fraction of γ and γ′ phases as a function of temperature for CM247LC and CM247LC NHf. Calculations were performed with Thermocalc and the TCNI5 database

One aspect of Ni-base superalloy heat treatment that is only occasionally discussed in the context of AM is homogenization. Homogenization treatments are utilized for many cast alloys in order to remove the solute concentration gradients that occurred due to elemental partitioning during solidification. A uniform precipitate distribution is preferential for precipitation strengthened alloys, and any solute concentration differences will lead to non-uniform precipitate distributions. Directionally solidified cast Ni-base superalloys are prone to significant micro-segregation that is nearly identical in partition coefficient to that observed on the L-PBF fabricated CM247LC. One key difference between a directionally solidified cast part and one that is fabricated via L-PBF, is the cooling rate. The cooling rate will directly influence the spacing between areas of high and low solute concentration and thereby change the time and temperature required to completely homogenize the alloy. The relation between the secondary dendrite arm spacing (SDAS) and the time for solidification is given by equation 25,

$$SDAS = kt^{n} \tag{25}$$

where k and n are material related constants and t is time [37]. As solidification time decreases, the SDAS decreases, suggesting that the high cooling rate of the L-PBF process will result in small SDAS spacings that would reduce homogenization times. Figure 9.10 shows an optical image of an etched directionally cast CM247LC. A primary dendrite is seen near the middle of the image (running vertical) and SDA are seen coming off of (running horizontal) the primary dendrite. From this image, the SDAS can be estimated at ~150 µm. Secondary dendrites were not observed in the L-PBF CM247LC microstructures, but as a rough approximation, the distance between cells, ~1 µm, will be taken as the SDAS. A rough approximation of the time required to homogenize an alloy can be made with equation 24 and 25

$$\tau = \frac{l^{2}}{\pi^{2} D} \tag{24}$$

$$D = D_{O} e^{-Q/RT} \tag{25}$$

where l is half of the SDAS, D is the diffusivity of solute at the temperature of homogenization, and τ is the relaxation time, T is the temperature of homogenization, Q is the activation energy, and R is the ideal gas constant. The equation for the relaxation time is based off of a mathematical model of a simplified 1D sinusoidal segregation profile [26]. The relaxation time is the time for the amplitude of the sinusoidal function to drop to 1/e of its original value. The relaxation time is a rough estimate for homogenization time. If one considers a γ' former, such as Ti, one can calculate a rough time for homogenization. In the Ni-Ti binary system, Ti has a $D_o = 4.1\text{x}10^{-4}$ m^2s^{-1} and a Q = 275 kJ/mol [148]. Using the diffusion values for Ti in Ni, a homogenizing temperature of 1260 °C, and the SDAS values stated above, the homogenization time for the directionally solidified CM247LC and L-PBF fabricated CM247LC is ~3600 s and 0.1 s respectively. While the real-world homogenization times will be different in CM247LC, as it contains 10 more elements than the Ni-Ti system, the calculation shows that the fine solidification structure of an L-PBF alloy would substantially shorten homogenization times. The level of homogenization in a solutionized L-PBF fabricated sample has yet to be investigated.

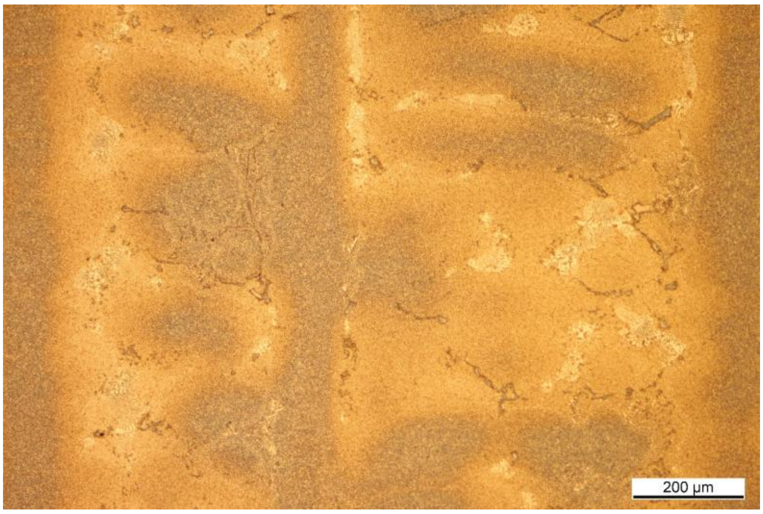

Figure 9.10: Optical image of etched CM247LC. The cross section is parallel to the casting direction. The blueish tints in the image are dendtrites and the orange tint areas are interdentridic.

9.4 Conclusions

CM247LC NHf, was discovered to have a few key differences from CM247LC in terms of heat treat response.

- The new CM247LC NHf alloy has lower peak hardness than the CM247LC alloy. This was attributed to the lower γ' volume fraction. The change in carbide morphology may also play a role.
- The new CM247LC NHf alloy is less susceptible to strain age cracking. It was hypothesized that this was due to a lower γ' volume fraction and reduced lattice misfit from the removal of Hf.
- Ductility of the alloy, main concern with removal of Hf, was not able to be determined due to the lack of tensile testing.
- The finer solidification structure of the L-PBF fabricated alloy will enable homogenization to occur during a standard solutionizing heat treatment.

Chapter 10 Conclusions and Future Outlook

10.1 Conclusions

The major conclusions from this thesis work that pertain to the Al-base superalloy are summarized below.

- A new high-strength Al-Mg-Zr alloy designed specifically for AM was successfully fabricated via L-PBF with minimal defects and high density. It was determined that the excellent processability of the alloys was attributed to primary Al_3Zr precipitates serving for inoculates for solidification crack resistant fine equiaxed α-Al grains.
- The as-fabricated alloy displayed a bimodal grain structure with fine equiaxed grains at the bottom of the melt pools and columnar grains occupying the remainder of the melt pool. This unique grain microstructure was determined to be the result of solidification front velocities increasing to the point where primary Al_3Zr precipitation was suppressed.
- A new microstructure modification strategy for the L-PBF process, laser rescanning, was developed. Laser rescanning of the consolidated Al-Mg-Zr alloy results in grain refinement which is attributed to the formation of shallower melt pools upon rescanning due to reduction of laser energy transfer to the solid. The shallower melt pool upon rescanning melts the columnar grain region at the top of the original melt pool but not the lower equiaxed region.
- The peak-aged Al-Mg-Zr alloy displayed both continuous and discontinuous precipitation of coherent secondary $L1_2$-structured Al_3Zr. The unique microstructure and nano-scale $L1_2$-structured precipitates resulted in the peak-aged Al-Mg-Zr alloys display both high strength, ~350 Mpa yield strength, and high ductility, ~18 % elongation at fracture.
- The as-fabricated alloys display higher yield strengths than the peak-aged alloys at temperatures of 150˚C and above. This strength reduction in the aged condition was

attributed to the coarsening of grain-boundary precipitates during aging, which leads to less inhibition of grain-boundary sliding.

- During long-duration (168 h) creep tests, both as-fabricated and peak-aged samples display nearly-identical creep behavior. The similarity in creep properties is explained by the in-situ aging that occurs for the as-fabricated sample during the creep test at 260 °C.

The major conclusions from this thesis work that pertain to the Ni-base superalloy are summarized below.

- Micro-cracking in CM247LC was attributed to both solidification and liquation cracking. The dendritic appearance of the micro-crack surfaces is indicative of fracture in the liquid phase and thus can be identified as solidification cracking.
- By utilizing thermodynamic simulations and experimental observations a new alloy was developed, CM247LC NHf, to reduce the solidification cracking susceptibility of CM247LC.
- Samples fabricated with CM247LC NHf had between a 36% to 75% reduction in crack density, depending on the parameters used, compared to the CM247LC alloy.
- The new CM247LC NHf alloy has lower peak hardness than the CM247LC alloy. This was attributed to the lower γ' volume fraction.
- The new CM247LC NHf alloy is less susceptible to strain age cracking. It was hypothesized that this was due to a lower γ' volume fraction and reduced lattice misfit from the removal of Hf.

10.2 Future Outlook

During the course of this thesis work, a few topics have been briefly touched on that the author believes should receive greater attention.

- **Laser-Material Interactions.** The physics of laser-material interaction is well studied and is covered in numerous text books [14,15]; however, when it comes to laser-based AM new variables are introduced. For instance, at the high beam scanning velocities of L-PBF (hundreds to thousands of mm/s) what is the laser radiation actually interacting with? Is the beam only hitting the liquid, or is it partially on liquid and partially on powder? These are important questions as the absorption of near-IR laser radiation will be different depending on if the laser interacts with liquid, bulk solid, or metallic powder. Also, how does the laser-vapor interactions (plasma and particles) influence the power reaching the substrate?

- **Melt pool behavior.** Again, the physics of heat transfer and fluid flow in a laser weld is well understood; however, as before, there are new variables with laser-based AM. The melt pool geometry will influence the solidification microstructure, and therefore the final mechanical properties. It is well known that surface roughness influences wettability, and that wettability will influence how a liquid spreads on a surface. What remains unclear, is how the presence of powder and variable surfaces will influence the melt pool spreadability during the AM process. Also, convection in the melt pool has been shown to strongly influence the geometry of laser weld melt pools [97], but this aspect remains largely untouched in the AM literature. There are numerous ways to modify the surface tension driven convection in a melt pool, whether via surface active elements that modify the surface tension or via thermal gradients, and hence tailor the melt pool geometry.
- **Heterogeneous microstructures of Al-Mg-Zr.** The bi-modal grain microstructures of L-PBF fabricated Al-Mg-Zr resulted an alloy with high strength and high ductility. Literature on heterogeneous microstructures have shown that it is possible to tailor the strength and ductility by modifying the ratio of fine to coarse grains and how they are distributed [122,123,149]. By careful control of the thermal gradients, solidification front velocity, and amount of inoculates, one could optimize the microstructure for the highest strength and ductility possible.
- **Micro-Cracking in CM247LC**. Micro-cracking was reduced via a combination of process and alloy modification, but it still occurs. Further process and alloy optimization are required before crack-free L-PBF parts is to be realized.
- **Thermal History.** It became apparent during work on the CM247LC that both geometry and thermal history of a L-PBF fabricated part will significantly influence the micro-crack density, possibly more than the alloy. More understanding of how the thermal conditions and therefore thermal residual stress evolves in parts with different geometries and delays between scanning.
- **Mechanical Property Testing of CM247LC:** Future tensile testing is to be performed on a Gleeble machine at room temperature and 760°C (minimum ductility temperature range for superallloys [35]). Tensile dog-bone specimens (3 mm thick) were cut from specimen blanks via milling (profile) and wire Electro-discharge Machining (EDM) with the dimensions shown in Figure 10.1. EDM surfaces were ground with P600 paper to remove the EDM re-cast layer.

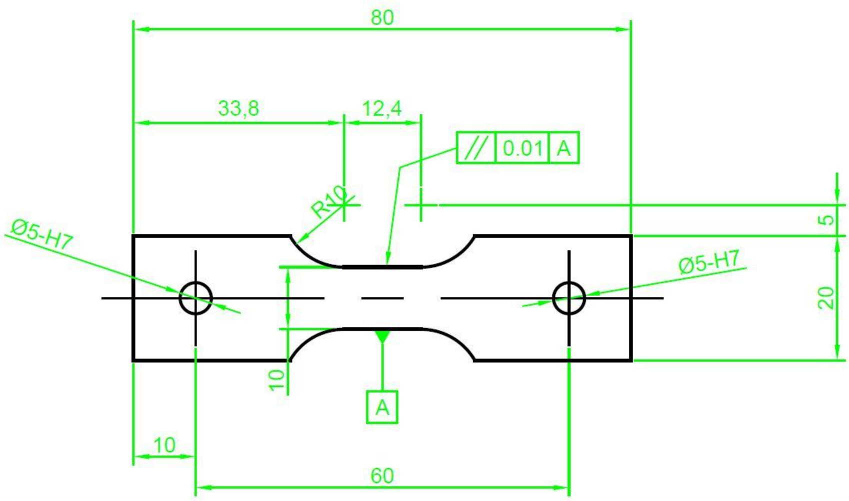
80
33,8
12,4
// 0.01 A
R10
5
Ø5-H7
Ø5-H7
20
10
A
10
60

Figure 10.1: Dimensions of the dogbone specimens. Specimens were 3 mm thick.

Appendix A– Supplementary Data

Table 0-1: Values used in the normalized enthalpy calculations

Cond.	Spot Size: a (µm, $1/e^2$)	Power: P (W)	Scan Speed: u (mm/s)	Absorptivity: A	Thermal Diffusivity at 0.5 T_m : D (cm^2/s)	Density: ρ (Kg/m^3)	Melting Temperature: T_m (K)	Specific Heat Capacity: (C) J/(K Kg)
1	45	200	600	0.3	0.040	8540	1555	580
2	27.5	175	750	0.3	0.040	8540	1555	580
References					[86] CMSX-4			[87] at 1323 K

Table 0-2: Nominal composition of CM247LC used in TCNI5 calculations

wt. %	Al	B	C	Co	Cr	Hf	Mo	Ni	Ta	Ti	W	Zr
CM247LC	5.6	0.015	0.07	9.2	8.1	1.4	0.5	Bal	3.2	0.7	9.5	0.015

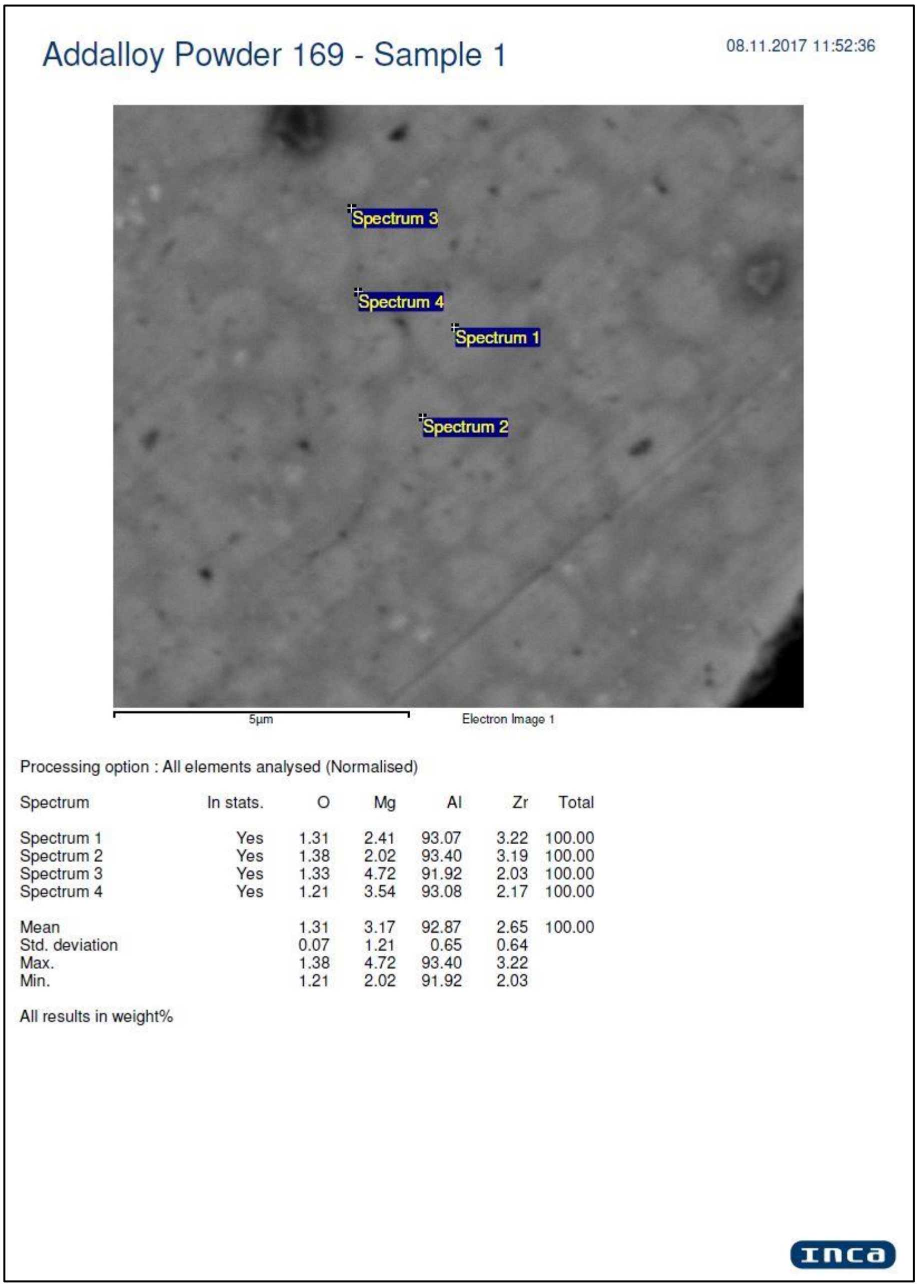
Spectrum 3
Spectrum 4
Spectrum 1
Spectrum 2
5µm
Electron Image 1
INCA

Addalloy Powder 169 - Sample 1

08.11.2017 11:52:36

Processing option : All elements analysed (Normalised)

Spectrum	In stats.	O	Mg	Al	Zr	Total
Spectrum 1	Yes	1.31	2.41	93.07	3.22	100.00
Spectrum 2	Yes	1.38	2.02	93.40	3.19	100.00
Spectrum 3	Yes	1.33	4.72	91.92	2.03	100.00
Spectrum 4	Yes	1.21	3.54	93.08	2.17	100.00
Mean		1.31	3.17	92.87	2.65	100.00
Std. deviation		0.07	1.21	0.65	0.64	
Max.		1.38	4.72	93.40	3.22	
Min.		1.21	2.02	91.92	2.03	

All results in weight%

Figure 0.1: SEM-EDX data of Al-3.66Mg-1.57Zr (wt.%, batch 5) powder shown in Figure 4.1.

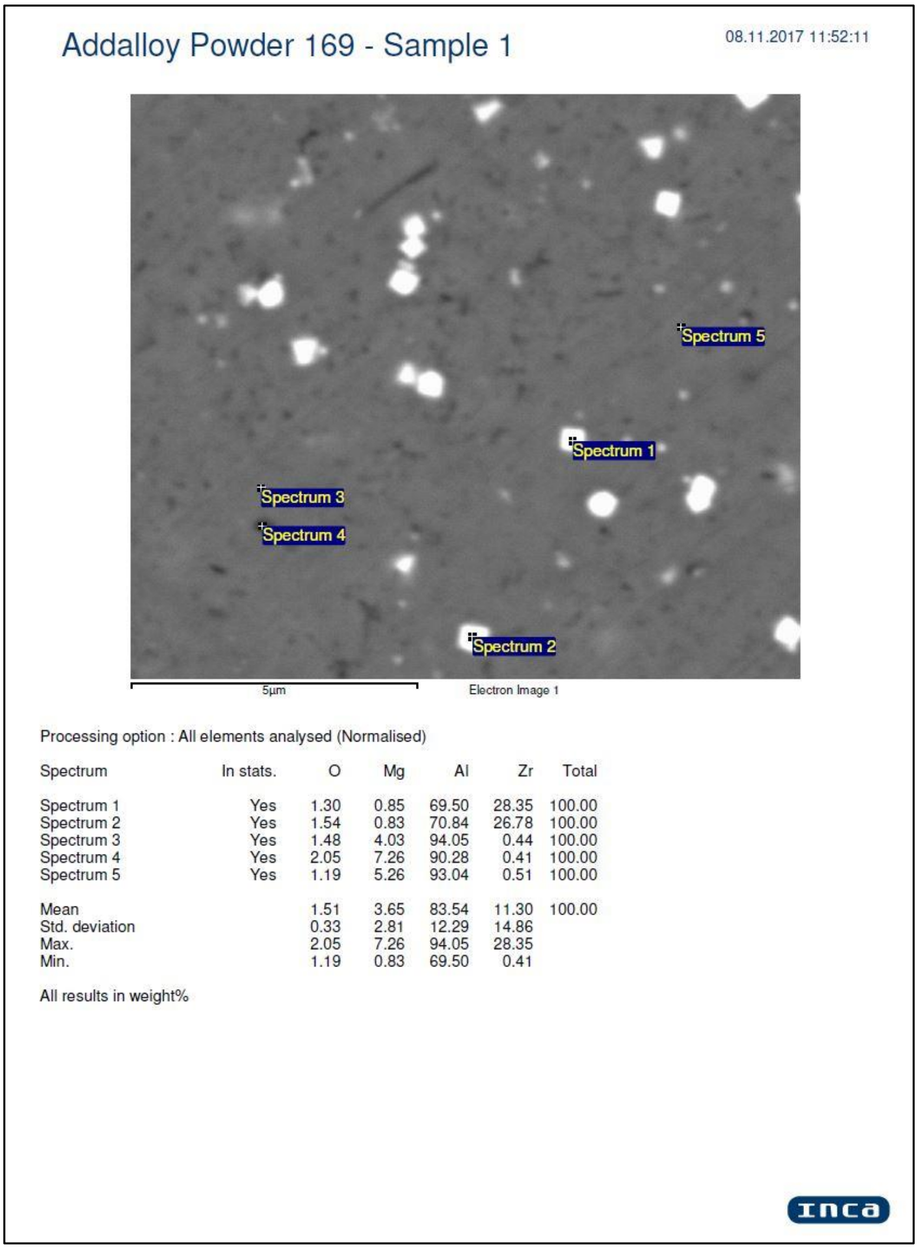

Addalloy Powder 169 - Sample 1

08.11.2017 11:52:11

Spectrum 5
Spectrum 1
Spectrum 3
Spectrum 4
Spectrum 2
5µm
Electron Image 1

Processing option : All elements analysed (Normalised)

Spectrum	In stats.	O	Mg	Al	Zr	Total
Spectrum 1	Yes	1.30	0.85	69.50	28.35	100.00
Spectrum 2	Yes	1.54	0.83	70.84	26.78	100.00
Spectrum 3	Yes	1.48	4.03	94.05	0.44	100.00
Spectrum 4	Yes	2.05	7.26	90.28	0.41	100.00
Spectrum 5	Yes	1.19	5.26	93.04	0.51	100.00
Mean		1.51	3.65	83.54	11.30	100.00
Std. deviation		0.33	2.81	12.29	14.86	
Max.		2.05	7.26	94.05	28.35	
Min.		1.19	0.83	69.50	0.41	

All results in weight%

Figure 0.2: SEM-EDX data of white precipitates in the Al-3.66Mg-1.57Zr (wt.%, batch 5) powder shown in Figure 4.1.

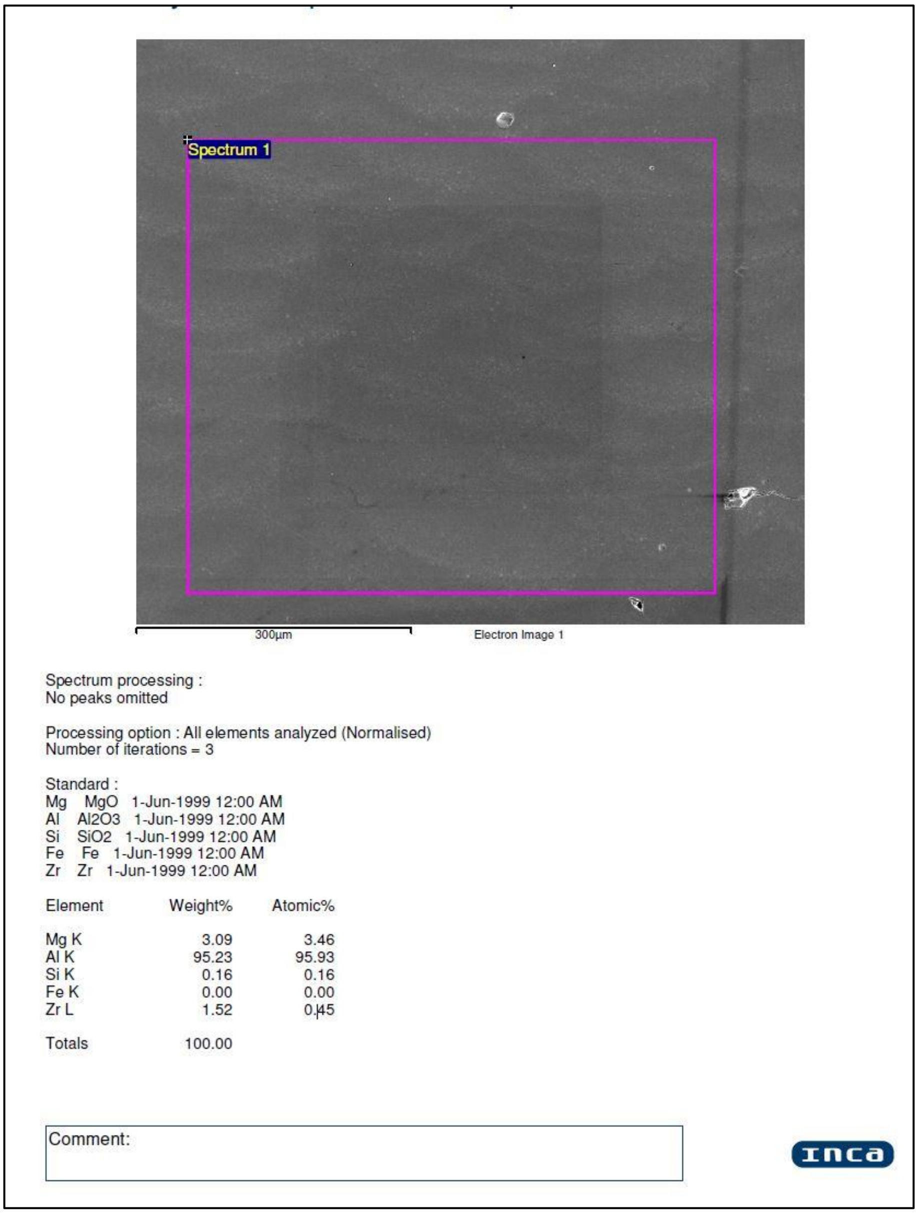

Spectrum processing :
No peaks omitted

Processing option : All elements analyzed (Normalised)
Number of iterations = 3

Standard :
Mg MgO 1-Jun-1999 12:00 AM
Al Al2O3 1-Jun-1999 12:00 AM
Si SiO2 1-Jun-1999 12:00 AM
Fe Fe 1-Jun-1999 12:00 AM
Zr Zr 1-Jun-1999 12:00 AM

Element	Weight%	Atomic%
Mg K	3.09	3.46
Al K	95.23	95.93
Si K	0.16	0.16
Fe K	0.00	0.00
Zr L	1.52	0.45
Totals	100.00	

Comment:

Figure 0.3: SEM-EDX data taken from an as-fabricated Al-3.60Mg-1.18Zr (wt. %, Batch 2) alloy.

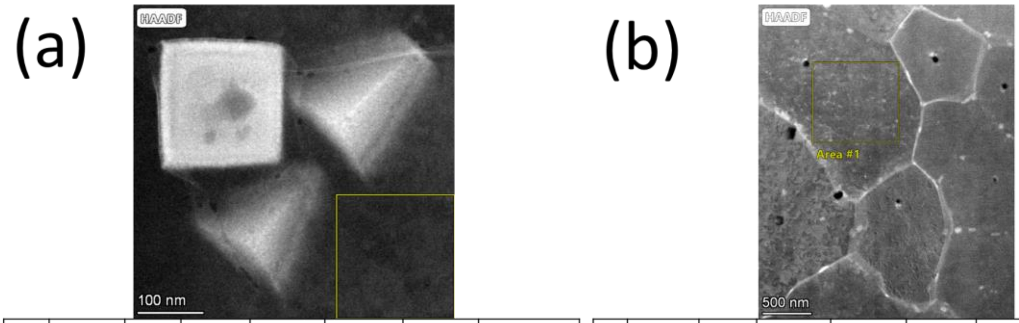

Z	Element	Family	Atomic Fraction (%)	Atomic Error (%)	Mass Fraction (%)	Mass Error (%)	Fit error (%)
8	O	K	4.93	1.58	2.97	0.55	1.68
12	Mg	K	2.70	1.02	2.48	0.68	3.59
13	Al	K	92.09	34.72	93.61	25.47	2.16
40	Zr	K	0.28	0.10	0.95	0.21	1.78

Z	Element	Family	Atomic Fraction (%)	Atomic Error (%)	Mass Fraction (%)	Mass Error (%)	Fit error (%)
8	O	K	1.57	0.52	0.93	0.18	3.92
12	Mg	K	2.74	1.05	2.47	0.68	0.10
13	Al	K	95.34	36.70	95.41	26.28	2.68
40	Zr	K	0.35	0.12	1.19	0.27	0.59

Figure 0.4: STEM-EDX data taken from an as-fabricated Al-3.60Mg-1.18Zr sample (wt.%, Batch 2). (a) ADF STEM image and STEM-EDX data from a region adjacent from a primary L12 structured Al3Zr precipitate. (b) ADF STEM image and STEM-EDX data from a grain from the coarse grain region.

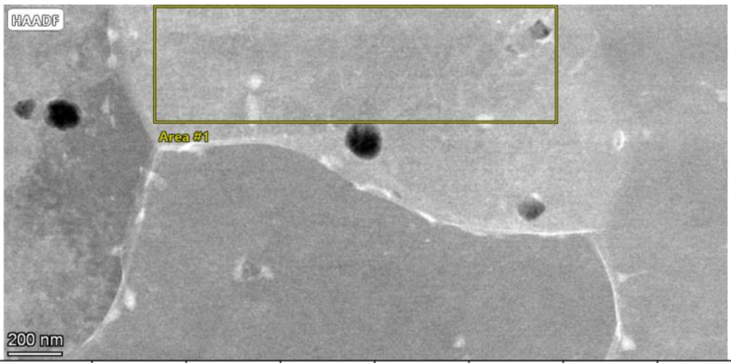

Z	Element	Family	Atomic Fraction (%)	Atomic Error (%)	Mass Fraction (%)	Mass Error (%)	Fit error (%)
8	O	K	1.51	0.49	0.89	0.17	2.39
12	Mg	K	3.04	1.16	2.72	0.74	0.64
13	Al	K	94.78	36.29	94.44	25.92	2.83
14	Si	K	0.10	0.04	0.10	0.03	10.51
26	Fe	K	0.06	0.02	0.13	0.03	1.45
40	Zr	K	0.51	0.18	1.71	0.39	0.37

Figure 0.5: ADF-STEM image and STEM-EDX data taken from a grain (same grain as shown by the white circle in Figure 4.10) in the coarse grain region of an as-fabricated Al-3.60Mg-1.18Zr sample (wt.%, Batch 2).

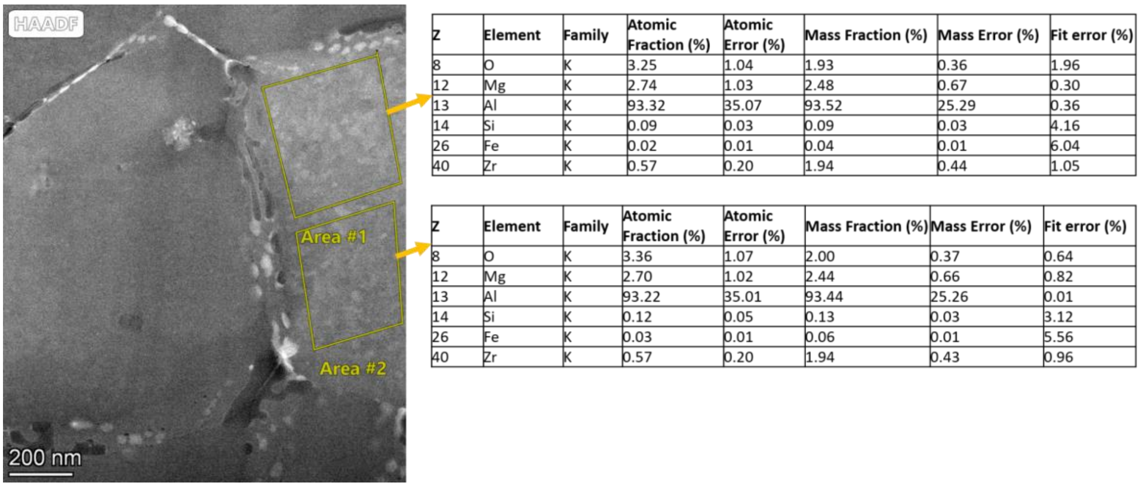

Z	Element	Family	Atomic Fraction (%)	Atomic Error (%)	Mass Fraction (%)	Mass Error (%)	Fit error (%)
8	O	K	3.25	1.04	1.93	0.36	1.96
12	Mg	K	2.74	1.03	2.48	0.67	0.30
13	Al	K	93.32	35.07	93.52	25.29	0.36
14	Si	K	0.09	0.03	0.09	0.03	4.16
26	Fe	K	0.02	0.01	0.04	0.01	6.04
40	Zr	K	0.57	0.20	1.94	0.44	1.05

Z	Element	Family	Atomic Fraction (%)	Atomic Error (%)	Mass Fraction (%)	Mass Error (%)	Fit error (%)
8	O	K	3.36	1.07	2.00	0.37	0.64
12	Mg	K	2.70	1.02	2.44	0.66	0.82
13	Al	K	93.22	35.01	93.44	25.26	0.01
14	Si	K	0.12	0.05	0.13	0.03	3.12
26	Fe	K	0.03	0.01	0.06	0.01	5.56
40	Zr	K	0.57	0.20	1.94	0.43	0.96

Figure 0.6: STEM HAADF image and STEM-EDX data from the coarse grain region of an as-fabricated Al-2.90Mg-2.10Zr (wt. %, Batch 3) sample. Area #1 and Area #2 are the areas that HR-STEM was performed in.

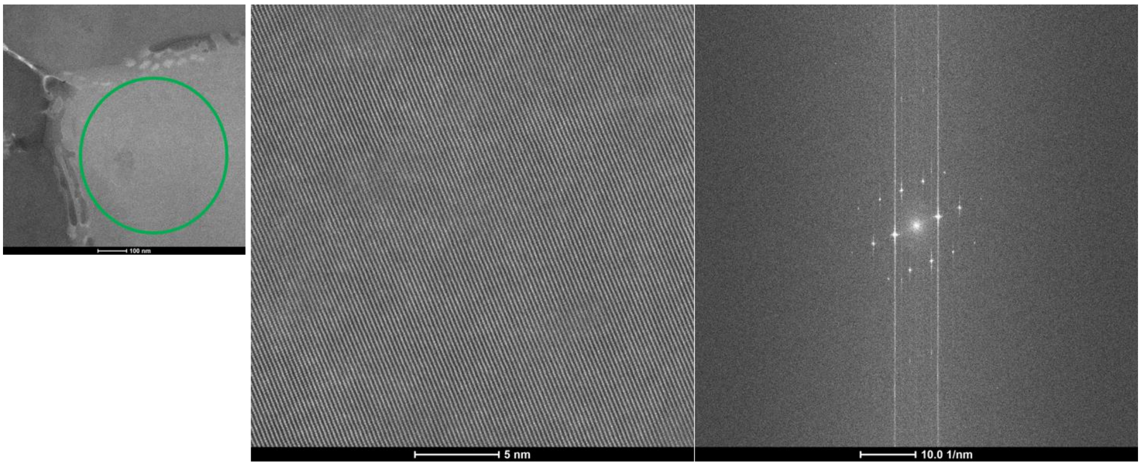

Figure 0.7: (left) STEM HAADF image of region of interest. Area #1 in Figure 0.6. (middle) HR-STEM image (right) FFT of HR-STEM image taken down the [112] zone axis. Note the absence of superlattice reflections indicative of the $L1_2$ phase.

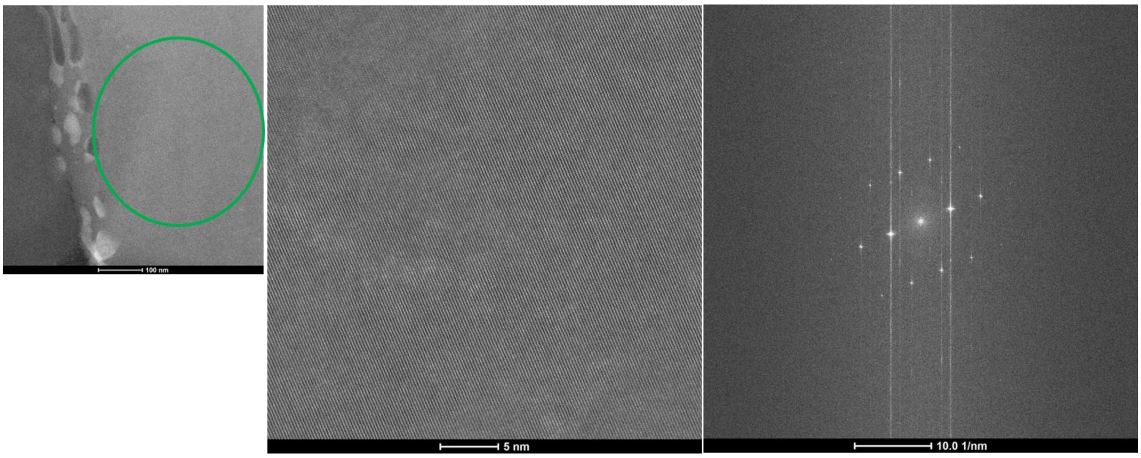

Figure 0.8: (left) STEM HAADF image of region of interest. Area #2 in Figure 0.6. (middle) HR-STEM image (right) FFT of HR-STEM image taken down the [112] zone axis. Note the absence of superlattice reflections indicative of the $L1_2$ phase.

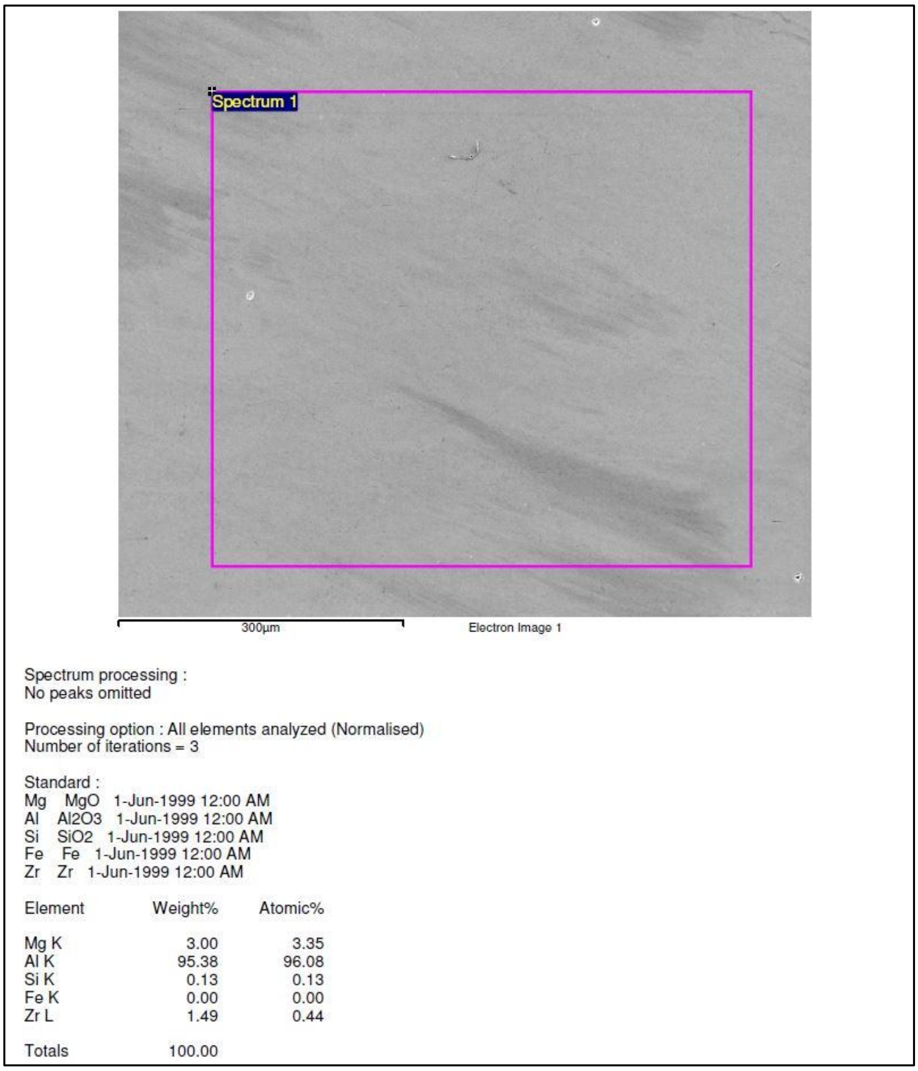

Spectrum processing :
No peaks omitted

Processing option : All elements analyzed (Normalised)
Number of iterations = 3

Standard :
Mg MgO 1-Jun-1999 12:00 AM
Al Al2O3 1-Jun-1999 12:00 AM
Si SiO2 1-Jun-1999 12:00 AM
Fe Fe 1-Jun-1999 12:00 AM
Zr Zr 1-Jun-1999 12:00 AM

Element	Weight%	Atomic%
Mg K	3.00	3.35
Al K	95.38	96.08
Si K	0.13	0.13
Fe K	0.00	0.00
Zr L	1.49	0.44
Totals	100.00	

Figure 0.9: SEM-EDX of an as-fabricated (double scanned) Al-3.60Mg-1.18Zr (wt.%, Batch 2) alloy.

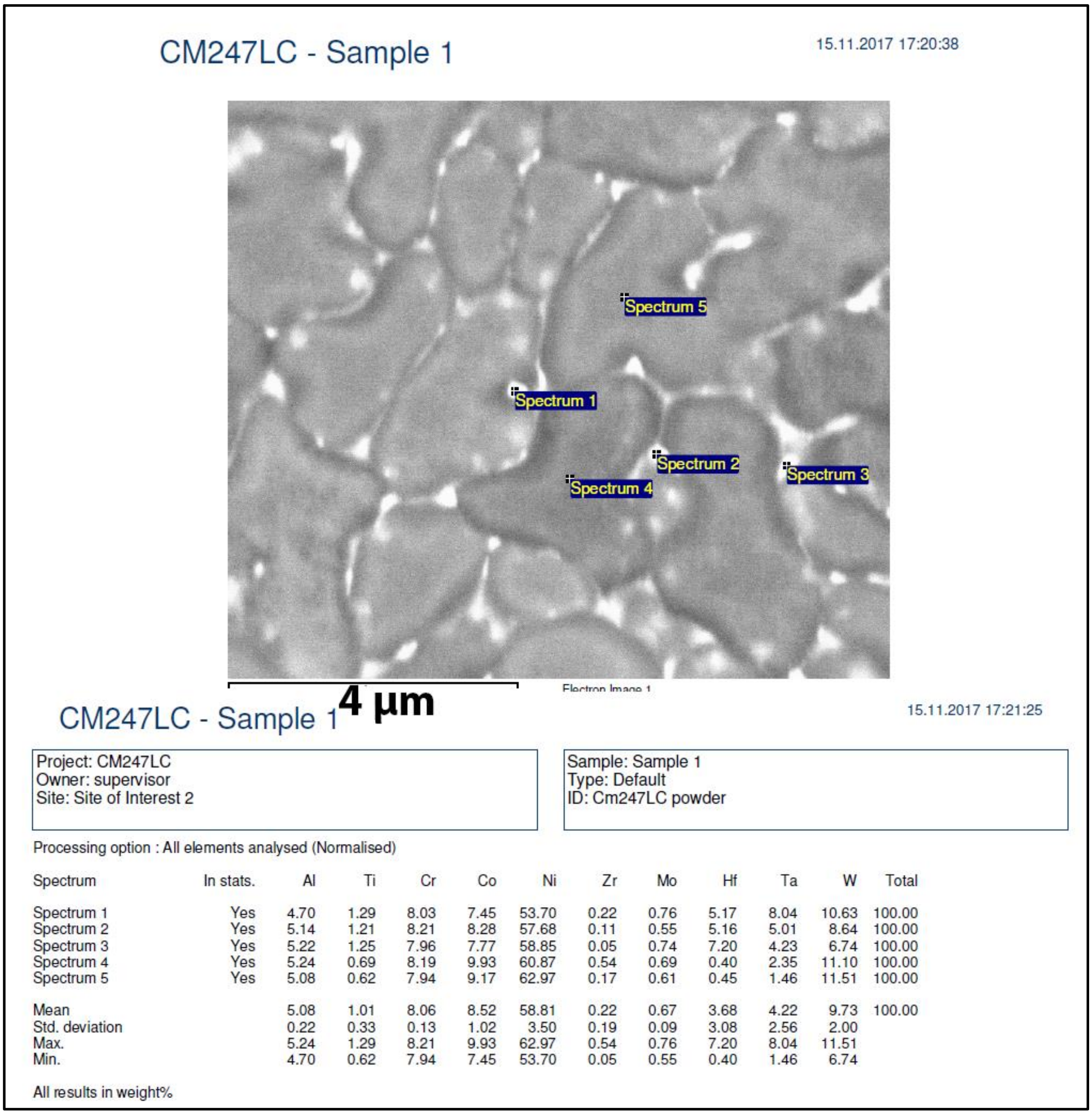

CM247LC - Sample 1

15.11.2017 17:20:38

CM247LC - Sample 1

15.11.2017 17:21:25

Project: CM247LC
Owner: supervisor
Site: Site of Interest 2

Sample: Sample 1
Type: Default
ID: Cm247LC powder

Processing option : All elements analysed (Normalised)

Spectrum	In stats.	Al	Ti	Cr	Co	Ni	Zr	Mo	Hf	Ta	W	Total
Spectrum 1	Yes	4.70	1.29	8.03	7.45	53.70	0.22	0.76	5.17	8.04	10.63	100.00
Spectrum 2	Yes	5.14	1.21	8.21	8.28	57.68	0.11	0.55	5.16	5.01	8.64	100.00
Spectrum 3	Yes	5.22	1.25	7.96	7.77	58.85	0.05	0.74	7.20	4.23	6.74	100.00
Spectrum 4	Yes	5.24	0.69	8.19	9.93	60.87	0.54	0.69	0.40	2.35	11.10	100.00
Spectrum 5	Yes	5.08	0.62	7.94	9.17	62.97	0.17	0.61	0.45	1.46	11.51	100.00
Mean		5.08	1.01	8.06	8.52	58.81	0.22	0.67	3.68	4.22	9.73	100.00
Std. deviation		0.22	0.33	0.13	1.02	3.50	0.19	0.09	3.08	2.56	2.00	
Max.		5.24	1.29	8.21	9.93	62.97	0.54	0.76	7.20	8.04	11.51	
Min.		4.70	0.62	7.94	7.45	53.70	0.05	0.55	0.40	1.46	6.74	

All results in weight%

Figure 0.10: SEM-EDX data of a CM247LC powder particle. Bright areas are enriched in Hf, Ti, and Ta.

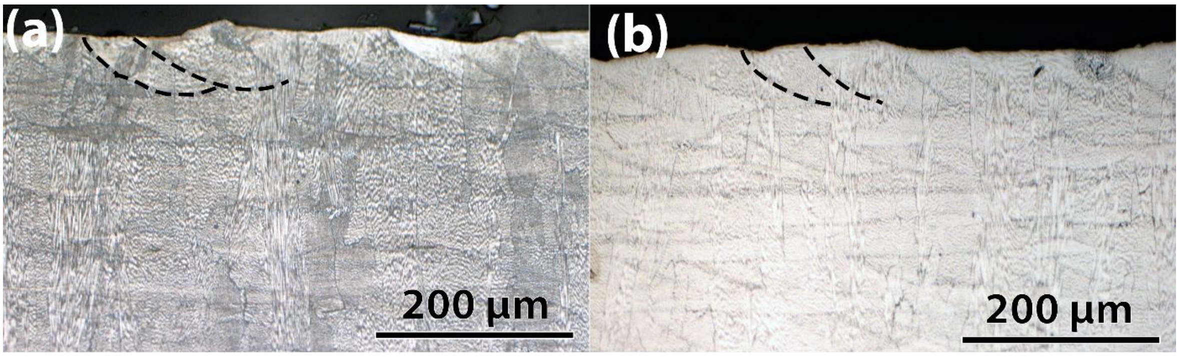

Figure 0.11: Optical images, with highlighted melt pools (dashed lines) on etched, as-fabricated CM247LC samples, produced using a) Machine 2 with a 100 mm diameter build plate b) Machine 2 with a 34.5 mm diameter build plate. No significant differences in melt pool dimensions were observed.

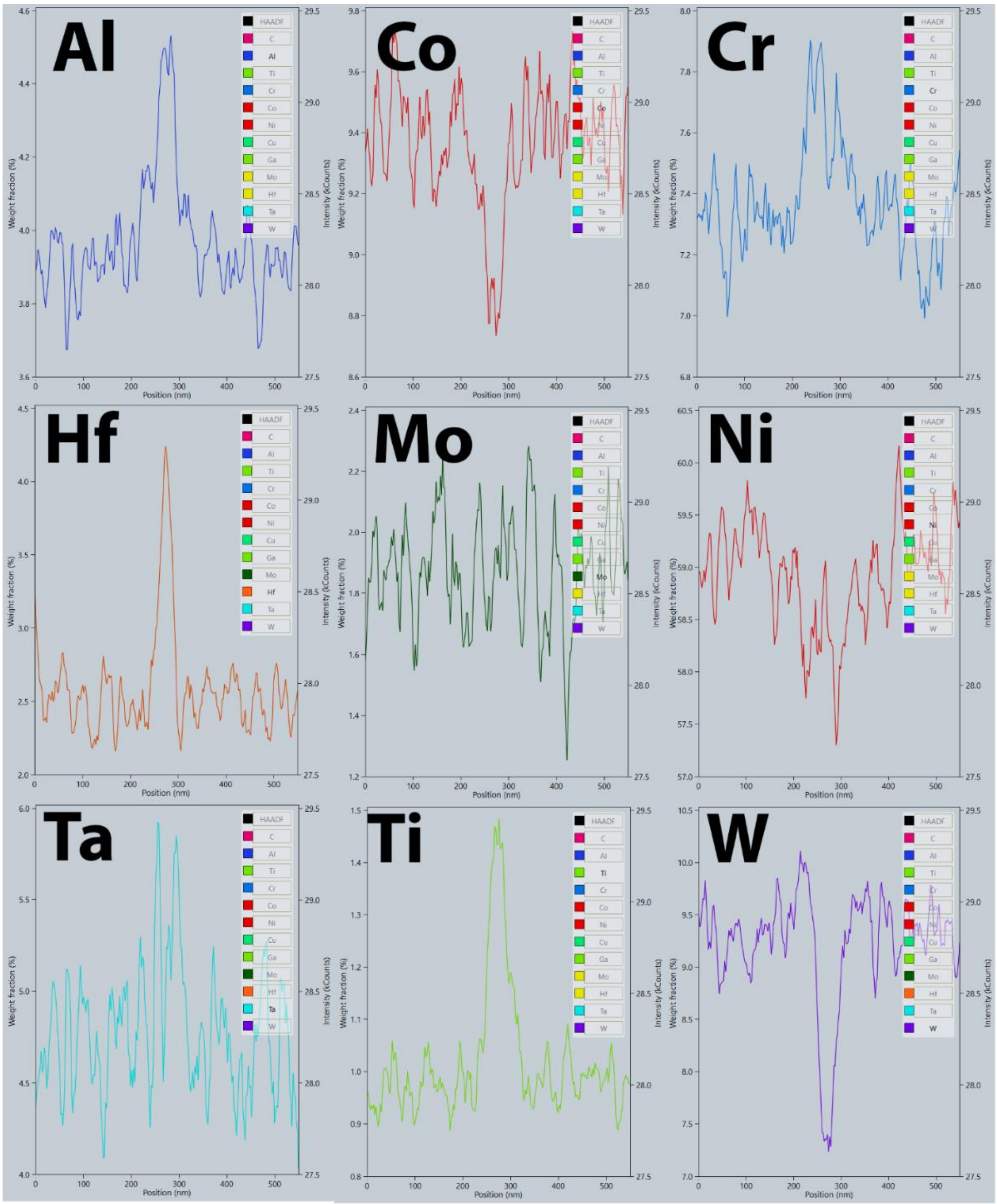

Figure 0.12: STEM-EDX line profile (averaged over the line width) quantification data taken from the region highlighted by the white box in Figure 2c. Chemical analysis performed with Al-K, Ti-K, Cr-K, Hf-L, Ta-L, W-L, Co-K, Ni-K, Zr-K, C-K lines

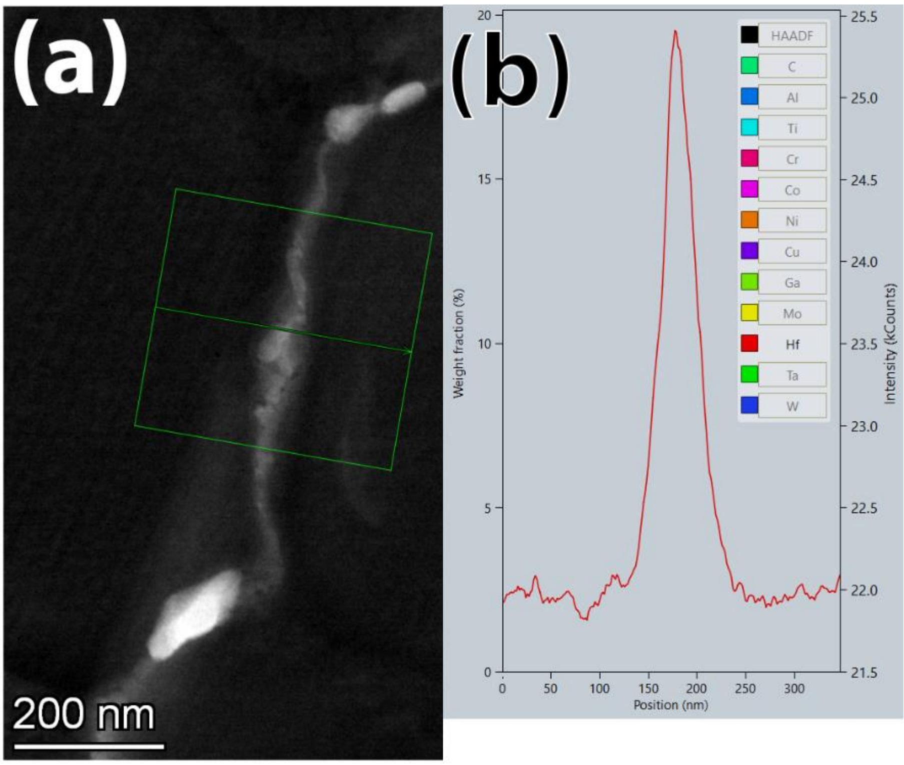

Figure 0.13: a) ADF-STEM image of the boundary shown in Supplement Figure 7. The green box highlights the region used for the STEM-EDX line profile. b) STEM-EDX line profile (averaged over the width) of the boundary in a). Hf enrichment on the boundary approaches 20 wt.%. Chemical analysis performed with the Hf-L lines.

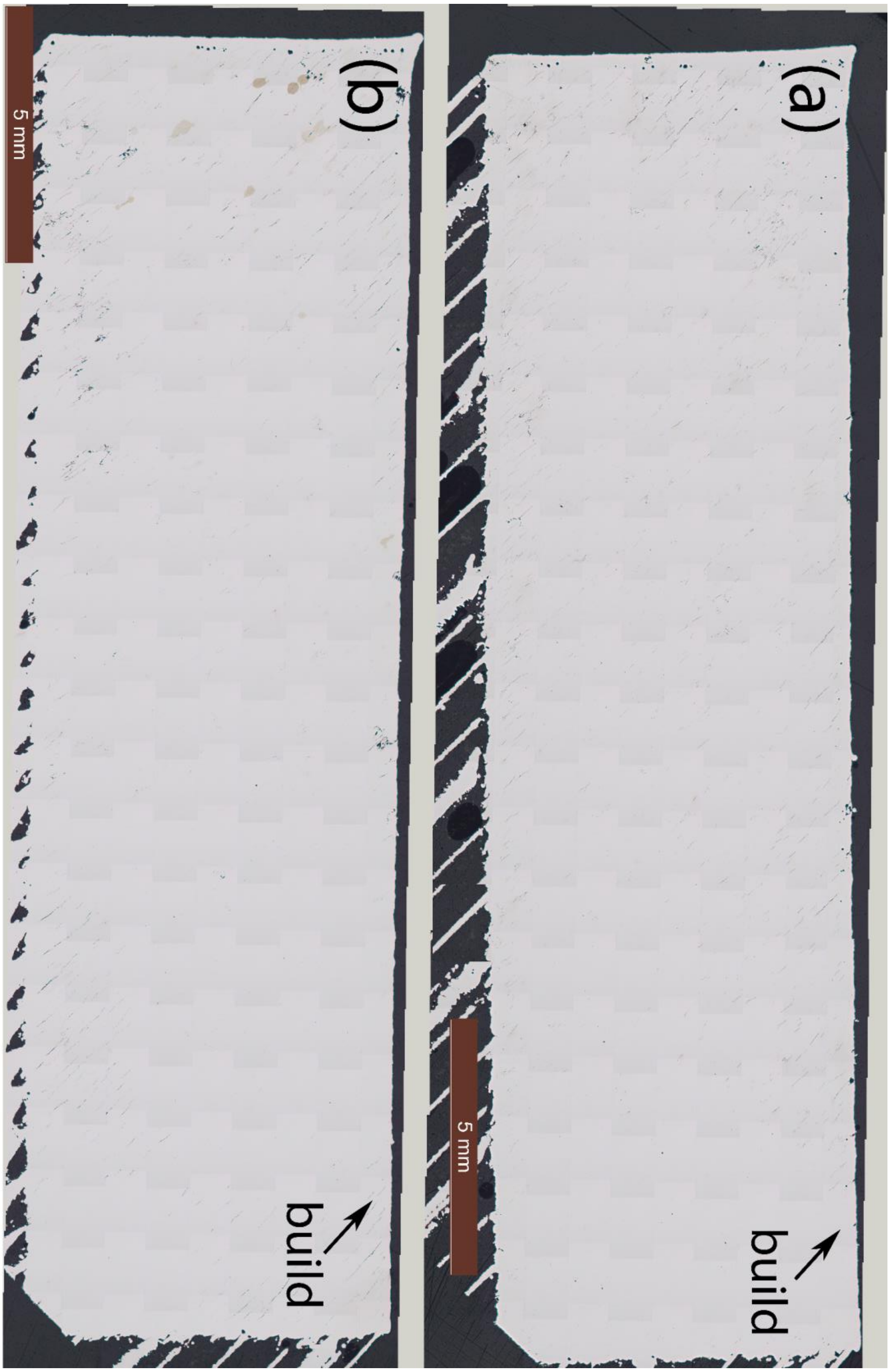
5 mm
(b)
build
(a)
5 mm
build

Figure 0.14: (a) Optical image of cross section of as-fabricated CM247LC cylinder. (b) Optical image of cross section of as-fabricated CM247LC NHf.

Table 0-3: Thermophysical properties and laser parameters used for the normalized power and normalized interaction time calculation.

units	none	W	m	W/ (m K)	K	K	m^2 /s	m/s	none	none
condition	Aborsptivity	Power	Beam radius	Thermal Cond.	T_M	T_0	thermal diffusivity	velocity	q*	v*
1	0.5	200	3.20E-05	9.3	1555	298	3.80E-06	6.00E-01	112	3.84
2	0.5	175	1.90E-05	9.3	1555	298	3.80E-06	7.50E-01	165	2.85
Reference				[150]	[86]	[86]	[150]			
Comments			(1/e)	@113°C	CM247LC	CM247LC	CM247LC @ 150 C			

References

[1] D. Thomas, S. Gilbert, Costs and Cost Effectiveness of Additive Manufacturing, (2014). https://doi.org/10.6028/NIST.SP.1176.

[2] L.N. Carter, C. Martin, P.J. Withers, M.M. Attallah, The influence of the laser scan strategy on grain structure and cracking behaviour in SLM powder-bed fabricated nickel superalloy, J. Alloys Compd. 615 (2014) 338–347. https://doi.org/10.1016/j.jallcom.2014.06.172.

[3] X. Wang, L.N. Carter, B. Pang, M.M. Attallah, M.H. Loretto, Microstructure and yield strength of SLM-fabricated CM247LC Ni-Superalloy, Acta Mater. 128 (2017) 87–95. https://doi.org/10.1016/j.actamat.2017.02.007.

[4] V.D. Divya, R. Muñoz-Moreno, O.M.D.M. Messé, J.S. Barnard, S. Baker, T. Illston, H.J. Stone, Microstructure of selective laser melted CM247LC nickel-based superalloy and its evolution through heat treatment, Mater. Charact. 114 (2016) 62–74. https://doi.org/10.1016/j.matchar.2016.02.004.

[5] M. Cloots, P.J. Uggowitzer, K. Wegener, Investigations on the microstructure and crack formation of IN738LC samples processed by selective laser melting using Gaussian and doughnut profiles, Mater. Des. 89 (2016) 770–784. https://doi.org/10.1016/j.matdes.2015.10.027.

[6] E. Chauvet, P. Kontis, E.A. Jägle, B. Gault, D. Raabe, C. Tassin, J.-J. Blandin, R. Dendievel, B. Vayre, S. Abed, G. Martin, Hot cracking mechanism affecting a non-weldable Ni-based superalloy produced by selective electron Beam Melting, Acta Mater. 142 (2018) 82–94. https://doi.org/10.1016/j.actamat.2017.09.047.

[7] M. Ramsperger, R.F. Singer, C. Körner, Microstructure of the Nickel-Base Superalloy CMSX-4 Fabricated by Selective Electron Beam Melting, Metall. Mater. Trans. A. 47 (2016) 1469–1480. https://doi.org/10.1007/s11661-015-3300-y.

[8] Y.S. Lee, M.M. Kirka, S. Kim, N. Sridharan, A. Okello, R.R. Dehoff, S.S. Babu, Asymmetric Cracking in Mar-M247 Alloy Builds During Electron Beam Powder Bed Fusion Additive Manufacturing, Metall. Mater. Trans. A. 49 (2018) 5065–5079. https://doi.org/10.1007/s11661-018-4788-8.

[9] L.N. Carter, M.M. Attallah, R.C. Reed, Laser Powder Bed Fabrication of Nickel-Base Superalloys: Influence of Parameters; Characterisation, Quantification and Mitigation of Cracking, in: Superalloys 2012, John Wiley & Sons, Inc., 2012: pp. 577–586. http://dx.doi.org/10.1002/9781118516430.ch64.

[10] J.N. DuPont, S.D. Kiser, J.C. Lippold, Welding Metallurgy and Weldability of Nickel-Base Alloys, Wiley, Hoboken, NJ, 2009. http://search.ebscohost.com/login.aspx?direct=true&AuthType=ip&db=nlebk&AN=289303&site=ehost-live.

[11] K.E. Knipling, D.C. Dunand, D.N. Seidman, Criteria for developing castable, creep-resistant aluminum-based alloys - A review, Int. J. Mater. Res. 97 (2006) 246–265.

[12] R. Kose, Additive Manufacturing: 4th industrial revolution, Empa Q. 51 (n.d.) 8–17.

[13] J. MAZUMDER, CHAPTER 3 - Laser Welding, in: M. BASS (Ed.), Mater. Process. Theory Pract., Elsevier, 1983: pp. 113–200. https://doi.org/10.1016/B978-0-444-86396-6.50009-X.

[14] D. Bäuerle, Laser processing and chemistry, 4th ed., Berlin : Springer, 2011.

[15] W.M. Steen, J. Mazumder, Laser material processing, 4th ed., London : Springer, 2010. https://doi.org/10.1007/978-1-84996-062-5.

[16] D. Bäuerle, Laser Processing and Chemistry, Springer Berlin Heidelberg, 2011.

[17] J.C. Ion, Laser Processing of Engineering Materials : Principles, Procedure and Industrial Application, Butterworth-Heinemann, Amsterdam, 2005. http://search.ebscohost.com/login.aspx?direct=true&AuthType=ip&db=e000xww&AN=130225&site=ehost-live.

[18] D.B. Hann, J. Iammi, J. Folkes, A simple methodology for predicting laser-weld properties from material and laser parameters, J. Phys. Appl. Phys. 44 (2011) 445401. https://doi.org/10.1088/0022-3727/44/44/445401.

[19] A.M. Rubenchik, W.E. King, S.S. Wu, Scaling laws for the additive manufacturing, J. Mater. Process. Technol. 257 (2018) 234–243. https://doi.org/10.1016/j.jmatprotec.2018.02.034.

[20] W.E. King, H.D. Barth, V.M. Castillo, G.F. Gallegos, J.W. Gibbs, D.E. Hahn, C. Kamath, A.M. Rubenchik, Observation of keyhole-mode laser melting in laser powder-bed fusion additive manufacturing, J. Mater. Process. Technol. 214 (2014) 2915–2925. https://doi.org/10.1016/j.jmatprotec.2014.06.005.

[21] W.J. Sames, F.A. List, S. Pannala, R.R. Dehoff, S.S. Babu, The metallurgy and processing science of metal additive manufacturing, Int. Mater. Rev. 61 (2016) 315–360. https://doi.org/10.1080/09506608.2015.1116649.

[22] C. Limmaneevichitr, S. Kou, Experiments to simulate effect of Marangoni convection on weld pool shape, Weld. J. 79 (2000) 231S-237S.

[23] A. Robert, T. Debroy, Geometry of laser spot welds from dimensionless numbers, Metall. Mater. Trans. B. 32 (2001) 941–947. https://doi.org/10.1007/s11663-001-0080-0.

[24] S. Kou Verfasser, Welding metallurgy, 2003. https://search.ebscohost.com/login.aspx?direct=true&AuthType=ip&db=edsbvb&AN=edsbvb.BV016548906&site=eds-live.

[25] W. Kurz, D.J. Fisher, Fundamentals of solidification, (1989).

[26] D.A. Porter, K.E. Easterling, Phase transformations in metals and alloys, Second ed., [reprinted], Boca Raton - Fla. : CRC Press, 2004.

[27] S. Kou, Y.H. Wang, THREE-DIMENSIONAL CONVECTION IN LASER MELTED POOLS., Metall. Trans. Phys. Metall. Mater. Sci. 17 A (1986) 2265–2270. https://doi.org/10.1007/BF02645924.

[28] M.J. Aziz, Model for solute redistribution during rapid solidification, J. Appl. Phys. 53 (1982) 1158–1168. https://doi.org/10.1063/1.329867.

[29] M.J. Aziz, Model for solute redistribution during rapid solidification, J. Appl. Phys. 53 (1982) 1158–1168. https://doi.org/10.1063/1.329867.

[30] J.N. DuPont, Fundamentals of Weld Solidification, in: T. Lienert, T. Siewert, S. Babu, V. Acoff (Eds.), Weld. Fundam. Process., ASM International, 2011: p. 0. https://doi.org/10.31399/asm.hb.v06a.a0005609.

[31] M. Gaumann, W. Kurz, Why is it so difficult to produce an equiaxed microstructure during welding?, Present. Math. Model. Weld Phenom. Conf. 4 (1997) 125–136.

[32] M. Gäumann, C. Bezençon, P. Canalis, W. Kurz, Single-crystal laser deposition of superalloys: processing–microstructure maps, Acta Mater. 49 (2001) 1051–1062. https://doi.org/10.1016/S1359-6454(00)00367-0.

[33] W. Kurz, R. Trivedi, Rapid solidification processing and microstructure formation, Proc. Eighth Int. Conf. Rapidly Quenched Metastable Mater. 179 (1994) 46–51. https://doi.org/10.1016/0921-5093(94)90162-7.

[34] B. Geddes, Superalloys : Alloying and Performance, ASM International, 2010.

[35] R.C. Reed, The Superalloys: Fundamentals and Applications, Cambridge University Press, Cambridge, 2006. https://doi.org/10.1017/CBO9780511541285.

[36] A.M. Brown, M.F. Ashby, Correlations for diffusion constants, Acta Metall. 28 (1980) 1085–1101. https://doi.org/10.1016/0001-6160(80)90092-9.

[37] F.C. Campbell, Elements of Metallurgy and Engineering Alloys, 2008.

[38] Superalloys : a technical guide / M. Donachie, Jr., S. Donachie, 2002. http://search.ebscohost.com/login.aspx?direct=true&site=eds-live&db=edsnop&AN=edsnop.I000004077928.00 (accessed September 6, 2016).

[39] T. Pollock Sammy, Nickel-Based Superalloys for Advanced Turbine Engines: Chemistry, Microstructure and Properties, J. Propuls. Power. 22 (2006) 361–374.

[40] K.E. Knipling, D.C. Dunand, D.N. Seidman, Precipitation evolution in Al–Zr and Al–Zr–Ti alloys during isothermal aging at 375–425°C, Acta Mater. 56 (2008) 114–127. https://doi.org/10.1016/j.actamat.2007.09.004.

[41] K.E. Knipling, D.C. Dunand, D.N. Seidman, Precipitation evolution in Al–Zr and Al–Zr–Ti alloys during aging at 450–600°C, Acta Mater. 56 (2008) 1182–1195. https://doi.org/10.1016/j.actamat.2007.11.011.

[42] N.Q. Vo, J. Sorensen, E.M. Klier, A. Sanaty-Zadeh, D. Bayansan, D.N. Seidman, D.C. Dunand, Development of a Precipitation-Strengthened Matrix for Non-quenchable Aluminum Metal Matrix Composites, JOM. 68 (2016) 1915–1924. https://doi.org/10.1007/s11837-016-1896-z.

[43] K.E. Knipling, R.A. Karnesky, C.P. Lee, D.C. Dunand, D.N. Seidman, Precipitation evolution in Al–0.1Sc, Al–0.1Zr and Al–0.1Sc–0.1Zr (at.%) alloys during isochronal aging, Acta Mater. 58 (2010) 5184–5195. https://doi.org/10.1016/j.actamat.2010.05.054.

[44] H. Li, J. Bin, J. Liu, Z. Gao, X. Lu, Precipitation evolution and coarsening resistance at 400°C of Al microalloyed with Zr and Er, Scr. Mater. 67 (2012) 73–76. https://doi.org/10.1016/j.scriptamat.2012.03.026.

[45] G.K. Sigworth, S. Thomas-Sadowski, K. Frink, Best Practices in Aluminum Metalcasting, American Foundry Society, 2014. https://books.google.ch/books?id=xGOUoAEACAAJ.

[46] G.E. Totten, D.S. MacKenzie, Handbook of Aluminum: Vol. 1: Physical Metallurgy and Processes, 2003.

[47] I.G. Brodova, D.V. Bashlykov, A.B. Manukhin, V.V. Stolyarov, E.P. Soshnikova, Formation of nanostructure in rapidly solidified Al-Zr alloy by severe plastic deformation, Scr. Mater. 44 (2001) 1761–1764. https://doi.org/10.1016/S1359-6462(01)00791-6.

[48] T. Ohashi, R. Ichikawa, A new metastable phase in rapidly solidified Al-Zr alloys, Metall. Trans. 3 (1972) 2300–2302. https://doi.org/10.1007/BF02643251.

[49] M. Brochu, G. Portillo, Grain Refinement during Rapid Solidification of Aluminum–Zirconium Alloys Using Electrospark Deposition, Mater. Trans. 54 (2013) 934–939. https://doi.org/10.2320/matertrans.MD201228.

[50] E.A. Marquis, D.N. Seidman, D.C. Dunand, Effect of Mg addition on the creep and yield behavior of an Al–Sc alloy, Acta Mater. 51 (2003) 4751–4760. https://doi.org/10.1016/S1359-6454(03)00288-X.

[51] T.H. Courtney, Mechanical Behavior of Materials: Second Edition, Waveland Press, 2005. https://books.google.ch/books?id=QcYSAAAAQBAJ.

[52] D. Zhao, S. Lampman, Hot Tension and Compression Testing, in: H. Kuhn, D. Medlin (Eds.), Mech. Test. Eval., ASM International, 2000: p. 0. https://doi.org/10.31399/asm.hb.v08.a0003266.

[53] K.L. Murty, S. Gollapudi, K. Ramaswamy, M.D. Mathew, I. Charit, 3 - Creep deformation of materials in light water reactors (LWRs), in: K.L. Murty (Ed.), Mater. Ageing Degrad. Light Water React., Woodhead Publishing, 2013: pp. 81–148. https://doi.org/10.1533/9780857097453.1.81.

[54] T.G. Langdon, Grain boundary sliding revisited: Developments in sliding over four decades, J. Mater. Sci. 41 (2006) 597–609. https://doi.org/10.1007/s10853-006-6476-0.

[55] E.O. Olakanmi, Selective laser sintering/melting (SLS/SLM) of pure Al, Al–Mg, and Al–Si powders: Effect of processing conditions and powder properties, J. Mater. Process. Technol. 213 (2013) 1387–1405. https://doi.org/10.1016/j.jmatprotec.2013.03.009.

[56] N.T. Aboulkhair, I. Maskery, C. Tuck, I. Ashcroft, N.M. Everitt, The microstructure and mechanical properties of selectively laser melted AlSi10Mg: The effect of a conventional T6-like heat treatment, Mater. Sci. Eng. A. 667 (2016) 139–146. https://doi.org/10.1016/j.msea.2016.04.092.

[57] N.T. Aboulkhair, N.M. Everitt, I. Ashcroft, C. Tuck, Reducing porosity in AlSi10Mg parts processed by selective laser melting, Addit. Manuf. 1 (2014) 77–86. https://doi.org/10.1016/j.addma.2014.08.001.

[58] E. Brandl, U. Heckenberger, V. Holzinger, D. Buchbinder, Additive manufactured AlSi10Mg samples using Selective Laser Melting (SLM): Microstructure, high cycle fatigue, and fracture behavior, Mater. Des. 34 (2012) 159–169. https://doi.org/10.1016/j.matdes.2011.07.067.

[59] N. Read, W. Wang, K. Essa, M.M. Attallah, Selective laser melting of AlSi10Mg alloy: Process optimisation and mechanical properties development, Mater. Des. 1980-2015. 65 (2015) 417–424. https://doi.org/10.1016/j.matdes.2014.09.044.

[60] M.L. Montero-Sistiaga, R. Mertens, B. Vrancken, X. Wang, B. Van Hooreweder, J.-P. Kruth, J. Van Humbeeck, Changing the alloy composition of Al7075 for better processability by selective laser melting, J. Mater. Process. Technol. 238 (2016) 437–445. https://doi.org/10.1016/j.jmatprotec.2016.08.003.

[61] J.H. Martin, B.D. Yahata, J.M. Hundley, J.A. Mayer, T.A. Schaedler, T.M. Pollock, 3D printing of high-strength aluminium alloys, Nature. 549 (2017) 365–369.

[62] Q. Jia, P. Rometsch, P. Kürnsteiner, Q. Chao, A. Huang, M. Weyland, L. Bourgeois, X. Wu, Selective laser melting of a high strength AlMnSc alloy: Alloy design and strengthening mechanisms, Acta Mater. 171 (2019) 108–118. https://doi.org/10.1016/j.actamat.2019.04.014.

[63] R. Li, M. Wang, T. Yuan, B. Song, C. Chen, K. Zhou, P. Cao, Selective laser melting of a novel Sc and Zr modified Al-6.2Mg alloy: Processing, microstructure, and properties, Powder Technol. 319 (2017) 117–128. https://doi.org/10.1016/j.powtec.2017.06.050.

[64] A.B. Spierings, K. Dawson, P. Dumitraschkewitz, S. Pogatscher, K. Wegener, Microstructure characterization of SLM-processed Al-Mg-Sc-Zr alloy in the heat treated and HIPed condition, Addit. Manuf. 20 (2018) 173–181. https://doi.org/10.1016/j.addma.2017.12.011.

[65] L. Zhou, H. Pan, H. Hyer, S. Park, Y. Bai, B. McWilliams, K. Cho, Y. Sohn, Microstructure and tensile property of a novel AlZnMgScZr alloy additively manufactured by gas atomization and laser powder bed fusion, Scr. Mater. 158 (2019) 24–28. https://doi.org/10.1016/j.scriptamat.2018.08.025.

[66] A.B. Spierings, K. Dawson, T. Heeling, P.J. Uggowitzer, R. Schäublin, F. Palm, K. Wegener, Microstructural features of Sc- and Zr-modified Al-Mg alloys processed by selective laser melting, Mater. Des. 115 (2017) 52–63. https://doi.org/10.1016/j.matdes.2016.11.040.

[67] J.R. Croteau, S. Griffiths, M.D. Rossell, C. Leinenbach, C. Kenel, V. Jansen, D.N. Seidman, D.C. Dunand, N.Q. Vo, Microstructure and mechanical properties of Al-Mg-Zr alloys processed by selective laser melting, Acta Mater. 153 (2018) 35–44. https://doi.org/10.1016/j.actamat.2018.04.053.

[68] K. Schmidtke, F. Palm, A. Hawkins, C. Emmelmann, Process and Mechanical Properties: Applicability of a Scandium modified Al-alloy for Laser Additive Manufacturing, Lasers Manuf. 2011 - Proc. Sixth Int. WLT Conf. Lasers Manuf. 12 (2011) 369–374. https://doi.org/10.1016/j.phpro.2011.03.047.

[69] A.B. Spierings, K. Dawson, M. Voegtlin, F. Palm, P.J. Uggowitzer, Microstructure and mechanical properties of as-processed scandium-modified aluminium using selective laser melting, CIRP Ann. - Manuf. Technol. 65 (2016) 213–216. https://doi.org/10.1016/j.cirp.2016.04.057.

[70] A.B. Spierings, K. Dawson, K. Kern, F. Palm, K. Wegener, SLM-processed Sc- and Zr- modified Al-Mg alloy: Mechanical properties and microstructural effects of heat treatment, Mater. Sci. Eng. A. 701 (2017) 264–273. https://doi.org/10.1016/j.msea.2017.06.089.

[71] J.A. Lyndon, R.K. Gupta, M.A. Gibson, N. Birbilis, Electrochemical behaviour of the β-phase intermetallic (Mg2Al3) as a function of pH as relevant to corrosion of aluminium–magnesium alloys, Corros. Sci. 70 (2013) 290–293. https://doi.org/10.1016/j.corsci.2012.12.022.

[72] R.A. Karnesky, D.N. Seidman, D.C. Dunand, Creep of Al-Sc Microalloys with Rare-Earth Element Additions, Mater. Sci. Forum. 519–521 (2006) 1035–1040. https://doi.org/10.4028/www.scientific.net/MSF.519-521.1035.

[73] C. Booth-Morrison, D.N. Seidman, D.C. Dunand, Effect of Er additions on ambient and high-temperature strength of precipitation-strengthened Al–Zr–Sc–Si alloys, Acta Mater. 60 (2012) 3643–3654. https://doi.org/10.1016/j.actamat.2012.02.030.

[74] K.E. Knipling, D.C. Dunand, Creep resistance of cast and aged Al–0.1Zr and Al–0.1Zr–0.1Ti (at.%) alloys at 300–400°C, Scr. Mater. 59 (2008) 387–390. https://doi.org/10.1016/j.scriptamat.2008.02.059.

[75] D. Erdeniz, W. Nasim, J. Malik, A.R. Yost, S. Park, A. De Luca, N.Q. Vo, I. Karaman, B. Mansoor, D.N. Seidman, D.C. Dunand, Effect of vanadium micro-alloying on the microstructural evolution and creep behavior of Al-Er-Sc-Zr-Si alloys, Acta Mater. 124 (2017) 501–512. https://doi.org/10.1016/j.actamat.2016.11.033.

[76] N.E. Uzan, R. Shneck, O. Yeheskel, N. Frage, High-temperature mechanical properties of AlSi10Mg specimens fabricated by additive manufacturing using selective la-

ser melting technologies (AM-SLM), Addit. Manuf. 24 (2018) 257–263. https://doi.org/10.1016/j.addma.2018.09.033.

[77] Y.-C. Hagedorn, J. Risse, W. Meiners, N. Pirch, K. Wissenbach, R. Poprawe, Processing of nickel based superalloy MAR M-247 by means of High Temperature - Selective Laser Melting (HT - SLM), in: 2014: pp. 291–295. https://www.scopus.com/inward/record.uri?eid=2-s2.0-84892160456&partnerID=40&md5=62302042d538a33753c4a18268898c63.

[78] N. Kalentics, N. Sohrabi, H.G. Tabasi, S. Griffiths, J. Jhabvala, C. Leinenbach, A. Burn, R.E. Logé, Healing cracks in Selective Laser Melting by 3D Laser Shock Peening, Addit. Manuf. (2019) 100881. https://doi.org/10.1016/j.addma.2019.100881.

[79] N.J. Harrison, I. Todd, K. Mumtaz, Reduction of micro-cracking in nickel superalloys processed by Selective Laser Melting: A fundamental alloy design approach, Acta Mater. 94 (2015) 59–68. https://doi.org/10.1016/j.actamat.2015.04.035.

[80] R. Engeli, T. Etter, S. Hövel, K. Wegener, Processability of different IN738LC powder batches by selective laser melting, J. Mater. Process. Technol. 229 (2016) 484–491. https://doi.org/10.1016/j.jmatprotec.2015.09.046.

[81] K. Kunze, T. Etter, J. Grässlin, V. Shklover, Texture, anisotropy in microstructure and mechanical properties of IN738LC alloy processed by selective laser melting (SLM), Mater. Sci. Eng. A. 620 (2015) 213–222. https://doi.org/10.1016/j.msea.2014.10.003.

[82] P. Kanagarajah, F. Brenne, T. Niendorf, H.J. Maier, Inconel 939 processed by selective laser melting: Effect of microstructure and temperature on the mechanical properties under static and cyclic loading, Mater. Sci. Eng. A. 588 (2013) 188–195. https://doi.org/10.1016/j.msea.2013.09.025.

[83] V.D. Divya, R. Muñoz-Moreno, O.M.D.M. Messé, J.S. Barnard, S. Baker, T. Illston, H.J. Stone, Microstructure of selective laser melted CM247LC nickel-based superalloy and its evolution through heat treatment, Mater. Charact. 114 (2016) 62–74. https://doi.org/10.1016/j.matchar.2016.02.004.

[84] L. Rickenbacher, T. Etter, S. Hoevel, K. Wegener, High temperature material properties of IN738LC processed by selective laser melting (SLM) technology, Rapid Prototyp. J. 19 (2013) 282–290. https://doi.org/10.1108/13552541311323281.

[85] A.B. Spierings, K. Dawson, K. Kern, F. Palm, K. Wegener, SLM-processed Sc- and Zr- modified Al-Mg alloy: Mechanical properties and microstructural effects of heat treatment, Mater. Sci. Eng. A. 701 (2017) 264–273. https://doi.org/10.1016/j.msea.2017.06.089.

[86] R.E. Aune, L. Battezzati, R. Brooks, I. Egry, H.-J. Fecht, J.-P. Garandet, M. Hayashi, K.C. Mills, A. Passerone, P.N. Quested, E. Ricci, F. Schmidt-Hohagen, S. Seetharaman, B. Vinet, R.K. Wunderlich, Thermophysical properties of IN738lc, MM247lc and CMSX-4 in the liquid and high temperature solid phase, in: Superalloys 718 625 706 Deriv. Proc., 2005: pp. 467–476. http://urn.kb.se/resolve?urn=urn:nbn:se:kth:diva-43342 (accessed October 14, 2011).

[87] R. Przeliorz, J. Piatkowski, THERMOPHYSICAL PROPERTIES OF NICKEL-BASED CAST SUPERALLOYS, Metalurgija. 54 (2015) 543–546.

[88] C.A. Schneider, W.S. Rasband, K.W. Eliceiri, NIH Image to ImageJ: 25 years of image analysis, Nat. Methods. 9 (2012) 671.

[89] J. Xu, X. Lin, Y. Zhao, P. Guo, X. Wen, Q. Li, H. Yang, H. Dong, L. Xue, W. Huang, HAZ Liquation Cracking Mechanism of IN-738LC Superalloy Prepared by Laser Solid

Forming, Metall. Mater. Trans. A. 49 (2018) 5118–5136. https://doi.org/10.1007/s11661-018-4826-6.

[90] S. Griffiths, M.D. Rossell, J. Croteau, N.Q. Vo, D.C. Dunand, C. Leinenbach, Effect of laser rescanning on the grain microstructure of a selective laser melted Al-Mg-Zr alloy, Met. Addit. Manuf. Microstruct. Prop. 143 (2018) 34–42. https://doi.org/10.1016/j.matchar.2018.03.033.

[91] J. Murray, A. Peruzzi, J.P. Abriata, The Al-Zr (aluminum-zirconium) system, J. Phase Equilibria. 13 (1992) 277–291. https://doi.org/10.1007/BF02667556.

[92] K.E. Knipling, D.C. Dunand, D.N. Seidman, Nucleation and Precipitation Strengthening in Dilute Al-Ti and Al-Zr Alloys, Metall. Mater. Trans. A. 38 (2007) 2552–2563. https://doi.org/10.1007/s11661-007-9283-6.

[93] Malgorzata Warmuzek, Intermetallic Phases in Aluminum-Silicon Technical Cast Alloys, in: Alum.-Silicon Cast. Alloys, ASM International, 2017.

[94] A. Plotkowski, O. Rios, N. Sridharan, Z. Sims, K. Unocic, R.T. Ott, R.R. Dehoff, S.S. Babu, Evaluation of an Al-Ce alloy for laser additive manufacturing, Acta Mater. 126 (2017) 507–519. https://doi.org/10.1016/j.actamat.2016.12.065.

[95] S. HORI, S. SAJI, A. TAKEHARA, Metastable phase and grain refinement in rapidly solidified Al-Zr alloys, J. Jpn. Inst. Light Met. 31 (1981) 793–797. https://doi.org/10.2464/jilm.31.793.

[96] C. Limmaneevichitr, S. Kou, Flow visualisation demonstrating surface-tension driven convection in the weld pool, Uicee, Faculty Engineering, Clayton, 2001.

[97] C. Limmaneevichitr, S. Kou, Visualization of Marangoni convection in simulated weld pools, Weld. J. 79 (2000) 126S-135S.

[98] D. Herzog, V. Seyda, E. Wycisk, C. Emmelmann, Additive manufacturing of metals, Acta Mater. 117 (2016) 371–392. https://doi.org/10.1016/j.actamat.2016.07.019.

[99] W.J. Sames, K.A. Unocic, R.R. Dehoff, T. Lolla, S.S. Babu, Thermal effects on microstructural heterogeneity of Inconel 718 materials fabricated by electron beam melting, J. Mater. Res. 29 (2014) 1920–1930. https://doi.org/10.1557/jmr.2014.140.

[100] R.R. Dehoff, M.M. Kirka, W.J. Sames, H. Bilheux, A.S. Tremsin, L.E. Lowe, S.S. Babu, Site specific control of crystallographic grain orientation through electron beam additive manufacturing, Mater. Sci. Technol. 31 (2015) 931–938. https://doi.org/10.1179/1743284714Y.0000000734.

[101] C Kenel, G. Dasargyri, T. Bauer, A. Colella, A.B. Spierings, C. Leinenbach, K. Wegener, Selective laser melting of an oxide dispersion strengthened TiAl alloy towards production of complex structures, (n.d.).

[102] Evren Yasa, Jan Deckers, Jean-Pierre Kruth, The investigation of the influence of laser re-melting on density, surface quality and microstructure of selective laser melting parts, Rapid Prototyp. J. 17 (2011) 312–327. https://doi.org/10.1108/13552541111156450.

[103] J. Xie, A. Kar, Laser welding of thin sheet steel with surface oxidation, Weld. J. Miami Fla. 78 (1999) 343-s.

[104] L.K. Ang, Y.Y. Lau, R.M. Gilgenbach, H.L. Spindler, Analysis of laser absorption on a rough metal surface, Appl. Phys. Lett. 70 (1997) 696–698. https://doi.org/10.1063/1.118242.

[105] D. Bergström, J. Powell, A.F.H. Kaplan, The absorptance of steels to Nd:YLF and Nd:YAG laser light at room temperature, Appl. Surf. Sci. 253 (2007) 5017–5028. https://doi.org/10.1016/j.apsusc.2006.11.018.

[106] T. Forsman, A.F.H. Kaplan, J. Powell, C. Magnusson, Nd:YAG laser welding of aluminum; Factors affecting absorptivity, Lasers Eng. 8 (1999) 295–309.

[107] Nikolay K. Tolochko, Yurii V. Khlopkov, Sergei E. Mozzharov, Michail B. Ignatiev, Tahar Laoui, Victor I. Titov, Absorptance of powder materials suitable for laser sintering, Rapid Prototyp. J. 6 (2000) 155–161. https://doi.org/10.1108/13552540010337029.

[108] A.F.H. Kaplan, Local absorptivity modulation of a 1µm-laser beam through surface waviness, Appl. Surf. Sci. 258 (2012) 9732–9736. https://doi.org/10.1016/j.apsusc.2012.06.020.

[109] M.J. Matthews, G. Guss, S.A. Khairallah, A.M. Rubenchik, P.J. Depond, W.E. King, Denudation of metal powder layers in laser powder bed fusion processes, Acta Mater. 114 (2016) 33–42. https://doi.org/10.1016/j.actamat.2016.05.017.

[110] A. Bauereiß, T. Scharowsky, C. Körner, Defect generation and propagation mechanism during additive manufacturing by selective beam melting, J. Mater. Process. Technol. 214 (2014) 2522–2528. https://doi.org/10.1016/j.jmatprotec.2014.05.002.

[111] S. Bao, K. Tang, A. Kvithyld, M. Tangstad, T.A. Engh, Wettability of Aluminum on Alumina, Metall. Mater. Trans. B. 42 (2011) 1358–1366. https://doi.org/10.1007/s11663-011-9544-z.

[112] D.-J. Wang, S.-T. Wu, The influence of oxidation on the wettability of aluminum on sapphire, Acta Metall. Mater. 42 (1994) 4029–4034. https://doi.org/10.1016/0956-7151(94)90180-5.

[113] D. Quéré, Rough ideas on wetting, Fundam. Probl. Stat. Phys. 313 (2002) 32–46. https://doi.org/10.1016/S0378-4371(02)01033-6.

[114] A.V. Mikhaylovskaya, A.G. Mochugovskiy, V.S. Levchenko, N.Yu. Tabachkova, W. Mufalo, V.K. Portnoy, Precipitation behavior of L12 Al3Zr phase in Al-Mg-Zr alloy, Mater. Charact. 139 (2018) 30–37. https://doi.org/10.1016/j.matchar.2018.02.030.

[115] E. Nes, H. Billdal, The mechanism of discontinuous precipitation of the metastable Al3Zr phase from an Al-Zr solid solution, Acta Metall. 25 (1977) 1039–1046. https://doi.org/10.1016/0001-6160(77)90133-X.

[116] N. Ryum, Precipitation and recrystallization in an A1-0.5 WT.% Zr-alloy, Acta Metall. 17 (1969) 269–278. https://doi.org/10.1016/0001-6160(69)90067-4.

[117] T. Haugan, E. Nes, N. Ryum, Precipitation Reactions in Ai-Zr-Alloys, MRS Proc. 21 (1982) 495. https://doi.org/10.1557/PROC-21-495.

[118] K.B. Hyde, A.F. Norman, P.B. Prangnell, The effect of cooling rate on the morphology of primary Al3Sc intermetallic particles in Al–Sc alloys, Acta Mater. 49 (2001) 1327–1337. https://doi.org/10.1016/S1359-6454(01)00050-7.

[119] R.A. Ricks, A.J. Porter, R.C. Ecob, The growth of γ' precipitates in nickel-base superalloys, Acta Metall. 31 (1983) 43–53. https://doi.org/10.1016/0001-6160(83)90062-7.

[120] G.K. Sigworth, T.A. Kuhn, Grain Refinement of Aluminum Casting Alloys[1], in: S. Viswanathan, D. Apelian, R.J. Donahue, B. DasGupta, M. Gywn, J.L. Jorstad, R.W. Monroe, M. Sahoo, T.E. Prucha, D. Twarog (Eds.), Casting, ASM International, 2008: p. 0. https://doi.org/10.31399/asm.hb.v15.a0005302.

[121] T.M. Osman, J.D. Rigney, Introduction to the Mechanical Behavior of Metals, in: H. Kuhn, D. Medlin (Eds.), Mech. Test. Eval., ASM International, 2000: p. 0. https://doi.org/10.31399/asm.hb.v08.a0003254.

[122] X. Wu, Y. Zhu, Heterogeneous materials: a new class of materials with unprecedented mechanical properties, Mater. Res. Lett. 5 (2017) 527–532. https://doi.org/10.1080/21663831.2017.1343208.

[123] Y. Zhao, T. Topping, Y. Li, E.J. Lavernia, Strength and Ductility of Bi-Modal Cu, Adv. Eng. Mater. 13 (2011) 865–871. https://doi.org/10.1002/adem.201100019.

[124] T.H. Sanders, Aluminum-lithium alloys, Warrendale PA Metall. Soc. AIME 1981 388 P. (1981).

[125] F. Li, Microstructural evolution and mechanismsof superplasticity in an Al-4-5%Mg alloy, Mater. Sci. Technol. 13 (1997) 17–23. https://doi.org/10.1179/mst.1997.13.1.17.

[126] S.B. Prabu, K.A. Padmanabhan, Chapter 8 - Superplasticity in and Superplastic Forming of Aluminum–Lithium Alloys, in: N. Eswara Prasad, A.A. Gokhale, R.J.H. Wanhill (Eds.), Alum.-Lithium Alloys, Butterworth-Heinemann, Boston, 2014: pp. 221–258. https://doi.org/10.1016/B978-0-12-401698-9.00008-2.

[127] F. Tang, B.Q. Han, M. Hagiwara, J.M. Schoenung, Tensile Properties of a Nanostructured Al-5083/SiCp Composite at Elevated Temperatures, Adv. Eng. Mater. 9 (2007) 286–291. https://doi.org/10.1002/adem.200600270.

[128] V. Sklenicka, J. Dvorak, P. Kral, M. Svoboda, M. Kvapilova, T.G. Langdon, Factors influencing creep flow and ductility in ultrafine-grained metals, Mater. Sci. Eng. A. 558 (2012) 403–411. https://doi.org/10.1016/j.msea.2012.08.019.

[129] M. Kawasaki, V. Sklenička, T.G. Langdon, An evaluation of creep behavior in ultrafine-grained aluminum alloys processed by ECAP, J. Mater. Sci. 45 (2010) 271–274. https://doi.org/10.1007/s10853-009-3975-9.

[130] D. Williams, E. P. Butler, Grain Boundary Discontinuous Precipitation Reactions, 1981. https://doi.org/10.1179/imr.1981.26.1.153.

[131] C. Herzig, Y. Mishin, Grain Boundary Diffusion in Metals, in: P. Heitjans, J. Kärger (Eds.), Diffus. Condens. Matter Methods Mater. Models, Springer Berlin Heidelberg, Berlin, Heidelberg, 2005: pp. 337–366. https://doi.org/10.1007/3-540-30970-5_8.

[132] J.C. Lippold, Welding metallurgy and weldability, 2015. http://www.books24x7.com/marc.asp?bookid=63808 (accessed September 27, 2019).

[133] G. Matache, D.M. Stefanescu, C. Puscasu, E. Alexandrescu, Dendritic segregation and arm spacing in directionally solidified CMSX-4 superalloy, Int. J. Cast Met. Res. 29 (2016) 303–316. https://doi.org/10.1080/13640461.2016.1166726.

[134] S. Kou, Solidification and liquation cracking issues in welding, JOM. 55 (2003) 37–42. https://doi.org/10.1007/s11837-003-0137-4.

[135] J.-W. Park, J.M. Vitek, S.S. Babu, S.A. David, Stray grain formation, thermomechanical stress and solidification cracking in single crystal nickel base superalloy welds, Sci. Technol. Weld. Join. 9 (2004) 472–482. https://doi.org/10.1179/136217104225021841.

[136] B. Hu, I.M. Richardson, Mechanism and possible solution for transverse solidification cracking in laser welding of high strength aluminium alloys, Mater. Sci. Eng. A. 429 (2006) 287–294. https://doi.org/10.1016/j.msea.2006.05.040.

[137] N. Wang, S. Mokadem, M. Rappaz, W. Kurz, Solidification cracking of superalloy single- and bi-crystals, Acta Mater. 52 (2004) 3173–3182. https://doi.org/10.1016/j.actamat.2004.03.047.

[138] Superalloys : Alloying and Performance, 2010. http://search.ebscohost.com/login.aspx?direct=true&db=nlebk&AN=395922&site=eds-live (accessed October 7, 2019).

[139] J. Zhang, R.F. Singer, Effect of grain-boundary characteristics on castability of nickel-base superalloys, Metall. Mater. Trans. A. 35 (2004) 939–946. https://doi.org/10.1007/s11661-004-0018-7.

[140] K. Heck, R. Blackford, R.F. Singer, Castability of directionally solidified nickel base superalloys, Mater. Sci. Technol. 15 (1999) 213–220. https://doi.org/10.1179/026708399101505617.

[141] T.D. Anderson, J.N. DuPont, T. DebRoy, Origin of stray grain formation in single-crystal superalloy weld pools from heat transfer and fluid flow modeling, Acta Mater. 58 (2010) 1441–1454. https://doi.org/10.1016/j.actamat.2009.10.051.

[142] R. Aune, L. Battezzati, R. Brooks, I. Egry, H.-J. Fecht, J.-P. Garandet, K.C. Mills, A. Passerone, P.N. Quested, E. Ricci, S. Schneider, S. Seetharaman, R.K. Wunderlich, B. Vinet, Surface tension and viscosity of industrial alloys from parabolic flight experiments - Results of the ThermoLab project, Microgravity Sci. Technol. 15 (2005) 11–14.

[143] D. Lacroix, G. Jeandel, C. Boudot, Solution of the radiative transfer equation in an absorbing and scattering Nd:YAG laser-induced plume, J. Appl. Phys. 84 (1998) 2443–2449. https://doi.org/10.1063/1.368405.

[144] G. L. Erickson, K. Harris, R.E. Schwer, Directionally Solidified DS CM 247 LC-Optimized Mechanical Properties Resulting From Extensive gamma prime Solutioning, (n.d.).

[145] I. Dempster, R. Wallis, Heat Treatment Metallurgy of Nickel-Base Alloys, in: G.E. Totten (Ed.), Heat Treat. Nonferrous Alloys, ASM International, 2016: p. 0. https://doi.org/10.31399/asm.hb.v04e.a0006261.

[146] W.C. Johnson, On the elastic stabilization of precipitates against coarsening under applied load, Acta Metall. 32 (1984) 465–475. https://doi.org/10.1016/0001-6160(84)90120-2.

[147] S. Meher, L.K. Aagesen, L.J. Carroll, M.C. Carroll, T.M. Pollock, Understanding of Inverse Coarsening of γ' precipitates in Ni-base Superalloys, Microsc. Microanal. 22 (2016) 1258–1259. https://doi.org/10.1017/S1431927616007133.

[148] S. JUNG, T. YAMANE, Y. MINAMINO, K. HIRAO, H. ARAKI, S. SAJI, INTERDIFFUSION AND ITS SIZE EFFECT IN NICKEL SOLID-SOLUTIONS OF NI-CO, NI-CR AND NI-TI SYSTEMS, J. Mater. Sci. Lett. 11 (1992) 1333–1337. https://doi.org/10.1007/BF00729354.

[149] D. Witkin, Z. Lee, R. Rodriguez, S. Nutt, E. Lavernia, Al–Mg alloy engineered with bimodal grain size for high strength and increased ductility, Scr. Mater. 49 (2003) 297–302. https://doi.org/10.1016/S1359-6462(03)00283-5.

[150] L.W. Sink, G.S. Hoppin III, M. Fuji, Low-cost directionally-solidified turbine blades, volume 1, AiResearch Mfg. Co., Phoenix, AZ, United States, 1979.

Curriculum Vitae

Seth J. Griffiths

Güchstrasse 2, 8330 Pfäffikon, CH
+41 75 433 1692 | seth.griffiths@gmail.com
Date of Birth: 8 Feb. 1988
Nationality: USA
Swiss Permit: Aufenthaltsbewilligung (B)

EDUCATION

École polytechnique fédérale de Lausanne (EPFL) | Lausanne, CH
PhD Student Materials Science and Engineering | August 2016 - July 2020

Colorado School of Mines | Golden, CO, USA
M.S. Metallurgical and Materials Engineering | June 2010 – May 2012

University of Illinois at Urbana-Champaign | Urbana, IL, USA
B.S. Materials Science and Engineering | Aug. 2006 – May 2010

EXPERIENCE

Empa (Swiss Federal Laboratories for Materials Science and Technology) | Dübendorf, CH
Laboratory for Advanced Materials Processing
PhD Student | Aug. 2016– Current

- Researching the materials science of nickel superalloys and aluminum alloys fabricated by Additive Manufacturing, specifically Laser Powder Bed Fusion (L-PBF).

Boeing Research and Technology | Everett, WA, USA
Landing Gear Materials Process and Support Engineer | June 2014 – July 2016

- Provided metallurgical support for the design, manufacture, and repair of steel, aluminum, and titanium landing gear structure.
- Reviewed manufacturing plans of landing gear forgings and machined parts to ensure engineering drawing requirements were met.
- Performed fracture analysis of metallic landing gear components and authored reports documenting the results.

Boeing Research and Technology | Everett, WA, USA
Airframe Materials and Process Support Engineer | Oct. 2012 – June 2014

- Reviewed and approved engineering drawings and manufacturing plans of airframe components.
- Performed fracture analysis of metallic airframe components and authored reports documenting the results.
- Authored a titanium microstructure handbook (internal publication) for the titanium alloys and product forms (sheet, plate, forgings, castings and extrusions) commonly utilized in the airframe.

Boeing Research and Technology | Everett, WA, USA
Systems Materials and Process Support Engineer | June 2012 – Oct. 2012

- Reviewed supplier engineering data packages to ensure engineering specifications and requirements were met.

General Electric Aviation | Cincinnati, OH, USA
Airfoil Materials Development Internship | May 2009 – Aug. 2009

- Performed metallurgical characterization of nickel superalloys and ceramic coatings used in the hot section of aircraft turbine engines.

John Deere Power Systems | Cedar Falls, IA, USA
Manufacturing Engineering Internship | May 2008 – Aug. 2008

- Provided metallurgical engineering support for the induction heat treatment of engine crankshafts.

Tyco Valves and Controls | Prophetstown, IL, USA
Engineering Internship | May 2007 – Aug. 2007

- Assisted with experiments to determine performance characteristics of fluid jet pumps.

PUBLICATIONS RELATED TO THESIS WORK

- S. Griffiths, M. Rossell, J. Croteau, N. Vo, D.C. Dunand, C. Leinenbach, Effect of laser rescanning on the grain microstructure of a selective laser melted Al-Mg-Zr alloy, Mater. Charact. 143 (2018) 34–42.
- J.R. Croteau, S. Griffiths, M.D. Rossell, C. Leinenbach, C. Kenel, V. Jansen, D.N. Seidman, D.C. Dunand, N.Q. Vo, Microstructure and mechanical properties of Al-Mg-Zr alloys processed by selective laser melting, Acta Mater. 153 (2018) 35–44.
- S. Griffiths, J. Croteau, M. Rossell, R. Erni, A. De Luca, N. Vo, D. Dunand, C. Leinenbach, Coarsening-and creep resistance of precipitation-strengthened Al–Mg–Zr alloys processed by selective laser melting, Acta Mater. 188 (2020) 192–202.
- N. Kalentics, N. Sohrabi, H.G. Tabasi, S. Griffiths, J. Jhabvala, C. Leinenbach, A. Burn, R.E. Loge, Healing cracks in selective laser melting by 3D laser shock peening, Addit. Manuf. 30 (2019) 100881.

OTHER PUBLICATIONS

- A. Arabi-Hashemi, X. Maeder, R. Figi, C. Schreiner, S. Griffiths, C. Leinenbach, 3D magnetic patterning in additive manufacturing via site-specific in-situ alloy modification, Appl. Mater. Today. 18 (2020) 100512.
- N. Kalentics, M.O.V. de Seijas, S. Griffiths, C. Leinenbach, R.E. Logé, 3D laser shock peening– a new method for improving fatigue properties of selective laser melted parts, Addit. Manuf. 33 (2020) 101112.

CONFERENCE PRESENTATIONS

- S. Griffiths, C. Leinenbach, N. Vo, J. Croteau, D. Seidman, D, Dunand. Additive Manufacturing of L12 Strengthened Aluminum Superalloy Addalloy™, TMS 2018, Phoenix, USA. (14.03.2018) Oral presentation
- S. Griffiths, C. Leinenbach, N. Vo, J. Croteau, D. Seidman, D, Dunand. Additive Manufacturing of L12 Strengthened Aluminum Superalloy Addalloy™, AAMS 2018, Sheffield, UK. (04.09.2018) Oral presentation
- S. J. Griffiths, T. Ivas, R. Wrobel, C. Leinenbach. Selective Laser Melting of Gamma Prime Strengthened Nickel-base Superalloy CM247LC, AAMS 2019, Gothenberg Sweden. (20.09.2019) Oral presentation